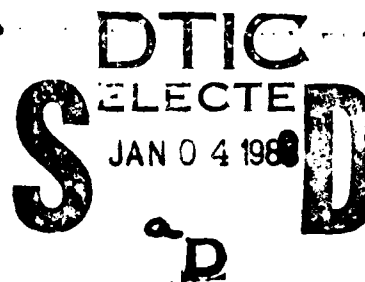


AD-A204 707

# Precipitation Phenomena: Deformation and Aging

Edited by **B.N.Doy**



DISTRIBUTION STATEMENT A  
Approved for public release  
Distribution Unlimited

## World Materials Congress



Published by



# **PRECIPITATION PHENOMENA: DEFORMATION AND AGING**

*Proceedings of an International Conference  
held in conjunction with the  
1988 World Materials Congress  
Chicago, Illinois, USA  
24-30 September 1988*

*Edited by*  
**B. N. Dey**

*Sponsored by*  
**ASM INTERNATIONAL'S Materials Sciences Division,  
Annealing and Recovery Committee**

*Published by*



The publication of this Conference Proceedings of the 1988 World Materials Congress has been made possible by the generous contribution of ELETROMETAL S.A.

Copyright © 1988  
by  
ASM INTERNATIONAL™  
All Rights Reserved

No part of this book may be reproduced, stored in a retrieval system, or transmitted, in any form or by any means, electronic, mechanical photocopying, recording, or otherwise, without the prior written permission of the publisher. No warranties, express or implied, are given in connection with the accuracy or completeness of this publication and no responsibility can be taken for any claims that may arise.

Nothing contained in this book is to be construed as a grant of any right or manufacture, sale, or use in connection with any method, process, apparatus, product, or composition, whether or not covered by letters patent or registered trademark, nor as a defense against liability for the infringement of letters patent or registered trademark.

Library of Congress Catalog Card Number 88-071671  
ISBN: 0-87170-338-6  
SAN: 204-7586

Printed in the United States of America

UNCLASSIFIED

SECURITY CLASSIFICATION OF THIS PAGE (When Data Entered)

REPORT DOCUMENTATION PAGE		READ INSTRUCTIONS BEFORE COMPLETING FORM
1. REPORT NUMBER ARO 25297.1-MS-CF	2. GOVT ACCESSION NO. N/A	3. RECIPIENT'S CATALOG NUMBER N/A
4. TITLE (and Subtitle) 1988 World Materials Congress Proceedings 24-30 Sep 88, Chicago <u>Eight Volumes</u>		5. TYPE OF REPORT & PERIOD COVERED Final 1 Oct 87 - 31 Mar 89
7. AUTHOR(s) S. G. Fishman and A. K. Dhingra, editors		6. PERFORMING ORG. REPORT NUMBER N/A
9. PERFORMING ORGANIZATION NAME AND ADDRESS ASM International Detroit, MI 48202		8. CONTRACT OR GRANT NUMBER(s) DAAL03-87-G-0128
11. CONTROLLING OFFICE NAME AND ADDRESS U. S. Army Research Office P. O. Box 12211 Research Triangle Park NC 27709		10. PROGRAM ELEMENT, PROJECT, TASK AREA & WORK UNIT NUMBERS N/A
14. MONITORING AGENCY NAME & ADDRESS (if different from Controlling Office)		12. REPORT DATE 1988
		13. NUMBER OF PAGES
		15. SECURITY CLASS. (of this report) Unclassified
		15a. DECLASSIFICATION/DOWNGRADING SCHEDULE
16. DISTRIBUTION STATEMENT (of this Report)  Submitted for announcement only.		
17. DISTRIBUTION STATEMENT (of the abstract entered in Block 20, if different from Report)		
18. SUPPLEMENTARY NOTES The view, opinions, and/or findings contained in this report are those of the author(s) and should not be construed as an official Department of the Army position, policy, or decision, unless so designated by other documentation.		
19. KEY WORDS (Continue on reverse side if necessary and identify by block number) Composites, Sheet Steels, Electronic Materials, Wear Resistance, Precipitation Phenomena, High Integrity Castings, Inclusions, HSLA Steels		
20. ABSTRACT (Continue on reverse side if necessary and identify by block number) The proceedings of the 1988 World Materials Congress were published by ASM and consists of the following volumes: 1. Microalloyed HSLA Steels Conference Proceedings / 2. Inclusions and Their Influence on Material Behavior 3. High Integrity Castings / 4. Precipitation Phenomena: Deformation and Aging, 5. Wear Resistance of Metals and Alloys <span style="float: right;">(over) &gt;</span>		

DD FORM 1 JAN 73 1473 EDITION OF 1 NOV 65 IS OBSOLETE

UNCLASSIFIED

SECURITY CLASSIFICATION OF THIS PAGE (When Data Entered)

88 12 28 025

ABSTRACT CONTINUED:

- 6. Electronic Materials and Processing ,
- 7. Corrosion-Resistant Automotive Sheet Steels ,
- 8. Cast Reinforced Metal Composites .

JES

Proc # 70.00

**Program Organizer**

Biswa N. Dey, SUNY, Utica, New York 13504

**Chief Session Chairman**

Biswa N. Dey, SUNY, Utica, New York 13504

**Session Chairmen**

- Session 1: Y. I. Ustinovshikov, Division of Academy of Sciences, Izhevsk, USSR  
J. E. Flinn, Idaho National Engineering Laboratories, Idaho Falls, Idaho
- Session 2: H. Zhou, Xi'an Jiaotong University, Xian Shaanxi Province, The People's  
Republic of China  
F. D. S. Marquis, South Dakota School of Mines, Rapid City, South Dakota
- Session 3: E. M. P. Silva, Universidade Federal de Minas Gerais, Belo Horizonte,  
MG Brazil  
C. S. Pande, Naval Research Laboratories, Washington, DC
- Session 4: E. Szpunar, 05-230 Kobylka, K. Warszawy, ul. Modrzewskiego 2A Poland  
D. Atteridge, Oregon Graduate Center, Beaverton, Oregon



Sold by:  
ASM International  
9639 Kinsman Road  
Metals Park, OH 44073  
Price:

Accession For	
NTIS	CRA&I <input checked="" type="checkbox"/>
DTIC	TAB <input type="checkbox"/>
Unclassified	<input type="checkbox"/>
Justification	
By <i>70.00 per call</i>	
Distribution	
Availability Codes	
Dist	Avail and/or Special
<i>A-1 21</i>	

III 88 12 28 020

## **PREFACE**

The articles included in this publication are from a program on precipitating alloys, mostly ferrous. These interesting investigations are of immense value for both nuclear and non-nuclear applications. The papers deal with the effects of aging and deformation, in theory and experiments. Because of time limitation, not all the papers intended for presentation at the conference, could be included in this publication. I am thankful to all the presenters, who have made this international conference possible. I am also grateful to all chairmen of the sessions for kindly agreeing to help for the smooth running of the program. I am thankful to all members of the sponsoring committee for their encouragements. I wish to thank also, my wife Gouri, my daughter Jhilmil and my son Spondon, for their patient assistance in collecting and reorganizing many sections of the edited manuscripts to fulfill our goal of the planned publication.

B. N. Dey  
September 1988  
Chicago

## TABLE OF CONTENTS

<b>Precipitation Phenomena: Deformation and Aging—A Phenomenal Affair . . . . .</b>	<b>1</b>
B. N. Dey	
<b>Effects of Prior and Simultaneous Deformation on the Sensitization of Austenitic Stainless Steels . . . . .</b>	<b>3</b>
A. Advani, D. Atteridge, S. M. Bruemmer	
<b>Static Recrystallization of Cold Deformed Austenitic and Ferritic Stainless Steels . . . . .</b>	<b>19</b>
R. Barbosa, D. B. Santos	
<b>Effect of Precipitation of Secondary Phases in 17-14-2 Austenitic Chromium-Nickel-Molybdenum Steels on the Evolution of Low-Cycle Fatigue Cracking . . . . .</b>	<b>25</b>
E. Szpunar, J. Wawszczak	
<b>Aging Behavior of Double Quenched and Cold Worked Multiphase Stainless Steels . . . . .</b>	<b>35</b>
F. D. S. Marquis, S. F. Wang, J. Qadri, M. Hadji, M. N. Datar	
<b>Precipitating of Second Phase in Solid Solutions . . . . .</b>	<b>53</b>
Yu. I. Ustinovshikov	
<b>Thermomechanical Treatment of an Fe-Mn-Al-C Sideband Alloy . . . . .</b>	<b>69</b>
K. H. Han, T. S. Kang, D. E. Laughlin	
<b>The Effect of Warm Rolling and Intercritical Annealing on the Microstructure of a HSLA Steel . . . . .</b>	<b>77</b>
R. Barbosa, D. B. Santos	
<b>Strain-Aging of Low-Carbon Martensite . . . . .</b>	<b>83</b>
Y. Li, G. Yu, H. Zhou	
<b>Deformation and Aging Behaviors of Low Activation Stainless Steel Composites . . . . .</b>	<b>91</b>
F. D. S. Marquis, M. Hadji, N. AroonKiatkong, R. Bhatnagar	
<b>Influence of Dynamic Strain Aging on the Work Hardening of a Fe-Mn-Al Steel in the Temperature Range 20 to 700°C . . . . .</b>	<b>107</b>
C. Godoy, B. Gonzalez, P. R. Cetlin, E. M. de Paula e Silva	



# PRECIPITATION PHENOMENA: DEFORMATION AND AGING- A PHENOMENAL AFFAIR

B. N. Dey  
SUNY  
Utica, New York, USA

Precipitation processes in alloys, both ferrous and non-ferrous, are extremely important for strengthening mechanisms in alloys and their structural applications in chemical, nuclear and non-nuclear industries, as well as other high technology areas.

Age-hardening alloys have been a subject of extensive studies in the past since Wilm (1911) first observed it in 1906 and Merica et al (1920) followed up with other investigations. About seven decades earlier, Karsten (1939) discovered one of the ingredients, viz. inter-metallics, which are interrelated with the precipitation processes.

Precipitation may be defined as the decomposition of a solid solution (the parent matrix) into a new phase of different composition (the precipitate) and the initial solid solution with diminished solute concentration (depleted matrix). Changes in the physical properties (such as resistivity, etc.) chemical properties (such as corrosion, etc.) and the mechanical properties, such as hardness, damping and so on, accompany precipitation (see Christian, 1974; Smoluchowski, 1951; Ustinovshikov, 1938; Dey, 1965, 1965, 1986).

On aging some precipitating alloys after quenching from their solution treatment temperature, two processes usually occur before the equilibrium phases are finally formed:

- i) Clustering: the process which, accompanied by a marked change in the electrical properties and by energy release-occurs at the very

early stage of aging and results in the formation of a great number of sub-electronmicroscopic solute atom clusters;

- ii) Zone formation: the process in which Guinier-Preston zones grow following initial clustering, and hardening as well as x-ray diffraction effects take place. The hardening effects has been attributed to the transition structures, which when transform to the equilibrium phases cause softening. Handling strain causing increase in the internal friction of furnace-cooled Al alloys testifies to this latter case (Dey, 1965).

Cold working, both prior to and after precipitation hardening treatments is a matter of intrinsic interest, as the changing concentration of imperfections affect both the precipitation and the reaction temperature. Physical, mechanical and other behaviors of the alloys are extremely sensitive to the deformation and subsequent processes. Minor plastic deformation immediately after quenching increased the hardness of an Al alloy (Graf and Guinier 1954). Studies of different sorts involving carbide precipitations and effect of deformations have been reported during the last thirty years (Ustinovshikov, 1984, 1985). Also, continuous and cyclic deformation research with the help of modern day technology has shed new light into both the theory and the actual observations of ferrous and non-ferrous precipitating systems. The following papers will undoubtedly show the current state of the affair.

CHRISTIAN, J. W., The Theory of Transformation in Metals and Alloys, Pergamon (1974)

DEY, B. N., J. Phys. Soc. (Japan), 20 533 (1965)

Canad. J. Phys. 43, 1347 (1965)

in "Role of Interfaces in Material Damping", ASM, (1980)

GRAF, R. AND GUINIER A., Compt. Rend. 238, 819, (1954)

KARSTEN, K., Pogg. Ann. 46, 160 (1839)

MERICA, P., Waltenburg, R. G., AND SCOTT, H., Trans AIME, 64, 41 (1920)

SMOLUCHOWSKI, R., Phase Transformation in Solids, Wiley and Chapman (1951)

USTINOVSHIKOV, Y., Precipitation in Solids, Sci. Press (Moscow) (1988)

Met. Sci., 18, 337 (1984)

WILM, A., Metallurgic, 8, 225 (1911)

# EFFECTS OF PRIOR AND SIMULTANEOUS DEFORMATION ON THE SENSITIZATION OF AUSTENITIC STAINLESS STEELS

**Ashok H. Advani, David G. Atteridge**

Oregon Graduate Center  
Beaverton, Oregon 97006-1999, USA

**Stephen M. Bruemmer**

Battelle-Northwest  
Richland, Washington 99352, USA

## ABSTRACT

The presence of prior or simultaneous deformation results in an acceleration in the kinetics and, perhaps, an alteration in the thermodynamics of sensitization. This has been observed in a study on the effects of prior and simultaneous strain on the precipitation of carbides and development of sensitization in Types 304 and 316 austenitic stainless steels. Samples were strained to different levels using standard and specifically designed variable strain tensile specimens. Carbide precipitation and sensitization behavior was examined using analytical electron microscopy (AEM) and electrochemical potentiokinetic reactivation (EPR) tests.

The extent to which the kinetics of sensitization is accelerated depends directly on the amount of strain present in the material. Specimens subjected to increasing strain levels sensitize at shorter times and achieve higher degree of sensitization (DOS) values. Lower chromium minimums and wider, asymmetric chromium-depletion profiles have also been observed (using AEM) in strained versus unstrained samples. Asymmetric depletion profiles are associated with selected grain boundaries where strain-induced grain boundary migration has taken place. Carbides on these grain boundaries tend to extend preferentially into one grain instead of growing as thin, flat plates as found on unstrained boundaries.

## INTRODUCTION

Stainless steels (SS) are susceptible to intergranular (IG) corrosion and stress corrosion cracking (SCC) in certain aqueous

environments (e.g., high-temperature oxygenated water). This susceptibility is caused by a change in the grain boundary microchemistry which occurs when the material is heat treated in, or slow cooled through, a particular temperature range (500-900°C).

The primary composition change involved is the depletion of chromium in the region adjacent to the grain boundary caused by grain boundary precipitation of chromium-rich carbides.<sup>1-6</sup> Chromium depletion (or sensitization) depends on a critical balance between the thermodynamics of carbide precipitation and kinetics of chromium diffusion. Thus, variables affecting this critical balance control the sensitization response of the material.

Plastic deformation has been known to be a key variable affecting rates of reactions occurring in materials. Reaction thermodynamics and kinetics, for example, may be modified by the deformation process.<sup>7</sup> Sensitization development is, likewise, altered by the presence of strain.<sup>1,8-18</sup> However, limited data exists to quantify the effects of straining on sensitization development. This data is vital to understanding the effects of thermomechanical processing and fabrication on the sensitization phenomena.

In this work, a systematic study has been carried out to evaluate the effect of straining prior to, or during, isothermal treatment on the sensitization response of Types 304 and 316 austenitic SS. Degree of sensitization has been measured using indirect electrochemical and direct analytical methods.

## EXPERIMENTAL PROCEDURE

**MATERIALS** - High carbon, Types 304 and 316 stainless steel heats were used to examine the effects of deformation on sensitization. The composition of the heats are given in Table 1. All heats were received in the mill processed condition and solution annealed (1100°C/1 hour) before subsequent experimentation. Solution annealed specimen grain sizes were found to vary from 110 to 150 $\mu$ m.

**DEFORMATION SPECIMENS** - Three types of deformation tests were performed. They consisted of two types of prior deformation tests and one type of simultaneous deformation test. Prior deformation specimens were strained at ambient temperature prior to isothermal exposure while simultaneous deformation specimens were subjected to continuous deformation at a set strain rate during isothermal exposure.

One type of prior deformation specimens were given a selected prior strain and then subjected to an interrupted, additive isothermal heat treatment cycle. These specimens were fabricated from high-carbon Type 316 SS and were used to determine the effect of the magnitude of single-step prior strain on sensitization development. The second type of prior deformation specimens were fabricated from high-carbon Type 304 and 316 SS and were subjected to ambient straining at a fixed strain rate between each heat treating step of an interrupted, additive isothermal heat treatment cycle.

Strain magnitude effects of prior (single-step) deformation on sensitization were investigated using a specifically designed, variable strain tensile specimen. The specimen was flat, 300mm in length and had a width varying from approximately 25 to 7.5mm along a gage length of 175mm. Ambient uniaxial tensile testing on this specimen produced a range of strains from 0 to 40% prior to necking. Strains were estimated by marking the gage at 12.5mm intervals and measuring the reduction in cross sectional areas at each interval.

Sections corresponding to 0.4, 2.8, 8.5, 13.5, and 30% average strain were cut from the variable strain specimen. These were then aged alongside an unstrained, annealed specimen at 625°C. Incremental heat

treatments were performed using variable time steps out to a total time of 100 hours at 625°C. Sensitization measurements were made on the material after each heat treatment step.

The effects of uniaxial deformation during isothermal treatment was investigated using flat, dogbone-shaped tensile specimens. Specimens were deformed at constant extension rates varying from 1 to 6% strain per hour. Isothermal heating was attained using a clamshell furnace surrounding the tensile specimens. Unstrained specimens were attached to the gage section of the tensile specimen during heat treatment to ensure that the control specimens were subjected to an identical thermal history. Temperatures were measured along the gage section during heat treatment and were found to be within 5°C of the specified 600°C for these tests. Initial isothermal exposure durations were between 0.5 and 1 hour at 600°C. Larger exposure times were subsequently used to achieve total test times between 5 and 15 hours. Degree of sensitization measurements were carried out after each isothermal exposure.

The multistep prior deformation test and control specimen configurations were the same as those used for the simultaneously strained specimens. The multistep specimens were deformed at ambient temperature at strain rates comparable to those used at elevated temperature for the simultaneously strained specimens. The magnitude of strain for each ambient strain cycle was similar to that received by the respective simultaneously strained specimen during its next thermal cycle. Therefore, the strain magnitude received by multistep prior and simultaneously strained specimens deformed at the same strain rate were similar at the end of each respective heating cycle. This was done to enable a more direct comparison between prior and simultaneous deformation. DOS measurements were made after each isothermal exposure step and prior to the next straining step.

### SENSITIZATION MEASUREMENT -

Sensitization response of the different specimens was measured using the EPR test. EPR tests were performed using the method proposed by Clarke.<sup>19-21</sup> The EPR test has

Table 1 - Bulk Compositions and Grain Sizes of Stainless Steel Heats

AISI	Heat	C	Cr	Ni	Mo	Mn	Si	P	S	N	B
304	C-6	0.062	18.48	8.75	0.20	1.72	0.39	0.013	0.013	0.065	---
	C-7	0.072	18.53	9.33	0.43	1.74	0.46	0.046	0.017	0.036	---
316	SS-16	0.058	17.11	11.43	2.16	1.77	0.41	0.014	0.005	0.008	0.002

been shown to be a reliable, quantitative method of measuring the DOS for a SS material and can be related to grain boundary chromium depletion.<sup>5,6</sup>

The laboratory variation of the EPR test was used to determine DOS for the single-step prior deformation specimens. The field variation of the EPR test was used to determine DOS for the multistep prior and simultaneous deformation tests. These test variations have been found to produce equivalent results.<sup>22,23</sup> Experimental parameters employed are summarized in Table 2.

Table 2 - Experimental Parameters for EPR Tests

Instrument:	Instruspec* Model WC-5
Electrolyte:	0.5 M H <sub>2</sub> SO <sub>4</sub> + 0.01 M KSCN at 30°C
Specimen	
Preparation:	1- $\mu$ m Diamond Polish
Passivation	
Conditions:	Potential of 0.2V (SCE) for 2 minutes
Reactivation	
Scan Rate:	6V/hour (AISI 304 SS) 3V/hour (AISI 316 SS)

\*Registered Trademark

In addition to the indirect EPR method of detecting sensitization development, limited direct examination of changes in grain boundary microchemistry (using AEM) were also made. Samples were mechanically thinned (to less than 150 $\mu$ m) and subsequently jet polished using a solution of 3 volume percent perchloric acid in methanol. Examination of grain boundary microchemistry was made using a Philips EM 400T scanning transmission electron microscope (STEM) equipped with an ultra-thin window, energy dispersive x-ray detector. Quantification of x-ray spectra was made using the Cliff-Lorimer technique.<sup>24</sup>

## RESULTS AND DISCUSSION

### PRIOR DEFORMATION EFFECTS ON

**SENSITIZATION** - The presence of strain prior to heat treatment sharply accelerated sensitization development. Specimens strained to levels greater than 1% were observed to sensitize more rapidly and achieve higher DOS values than unstrained specimens with identical heat treatment schedules (Fig 1). The DOS value after 100 hours of exposure was found to more than double due to the presence of 13.5% prior strain.

Prior deformation appears to linearly increase DOS, at least after 100 hours of exposure at 625°C and up to a strain level of 13.5% (Fig 2). Deforming to 30% strain level

results in EPR-DOS values higher than that of the 13.5% strain sample. The data, however, has not been used for quantitative analysis due to the presence of intragranular attack.

The acceleration of sensitization with deformation illustrates the critical importance of thermomechanical, not just thermal, effects on sensitization development. An increase in the prestrain level is observed to decrease the "time to sensitize" the Type 316 heat (time to reach an EPR value of 5 C/cm<sup>2</sup>) (Fig 3). This can be assumed to reflect a reduction in chromium carbide nucleation time as a function of strain present in the material.

The presence of strain prior to the sensitization heat treatment also has a pronounced effect on the rate at which the DOS value increases after initial sensitization. Acceleration of sensitization kinetics appears to be a direct function of the applied strain. Deformation induced accelerated sensitization development has also been observed by other investigators.<sup>8-18</sup>

Differences in sensitization kinetics with increasing deformation has been postulated to be due to increased dislocation density with strain, thereby enhancing dislocation pipe diffusion of chromium. If the effective chromium diffusivity is a function of mobile dislocations, then the density of dislocations created by the straining process will control chromium diffusion, which in turn controls carbide growth, depletion width and DOS. Hart has proposed a relation to account for changes in diffusivity of substitutional impurities with changes in dislocation density.<sup>25</sup> This relation has been quantified to account for dislocation density effects on chromium diffusivity in austenitic SS.<sup>11</sup>

A near-linear increase in dislocation density with strain has been observed by the authors after 100 hours of ageing at 625°C (Fig 4). The plot depicts a markedly higher dislocation density for the 13.5% strain specimen, as compared to the annealed (unstrained) specimen, and can explain the acceleration in kinetics of sensitization. Measurement of dislocation density values in as-strained specimens is being carried out to obtain a more fundamental understanding of stress effects on chromium diffusivity and sensitization development in austenitic SS.

Optical micrographs (Fig 5) after EPR tests corroborate the changes in DOS found after 10 hours of exposure, as seen in Fig 6. The extent of grain boundary attack after 10 hours of ageing at 625°C was seen to increase with increasing strain level up to about 20% strain, while extensive intragranular attack is seen on specimens

with strains greater than 20%. Observation of this nature have also been made in the work of Pednekar et al,<sup>13</sup> and other researchers.<sup>13-17</sup>

Increasing grain boundary attack as a function of strain suggests that deformation can promote a more uniform development of chromium depletion along grain boundaries in much shorter exposure times than thermal exposure alone. Continuous depletion along grain boundaries is often referred to as a prerequisite for IGSCC. The presence of EPR attack within the grains, noted at higher strain levels, may be beneficial in that it decreases available carbon for IG precipitation and may, therefore, decrease sensitization.

**SIMULTANEOUS DEFORMATION EFFECTS ON SENSITIZATION** - Simultaneous straining also dramatically accelerated sensitization development. Measurable DOS is observed in shorter times, and EPR-DOS reaches higher values during additive 600°C anneals in strained versus unstrained specimens. Sensitization response as a function of heat treatment time is documented in Fig 7 for the two Type 304 stainless steels (Heats C-6 and C-7) for a strain rate of 6%/hour. Large EPR-DOS values ( $>10 \text{ C/cm}^2$ ) can be noted after only 1 hour at 600°C in the deformed specimens, whereas more than 9 hours were required to approach a comparable EPR-DOS in the control specimens. EPR-DOS values of more than  $35 \text{ C/cm}^2$  are observed after 9 hours for the C-6 strained specimen versus only about  $5 \text{ C/cm}^2$  for the unstrained specimen.

Differences of this magnitude substantiate the critical importance of thermomechanical effects on sensitization development. A simple isothermal heat treatment of many hours at 600°C does not result in significant attack in the EPR test, only isolated regions along some grain boundaries are ditched. On the other hand, strained specimens show almost continuous grain boundary attack after only one hour at 600°C.

Additional simultaneous strain experiments were conducted on the C-6 SS to determine the effect of deformation rate on the sensitization development. Specimens were deformed at a rate of 1 and 3% strain per hour and compared to the 6% results. Sensitization kinetics scaled consistently with increasing deformation rate, as shown in Fig 8. After 9 hours, EPR-DOS is about 7, 15, 23, and 35 for deformation rates of 0, 1, 3, and 6% per hour. Data for all four isothermal control (unstrained) specimens are also plotted in Fig 8 to give some indication of the data scatter in these measurements. Decreasing "time to sensitize" ( $\text{EPR} = 5 \text{ C/cm}^2$ ) observed with increasing strain rate (Fig 9) also indicate a decrease in nucleation time with increasing deformation. These differences in kinetics with increasing

deformation rate can be explained by changes in chromium diffusivity caused by enhanced dislocation pipe diffusion of chromium.

Grain boundary carbide precipitation and chromium depletion characteristics were examined on strained and unstrained Type 304 SS specimens. Bright field TEM micrographs are shown in the top of Fig 10 for the C-7 specimen after 9 hours at 600°C. EPR results for this specimen were presented in Fig 7a. A deformation rate of 6% per hour produces an accumulated strain of more than 50%. This damage is reflected in the high dislocation density which can be seen in the bright-field image (upper right, Fig 10). Dislocations are continuously created with time during the simultaneous deformation process leading to a continuously increasing dislocation density during isothermal exposure.

Grain boundary carbide morphologies are also quite different between the strained and unstrained samples. Carbides are elongated along the boundaries in the isothermal case, but extend preferentially into one grain with deformation. Not all boundaries exhibit this appearance. It is probable that only interfaces which are properly oriented with the applied uniaxial stress are influenced. Deformation may promote discontinuous carbide growth due to short-circuit diffusion paths created by the influx of dislocations. Discontinuous or cellular precipitation involves grain boundary diffusion and migration. Bettrabet et al.<sup>26</sup> have documented discontinuous precipitation of  $\text{Cr}_{23}\text{C}_6$  carbides in Type 304 SS after isothermal heat treatments.

Discontinuous carbide precipitation mechanisms, whether interface-energy driven<sup>27,28</sup> or chemically driven<sup>29</sup> will lead to the formation of asymmetric chromium depletion profiles. Precipitation resulting from volume diffusion where grain boundary migration does not occur will create nearly symmetric profiles.

Chromium depletion was mapped for both strained and unstrained specimens. Consistent with its much larger EPR-DOS, the strained specimens exhibited lower chromium minimums and wider depletion widths. Depletion profile characteristics for the two C-7 specimens are illustrated in the lower portion of Fig 10.

Differences in symmetry between the two profiles can be noted with the strained specimen's profile skewed to one side of the interface. Depletion extends preferentially into the same grain as noted for carbide growth. Chromium minimums were measured at about 8 wt% for the strained versus 13 wt% for the unstrained specimen. The measured minimum for the deformed SS at

600°C is about 2 wt% lower than that observed for an isothermally treated specimen at 600°C, regardless of heat treatment time.<sup>5</sup>

The asymmetry in depletion profiles of strained specimens typically results in the minimum chromium concentration being measured some distance from the grain boundary. Minimum chromium was found to be about 20 to 30 nm from the interface as demonstrated for the C-7 specimen in Fig 10. Grain boundary migration appears to be a key in the accelerated sensitization kinetics. It should be noted that asymmetric chromium depletion profiles caused by grain boundary migration are also possible in isothermal, unstrained specimens. Their development is, however, after significantly longer ageing times, and the presence of strain appears to be a key factor in accelerating their occurrence. Deformation promotes grain boundary migration at lower temperatures and directly influences chromium depletion width and DOS. The effect on chromium minimum concentration due to deformation may be caused by changes in grain boundary or carbide interface thermodynamics.

Simultaneous deformation was also found to accelerate sensitization development in the Type 316 SS at 600°C. Carbide nucleation and subsequent sensitization are slow at 600°C due to the presence of molybdenum in these heats. Data for unstrained and specimens strained at 6%/hour are presented in Fig 11. Without deformation, measurable EPR-DOS is not detected until an exposure of 30 hours and only reaches a value slightly more than 5 C/cm<sup>2</sup> after 50 hours at 600°C. The simultaneously deformed specimen, on the other hand, shows a measurable DOS at short times (approximately 2 hours) and increases to about 10 C/cm<sup>2</sup> after 5 hours, 20 C/cm<sup>2</sup> after 10 hours and 25 C/cm<sup>2</sup> after 13 hours. These values are significantly larger than the control specimen reached in 50 hours and indicate changes in both "time to sensitize" and kinetics of chromium depletion zone development. Simultaneous deformation effects are consistent for both Type 304 and 316 SS.

**MULTISTEP PRIOR DEFORMATION EFFECTS ON SENSITIZATION** - In order to better compare simultaneous and prior deformation, multistep prior deformation experiments were performed on both Types 304 and 316 SS. Specimens were subjected to strain magnitudes, strain rates and isothermal time steps identical to simultaneously strained specimens, except that the deformation was carried out at ambient temperature. Multistep prior deformation EPR-DOS tracked quite well with simultaneous strain data as shown in Figs 12a and b. For the Type 316 case (Fig 12a), the prior deformation specimens exhibited measurable DOS after only 1 hour versus 3 hours for the simultaneous strain and about 30 hours for the unstrained specimen. It appears that the

simultaneously strained specimen does tend to promote slightly larger EPR-DOS as time at temperature is increased. The difference is, however, not thought significant. In fact, the opposite behavior, when comparing multistep prior and simultaneous strain, is demonstrated in Fig 12b for the Type 304 heat. Prior deformation rates of 3% strain per hour resulted in larger EPR-DOS at all times. Detailed conclusions cannot be made from these few comparisons, but do indicate that prior or simultaneous deformation promote similar acceleration of sensitization kinetics. This may imply that changes in density of dislocations due to simultaneous straining during heat treatment are similar to that produced during prior deformation and subsequent isothermal treatment.

Chromium depletion characteristics were also examined for the Type 304 heat specimens subjected to multistep prior deformation after 9 hours at 600°C. Minimums were again lower than for the unstrained isothermal exposures. However, minimums were still higher than for the simultaneously deformed specimens. Chromium concentrations were measured down to about 9.2 wt% for the prior deformation specimens versus 8 wt% for the simultaneous specimens. Profiles again were found to be slightly asymmetric after the cumulative prior deformation and heat treatment sequence. Total depletion zone widths were comparable for the two deformation conditions. It is not known whether differences in profile characteristics are significant, thereby implying mechanistic differences in the effects of prior and simultaneous deformation on sensitization, or whether data scatter masks the fact that they are essentially the same.

#### SUMMARY

The effects of prior and simultaneous deformation on sensitization development have been studied for Types 304 and 316 austenitic SS. The experimentation discussed above indicates deformation is a key variable affecting the sensitization response of both 304 and 316 SS.

Lower grain boundary chromium minimums are observed in deformed specimens, which may indicate an alteration in reaction thermodynamics with deformation. Results also indicate an acceleration in sensitization kinetics with straining prior to, or simultaneous with, the sensitization heat treatment. Specimens subjected to increasing deformation exhibit lower "times to sensitize" and achieve higher DOS values as a function of both strain and strain

by an increase in chromium diffusivity which, in turn, is hypothesized to be due to a deformation induced dislocation density increase. Wider, asymmetric chromium depletion profiles observed on strained specimens may also contribute to the observed increase in kinetics of sensitization development.

Deformation also promotes a higher density of grain boundary carbide precipitates, different carbide morphologies and a decrease in the time needed to achieve a uniform chromium depletion zone along grain boundaries. The latter phenomenon has been associated with material susceptibility to intergranular corrosion and stress corrosion. Deformation above 20% prior strain, however, induces a combination of inter- and intra-grain precipitation and, therefore, reduces sensitization susceptibility.

#### REFERENCES

1. Bain, E.C., R.H. Aborn, J.J.B. Rutherford, Trans. Amer. Soc. Steel Treating, 21, 481, (1933).
2. Stawstrom, C., M. Hillert, J. Iron Steel Inst., 207, 77, (1969).
3. Tedmon Jr., C.S., D.A. Vermilyea, J.H. Rosolowski, J. Electrochem. Soc., 118, 192, (1971).
4. Bruemmer, S.M., Corrosion, 42, No. 1, 27, (1986).
5. Bruemmer, S.M., L.A. Charlot, B.W. Arey, Sensitization Development in Austenitic Stainless Steel: I. Correlation Between STEM-EDS and EPR Measurements, submitted to Corrosion, November 1986.
6. Bruemmer, S.M., "Quantitative Measurement and Modeling of Sensitization Development in Stainless Steels," PhD Thesis, Oregon Graduate Center, Beaverton, Oregon, May 1988.
7. Christian, J.W., "The Theory of Transformations in Metals and Alloys Part I - Equilibrium and general Kinetic Theory," Pergamon Press Ltd., 2nd ed., 12, (1975).
8. Solomon, H.D., Corrosion, 36, No. 7, 356, (1985).
9. Solomon, H.D., D.C. Lord, Corrosion, 36, No. 8, 395, (1980).
10. Solomon, H.D., Corrosion, 41, No. 9, 512, (1980).
11. Andresen, P.L., H.D. Solomon, D.F. Taylor, EPRI NP-1823/Project 1072-1, Final Report for 1981, Electric Power Research Institute, California, May 1981.
12. Tedmon, C.S., D.A. Vermilyea, D.E. Broecker, Corrosion, 27, 104, (1971).
13. Pednekar, S., S. Smialowska, Corrosion, 36, No. 10, 565, (1980).
14. Briant, C.L., A.M. Ritter, Metall. Trans. 11A, 2009, (1980).
15. Cihal, V., "Intergranular Corrosion of Steels and Alloys," Elsevier Science Publishers B.V., 146, (1984).
16. Rondelli, G., B. Mazza, T. Pastore, B. Vicentini, "Electrochemical Methods in Corrosion Research," Edited by M. Dupont, Materials Science Forum, 8, 593, (1986).
17. Bose, A., P.K. De, Corrosion, 43, No. 10, 624, (1987).
18. Bruemmer, S.M., L.A. Charlot, D.G. Atteridge, Sensitization Development in Austenitic Stainless Steel: II. Measurement and Prediction of Thermomechanical History Effects, Submitted to Corrosion, December 1986.
19. Clarke, W.L., NUREG-0251-1, August 1976, and NUREG/CR-1095, February 1981, US. Nuclear Regulatory Commission, February 1981. Available from NTIS, Springfield, Virginia 22161.
20. Clarke, W.L., R.L. Cowan, W.L. Walker, "Intergranular Corrosion of Stainless Alloys," ASTM STP 655 - Edited by R.F. Steigerwald, ASTM, Philadelphia, 99, (1978).
21. Clarke, W.L., D.C. Carlson, Materials Performance, 19, No. 3, 16, (1980).
22. Atteridge, D.G., R.E. Page, S.M. Bruemmer, NUREG/CR-3613, 2, Annual Report for 1984, U.S. Nuclear Regulatory Commission, Washington D.C., (1985).
23. Atteridge, D.G., S.M. Bruemmer, NUREG/CR-3613, 3, No.2, Annual Report for 1985, U.S. Nuclear Regulatory Commission, Washington D.C., (1986).
24. Cliff, G. and G.W. Lorimer, Proc. of the Fifth European Congress on Electron Microscopy, Institute of Physics, Bristol, 140, (1971).
25. Hart, E.W., Acta Metall., 5, 597, (1957).
26. Betrabet, H.S., K. Nishimoto, B.E. Wilde, and W.A.T. Clarke, Corrosion, 43, No. 2, 77, (1987).
27. Tu, K.N., D. Turnbull, Acta Metall., 15, 369, (1967).
28. Tu, K.N., D. Turnbull, Acta Metall., 15, 1317, (1967).
29. Fournell, R., and J.B. Clark, Metall. Trans., 34, 1972, (1957).



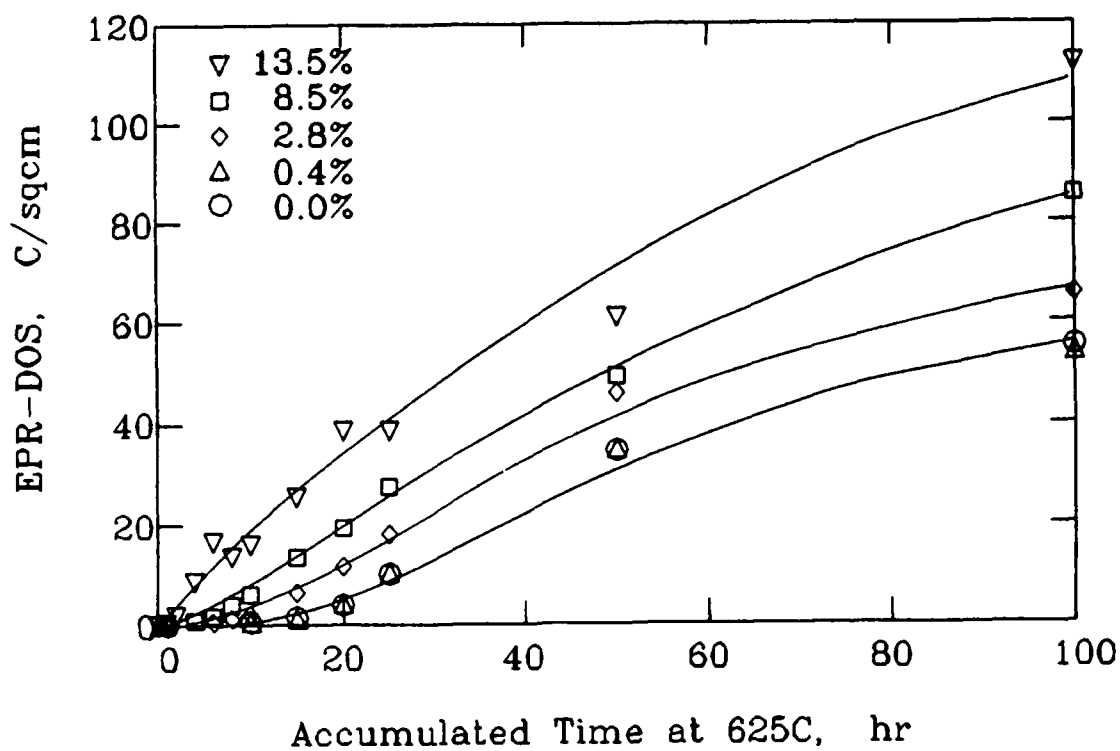


Fig. 1 - Prior Deformation Effects on Sensitization Development in Type 316 SS.

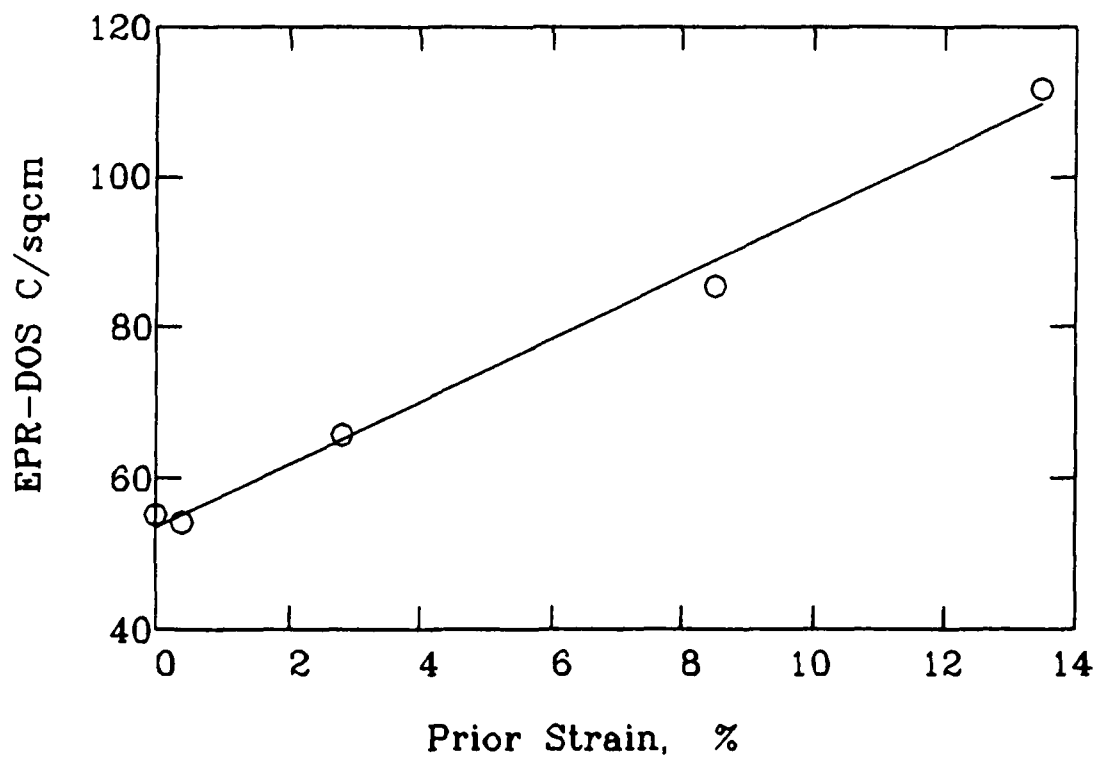


Fig. 2 - Variation of EPR-DOS with Prior Strain After 100 Hours of Ageing at 625°C for Type 316 SS.

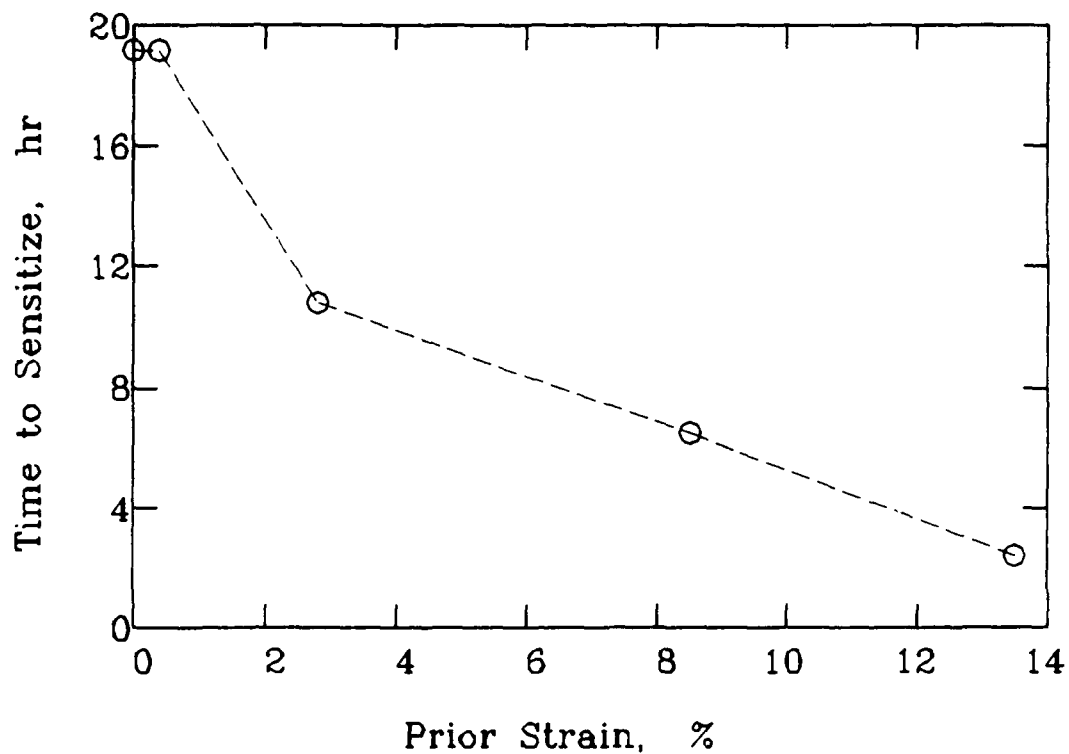


Fig. 3 - Prior Strain Effects on "Time to Sensitization"  
(EPR-DOS =  $5 \text{ C/cm}^2$ ) for Type 316 SS.

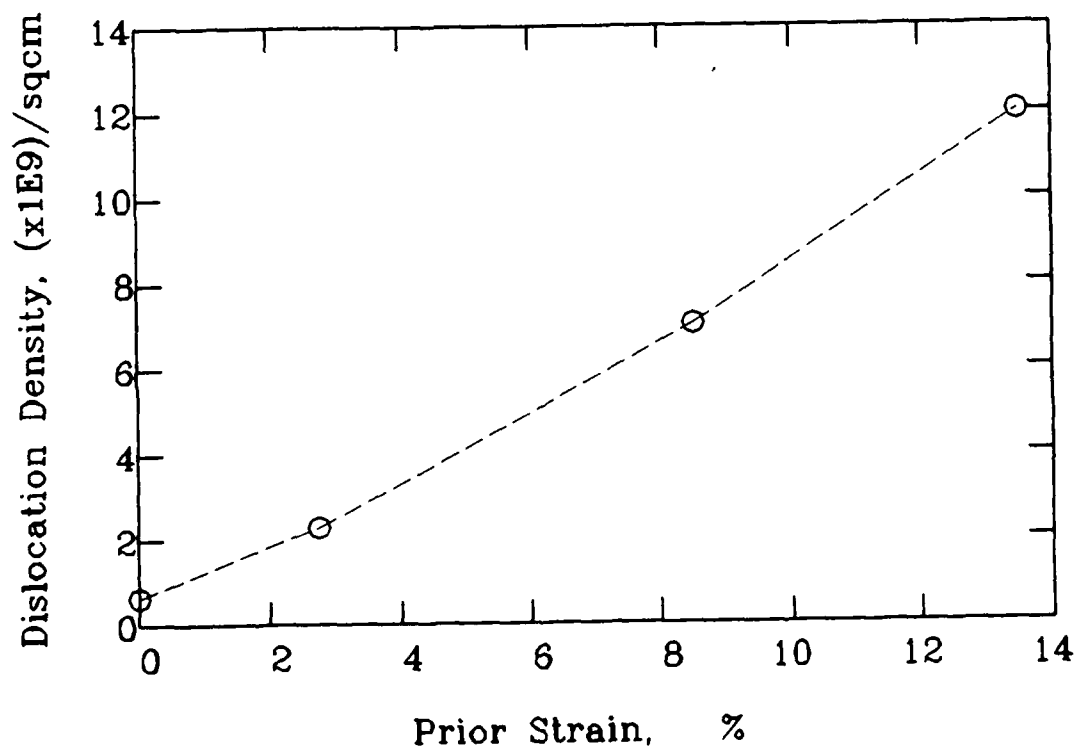


Fig. 4 - Variation in Dislocation Density with Prior Strain  
for Type 316 SS. Dislocation density measurements  
were made on prior strained specimens after 100 hours  
of ageing at  $625^\circ\text{C}$ .

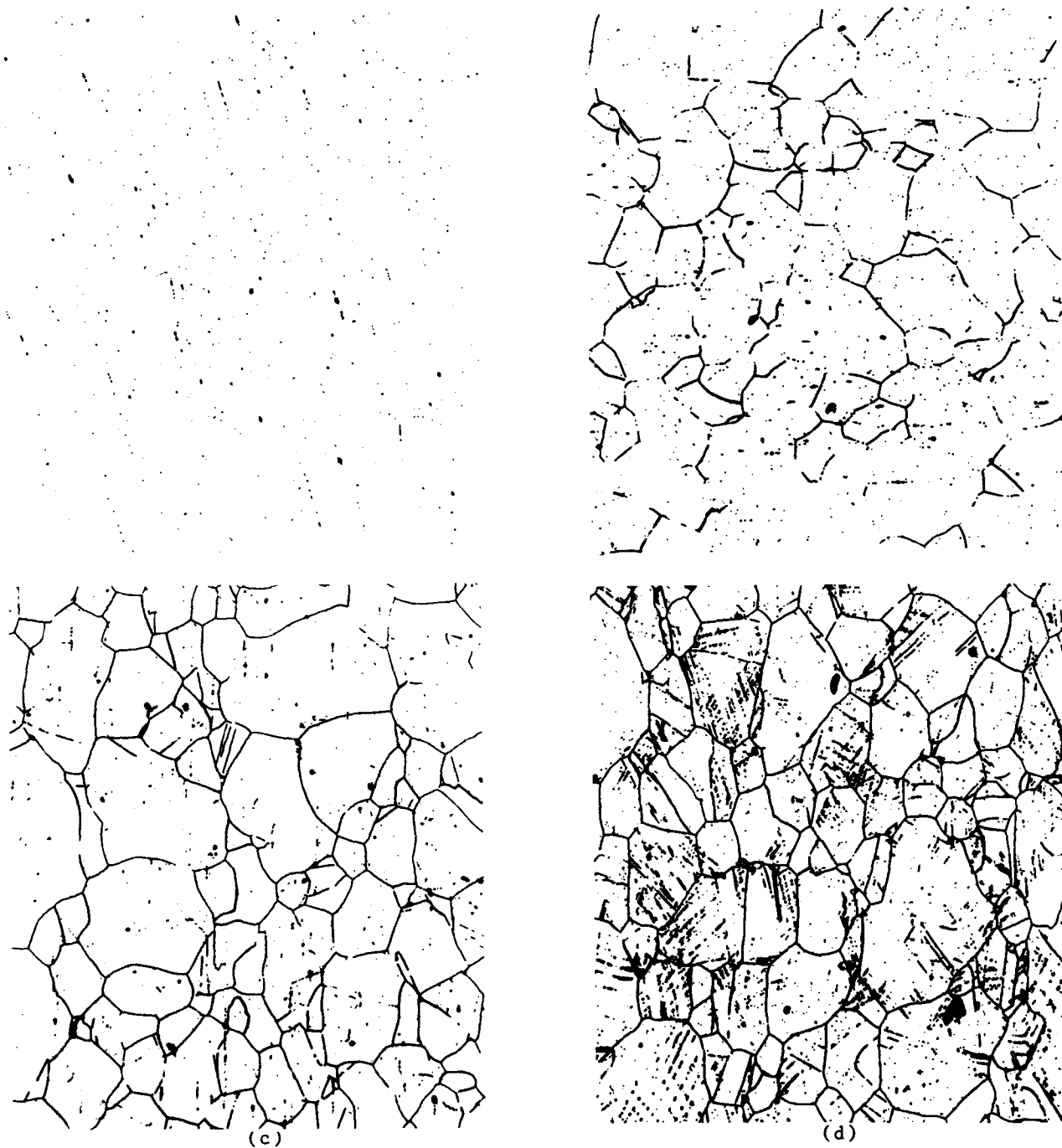


Fig. 5 - Optical Micrographs Indicating Changes in Extent of EPR Test Attack for (a) 0%, (b) 8.5%, (c) 13.5%, and (d) 30% Prior Strained Specimens (Type 316 SS).

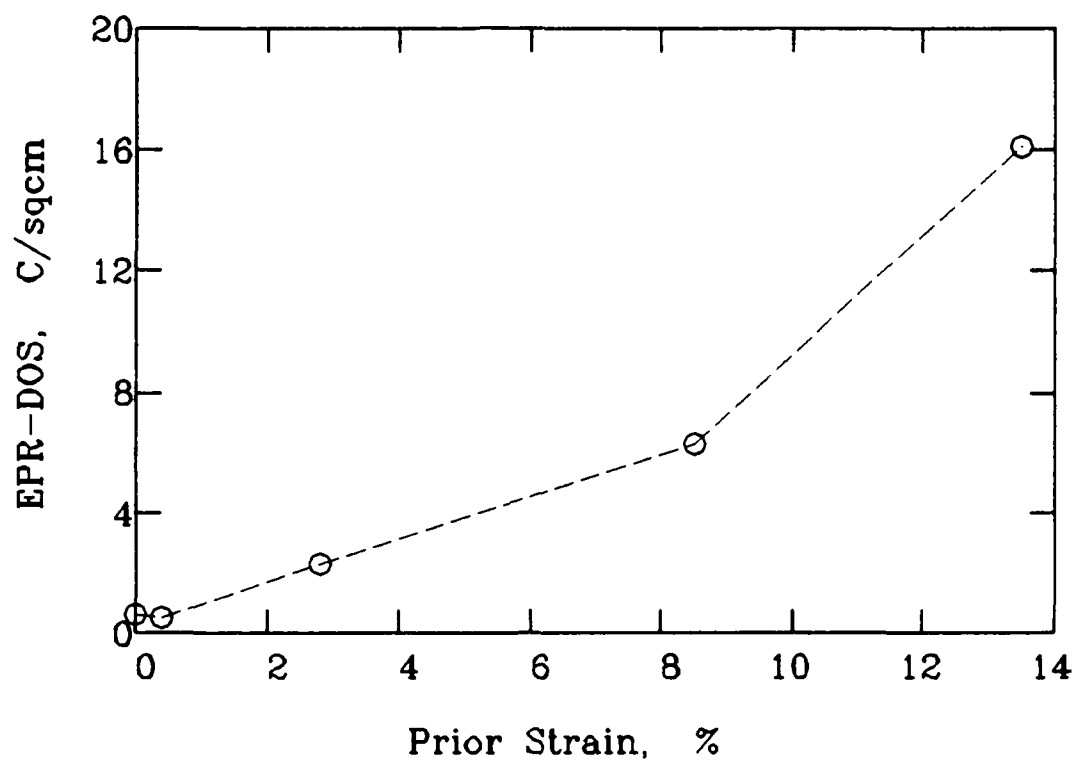


Fig. 6 - Variation of EPR-DOS with Prior Deformation  
After 10 Hours of Ageing at 625°C for Type 316 SS.

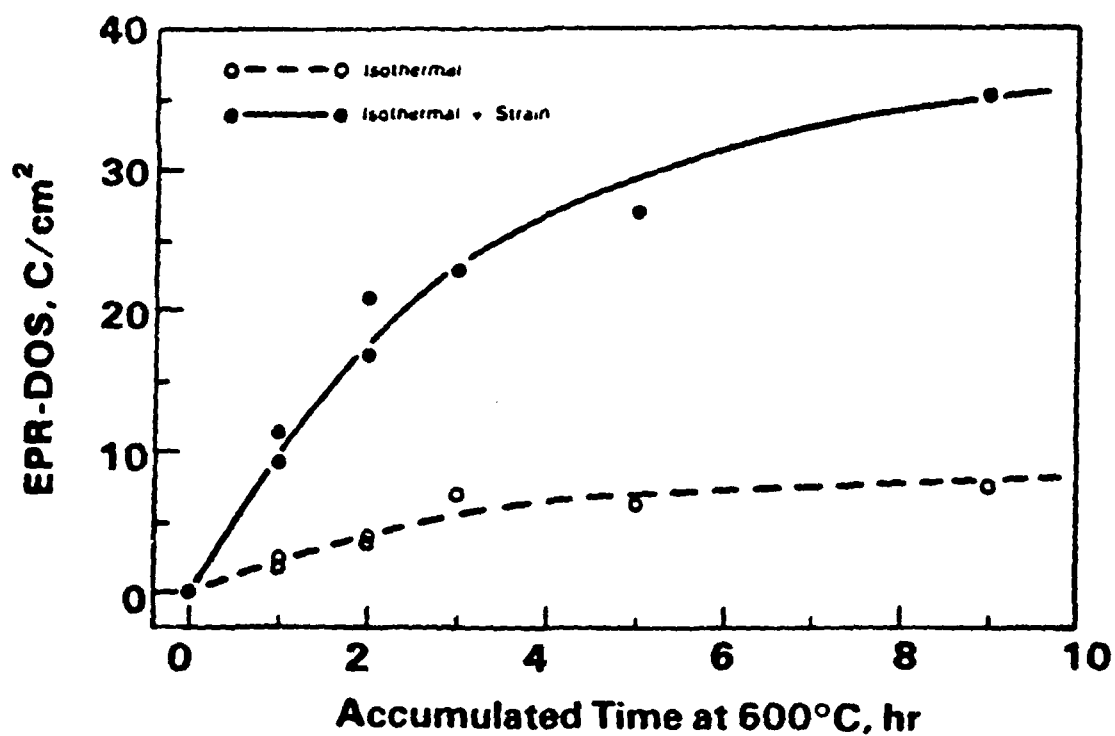
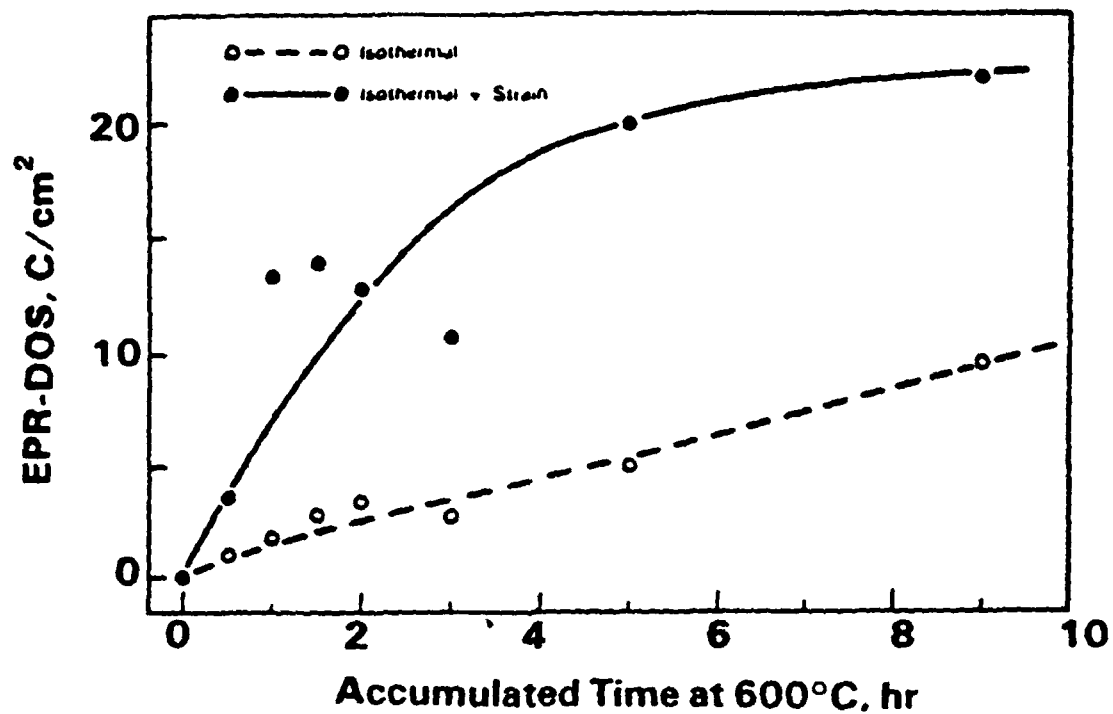


Fig. 7 - Simultaneous Deformation Effects on Sensitization Development in Type 304 SS: (a) Heat C-7, (b) Heat C-6. Specimens were deformed at a constant strain rate of 6%/hour.

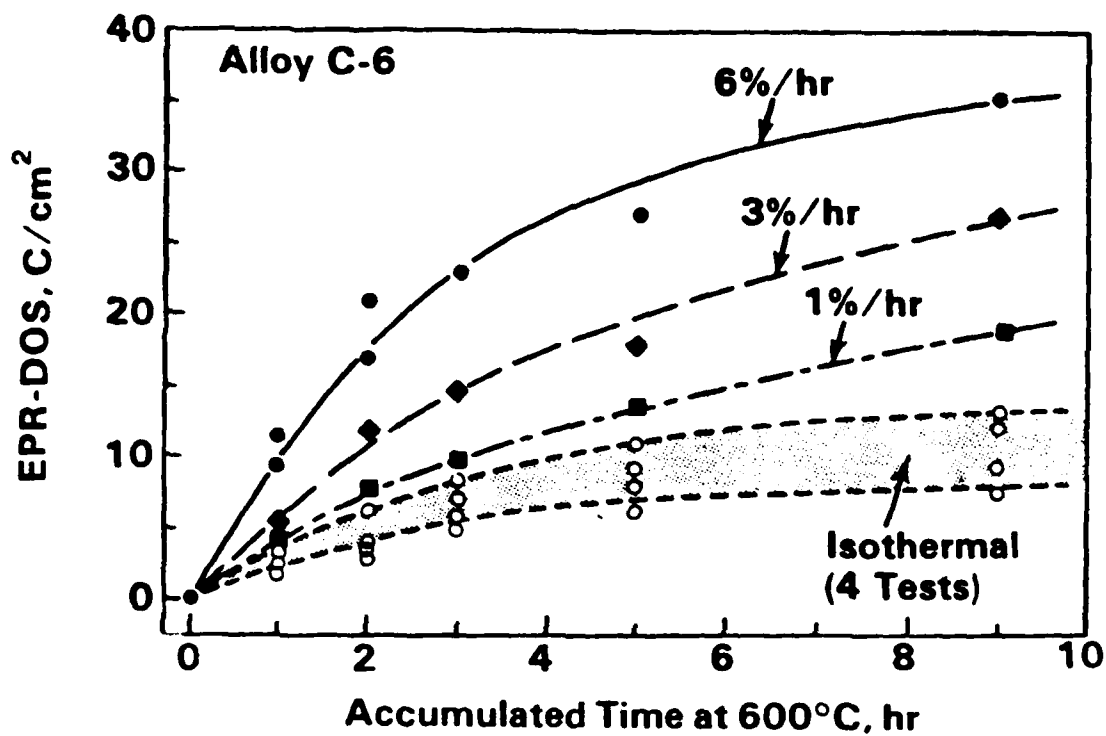


Fig. 8 - Simultaneous Deformation Rate Effects on Sensitization Development in Type 304 SS (Heat C-6) at 600°C.

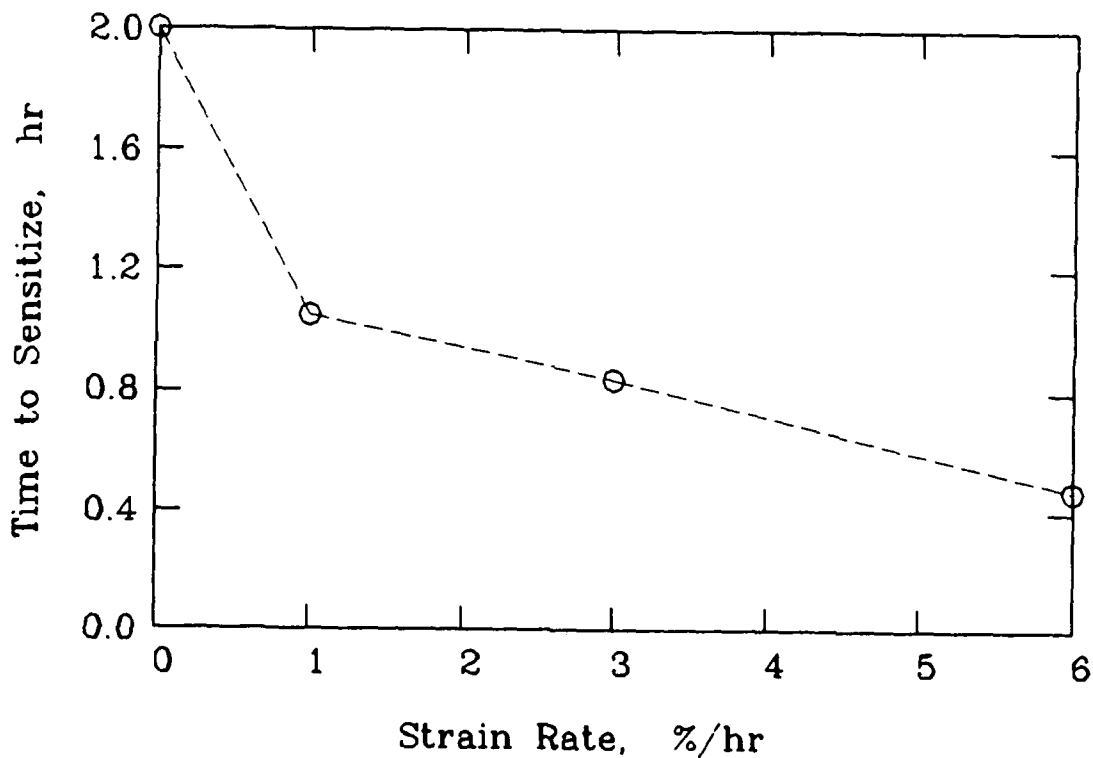
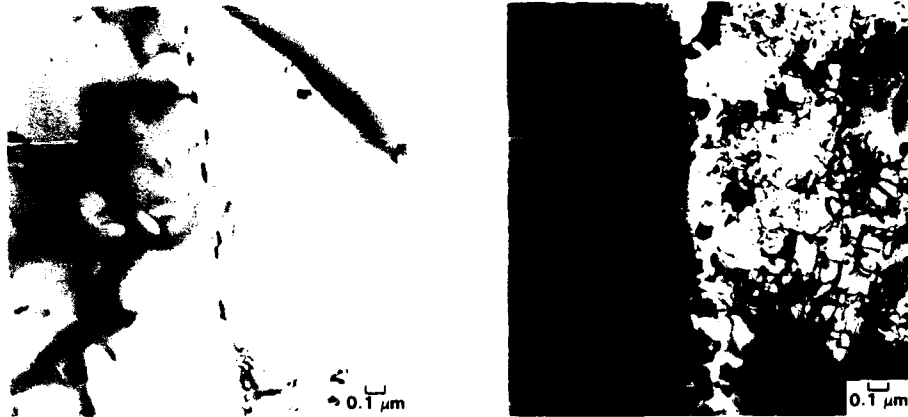


Fig. 9 - Simultaneous Deformation Strain Rate Effects on "Time to Sensitize" (EPR-DOS = 5 C/cm<sup>2</sup>) for Type 304 SS, Heat C-6.

### Microstructure



### Microchemistry

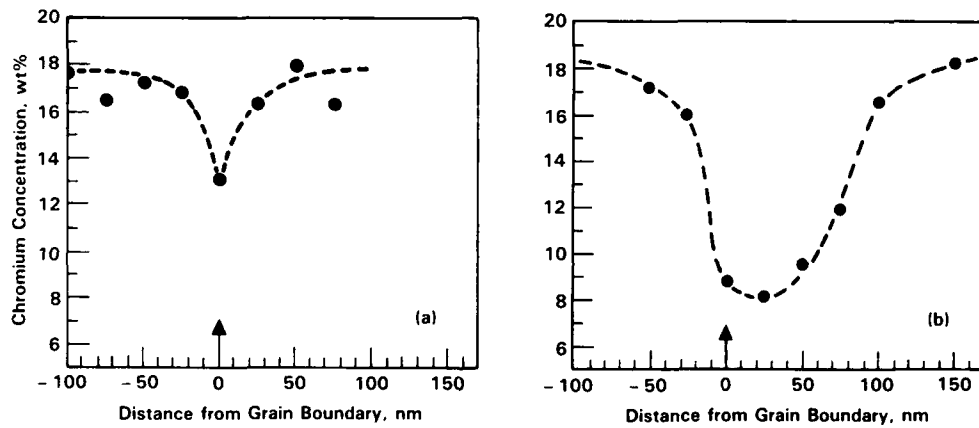


Fig. 10 - Transmission Electron Micrographs Illustrating Grain Boundary Carbide Precipitate Morphologies in Strained and Unstrained Specimens. Grain boundary chromium depletion profiles in unstrained (a) and strained (b) C-7 specimens after cumulative heat treatment of 9 hours at 600°C.

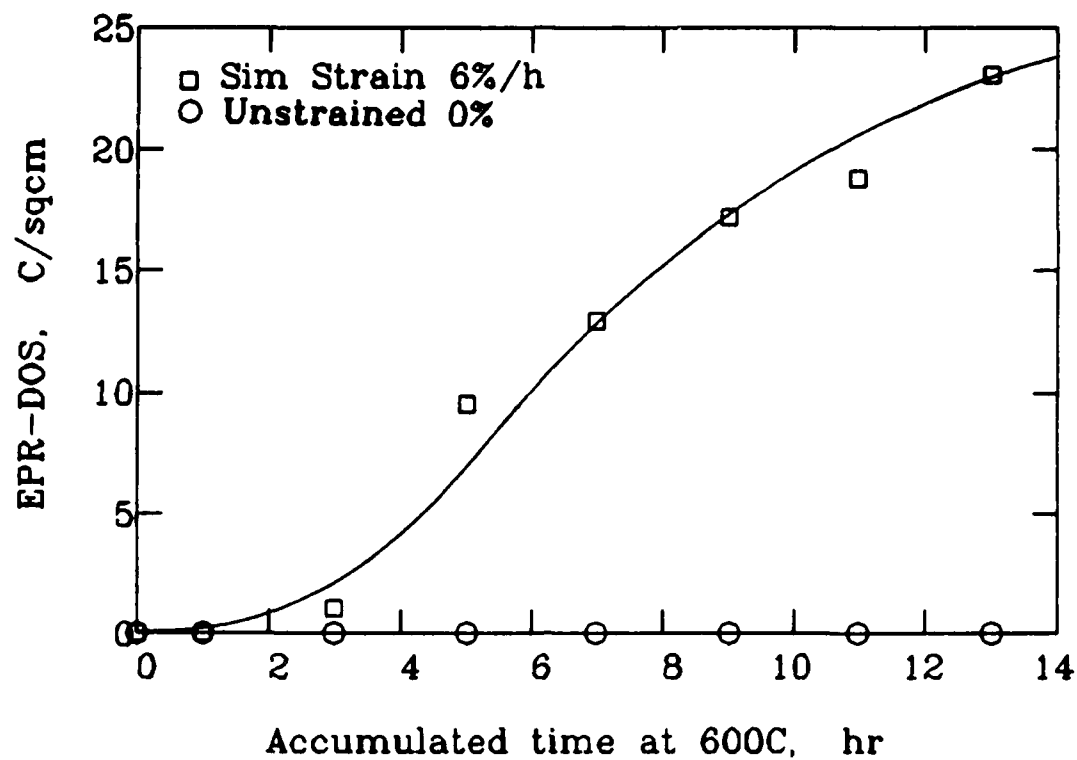


Fig. 11 - Simultaneous Deformation Effects on Sensitization Development in Type 316 SS.



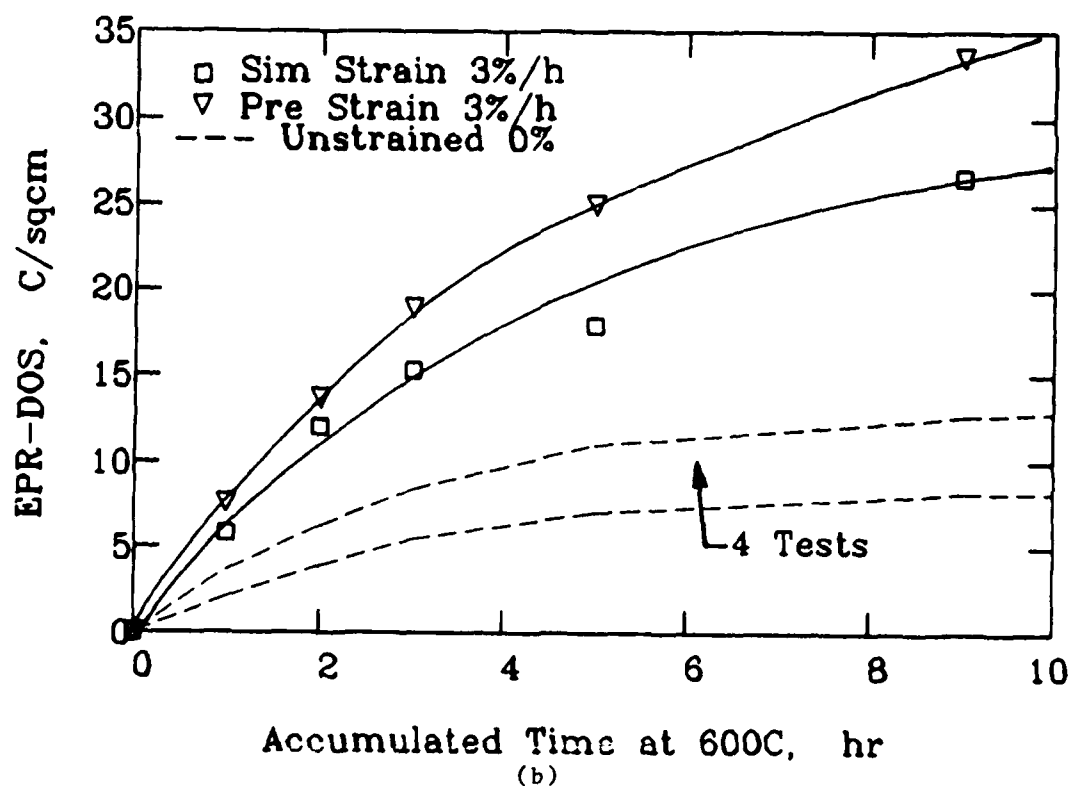
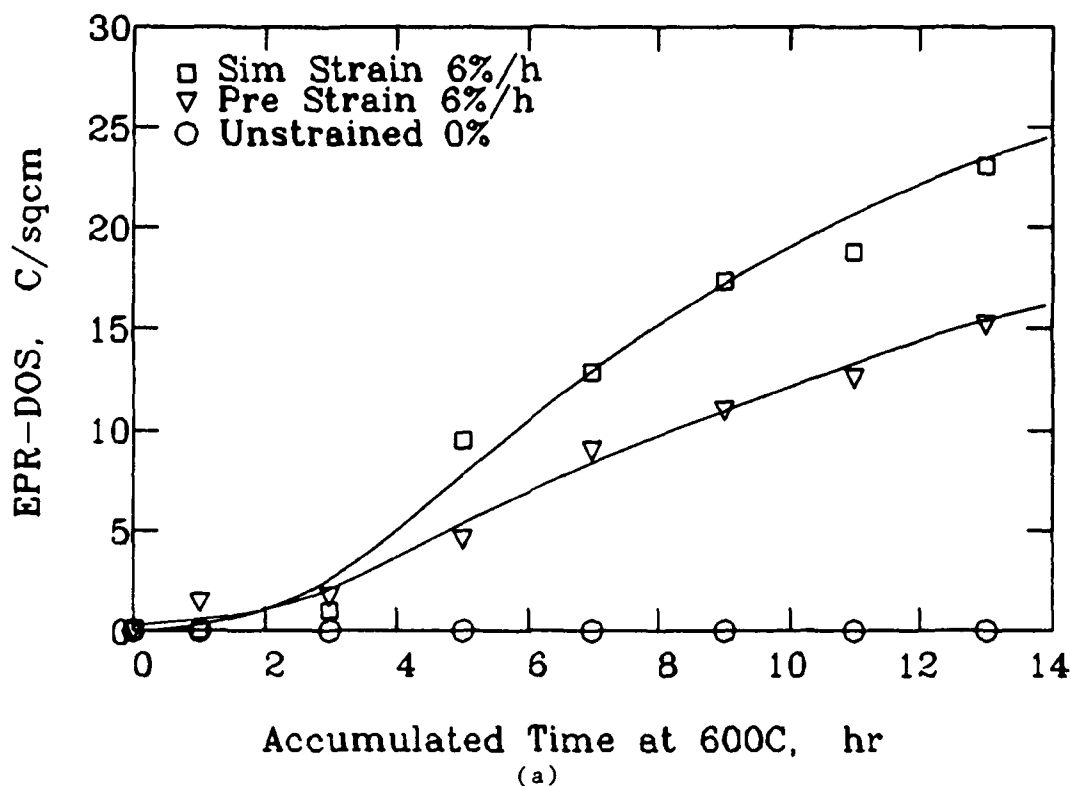


Fig. 12 - Comparison of Multistep-Prior and Simultaneous Deformation Effects on Sensitization Development in (a) Type 316 Heat SS-16 and (b) Type 304 Heat C-6.

# STATIC RECRYSTALLIZATION OF COLD DEFORMED AUSTENITIC AND FERRITIC STAINLESS STEELS

Ronaldo Barbosa, Dagoberto B. Santos

Dept. of Metallurgical Engineering,  
Universidade Federal de Minas Gerais  
Rua Espírito Santo 35, s.206-Centro  
30160- Belo Horizonte- M.G.- Brazil

## ABSTRACT

Austenitic and ferritic stainless steels frequently present hot ductility problems during processing. Static recrystallization can restore a work hardened microstructure and refine the grain size, thus reducing the tendency for cracks to appear place. Knowledge of the kinetics of recrystallization is therefore of interest. The goal of the present work was to study the kinetics of static recrystallization in austenitic stainless steels type 304 and 316 and ferritic stainless steels types 430 and 430M. The latter is a modified version of type 430 to which Nb and Ti were added. It was observed that nucleation occurs mainly at grain and twin boundaries for the austenitic stainless steels. Some intragranular nucleation also took place in the 316 steel. Type 430 steels, on the other hand, only show nucleation at grain boundaries. The kinetics of recrystallization are slower in 316 steels as compared to type 304. This is associated with the presence of Mo in the 316 grade. The 430M steels display a slower rate of recrystallization than type 430. This is attributed to the presence of Nb in the modified grade. The time exponent  $k$  of the Avrami equation was calculated for all grades. An average  $k$  value of 1 suitably describes the kinetics for all steels. The expression  $t_{50} \propto \epsilon^{-1.7}$  for the dependence of the time for 50% recrystallization on strain is applicable to steels 304, 430 and 430M. However, a higher strain exponent of 3.75 applied to the 316 steels. Activation energies for the recrystallization process were calculated. Their values are 547, 355 and 120 kJ/mol for the 316, 304 and 430M steels respectively.

AUSTENITIC AND FERRITIC STAINLESS steels are convenient materials in which to study the kinetics of recrystallization because no transformation occurs when samples are cooled to room temperature. The recrystallization of austenitic stainless steels has been extensively

studied (1-4). However, most researchers have followed the recrystallization taking place after hot working. This is of particular interest, since austenitic stainless steels frequently present problems of hot workability (1). Recrystallization refines the microstructure, thus decreasing the occurrence of cracks. Control of the recrystallization process during hot deformation is usually employed to improve the hot ductility. The other alternative is reheating the steel after a certain number of cold or hot deformation steps have been applied. However, little research has been carried out with respect to the recrystallization of austenitic stainless steels after cold deformation.

Ferritic stainless steels are those containing high levels of Cr and small quantities of Ni. The literature covering the kinetics of recrystallization in these materials is not as extensive as the one available for the austenitic grades. However, processing ferritic steels to obtain adequate formability and meet strength specifications requires care in both the cold and hot deformation stages (5).

The aim of the present work was to investigate the recrystallization process after the cold rolling of austenitic stainless steels types 304 and 316 and ferritic stainless steels types 430 and 430M.

## EXPERIMENTAL TECHNIQUES

Chemical compositions of the materials used are given in Table 1. Austenitic stainless steels are highly alloyed with Cr and Ni. On the other hand, ferritic stainless steels are those containing 16-30% Cr and a negligible quantity of Ni. The near absence of Ni makes ferritic stainless a more economical material. Austenitic stainless is competitive because of lower maintenance and repair costs. Mechanical properties are also better in austenitic steels. However, ferritic stainless steels are increasingly being preferred if corrosion resistance is the main design criterion (5).

Samples were cold rolled with reductions of 20 and 40 %. They were then annealed at temperatures ranging from 800 to 1040 °C and quenched for metallographic examination.

Table 1 - Chemical composition of alloys used. All values are given in wt%.

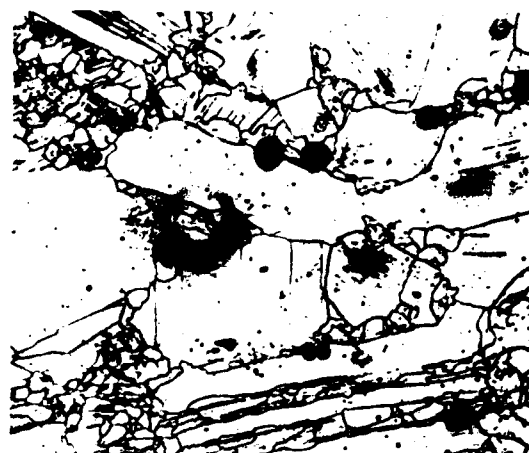
Steel	304	316	430	430M
C	0.06	0.07	0.047	0.027
Cr	18.4	17.3	16.1	17.1
Ni	8.8	10.9	0.37	
Mo	0.081	2.06		
Mn	1.35	1.44	0.54	0.48
Si	0.43	0.61	0.36	0.30
P	0.017	0.017	0.026	0.027
S		0.020	0.004	0.008
N			0.036	0.002
Nb				0.13
Ti				0.43
Grain Size, $\mu\text{m}$	110	180	60	60

Grain size measurements were carried out using the mean linear intercept method. Statistical errors were kept within 10 %. Point counting was employed to measure the fraction of material recrystallized. A sufficient number of points was counted to ensure that an error of less than 10 % was obtained. In both cases, the measurements were made to a 95 % confidence level. Samples for metallography were prepared in the standard way. Etching of the 316 steel was performed using Nygren's reagent (5 gr of  $\text{Cu}_2\text{Cl}_2$ , 5 gr of  $\text{FeCl}_3$ , 100 ml of  $\text{HCl}$ , 80 ml of  $\text{C}_2\text{H}_5\text{OH}$  diluted in 300 ml of  $\text{H}_2\text{O}$ ). Steels 304, 430 and 430M were etched electrolytically with nitric acid (10-12V for 5 to 15s).

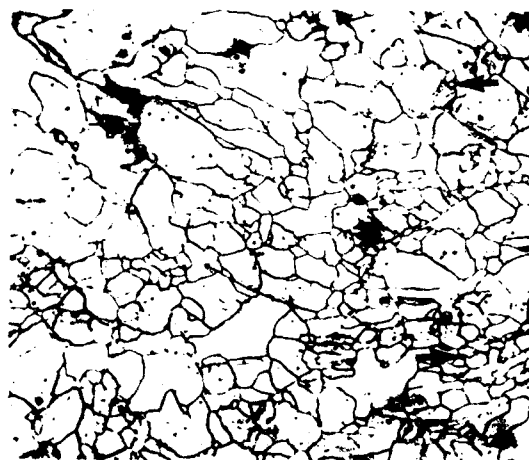
## RESULTS AND DISCUSSION

### Qualitative Observations

Figures 1 and 2 show the development of recrystallization in type 304 and 316 steels respectively. The nucleation of recrystallizing grains is similar in both steels. Grain and annealing twin boundaries are preferential sites. However, Figure 2 also shows that intragranular nucleation occurs in 316 steel. Grains which are recrystallized continue to grow. Figure 1b shows that nucleation can also occur on the grain



(a)



(b)

Figure 1- Microstructure of recrystallizing austenite in type 304 steel. Samples were deformed 20% and annealed at 940°C. Fraction recrystallized is 11% after 65s (a) and 65% after 500s (b). Arrows indicate new grains formed from freshly recrystallized material. (Mag. 100X)

boundaries of recrystallized grains. This has been called a repeated nucleation process (2). As deformation increases, deformation bands increasingly become preferential nucleation sites (Figure 2b).

The evolution of recrystallization in ferritic stainless steel is seen in Figure 3. Recrystallized grains can be distinguished from deformed ones by the differences in size. The main nucleation sites are grain boundaries alone, since no annealing twins are available for recrystallization. There is also no visible evidence for intragranular nucleation. Therefore, the only nucleation sites available for nucleation in ferritic stainless steels are at grain boundaries. Figure 4 shows evidence for the presence of coarse Nb(CN)



Figure 2- Microstructure of recrystallizing austenite in type 316 steel. Samples were annealed at 940°C. Fraction recrystallized is 24% after 9840s (a) and 65%, after 1500s (b). Deformation given was 20% (a) and 40% (b). (Mag. 100X)

at grain boundaries. Finer precipitates will have been formed during rolling. This is expected to slow the rate of recrystallization in 430M steels as compared to the Nb free grade.

#### Quantitative Observations

Figures 5 to 7 show the progress of recrystallization with annealing time for the type 304, 316, 430 steels respectively. In general, the rate of recrystallization increases with increases in the pre-deformation or the annealing temperature. Recrystallization in type 316 steel is slower than in type 304. This has been attributed to the presence of Mo (2,4,6). The retarding effect of Mo is greater at lower temperatures or strains, an observation which is consistent with those of previous workers (4). It is suggested in the

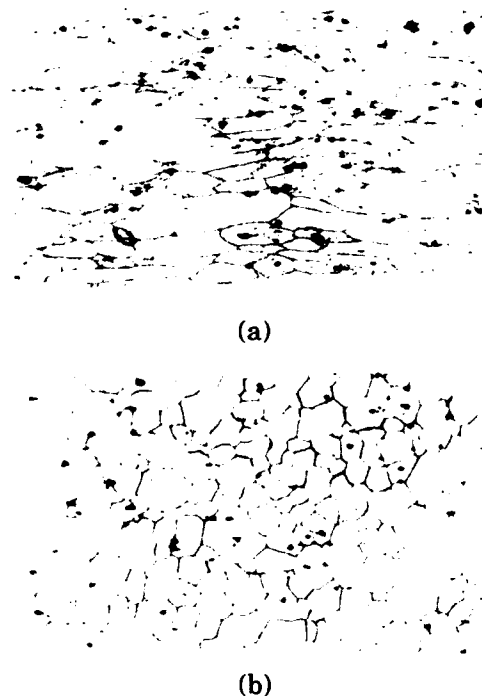


Figure 3- Microstructure of recrystallizing austenite in type 430M steel. Samples were deformed 40% and annealed at 900°C. Fraction recrystallized is 0% for 10s (a) and 60% for 420s (b). (Mag. 100X)



Figure 4- 430M type steel deformed 40% and annealed for 10s at 900°C. Arrow shows presence of Nb(CN).

literature that Mo, when in solid solution, affects the mobility of grain boundaries (2,4). It is further suggested that Mo will form Mo-C and Mo-N complexes in austenitic stainless steels (4,7). It is

worth mentioning that increases in Ni content have no effect on recrystallization rate (8).

Adding Nb to ferritic stainless steels decreases the recrystallization rate. It is well known that Nb in deformed austenite either in solution or as carbonitrides will retard or even suppress recrystallization (9). However, there is little information on its effect on the recrystallization rate of ferrite.

The dependence of the recrystallized fraction on time can be modelled by using an Avrami equation

$$X_v = 1 - \exp(-\beta t^k) \quad (1)$$

where  $t$  is the annealing time, and  $\beta$  and  $k$  are constants. Plotting  $\log_{10}(\ln(1/(1-X_v)))$  versus  $\log_{10} t$  gives straight lines, as shown in Figure 8. The slope of the curves is  $k$ , the time exponent in equation (1). The graphs for the other steels are similar to the one in Figure 8. For this reason, only the results for the 304 steel are displayed. The values of  $k$  varied from 0.8 to 1 for the type 304 steel. No systematic changes could be associated with temperature or strain variations.

Similar findings have also been reported recently (2). On the other hand, it has been observed that if grain size is increased, then the  $k$  values will decrease (3). However, this only occurs when the original grain size is larger than 200  $\mu\text{m}$ . In the present investigation, an average  $k$  of 0.9 was obtained for the 304 steels. This value is independent of either strain or annealing temperature. Average values of  $k$  for the other grades are 0.8, 1.1 and 0.9 for the type 316, 430M and 430 steels. This is consistent with nucleation occurring mainly at grain boundaries (10). A range of values for  $k$  between 0.5 and 2 has been reported for austenitic stainless steels (4). Recently, it has been pointed out that as-cast material presents wider variations in  $k$  than wrought ones (2). Thus, an average  $k$  value of 1 is reasonable for the austenitic and ferritic stainless steels tested. The ferritic stainless displayed a slightly higher average than the austenitic steels. This can be explained in terms of the relative absence of stacking faults in ferrite as compared to austenite.

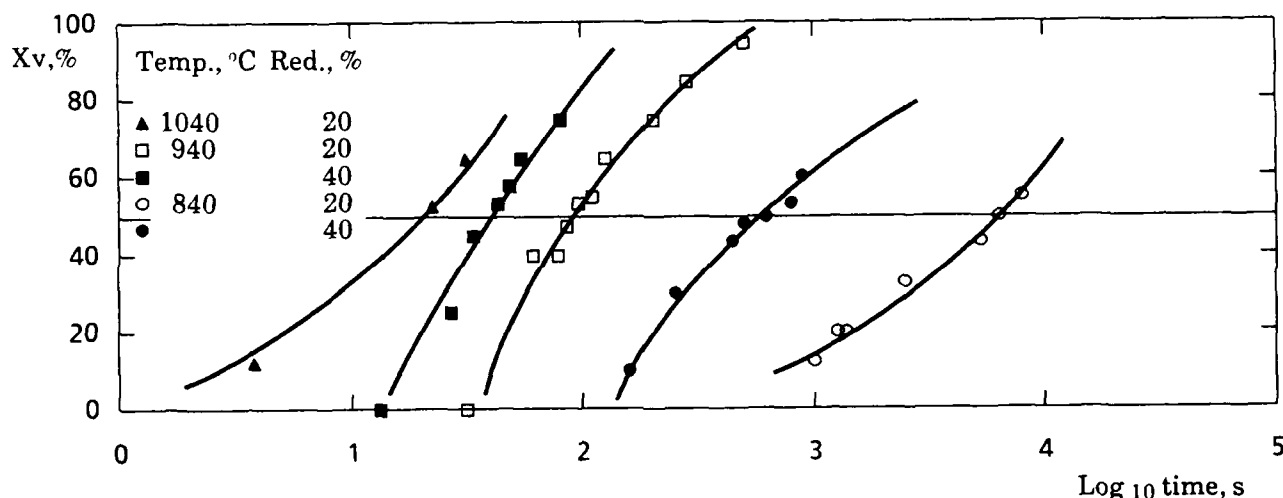


Figure 5- Evolution of the fraction recrystallized with annealing time for the type 304 steel.

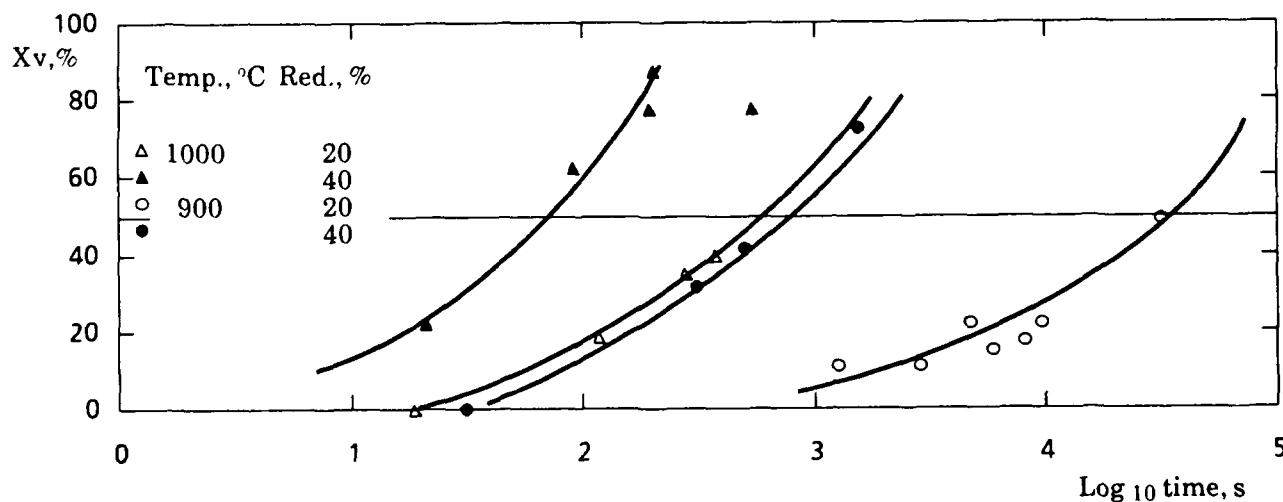


Figure 6- Evolution of the fraction recrystallized with annealing time for the type 316 steel.

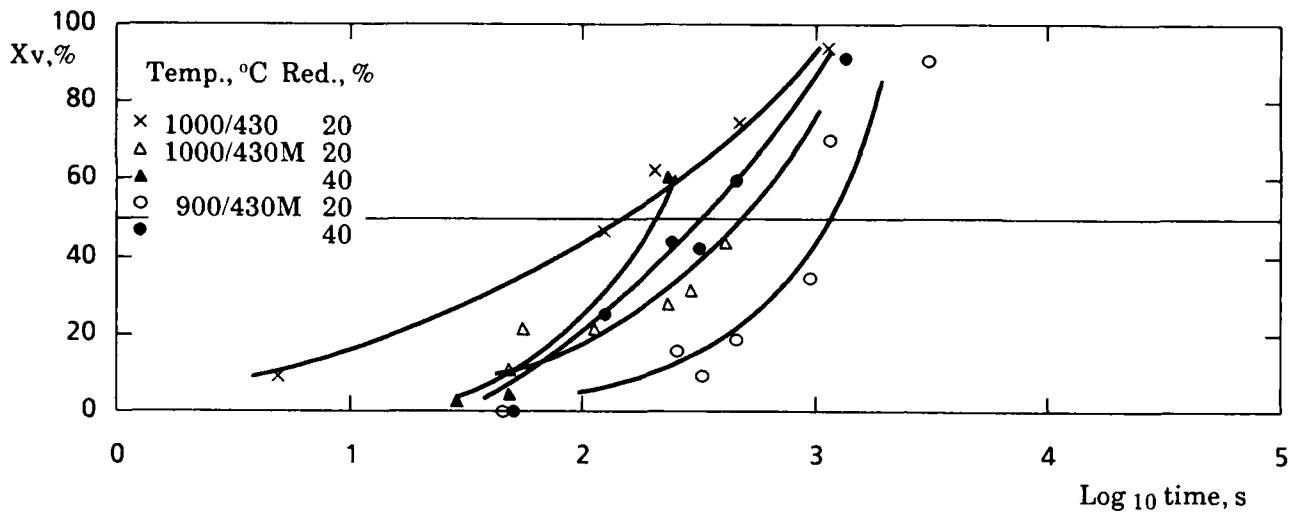


Figure 7- Evolution of the fraction recrystallized with annealing time for the type 430 and 430M steels.

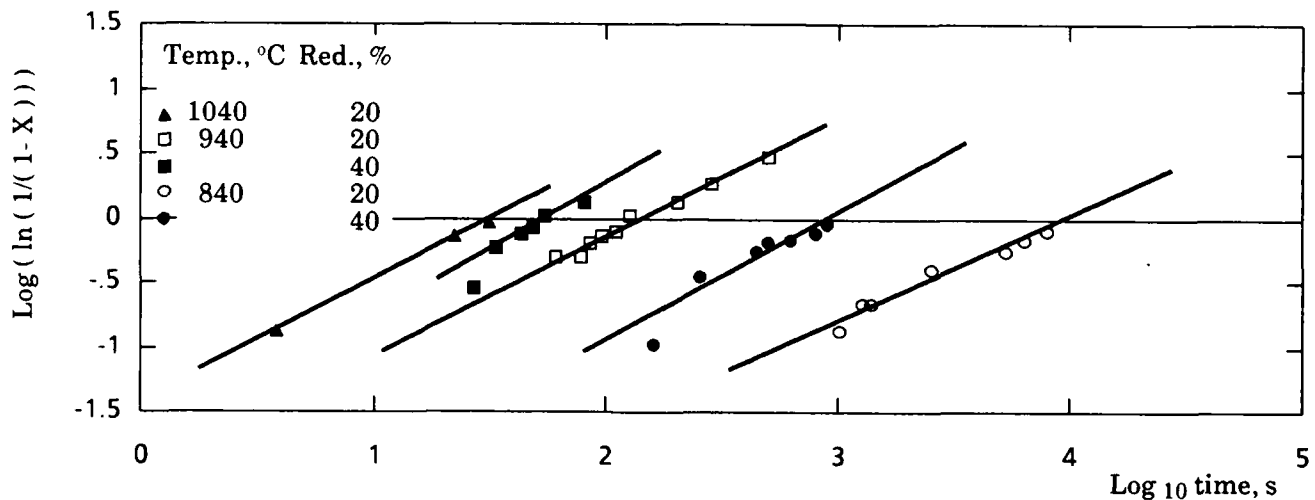


Figure 8- Evolution of the fraction recrystallized with annealing time for the type 304 steel .

The dependence of  $t_{50}$ , the time for 50% of the material to recrystallize, on the equivalent strain in rolling is shown in Figure 9. An expression of the form  $t_{50} \propto \epsilon^n$  has been proposed for C-Mn and Nb microalloyed steels (11). A thorough review of these steels (12) has shown that the value of  $n$  is 4. In the present investigation,  $n$  was found to be 1.7 for most of the steels. The type 316, however, displayed  $n$  values varying with temperature from 4.7 to 2.8 at 900 and 1000 °C, respectively. Although the average (3.7) is close to  $n \approx 4$ , values reported for the austenitic stainless steels are consistently lower and approximately 2 (2,3,4).

The retarding effects of adding Mo to the steel can be readily calculated for a given temperature from the expression

$$R_{316/304} = \log_{10} \left( \frac{t_{50/316}}{t_{50/304}} \right) \quad (2)$$

Here,  $R$  is the recrystallization rate retarding parameter of the 316 steel in relation to the 304 steel.  $R_{316/304}$  is 2.4 at 1000 °C. This is higher than the value of 1.6 calculated from the literature for the same ratio (2).

An activation energy for recrystallization can be computed if it is assumed that

$$t_x \propto \exp \left( \frac{Q_{rex}}{RT} \right) \quad (3)$$

Here,  $t_x$  is the time for a given fraction of the material to recrystallize. In the present paper,  $t_x$  is equal to  $t_{50}$ .  $Q_{rex}$  is the activation energy for recrystallization,  $T$  the absolute annealing temperature and  $R$  the universal gas constant. The activation energies obtained were 547, 355 and 120 kJ/mol for the 316, 304 and 430M steels,

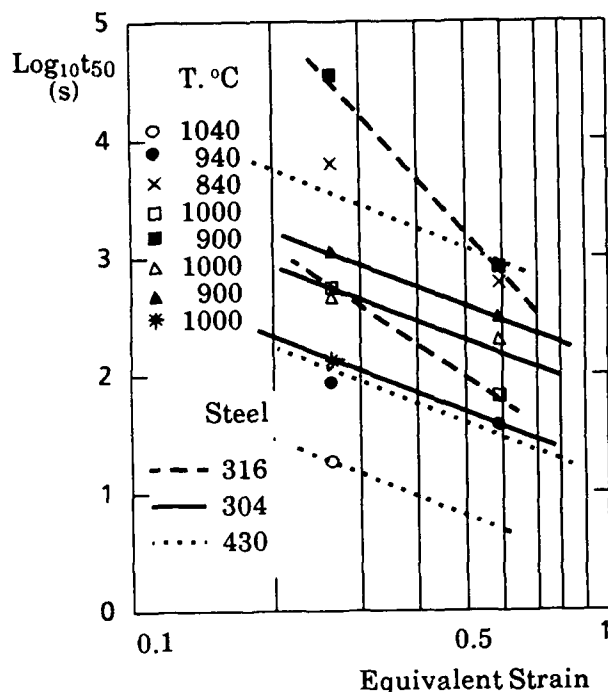


Figure 9. Dependence of  $t_{50}$  on the equivalent strain given in the previous pass.

respectively.  $Q_{\text{rex}}$  values reported in the literature are 525 to 336 kJ/mol for the 316 steel (2,4,13) and 425 to 334 kJ/mol for the type 304 (2-4,14). No reports were found on activation energy values for ferritic stainless steels.

### CONCLUSIONS

- 1- Nucleation in austenitic stainless steels occurs mostly at grain and annealing twin boundaries. Intragranular nucleation is also possible in 316 type steel.
- 2- Nucleation in ferritic stainless steels takes place at grain boundaries only.
- 3- The kinetics of static recrystallization are slower in type 316 than in 304 steels. This is attributed to the presence of Mo in the 316 steel.
- 4- Recrystallization is delayed in 430M steels when compared to 430 ones. This is due to the retarding effects of Nb and Ti either in solution or as precipitates.
- 5- Recrystallization follows an Avrami type dependence on annealing time. The values of the time exponent  $k$  in the present research are 0.9, 0.8, 1.1 and 0.9 for the 304, 316, 430M and 430 steels, respectively. No systematic dependence of  $k$  on either strain or annealing temperature is observed.
- 6- The dependence of  $t_{50}$  on the strain is suitably described by  $t_{50} \propto \epsilon^{-1.7}$  for most of the steels studied. The type 316, however, shows a higher strain exponent of 3.75.
- 5- The calculated values of activation energy for recrystallization are 547, 355 and 120 kJ/mol for the 316, 304 and 430M steels, respectively.

### ACKNOWLEDGEMENTS

The authors are grateful to Cia Aços Especiais Itabira, ACESITA for supplying the steels. Thanks are also due to Professor J.J. Jonas and Dr. S.Yue of McGill University for their many helpful comments and continuing encouragement. RB expresses his thanks to the World University Service of Canada for the award of a travelling fellowship and to the UFMG for granting a period of sabbatical leave during which this work was carried out. DBS acknowledges with gratitude the financial support received from FINEP and CNPq during this work.

### REFERENCES

- 1- Ahlblom, B. and R. Sandström, *Int. Met. Rev.* **27**, 1-27 (1982)
- 2- Sandberg, A. and R. Sandström, *Mater. Sci. Technol.* **2**, 917-925 (1986)
- 3- Barraclough, D.R. and C.M. Sellars, *Met. Sci.* **13**, 257-267 (1979)
- 4- Towle, D.J. and T. Gladman, *Met. Sci.* **13**, 246-256 (1979)
- 5- Richard, P. and T. Sheppard, *Mater. Sci. Technol.* **2**, 841-847 (1986)
- 6- Svenson, U.: in "The Hot Deformation of Austenite", J.B. Ballance, ed. AIME, New York, N.Y., 1977, pp. 499-516
- 7- Keown, S.R.: in "Hot Working and Forming Processes", C.M. Sellars and G.J. Davies, eds., The Metals Society, London, U.K., 1980, pp. 140-147
- 8- Paxton, M.M. and L. Straalsund, *Nucl. Technol.* **25**, 546-552 (1975)
- 9- Andrade, H.L., M.G. Akben and J.J. Jonas, *Metall. Trans. A*, **14**, 1967-1977 (1983)
- 10- Cahn, J.W., *Acta Metall.* **4**, 449-459 (1956)
- 11- Sellars, C.M. and J.A. Whiteman, *Met. Sci.*, **13**, 187-194 (1979)
- 12- Sellars, C.M.: in "Hot Working and Forming Processes", C.M. Sellars and G.J. Davies, eds., The Metals Society, London, U.K., 1980, pp. 1-15
- 13- Ryan, N.D., H.J. McQueen and J.J. Jonas, *Can. Metall. Q.* **22**, no 3, 369-378 (1983)
- 14- Campbell, G.T., E.P. Abrahamson Jr. and N.J. Grant, *Metall. Trans. A*

# EFFECT OF PRECIPITATION OF SECONDARY PHASES IN 17-14-2 AUSTENITIC CHROMIUM-NICKEL- MOLYBDENUM STEELS ON THE EVOLUTION OF LOW-CYCLE FATIGUE CRACKING

**Eugeniusz Szpunar**

Institute of Atomic Energy,  
Poland

**Jerzy Wawszczak**

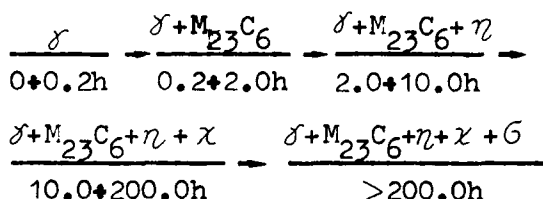
Warsaw University of Technology,  
Poland

AUSTENITIC CHROMIUM-NICKEL-MOLYBDENUM steels, widely used in nuclear power engineering as well as in chemical industry, should be characterized - for the sake of operational safety - by a high resistance against low-cycle fatigue. Processes of precipitation of interstitial and intermetallic phases, which take place in the course of fabrication of the installations and equipment, made from these steels, or during their service, affect their static mechanical properties merely to a low-degree while the influence of these processes on the dynamic properties, especially on the low-cycle fatigue resistance, can be of essential importance. That is why the effect of structural changes in austenitic steels, taking place during ageing after quenching, on the development of cracking under low-cycle fatigue load is the subject of investigation in several research institutions. The investigations so far carried out focussed mainly on the establishment of morphology and identification of the precipitated secondary phases while relatively few works were concentrated on the cracking process under low-cycle fatigue loads. The aim of the present work is to find out an interrelation between structural changes, occurring in austenitic steels of the 17-14-2 type during ageing, and the evolution of low-cycle fatigue cracking.

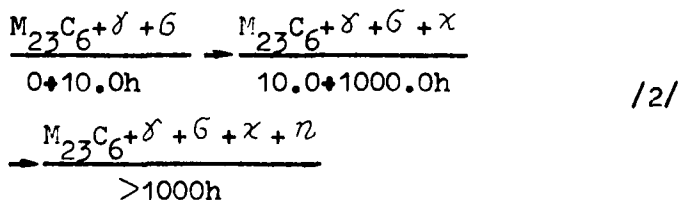
## STATE OF THE PROBLEM

PRECIPITATION PROCESSES OCCURRING IN THE OOH17N14M2 STEEL DURING AGEING - Of essential importance for determining the development of precipitation processes of interstitial and intermetallic phases

is the diagram /time-temperature-precipitation/ elaborated for the AISI 316L steel by Weisse and Strickler /1/. According to this diagram, the sequence of the precipitating phases and the ranges of their stability can be - for the ageing temperature being equal to that of the least durability of the non-equilibrium austenite /800 °C/ - presented by means of the following scheme:



The kinetics of growth of the individual interstitial  $M_{23}C_6$  and intermetallic  $\eta, \chi, \zeta$  phases as well as the proportions of these phases permit making the statement that the predominant phase is the  $\chi$  phase, while the volume proportions of the phases  $\eta$  and  $\zeta$  increase only when the ageing time exceeds 1000 h. The scheme of the precipitation process in the OOH17N14M2 steel at 815°C, verified by Bielanik /2/, is as follows:



The  $\zeta$  phase, occurring at the initial stage of the precipitation process, is - in the opinion of the authors /3, 4/ -



- the result of a partial decomposition of  $\delta$  ferrite which is present in this steel in small amounts. According to Szpunar and Bielanik /3, 4/, the onset of the precipitation of the  $\chi$  phase as well as of the preceding transient phases, occurs already after ageing times below 10 hours. These phases have a lath or plate structure, the proneness to gliding being therefore restricted in spite of their inconsiderable volume proportions, not exceeding 3 %.

**PHENOMENA ACCOMPANYING THE FATIGUE CRACKING** - Depending on the magnitude and location of the stress amplitude in the cycle and on the application of plain or notched specimens, a different approach is necessary to the interpretation of the fatigue of the material, subdivided into an initiation and a propagation stage, the research technique having to be adequately modified. The most manifest result of the fatigue test performed on notched specimens at a given load amplitude, is the number of cycles which is needed to bring the specimen to failure  $/N/$ . The number of cycles necessary for initiating the fracture process is generally neglected  $/N_i < 10^{-4} N/$ . By applying, in the quantitative interpretation of the kinetics of cracking, the "amplitude of the stress intensity factor"  $\Delta K_I$ , as it has been done by Paris and Erdogan /5/, it is possible to perform an analysis of the fatigue process at one or - at the most - at a few levels of the initial stress amplitude  $\Delta \sigma$ . By following the evolution of the crack and by expressing it as a function  $a = f(N)$  /where  $a$  is the length of the fatigue crack at a known instantaneous value of the nominal stress amplitude in the specimen/, one can determine the general form of the equation representing the kinetics of cracking /6, 7/ as

$$da/dN = C \lambda^n \quad /3/$$

where:

- $C, n$  - constants, of the material constant type,
- $\lambda$  - function describing any involution combination of the amplitude of the stress intensity factor and linearizing the kinetics equation /3/ in the double logarithmic coordinate system.

The most frequently used measure of the  $\lambda$  function is the relation  $\lambda = \Delta K_I$ , constituting the classical Paris for-

mula /4/:

$$da/dN = C \Delta K_I^m \quad /4/$$

The instantaneous cracking velocity as well as the crack trajectory are derivative of the process of formation and displacement of the heavy defected zone surrounding the bottom of the crack under propagation. The processes of plastic deformation taking place in this zone are determined by such factors as the level of stacking fault energy and the local arrangement of structural constituents as well as their shape, proportion, and properties.

The behaviour of aged austenitic steels during fatigue tests has got no extensive reflection in the literature. Most of the papers involved refer to phenomena accompanying the fatigue at a maximum cycle stress exceeding the yield stress or to fatigue taking place at elevated temperatures, i.e. when an active development of the cracks is accompanied by creep and oxidizing action of the environment. In the present work, the findings made by Yamaguchi and Kanazawa /8/ were taken advantage of, referring to the differentiation of the slip band arrangements and of the nature of fracture in specimens of the SUS 321 steel aged during various times and at various temperatures and then subjected to fatigue at elevated temperatures.

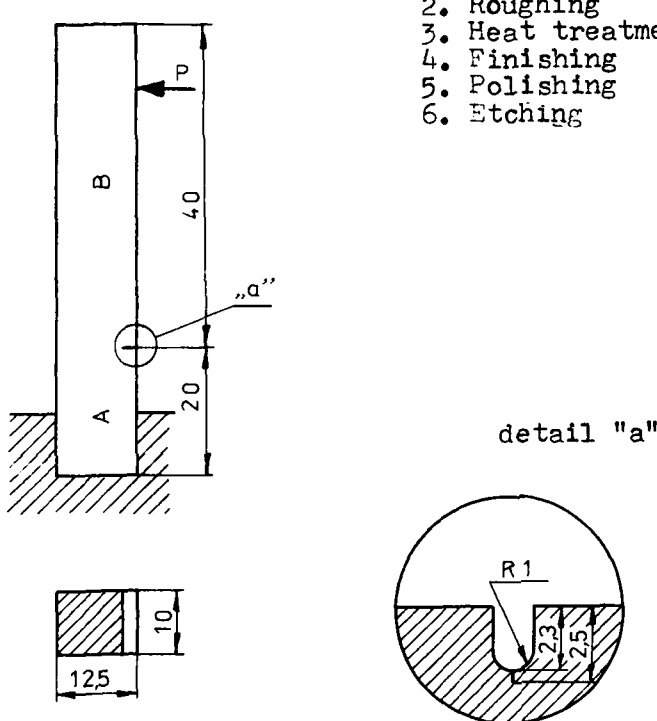
#### AIM OF THE WORK

The present work aimed at determining the effect of the degree of advancement of the precipitation process on the kinetics of development of fatigue cracks and on the fatigue life of the OOH17N14M2 steel aged at various temperatures. One hoped to reveal an effect of the precipitation process on the structure of slip bands in the neighbourhood of the propagating crack as well as on the topography of fatigue fractures. In view of the assumption as to the sensitiveness of this steel with respect to precipitation processes during fatigue cracking, it seemed to be interesting to make a comparison with the results of strength tests and hardness measurements performed for the same material in as-quenched condition. Similarly, taking into consideration the dislocation model of the plastic deformation in the crack region, one hoped to find a differentiation of the dislocation structure in the direct neighbourhood of the crack and in the regions situated far away from the cracking zone.

MATERIAL USED FOR INVESTIGATION  
AND INVESTIGATION PROCEDURE

The material subjected to investigation was the 00H17N14M2 steel of the fol-

lowing chemical composition: C - 0.028%,  
Mn - 1.93%, Si - 0.25%, Cr - 17.2%,  
Ni - 12.6%, S - 0.011%, P - 0.025%,  
Fe - balance. The specimens were prepared  
and subjected to examination according to  
Table 1.

Table 1			Preparation of specimens				Investigation programme							
Procedure of specimen preparation			Machining		<div>Operations:</div> <div>1. Cutting out</div> <div>2. Roughing</div> <div>3. Heat treatment</div> <div>4. Finishing</div> <div>5. Polishing</div> <div>6. Etching</div>									
Heat treatment			Treat-ments		Time h	Specimen numbers		Number of tested specimens						
			Tempering 250°C/2.5 h		Ageing 800°C	0	1.1 + 1.10		10	10	1	1B	3A	9B
						2	2.1 + 2.10		10	10	1	1B	3A	9B
						10	3.1 + 3.10		10	10	1	1B	3A	9B
						100	4.1 + 4.10		10	10	1	1B	3A	9B
						1000	5.1 + 5.10		10	10	1	1B	3A	9B

## RESULTS OF INVESTIGATION

**MICROSTRUCTURAL EXAMINATIONS** - Microstructural examinations served to determine the degree of changes provoked by ageing. The polygonal structure of super-saturated austenite, containing numerous twins, undergoes during ageing /2 h and 10 h/ a change manifesting itself by progressive vanishing of twin boundaries /Fig. 1a/. At the same time, also the decomposition of  $\delta$  ferrite takes place. This may be seen in Fig. 1a as elliptic chains of precipitate at the grain boundaries of austenite.

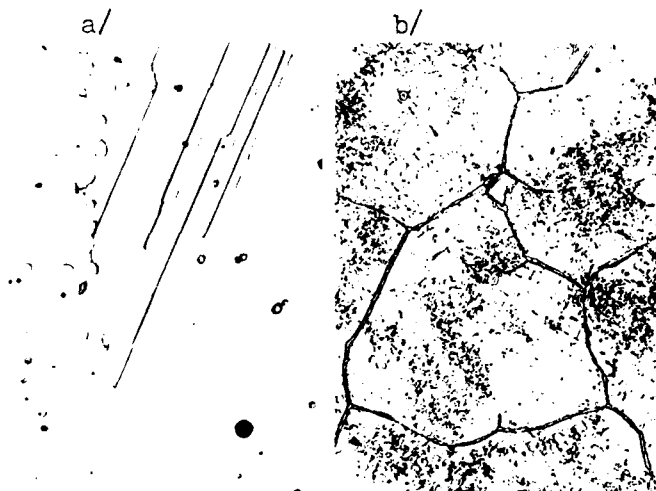


Fig. 1 - Structure of 00H17N14M2 steel  
a/ in as-quenched condition 1250°C/2.5 h  
b/ after quenching 1250°C/2.5 h and  
ageing 800°C/1000 h.  
Etched with Vilella's reagent. Magnification 200x.

An extension of the ageing time up to 100 hours markedly increases the etching intensity of austenite, this being an evidence of an advanced degree of evolution of the precipitation process. Similarly, minute precipitate particles within some, not numerous, grains can be seen.

By supplementary investigations, performed by electron diffraction technique on extraction replicas, the precipitated particles involved were identified to be the  $\chi$  phase. The structure rebuilding phenomena, occurring after 100 hours of ageing, intensify as the ageing time is extended until after holding the steel for 1000 hours at 800°C they reach a saturation state while the structure assumes a stable form /Fig. 1b/. Especially conspicuous is a continuous line of the precipitated  $\chi$  phase at grain boundaries as well as numerous minute particles of this phase within the austenite grains.

Elongated precipitated particles of the  $\chi$  phase within the grains decorate locally, by their shape, the remains of twin boundaries and give a distinct indication that their nucleation took place between the second and tenth hour of the ageing process /Fig. 1b/.

**STUDIES ON THE KINETICS OF FATIGUE CRACKING** - Fatigue specimens, of a shape shown in Table 1, were subjected after ageing to a pulsating - from the zero value - bending stress at a constant maximum bending force within the cycle giving in the notch region nominal stresses  $\sigma_{\max} = 192$  MPa, the frequency being 2.5 Hz. In the course of the fatigue test the length of the notch "a" in relation to the fatigue cracking cycle number "N" was recorded. The test was interrupted and the cracking cycle number "N" was determined after the bend angle had reached the predetermined value. The experimental cracking curve, written as  $N_2 = f/a$ , was approximated by the quadratic polynomial  $N = Aa^2 + Ba + C$ . By calculating the inverse of the derivative of the function in the form  $da/dN = 1/2Aa + B$  and making a compilation in relation to the amplitude of the intensity factor  $\Delta K$ , a series of pairs of corresponding points, which determine the curve  $da/dN = f(\Delta K)$  was obtained. The curve was, next, linearized and such a form of the quantity was sought which would satisfy the expression /5/:

$$\lg da/dN = n \lg \lambda + C \quad /5/$$

In the case under consideration, a satisfactory consistency with the experimental results was obtained by substituting for  $\lambda$  the expression /6/:

$$\lambda = (\Delta K_I)^\beta, \quad \beta = (\Delta K_I / \Delta K_{I\max})^2 \quad /6/$$

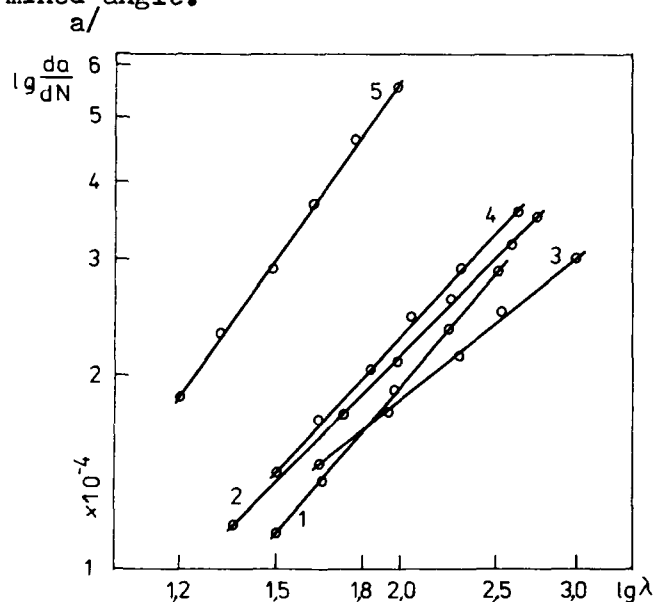
$$\Delta K_I = 4.2 M / (g b)^{1.5} F(a/b) \quad /7/$$

$$\Delta K_{I\max} = \Delta K_I, \quad a = a_{\max} \quad /8/$$

$$F(a/b) = \left[ (1 - a/b)^{-3} - (1 - a/b)^3 \right]^{0.5}$$

In the above-mentioned formulas, g and b are the dimensions of the specimen cross-section, M is the bending moment in the notch region while a and  $a_{\max}$  represent, respectively, the instantaneous and the maximum length of the fatigue crack corresponding to the critical bend angle. The correlation coefficient of the equation /5/ oscillated around 0.99. By calculating, for every specimen, the values C and n and determining, then, C and n

for the given state, a pencil of straight lines, as shown in Fig. 2a, was obtained. In view of insignificant differences in the value of  $C$  for all the specimens involved, an average  $C$  value was calculated  $/C = 7.41 \times 10^{-5}/$  whereupon, basing on the fixed " $C$ " value, the exponent " $n$ " for every state was determined, its value in relation to the ageing time being shown in Fig. 2b. As may be seen from Fig. 2b, the coefficient " $n$ " in the equation of the kinetics of fatigue cracking has a minimum value at an ageing time of 10 hours. Fig. 2c illustrates the effect of ageing time of the OOH17N14M2 steel on the fatigue life expressed by the cracking cycles number " $N$ " until the specimen has been bent through the predetermined angle.



b/

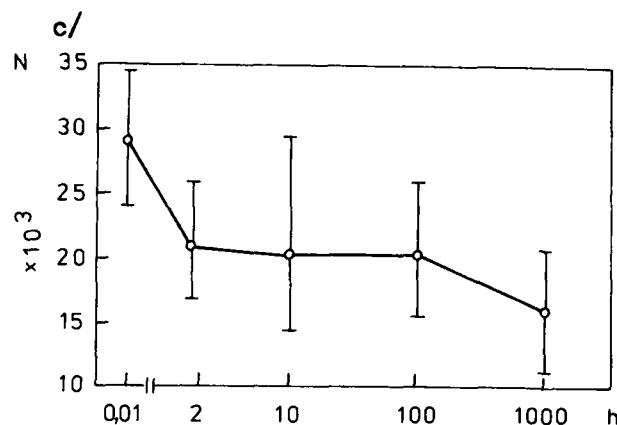
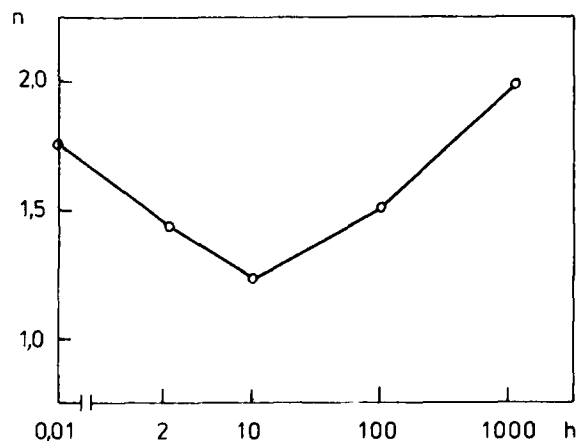


Fig. 2 - Results of fatigue tests:  
a/ averaged results of linearization of the curves, relating to the kinetics of fatigue cracking, by means of the function 5, where: 1 - after quenching, 2 - after ageing for 2 hours, 3 - after ageing for 10 hours, 4 - after ageing for 100 hours, 5 - after ageing for 1000 hours;  
b/ Variation of the exponent " $n$ " of the curves of fatigue cracking versus ageing time;  
c/ variation of the fatigue life " $N_c$ " versus ageing time.

RESULTS OF INVESTIGATION OF SLIP BANDS DENSITY IN THE PLASTICALLY DEFORMED BOTTOM OF THE FATIGUE NOTCH - On the basis of microstructural examination an attempt was made to assess the density of slip bands within the grains in the immediate neighbourhood of the fatigue crack. The results of microscopic examination of the region adjoining directly the crack are shown, for the as-quenched condition as well as after ageing for 100 hours, in Fig. 3. By calculating - for a given number of cracking cycles - the ratio of the number of grains containing slip bands to the control number of grains in the region of the bottom of the fatigue crack, a scheme of the increase in density of slip bands with increasing number of cracking cycles was obtained, as shown - for all structural states of the material - in Fig. 4.

As may be seen, a complete malleabilizing of the control number of grains in the region of the bottom of the fatigue notch is likely to appear ageing for not more than 10 hours.

As could be expected, a very distinct decrease in density of slip bands with the extension of ageing time and intensification of the precipitation process has exerted an effect on the dislocation

density in the region of the fatigue notch. Dislocation density not only depends on the conditions of fatigue cracking but is also a function of the distance from the bottom of the fatigue crack under propagation.

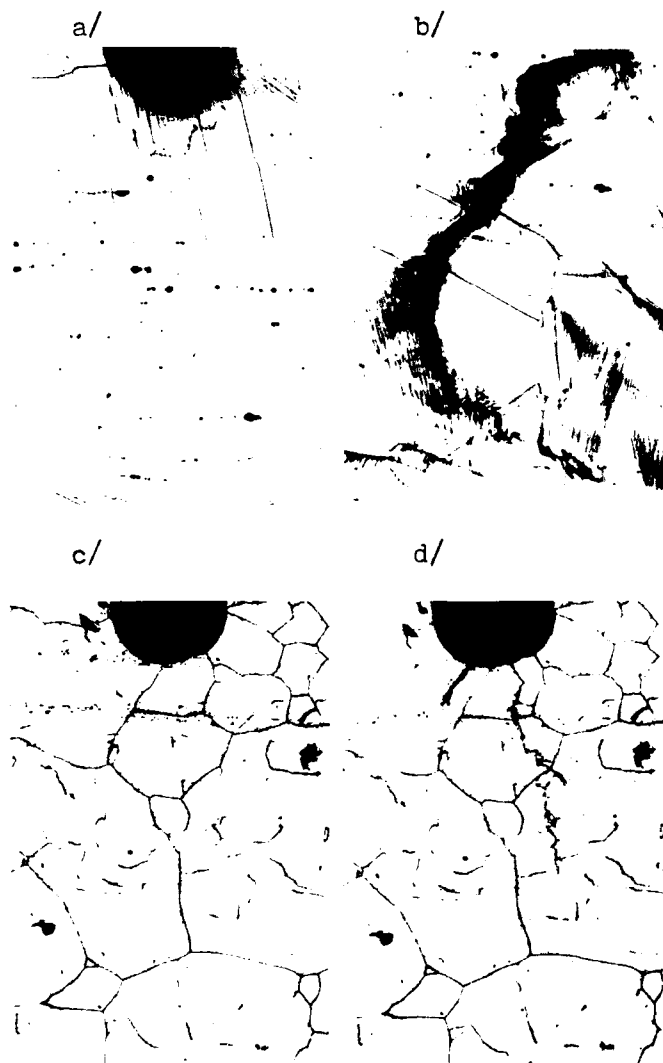


Fig. 3 - Microstructure in the region of the fatigue notch bottom after various cracking cycles number:  
a/ in as-quenched condition, 500 cracking cycles;  
b/ in as-quenched condition, 8000 cracking cycles;  
c/ after ageing for 100 h, 500 cracking cycles;  
d/ after ageing for 100 h, 8000 cracking cycles;  
Specimen etched with Vilella's reagent prior to fatigue testing. Magnification 150 x.

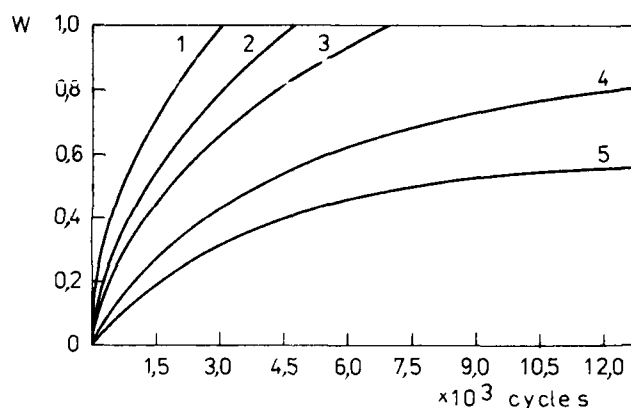


Fig. 4 - Change in density of slip bands in the fatigue notch region, expressed as the ratio of the number of grains in which slip occurs to the control number of grains "W" versus number of fatigue cracking cycles.  
1 - in as-quenched condition, 2 - after ageing for 2 h, 3 - after ageing for 10 h, 4 - after ageing for 100 h, 5 - after ageing for 1000 h.

Specimens for transmission electron microscopy examinations were prepared by cutting out thin slices /0.1 mm/ and by electrolytic thinning, until reaching a foil thickness, parallel to the fatigue crack surface, at a distance of 0.2, 1.5, 3.0 and 4.4 mm. For investigation purposes such a specimen was chosen from a given state which turned out to be closest, according to Fig. 2c, to the average value characteristic of the given state. A foil segment permits, depending on the perforation site, an approximate establishment of the number of cracking cycles, determining the pattern of the dislocation structure. For investigation, only regions having an identical orientation with respect to the axes of the zone: /110/ and /111/ were selected. A contrast juxtaposition of the patterns of distribution of dislocations and slip bands testify to the existence of an essential interrelation between the intensity of the precipitation process and the dislocation structure. After ageing for 100 hours, dislocation tangles are replaced by single dislocation loops or not numerous dislocation lines concentrated in the boundary region. Numerous slip bands, occurring in as-quenched condition /Fig. 5a/, undergo an essential reduction as the distance from the fracture surface is growing, or begin to vanish completely after ageing for 10 hours.

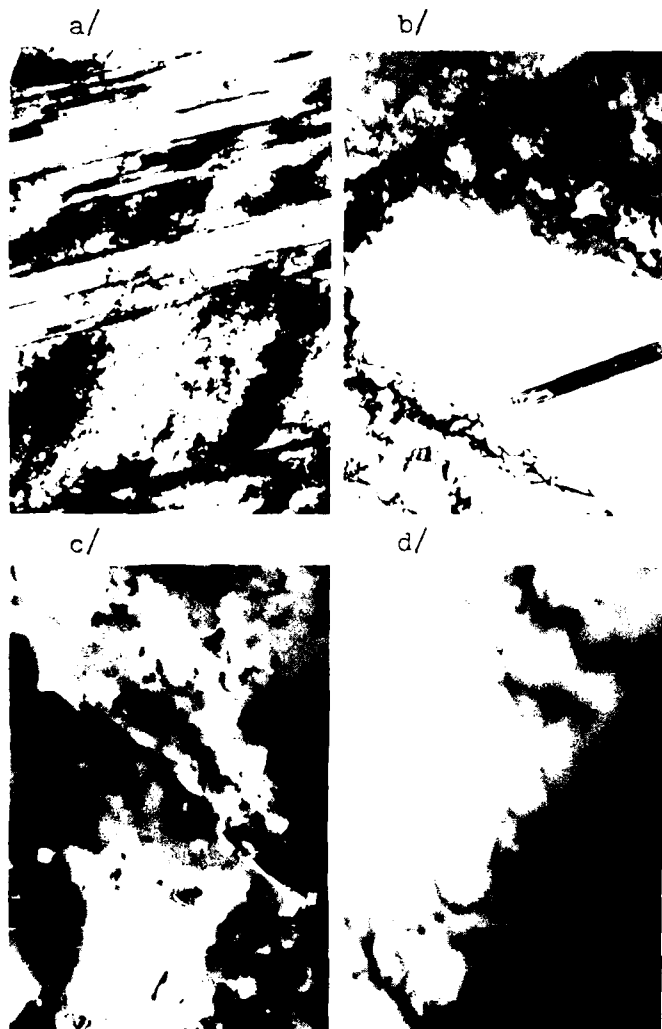


Fig. 5 - Arrangement of dislocations and slip bands in as-quenched condition and after ageing for 100 hours:  
a/ region in the immediate neighbourhood of the crack, as-quenched condition, cracking cycles number 800 - 15 000 magnification 7 000 x;  
b/ region at a distance of 4.5 mm from the crack, cracking cycles number 8 000 - 15 000, magnification 16 000 x;  
c/ region in the immediate neighbourhood of the crack, after ageing for 100 h, cracking cycles number 2 000 - 4 000, magnification 12 000 x;  
d/ region at a distance of 4.5 mm from the crack, cracking cycles number 8 000 - 15 000, magnification 16 000 x.

#### RESULTS OF FRACTOGRAPHIC EXAMINATION

- From among the many morphologic forms of fatigue fractures such ones, six in number, were chosen which correspond distinctly with the course of fatigue phenomena at various stages of the precipitation process. The successive pictures /Fig. 6/ represent the evolution of cracking from the as-quenched condition to that after ageing for 100 hours.



Fig. 6 - Passage of fatigue crack through twin boundary. Fatigue fracture of a specimen in as-quenched condition. Magnification 330 x. Fracture surface etched.



Fig. 7 - Microcracks in terrace arrangement. Fatigue fracture of a specimen after ageing for 100 h. Magnification 7 000 x. Fracture surface etched.

The topography of the fractures is constituted by developed systems of jogs of differentiated sizes and development directions. The lack of the phenomenon of plastic "crack closing" in the compression half-cycle /in view of a pulsating - from the zero value - course of the load cycle/ has caused in many regions a decay of the typical set of fatigue striae. In other regions, a

network of microcracks, up to 5  $\mu$ m long, situated at the intersection of slip planes with the cracking surface, was revealed. The successive pictures /Fig. 8 and 9/ represent the image of the austenite grain boundary decorated with precipitated particles of the  $\chi$  phase. In spite of a considerably higher magnification, the precipitated particles involved are after ageing for 100 h markedly smaller than those observable after ageing for 1000 h /Fig. 8/.



Fig. 8 - Precipitation at austenite grain boundary. Fatigue fracture of a specimen after ageing for 100 h. Magnification 3 600 x. Fracture surface etched.



Fig. 9 - Precipitation at austenite grain boundary. Fatigue fracture of a specimen after ageing for 1000 h. Magnification 2 600 x. Fracture surface etched.

A developing fatigue crack, coming across minute precipitated particles of the  $\chi$  phase /characteristic for short ageing times/, generally passed round these obstacles, thus increasing the amount of energy consumed for fracturing the specimen. The growth of the  $\chi$  phase particles to the sizes shown in Figs 10 and 11 has qualitatively changed the mechanism of cracking of these particles

from an intercrystalline to a transcrystalline one. This process concerned the particles of the phase precipitated within the grains /Fig. 10/ while in the boundary region the precipitated particles underwent decohesion along grain boundaries as shown in Fig. 11.



Fig. 10 - Region with cleavage cracking of the  $\chi$  phase within austenite grains. Fatigue fracture of a specimen aged for 1000 h. Magnification 5 000 x. Fracture surface etched.



Fig. 11 - Region of the austenite grain boundary decorated with precipitated particles of the  $\chi$  phase. Fatigue fracture of a specimen after ageing for 1000 h. Magnification 3 500 x. Fracture surface etched.

RESULTS OF MECHANICAL TESTING - The changes observed in the course of fatigue testing of the specimens aged for various times required a corroboration or some commentary ensuing from the investigation of other strength properties and from hardness measurements.

In Fig. 12, the variation of fatigue properties, expressed by "N" and "n", as well as of such mechanical

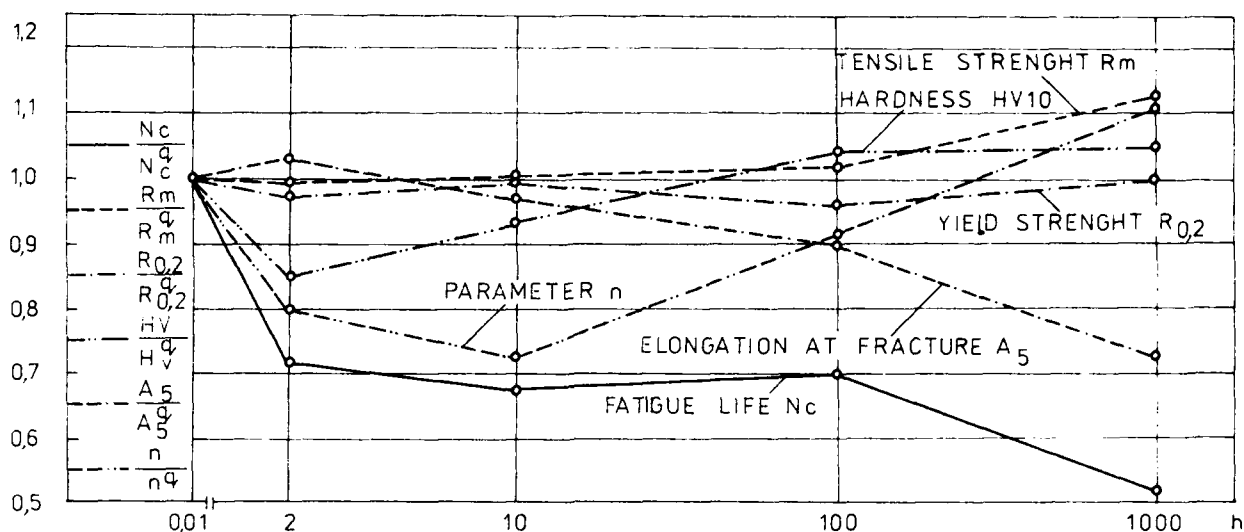


Fig. 12 - Effect of ageing time on selected mechanical properties of OCH17N14M2 steel

properties as tensile strength  $R_m$ , offset yield stress  $R_{0.2}$ , percent elongation after fracture  $A_5$  and Vickers hardness  $HV$  has been presented as a function of ageing time. In order to perform a simultaneous assessment of the sensitiveness of the individual parameters to the precipitation process, all the results of investigation have been represented in fraction form, in relation to the as-quenched condition assumed as a reference state.

As already suggested earlier, fatigue properties /particularly the fatigue life  $N_c$ / show, along with the elongation  $A_5$ , the highest sensitiveness to changes in intensity of the precipitation process.

#### DISCUSSION OF THE RESULTS

The fragments of an extensive investigation programme, presented in this paper, have fully corroborated the thesis on the effect of the precipitation of interstitial and intermetallic phases in the 17-14-2 chromium-nickel-molybdenum steel on the evolution of low-cycle fatigue cracking and on the low-cycle fatigue life. The processes of precipitation of interstitial and intermetallic phases, taking place in this steel, have a different meaning for the course of fatigue cracking. In view of a very low percentage of carbon in the steel under investigation, the process of precipitation - mainly of the  $M_{23}C_6$  type carbides - which normally takes place at the initial stages of the ageing

process, was very weakly accentuated and had only an inconsiderable effect on static mechanical properties and on the fatigue cracking process. In the steel under investigation, an essential influence on the properties was exerted by the processes of nucleation, growth and coagulation of the intermetallic  $\chi$  phase. In view of a low proportion of high-temperature  $\delta$  ferrite, its decomposition products did not show any remarkable effect on the mechanical properties.

Taking into consideration the material and the conditions of experimental procedure, the statement can be made that of a decisive importance, from the view-point of the fatigue life and the kinetics of fatigue cracking, is the proportion and morphology of the  $\chi$  phase. The processes of nucleation, growth and coagulation of the  $\chi$  phase are in the most unambiguous way described by the duration of ageing after quenching. That is why, in the following discussion, the ageing time has been adopted as the basic factor for performing the analysis.

The dependence of the fatigue life on the ageing time can be subdivided into three stages. The first stage of the initial period of ageing extends from 0 to 2 hours. Here, as a result of diffusion processes, precipitation of a small amount of carbides of the  $M_{23}C_6$  type takes place while the process of nucleation of the  $\chi$  phase has not begun as yet; one can assume that it is only in the incubation period. A decrease in hardness and in offset yield stress, and an increase in ductility, expressed by



percent elongation, occurs. These processes and the resulting changes in static properties entail a considerable shortening of the fatigue life. At the same time, they influence favourably the kinetics of cracking which is characterized by a decrease of the exponent "n" in the equation of the kinetics of fatigue cracking. A characteristic feature of this structural state is an intracrystalline cracking of austenite grains.

The second stage extends over the ageing time from 10 to 100 hours. In this period, marked changes occur in the structure, consisting in nucleation and growth of numerous particles of the  $\chi$  phase, mainly in the regions of austenite grains and twin boundaries as well as within austenite grains. Apart from that, decomposition of high-temperature  $\delta$  ferrite into the  $\delta$  phase and austenite takes place. Tensile strength and hardness show an increase, offset yield stress becomes stabilized while percentage elongation decreases. A decrease in density of slip bands in the region of the notch bottom is observable. In this range of precipitation processes, the fatigue life does not show any significant changes while the exponent in the equation of the kinetics of fatigue cracking increases. Fracture topography indicates that cracking goes through the precipitated particles of intermetallic phases.

The third stage covers the ageing period in the range from 100 to 1000 hours. A decrease in formation of new nuclei of the  $\chi$  phase is observed while the already existent precipitated particles grow and coagulate. Hardness and offset yield stress do not vary to an appreciable extent while the percentage elongation shows a decrease. In the region of the notch bottom, the density of slip bands distinctly decreases. The fatigue life becomes shorter while the exponent "n" in the equation of fatigue cracking increases. An analysis of the topography of fractures indicates that the ratio of the intercrystalline to the intracrystalline fracture increases.

The present work has demonstrated that even minor amounts of intermetallic phases, precipitating in the ageing process, are likely to exert an essential influence on the low-cycle fatigue life as well as on the kinetics of fatigue cracking. The topography of fractures depends on the morphology of the precipitated secondary phases and on the degree of advancement of the precipitation process. Fatigue fractures testify

to the interference of the traces of passage of the crack through the slip system with fatigue striae.

#### REFERENCES

1. B. Weiss, R. Strickler, *Metallurg* 3, 851 /1972/
2. J. Bielanik, Doctor's thesis, Silesian University of Technology, Gliwice /1987/
3. E. Szpunar, J. Bielanik, Report on the research work entitled "Investigation of the processes of precipitation of intermetallic phases in the OOH17N14M2 steel", Warsaw University of Technology, Plock /1985/
4. E. Szpunar, J. Bielanik, 4th International Congress on Heat Treatment of Materials, West Berlin /1985/
5. P. Paris, P. Erdogan, *Journal of Basic Engineering Trans., ASME* /1963/
6. J. Wawszczak, Doctor's thesis, Institute of Materials Science, Warsaw University of Technology /1981/
7. J. Wawszczak, *Mechanics* 104, Warsaw University of Technology 77/1987/
8. K. Yamaguchi, K. Kanazawa, *Transactions of National Research Institute for Metals*, vol. 25, 3 /1983/
9. K. Hatanaka, H. Kanabe, T. Yamada, *The Society of Materials Science, Japan Kyoto* /1972/
10. W. T. Troshchenko, "Cyklicheskaya deformatsiya i ustalost metallov", Naukova Dumka, Kiev /1985/
11. M. Siratori, T. Miesi, H. Maisita, "Vychislitel'naya mekhanika razrushe-niya", Izdatel'stvo "Mir", transl. from Japanese /1986/

# AGING BEHAVIOR OF DOUBLE QUENCHED AND COLD WORKED MULTIPHASE STAINLESS STEELS

F. D. S. Marquis, S. F. Wang, J. H. Qadri, M. Hadji, M. N. Datar

Department of Metallurgical Engineering  
South Dakota School of Mines and Technology  
Rapid City, South Dakota 57701, USA

## ABSTRACT

An investigation of athermal, stress assisted, strain induced and isothermal phase transformations and phase transformation strengthening has been carried out on three low carbon, low nitrogen and low phosphorus multiphase stainless steels of the types: Fe-Cr-Ni-Ti; Fe-Cr-Ni-Ti-Nb and Fe-Cr-Ni-Ti-Mo. The combination of Ti, Nb, Mo and P; low C and N contents with very high density of athermal and deformation induced transformation products; high density of substructure (dislocation, twins and stacking faults) increased the nucleation rate of MC carbides and delayed the heterogeneous precipitation of  $M_{23}C_6$  carbides at triple points and grain boundaries. The final microstructures consisted of the intertwinning phases: athermal, stress assisted and strain induced martensites, TiC, NbC, MoC and phosphides. Tensile strengths in excess of 180 Ksi were obtained at 293 K. These strength levels were maintained without any significant decrease up to 573 K. The Cr-Ni-Ti-Nb multiphase steel exhibited the best combination of ductility and resistance to dislocation motion in the temperature range 293 K to 773 K. However, in the temperature range 773 K to 973 K the best combination of these properties was exhibited by the Cr-Ni-Ti-Mo multiphase steel. The elevated temperature strength characteristics of these multiphase dispersions suggest that these steels may have a much better fatigue-creep behavior under in situ irradiation conditions than any commercial material currently available.

THE MECHANICAL PROPERTIES and corrosion resistance of stainless steels have justified their incorporation in nuclear reactors, chemical reactors, superheaters, boilers and in the construction industry. Currently a large amount of attention is being given to these

steels as the main candidates for first wall materials in fusion reactors. Two major types of stainless steels are commercially available, single phase (austenitic, ferritic and martensitic) and duplex (austenite/ferrite and ferrite/martensite). Only in the last decade, many millions of dollars have been spent worldwide in an attempt to maximize simultaneously the strength, toughness, formability and pitting/crevice corrosion resistance of stainless steels. This is justified by the complexity of these steels, where various phases and morphologies can be obtained, some of them being deleterious such as the sigma ( $\sigma$ ) and the Laves phases (1,2). This transfers to the materials scientist a heavy responsibility to insure that these alloys are properly designed and successfully employed.

The microstructural design and the prediction of the evolution of the microstructure under load, at elevated temperatures and under irradiation, is surrounded by tremendous complexity and thus very difficult to achieve. In addition to the preirradiation microstructural variables, the designer needs to consider stress, temperature, irradiation nature, dose, dose rate and He/dpa ratio. Most of the data now available concerning these variables has been obtained on austenitic stainless steels, both metastable such as 304 and stable such as 316 and PCA (3 to 7).

In order that these stainless steels can be successfully employed as first wall materials in fusion reactors, various major problems must be solved first: loss of ductility, sensitization, void swelling and helium embrittlement during elevated temperature irradiation (6 to 9). Based on the major problems encountered, attempts have been made recently to modify and improve these steels (10 to 15).

The objective of this research program, of which partial results are reported in this paper and elsewhere in this congress, (15) is to solve totally or partially some or all of the problems reported above.

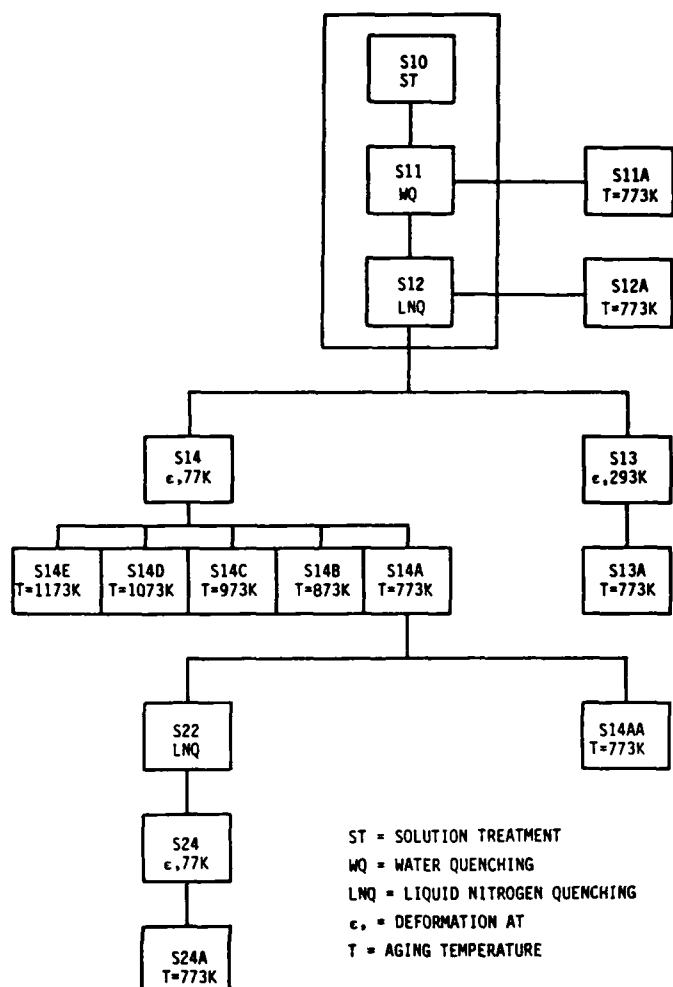


Fig.1 Flow diagram of the sequences of transformation, deformation and aging processing

The specific project goals are to design, manufacture and evaluate multiphase stainless steels (MPSS) consisting of complex mixtures of austenite ( $\gamma$ ), athermal martensite ( $\alpha'_A$ ), stress assisted and strain induced martensites ( $\epsilon'D$ ,  $\alpha'D$ ); very fine dispersions of intragranular carbides of the MC type: TiC, NbC and MoC and very fine dispersions of Fe-Ti phosphides. The long range evaluation program involves creep, creep-fatigue and irradiation creep-fatigue tests.

#### EXPERIMENTAL PROCEDURE

The compositions of the multiphase steels used in this investigation are presented in Table 1. Figure 1 shows a flow diagram of the sequences of deformation and aging processing carried out in order to achieve the desired microstructural design. Table 2 defines the precise nature of each process of deformation and aging. In the interpretation of this table and of the nomenclature presented in this paper, the following code must be used: the first

cycle of deformation and aging is designated by the first digit, 1, and the second cycle by the first digit, 2. The meaning of the second digits are: 0 = solution treatment, 1 = water quenching, 2 = liquid nitrogen quenching, 3 = deformation at 293 K up to 1.6 true plastic strain, 4 = deformation at 77 K up to 1.6 true plastic strain. Capital letters mean aging at

Table 1- Compositions of Precipitation Hardened Cold Worked Multiphase Stainless Steels

MPSS Comp.		Cr-Ni-Ti	Cr-Ni-Ti-Nb	Cr-Ni-Ti-Mo
Type 1	6 C 7 N	0.046 0.024	0.047 0.024	0.046 0.025
Type 2	24 Cr 28 Ni	16.00 11.95	16.03 13.64	15.91 16.17
Type 3	22 Ti 41 Nb 42 Mo	0.18 0.006 0.005	0.17 0.79 0.005	0.17 0.024 0.83
Type 4	14 Si 15 P 16 S 25 Mn	0.75 0.023 0.022 0.97	0.74 0.025 0.021 0.97	0.72 0.019 0.020 0.98
Calc. Cr Eqt.		17.13	17.54	17.83
Calc. Ni Eqt.		13.82	15.54	18.04

the following temperatures: A = 773 K, B = 873 K, C = 973 K, D = 1073 K, E = 1173 K. All the aging processes were carried out for a time period up to 1000 hours. Small letters mean: h = hours; m = minutes.

The microstructures were characterized by optical microscopy, scanning electron microscopy (SEM), conventional transmission electron microscopy (CTEM), and scanning transmission analytical electron microscopy (STAEM), (17). X-ray diffractometry, selected area diffraction (SAD), microdiffraction (MD) and magnetic measurements were used to identify, characterize and measure the amounts of the phases formed during each process of deformation and aging. Precipitate extraction methods were applied on grip portions of the tensile specimens which were immersed in a 10% solution of bromide in methanol, initially for 24 hours. The residues were then collected and prepared for X-ray diffraction analysis. Mechanical properties were measured using a Vickers diamond pyramid hardness tester, a Knoop microhardness indenter and a MTS mechanical testing machine. The yield strength  $\sigma_y$ , the tensile strength  $\sigma_u$ , and the elongation at fracture % El, were measured in the temperature range, 293 K to 973 K, and in

the strain rate range, 10<sup>-5</sup> to 10<sup>-3</sup> sec<sup>-1</sup>.

Table 2.- Deformation and Aging Processing

Proc. No.	Nature of Process
First Cycle of Deformation and Aging	
S10	Solution treatment.
S11	Water quenching following S10.
S12	Liquid nitrogen requeenching following S11.
S13	Deformation by rolling at room temperature (293 K) following S12.
S14	Deformation by rolling at 77 K following S13.
S11A	Aging at 773 K of S11.
S12A	Aging at 773 K of S12.
S13A	Aging at 773 K of S13 followed by water quenching (WQ).
S14A	Aging at 773 K of S14 followed by WQ.
S14B	Aging at 873 K of S14 followed by WQ.
S14C	Aging at 973 K of S14 followed by WQ.
S14D	Aging at 1073 K of S14 followed by WQ.
S14E	Aging at 1173 K of S14 followed by WQ.
S14AA	Aging at 773 K of S14A followed by WQ.
Second Cycle of Deformation and Aging	
S22	Liquid nitrogen quenching following S14A.
S24	Deformation by rolling at 77 K following S22.
S24R	Deformation by rolling at 77 K following recrystallization during S14C, S14D or S14E.
S24A	Aging at 773 K of S24 followed by WQ.

## RESULTS AND DISCUSSION

Both theoretical and experimental results which are part of those obtained in this research program are presented and discussed below:

### DESIGN OF MULTIPHASE STAINLESS STEELS

The design of these multiphase stainless steels is primarily a two fold design: the chemical design and the microstructural design, in order to achieve an optimized combination of physical and mechanical properties.

The chemical composition of these multiphase stainless steels was adjusted by manipulating the content of four major types of elements: carbon and nitrogen in the first; chromium and nickel in the second; titanium, niobium and molybdenum in the third, and silicon and manganese in the fourth. In order to obtain the formation of a passive oxide film and insure an effective corrosion and oxidation resistance, the chromium content was kept at approximately

16 wt%. The manganese and the silicon contents were kept at approximately 0.97 and 0.74 wt%, respectively, to insure deoxidation. The ratio Mn/Si was kept at above one in order to insure good fracture toughness. Strong carbide formers: Ti, Nb and Mo were added at approximately 0.18 wt% Ti, 0.80 wt% Nb and 0.80 wt% Mo in order to be able to produce a very fine dispersion of intragranular MC carbides. The formation of these carbides raised the  $M_s$  temperature and allowed the production of secondary hardening upon quenching to liquid nitrogen.

Although C and P have been reported with the capacity of retarding the formation of Laves phases at grain boundaries (14), their contents were kept here deliberately very low at approximately 0.046 and 0.024, respectively. This was in order to retard the formation of  $M_{23}C_6$  carbides at triple points and grain boundaries. However, the phosphorus content was kept at 0.024 in order to induce the formation of phosphides (Fe-Ti-P) and to balance the ratio of the MC/phosphide phases. Both phases were designed to refine the helium bubble distribution and improve void swelling resistance. In addition, the formation of a very fine dispersion of intragranular MC carbides appeared to have the capability of trapping helium bubbles at their interfaces, preventing the coarsening of these bubbles at the  $\gamma/\gamma$  grain boundaries which provides resistance to helium embrittlement. In the microstructural design, additional intragranular trapping for small helium bubbles was provided by very fine dispersions of tempered athermal, stress assisted and strain induced martensites.

The chromium and nickel contents were adjusted in order that the martensite start temperature ( $M_s$ ) was between room temperature (293 K) and liquid nitrogen temperature (77 K) and the martensite finish temperature ( $M_f$ ) was below 77 K. In these steels most of the austenite ( $\gamma$ ) was retained upon water or brine quenching. These alloys were then partially transformed to athermal martensite ( $\alpha'_A$ ) by requeenching in liquid nitrogen and held at 77 K to achieve temperature homogenization and full transformation as shown in Figure 2 and table 3. These microstructures (consisting of a mixture of austenite and martensite) were then deformed by rolling (ausmarforming) up to 1.6 true cumulative plastic strain at 293 K and 77 K. This resulted in the transformation of the metastable austenite into a very large volume fraction of martensites ( $\epsilon'_D$ ,  $\epsilon'_P$ ) as shown in Figures 3 to 6 and table 3. The two major roles of the athermal martensite were first to provide nucleation sites for the formation of stress assisted and deformation induced martensite, and, secondly, together with the latter refine the helium bubble distribution by providing interfaces capable of trapping fine helium bubbles. These microstructures (consisting of a mixture of austenite and martensite) were then prevented to reverse directly into austenite and

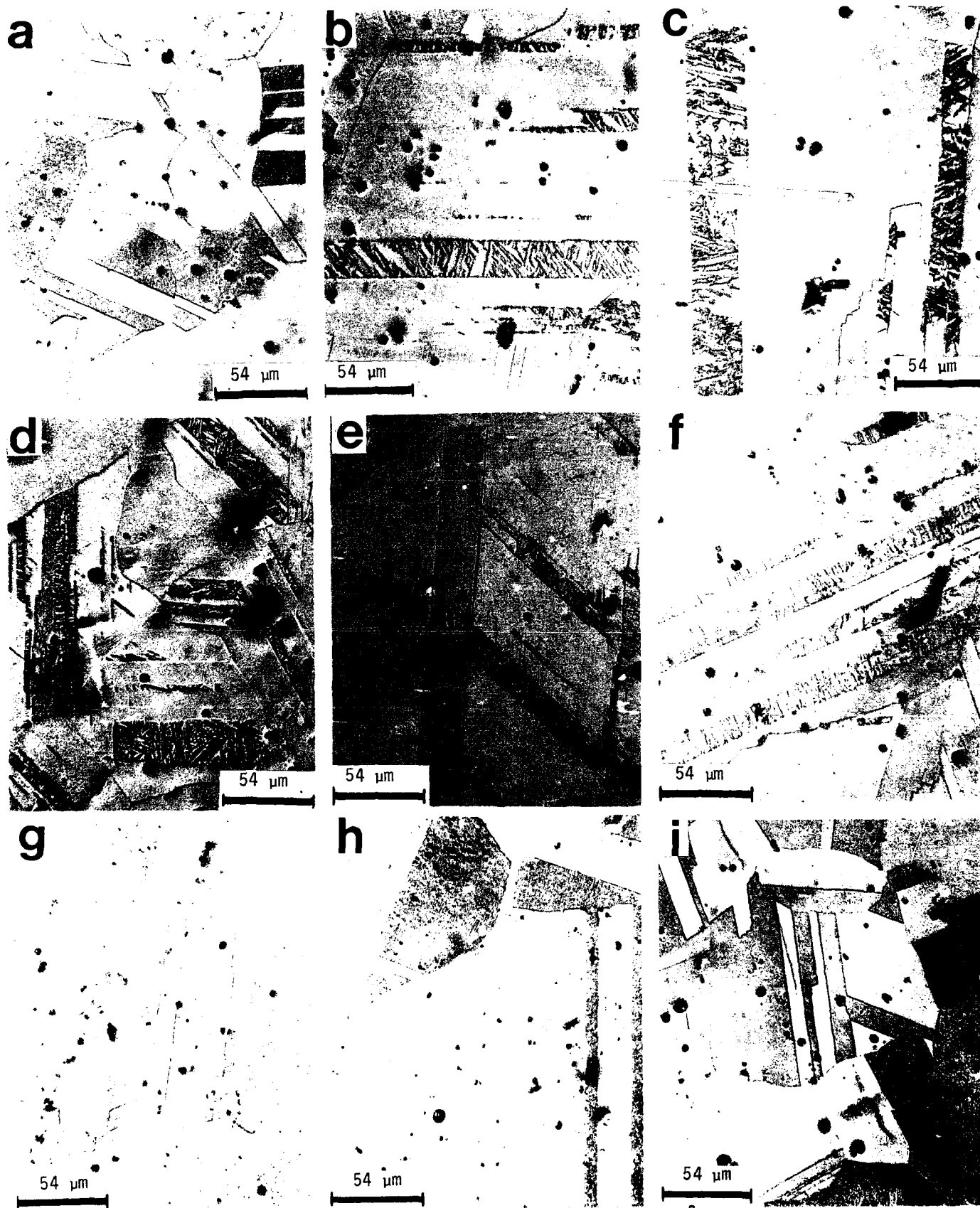


Fig.2 Water and liquid nitrogen quenching response of MPSS: a) to f) Fe-Cr-Ni-Ti; a) retained in S11, b) to f): morphology of  $\alpha'_A$  in S12; g) and h): Fe-Cr-Ni-Ti-Nb: morphology of  $\alpha'_A$  and  $\epsilon'_D$  in S12; i) Fe-Cr-Ni-Mo: retained in S12

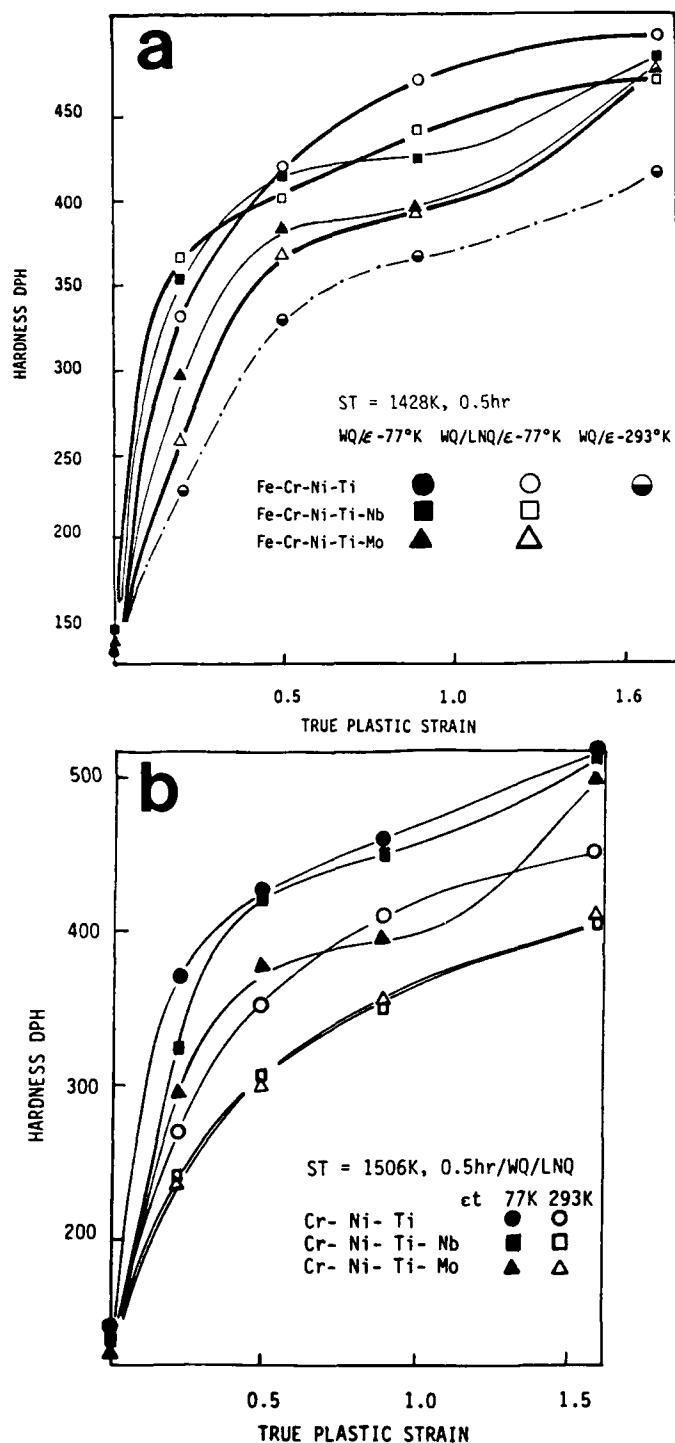


Fig.3 Effect of solution treatment temperature, amount of plastic strain and deformation temperature on the deformation behavior of MPSS

or recrystallize by heating very slowly (*ausmaraging*) at 773 K. This resulted in diffusion controlled transformations, involving nucleation and growth during which very fine intragranular dispersions of the most stable alloy carbides, of the MC type: TiC, NbC and MoC (by decreasing order of stability) were formed. During tempering three significant processes occurred: precipitation hardening,

stabilization of the martensite interfaces and raising of the  $M_s$  temperature due to the depletion of the austenite lattice of stabilizing solutes. Since the aging temperature was 773 K, the precipitation processes involve not only the diffusion of interstitial solutes of type 1 (carbon and nitrogen) but also substitutional solutes of type 3 (Ti, Nb and Mo) and type 2 (Cr). No significant diffusion of substitutional solutes of type 4 (Mn and Si) was observed. This is explained by the lower stability (i.e. less negative energy of formation of their carbides and nitrides). As a consequence of the additive application of ausmaraging (or amaraging for short) to a microstructure obtained by ausmarforming (or amarforming for short), the nucleation rate obtained for very stable MC types of carbides,  $dN/dt = N$ , was very large, much larger than the density of heterogeneous nucleation sites supplied by triple points and grain boundaries. This resulted in a very fine dispersion of intragranular carbides which raised the recrystallization temperatures of these microstructures to very high values, typically 1173 K as shown in Figures 7 through 13. In order to achieve further multiple refinement of the microstructure ( $\gamma$ ,  $\alpha'_A$ ,  $\epsilon'_D$ ,  $\alpha'_D$ ) these microstructures were then requenched in liquid nitrogen directly after precipitation hardening or after prior recrystallization, reapplied to additional cycles of deformation and aging as shown in Table 2. Upon the application of only two full cycles of amarforming and amaraging, very fine multiphase microstructures were obtained with a typical grain size between 1  $\mu\text{m}$  and 5  $\mu\text{m}$ . These microstructural refinements combined with thermally stable multiphase structures, with phases of considerably different chemical compositions, resulted in a very attractive combination of resistance to dislocation motion, crack propagation and corrosion resistance, in the temperature range 293 K to 773 K.

#### QUENCHING RESPONSE

The quenching response of the Cr-Ni-Ti, Cr-Ni-Ti-Nb and Cr-Ni-Ti-Mo steels is shown in figure 2. A small but significant increase in the water quenched hardness (typically DPH=122 to DPH=133) was observed with increasing solution treatment temperature 1373 K to 1506 K, in all steels. This hardness increment is explained mainly by the higher solute content of the austenite at higher solution treatment temperatures. Upon requeenching in liquid nitrogen a considerable increase in hardness (typically above DPH=20) was observed for all steels. This increment in the hardness is explained by the formation of athermal martensite with morphologies typically shown in figure 2. This requeench hardening increased with increasing volume fraction of athermal martensite formed, which increased as the calculated  $M_s$  increased. These  $M_s$  temperatures

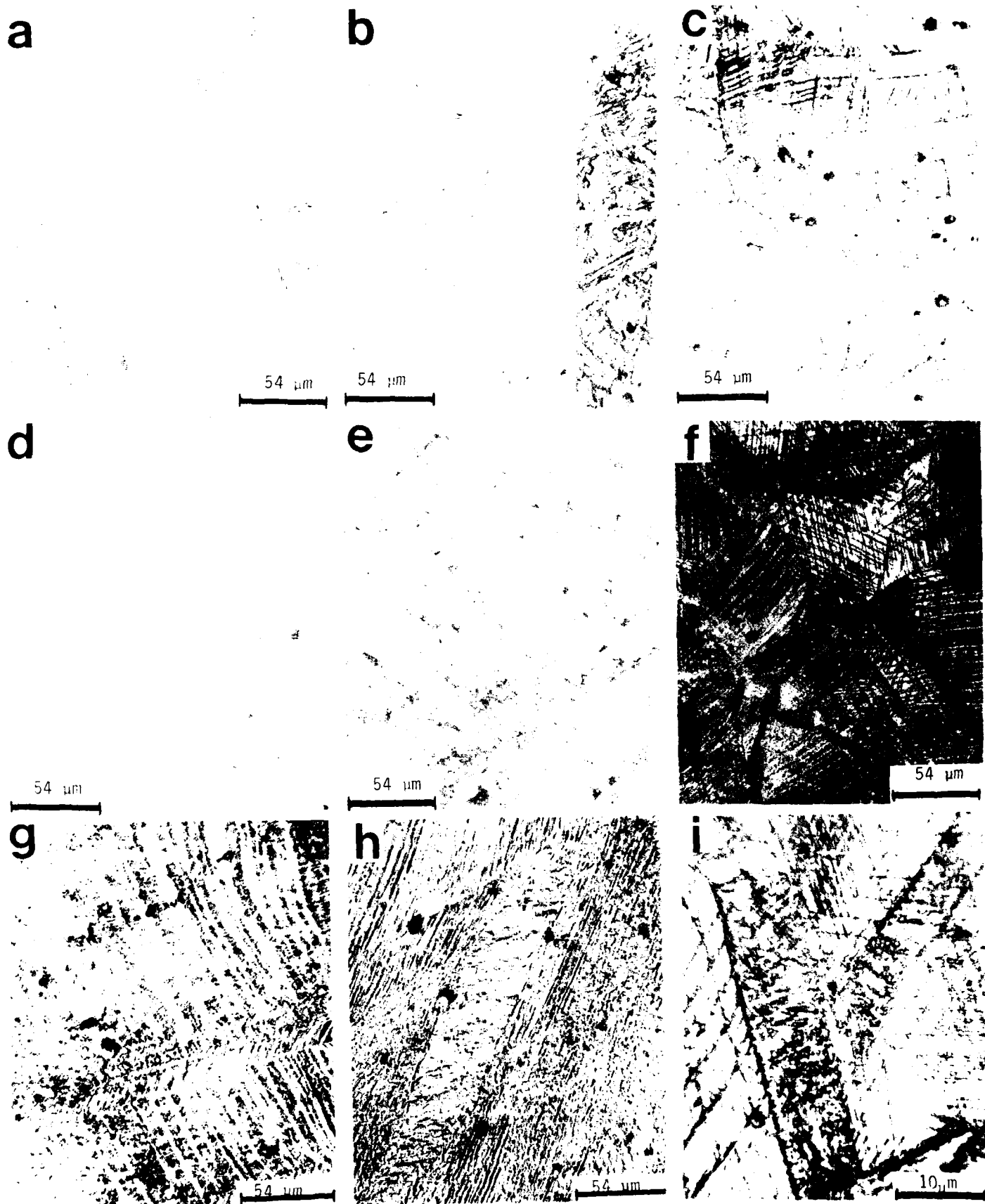


Fig.4 Formation of stress assisted and strain induced martensite in Cr-Ni-Ti MPSS by S13 and S14: a) and b):  $\epsilon=0.2$ , 293 K; showing  $\alpha_A$  and  $\alpha_D$ ; c)  $\epsilon=0.5$ , 293 K; d)  $\epsilon=0.29$ , 293 K, e)  $\epsilon=1.6$ , 293 K showing cellular structures; f)  $\epsilon=0.2$ , 77 K, g)  $\epsilon=0.5$ , 77 K, h)  $\epsilon=1.6$ , 77 K, i)  $\epsilon=0.2$ , 77 K

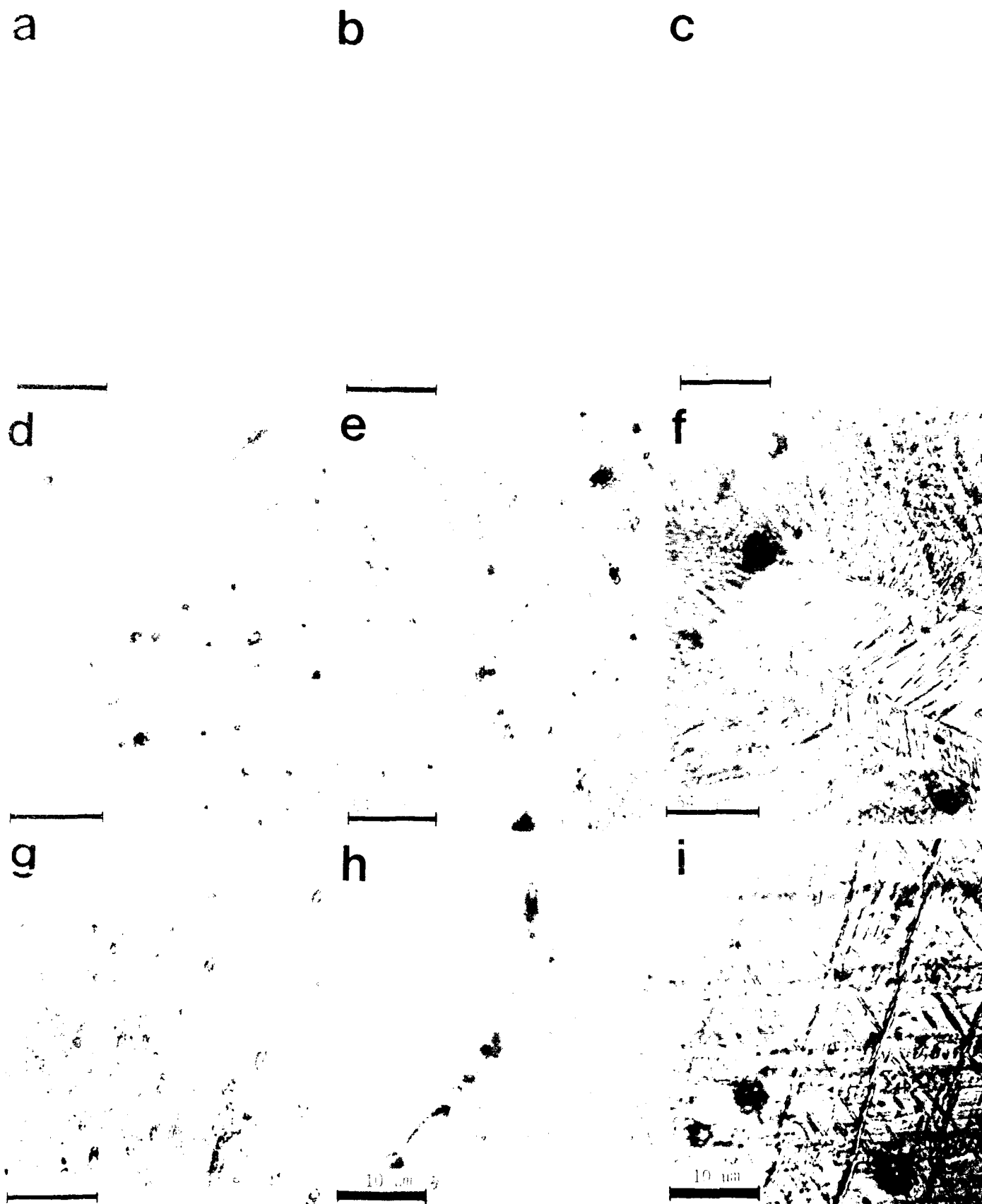


Fig. 5 Formation of stress assisted and strain induced martensites in Cr-Ni-Ti-Nb MPSS by S13 and S14: a)  $\epsilon=0.2$ , 293 K, b)  $\epsilon=0.5$ , 293 K, c)  $\epsilon=1.6$ , 293 K, d)  $\epsilon=0.2$ , 77 K showing  $\beta'$  and  $\beta''$ , e)  $\epsilon=0.2$ , 77 K, f)  $\epsilon=0.9$ , 77 K, g)  $\epsilon=1.6$ , 77 K, h) substructure in h)  $\epsilon=0.2$ , 77 K, i)  $\epsilon=0.9$ , 77 K



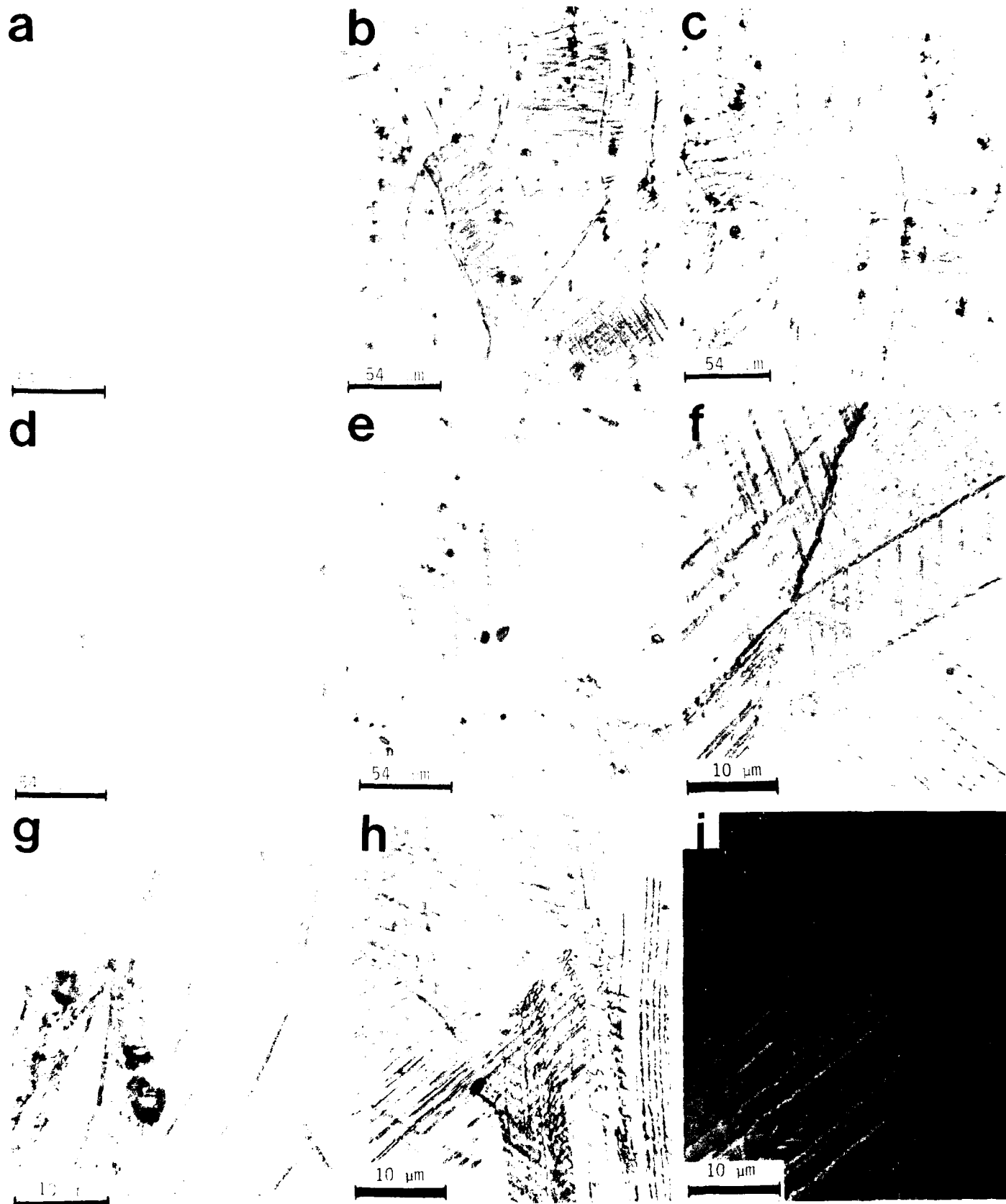


Fig.6 Formation of stress assisted and strain induced martensites in Cr-Ni-Ti-Mo MPSS by S13 and S14:  
a)  $\sigma=0.2$ , 293 K, b)  $\sigma=0.5$ , 293 K, c)  $\sigma=0.9$ , 293 K, d)  $\sigma=1.6$ , 293 K, e)  $\sigma=0.2$ , 77 K, f)  $\sigma=0.2$ , 77 K, g)  
 $\sigma=0.2$ , 77 K, h)  $\sigma=0.5$ , 77 K, i)  $\sigma=0.9$ , 77 K. Notice  $\epsilon'$  substructure in f) to i)

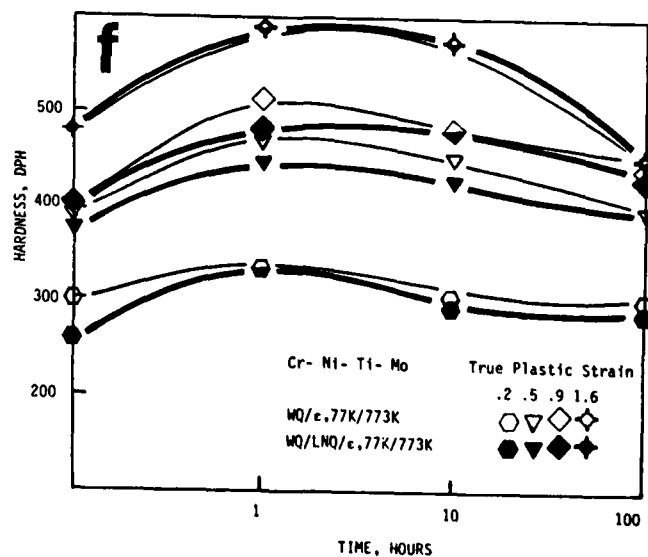
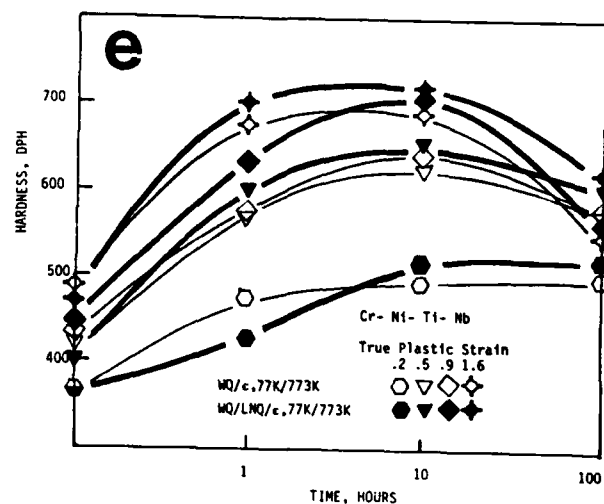
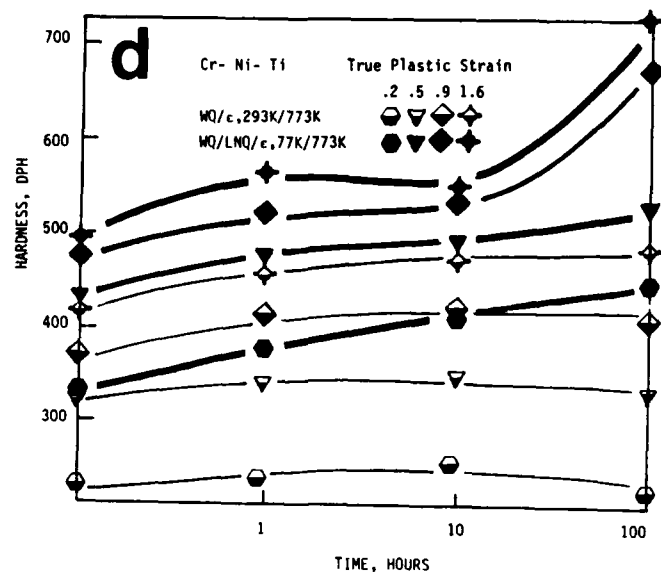
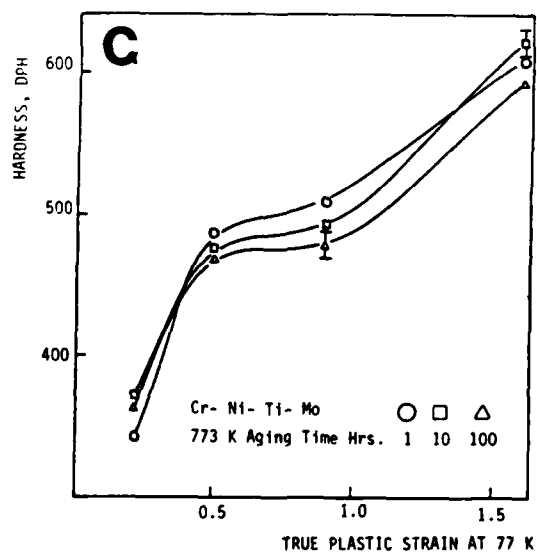
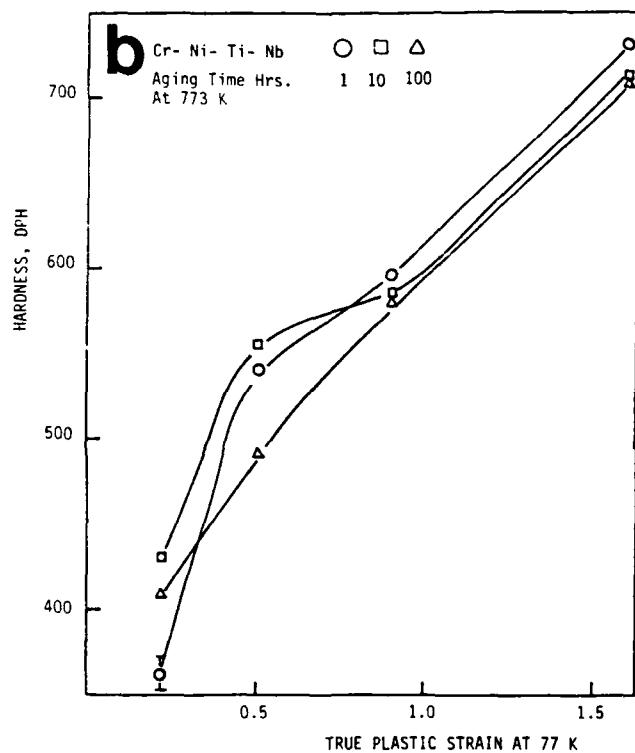
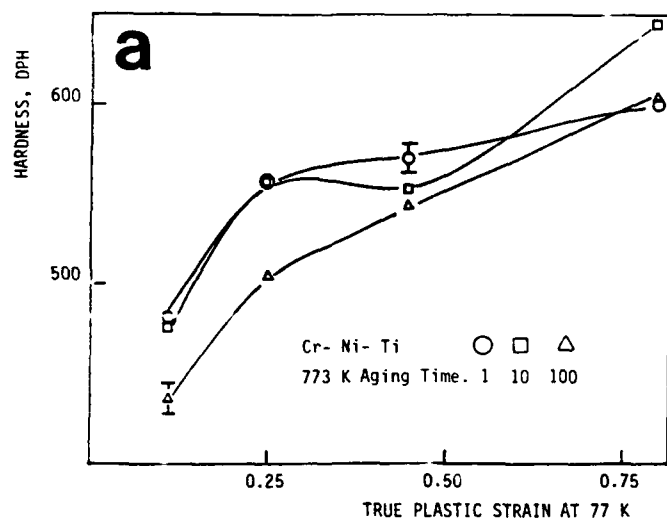


Fig.7 First cycle of aging of cold worked MPSS showing the effect of amount of deformation, deformation temperature, aging temperature and aging time on the hardness: a) to c) STT= 1506 K, d) to f) STT= 1428 K

were estimated to be 238 K, 188 K and 138 K for Cr-Ni-Ti, Cr-Ni-Ti-Nb and Cr-Ni-Ti-Mo steels respectively.

#### AGING OF QUENCHED SPECIMENS

The aging of quenched specimens, both water quenched and liquid nitrogen quenched showed little hardness increment during aging at 773 K. This is explained by the heterogenous precipitation at triple points and interfaces.

#### FIRST DEFORMATION CYCLE

The first deformation cycle (S13 and S14) showed considerable increase in the resistance to dislocation motion, as shown in figure 3. This deformation behavior is significantly influenced by the solution treatment temperature. The effect of the amount of deformation and deformation temperature on the microstructure is shown in figures 4, 5 and 6, for Cr-Ni-Ti, Cr-Ni-Ti-Nb and Cr-Ni-Ti-Mo steels respectively. For the same amount of plastic strain, larger amounts of deformation induced martensites ( $\epsilon'$ ,  $\alpha'$ ), larger increases in DPH,  $\sigma_y$  and  $\sigma_u$  and larger decreases in ductility were observed at lower temperature (77 K) in all steels. This is explained by an increase in the negative volume free energy  $\Delta G_V$  and a decrease in the total free energy  $\Delta G_T$  for the formation of martensite with the consequent decrease in the critical size of the embryos, and the correspondent increase in the nucleation rate  $N$  at lower deformation temperatures. This is in agreement with the classic theories of martensite nucleation as reported by Marquis

Table 3.- Combined Results of X-Ray Diffraction and Magnetic Susceptibility Analysis

STEEL	Cr-Ni-Ti		Cr-Ni-Ti-Nb		Cr-Ni-Ti-Mo	
TMT	X-ray Diff.	Magnetic Susc.	X-ray Diff.	Magnetic Susc.	X-ray Diff.	Magnetic Susc.
WQ	$\gamma$	WM	$\gamma$	NM	$\gamma$	NM
WQ+LNQ	$\gamma$ $\alpha_A$	WM	$\gamma$ $\alpha_A$	WM	$\gamma$	NM
$\epsilon_t$ 0.2	$\gamma, \alpha_A, \alpha_D$	SM	$\gamma, \alpha_A, \alpha_D$	SM	$\gamma, \alpha_A, \alpha_D$	MM
0.5	"	SM	"	SM	"	SM
77 K 0.9	"	SM	"	SM	"	SM
0.2	"	SM	"	SM	"	MM

TMT = Thermomechanical Treatment;  $\epsilon_t$  = true plastic strain; NM = non magnetic; WM = weakly magnetic; MM = mildly magnetic; SM = strongly magnetic.

(11,16) and Marquis and Thadhani (10) and Marquis and Fejokwu (12,13).

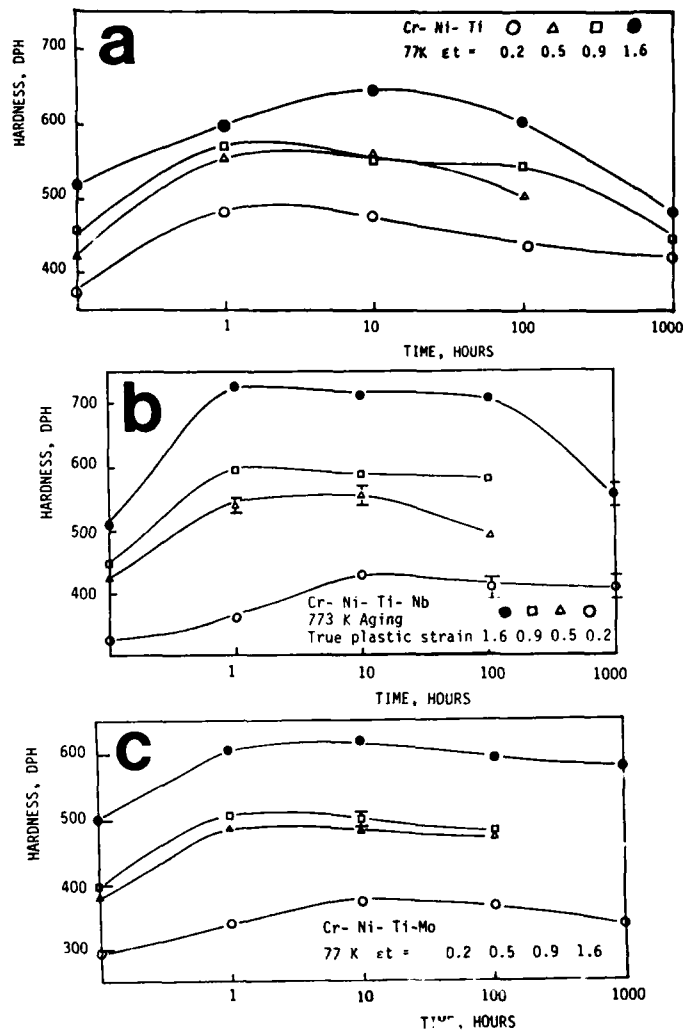


Fig.8 Aging behavior of MPSS solution treated at 1506 K

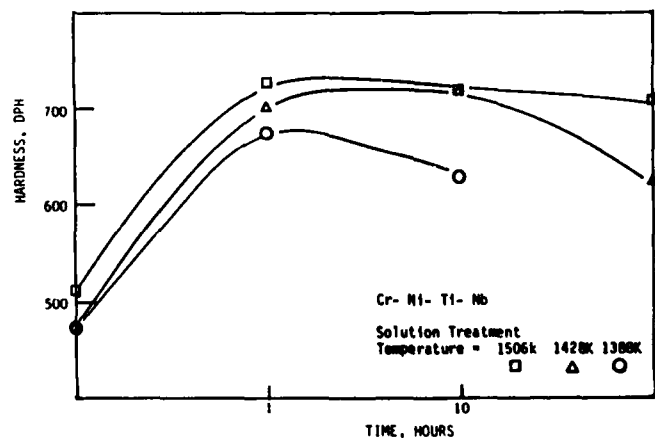
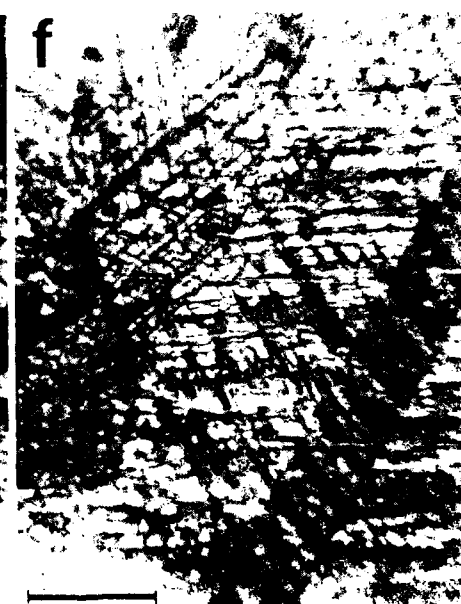


Fig.9 Effect of prior solution treatment temperature on the aging behavior of Cr-Ni-Ti-Nb MPSS



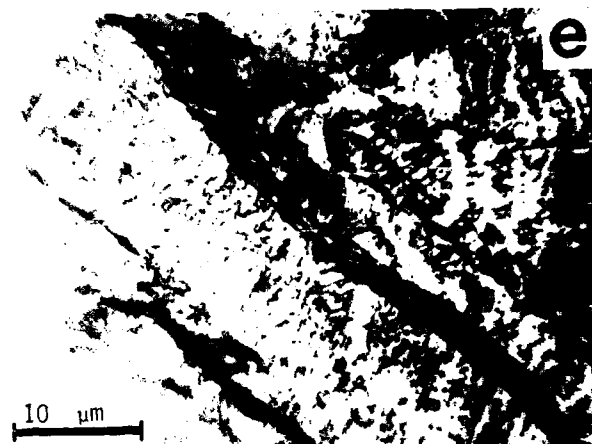
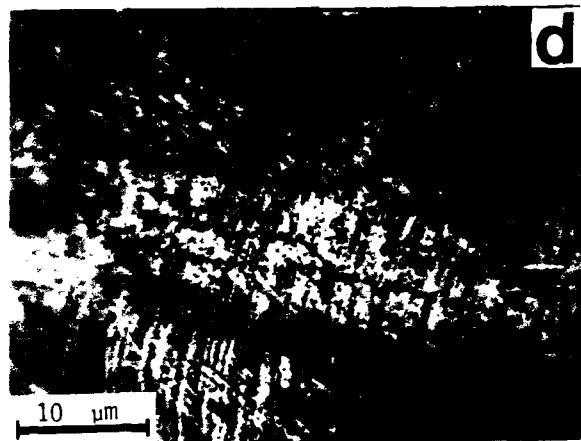
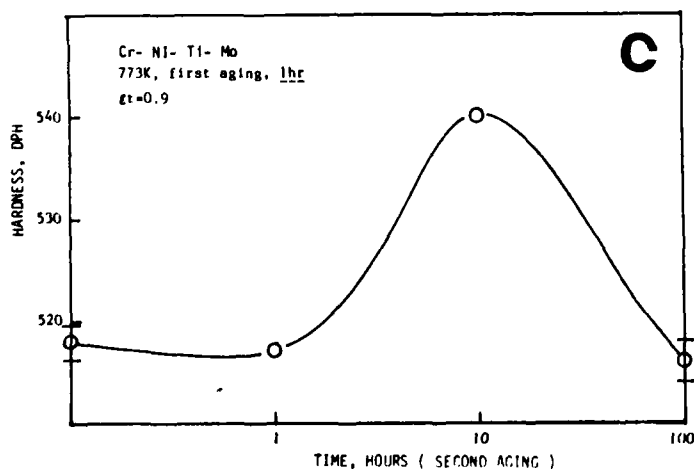
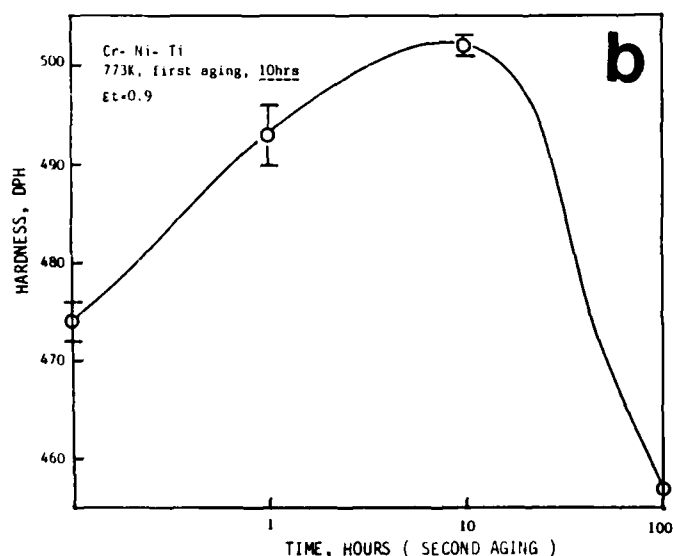
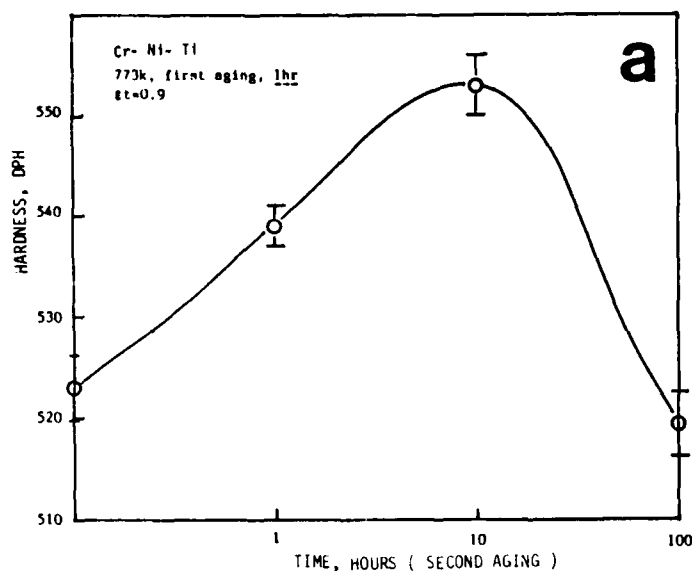


Fig.11 Second cycle of deformation aging: precipitation hardening, a) to c); fine and uniform dispersions of MC carbides in d) Cr-Ni-Ti and e) Cr-Ni-Ti-Mo

specimens did not exhibit much secondary hardening. This is explained by the fact that the  $M_s$  temperature was not raised significantly above 293 K by carbide and phosphide precipitation during the first cycle of aging. Thus the double aging followed by water quenching showed little hardening as expected. However the specimens that have been quenched in liquid nitrogen showed significant secondary hardening, which was explained by the second formation of athermal martensite, which was possible due to the significant raising of the  $M_s$  above 77 K during first cycle of aging. These microstructures, with the second generation of athermal martensite exhibit slightly better, but not very strong aging response.

#### SECOND CYCLE OF DEFORMATION AND AGING

The second cycle of deformation and aging of aged specimens (S24A) exhibited a complex behavior, of which typical results are presented in figure 11. Due to the significant levels of deformation hardening (strain and transformation) and precipitation hardening observed during the first cycle of deformation and aging, specimens were only deformed up to a

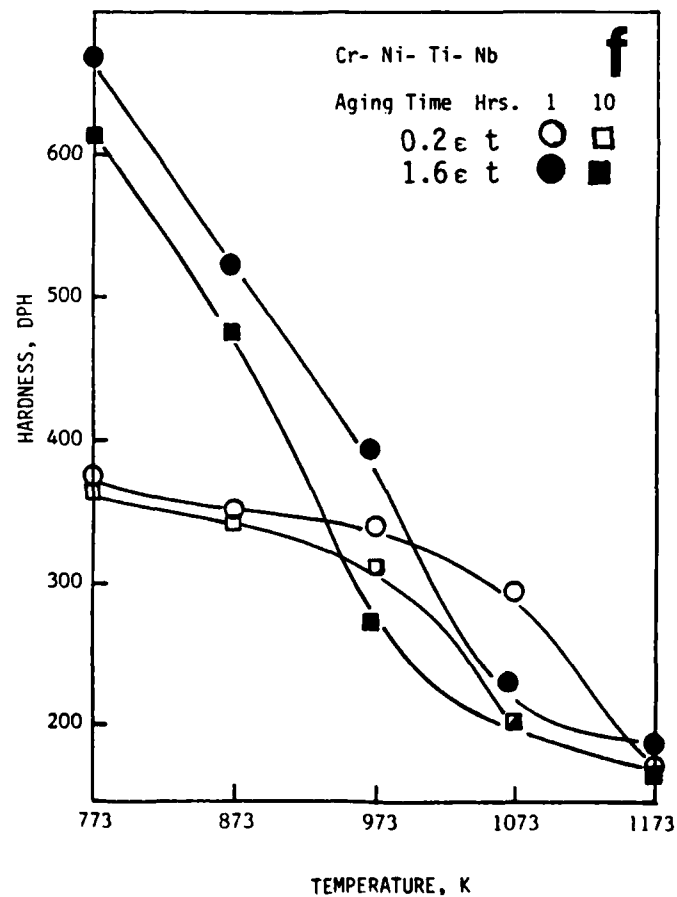
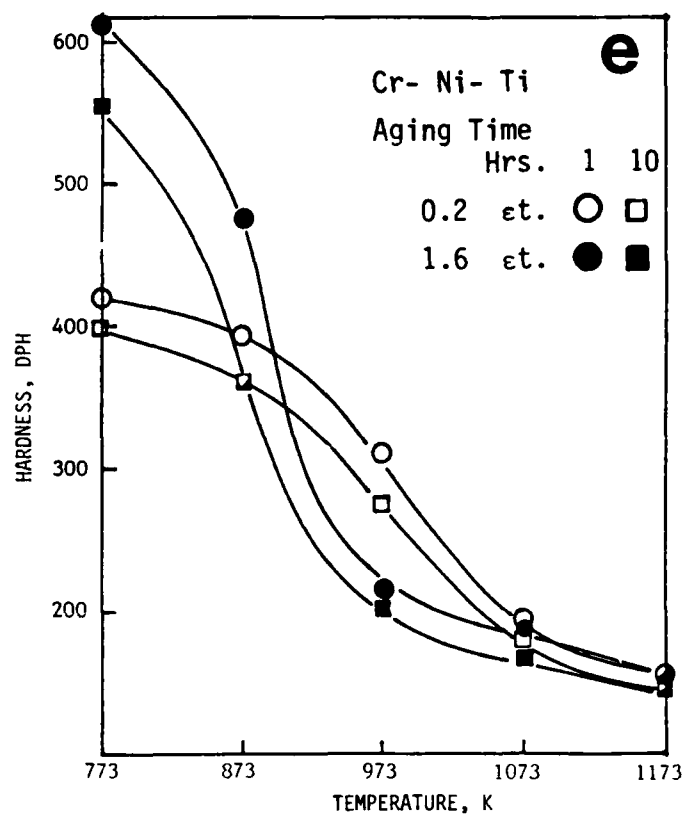
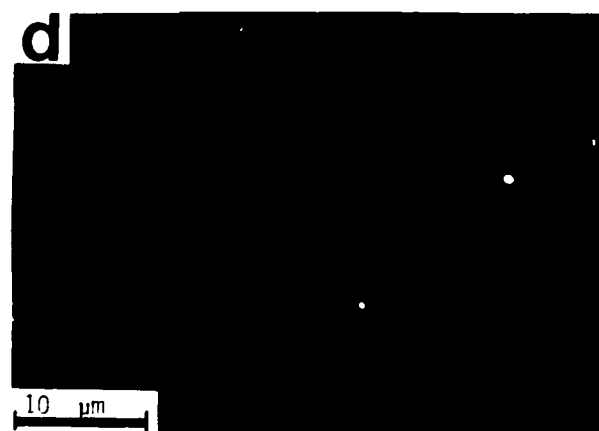
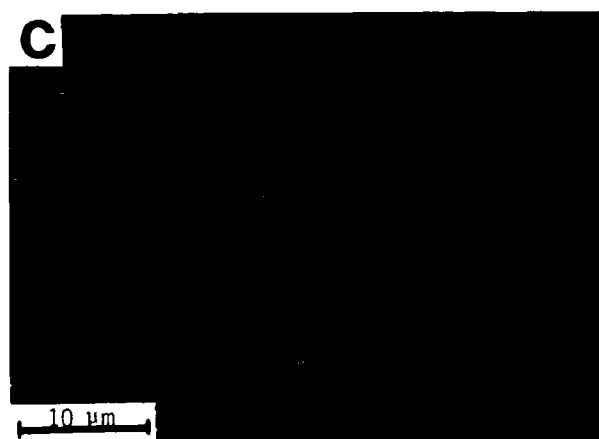


Fig.12 Annealing behavior of MPSS at 1173 K for 1 hour: a) and b) Cr-Ni-Ti; c) Cr-Ni-Ti-Nb; d) Cr-Ni-Ti-Mo; e) Cr-Ni-Ti; f) Cr-Ni-Ti-Nb

true plastic strain of 0.4 during the second cycle, then aged at 773 K. Results show small deformation hardening but considerable precipitation hardening. This is explained by a large number of nucleation sites (homogeneous and heterogeneous) developed during the second cycle of deformation and second cycle aging.

#### THERMAL STABILITY AND STRENGTH

The thermal stability and strength of the deformed microstructures obtained during S13, S14 and S24 was investigated. Their recovery and recrystallization behavior was studied in the temperature range 773 K to 1173 K. Typical results are shown in figure 12 for specimens that have been deformed to a true plastic strain of 0.2 and 1.6. Typical recovered and recrystallized microstructures are shown in figure 12. This data show that the minimum recrystallization temperatures (for 1 hour annealing time) are approximately 973 K for the Cr-Ni-Ti steel and 1073 K for the Cr-Ni-Ti-Nb and Cr-Ni-Ti-Mo steels. However these recrystallization temperatures were increased by approximately 100 K in each steel by prior precipitation of very fine MC carbides developed during aging at 773 K, for an aging time close to peak hardness.

#### DEFORMATION OF RECRYSTALLIZED MICROSTRUCTURES

The second cycle of deformation of partially or totally recrystallized specimens is depicted in figures 13 and 14. The amount of deformation hardening observed is considerable, but not as large as that observed during the first cycle of deformation. Typical microstructures showed a much smaller austenite grain size and very well defined formation of cell structures with none or very little (depending on the steel) deformation induced martensite formed. This is explained by the overlapping roles played by prior: austenite grain size, strain hardening and precipitation hardening. No doubt grain boundaries can act as nucleation sites for the formation of martensite. However during this second cycle of deformation, grain boundaries were observed to stabilize the parent phase and hinder the martensite formation. This is due to the fact that martensite growth relies on maintaining a certain coherency with the surrounding austenite, a high angle grain boundary being an effective barrier to plate growth. In addition the effect of prior strain hardening and precipitation hardening was observed to be of stabilization of austenite, which is in agreement with previous results (10).

#### ROOM TEMPERATURE MECHANICAL BEHAVIOR

The room temperature mechanical behavior of some of these multiphase structures is presented in figures 14 and 15 which show the combined effect of deformation and aging on  $\sigma_y$ ,  $\sigma_u$ ,  $\sigma_t$

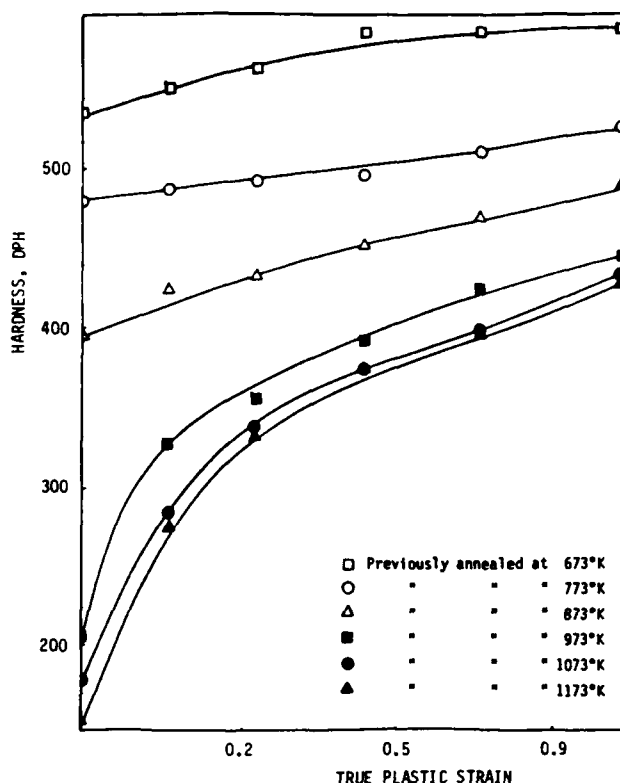


Fig.13 Deformation behavior of Cr-Ni-Ti-Nb MPSS

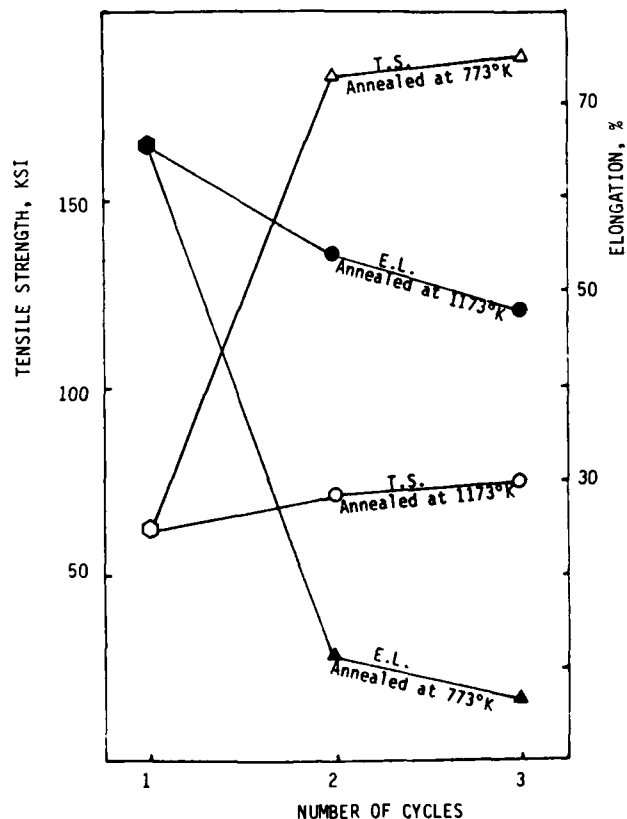


Fig.14 Room temperature mechanical behavior of Cr-Ni-Ti-Nb MPSS

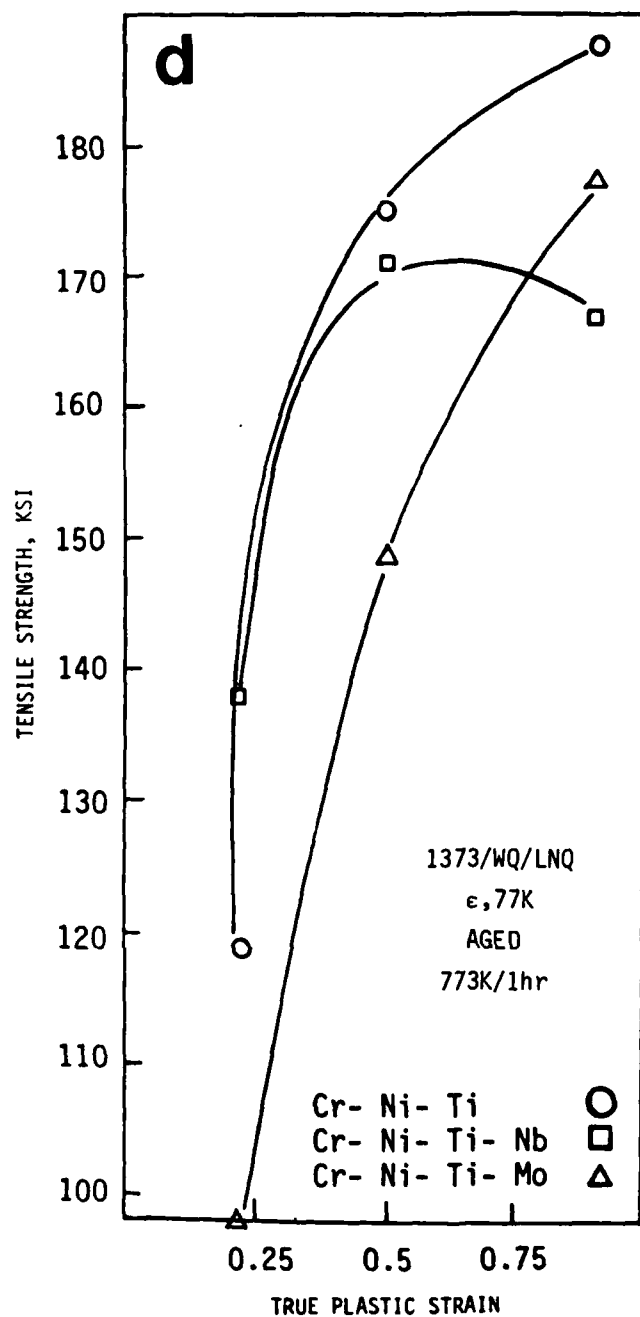
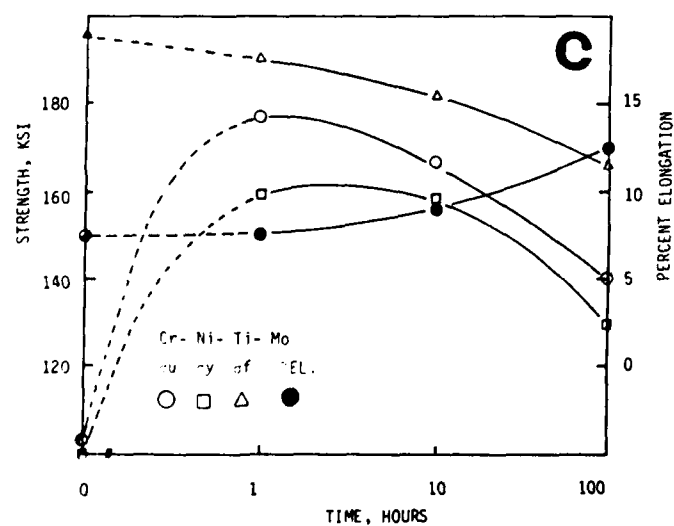
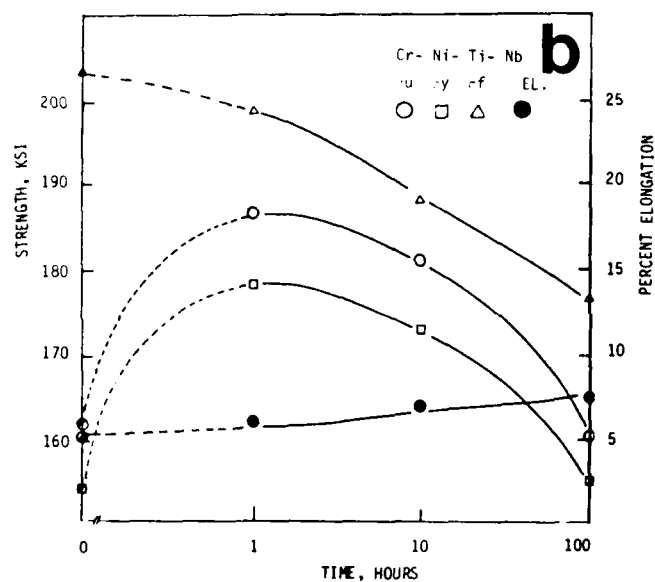
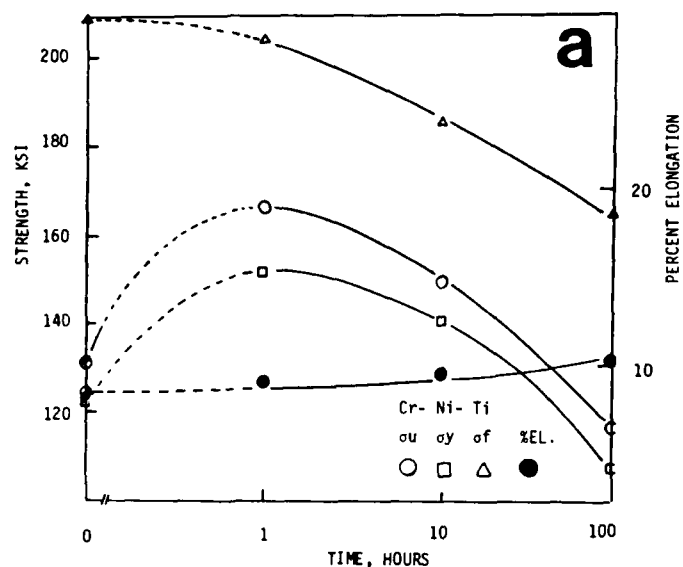


Fig.15 Room temperature mechanical behavior of MPSS showing the effect of aging on cold worked microstructures

and % El. It can be seen that for one hour aging at 773 K after 0.9 true plastic strain produces an overaged structure in Cr-Ni-Ti MPSS, but not in the Cr-Ni-Ti-Nb and Cr-Ni-Ti-Mo MPSS. This explained by the solubilities, volume fractions and precipitation kinetics of  $TiC$ ,  $NbC$  and  $MoC$ .

#### ELEVATED TEMPERATURE MECHANICAL BEHAVIOR

The elevated temperature mechanical behavior of these multiphase structures was investigated in the temperature range 293 K to 1173 K ( $543 K=0.3T_m$ ,  $1087 K=0.6T_m$ ). Typical results are



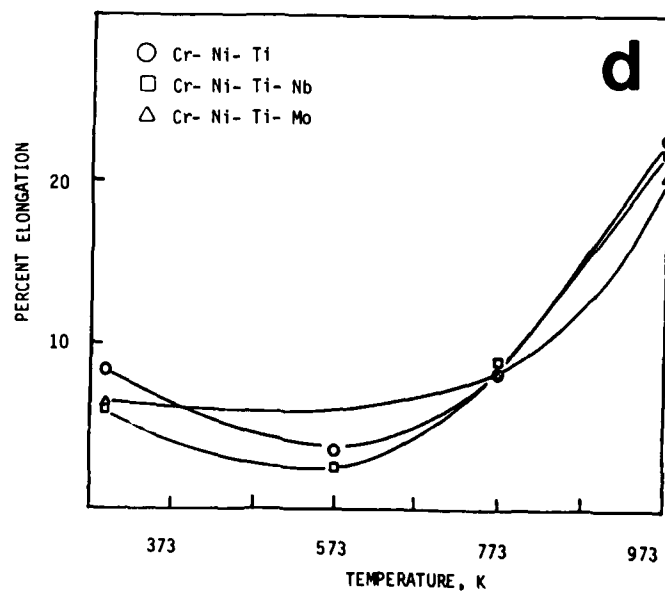
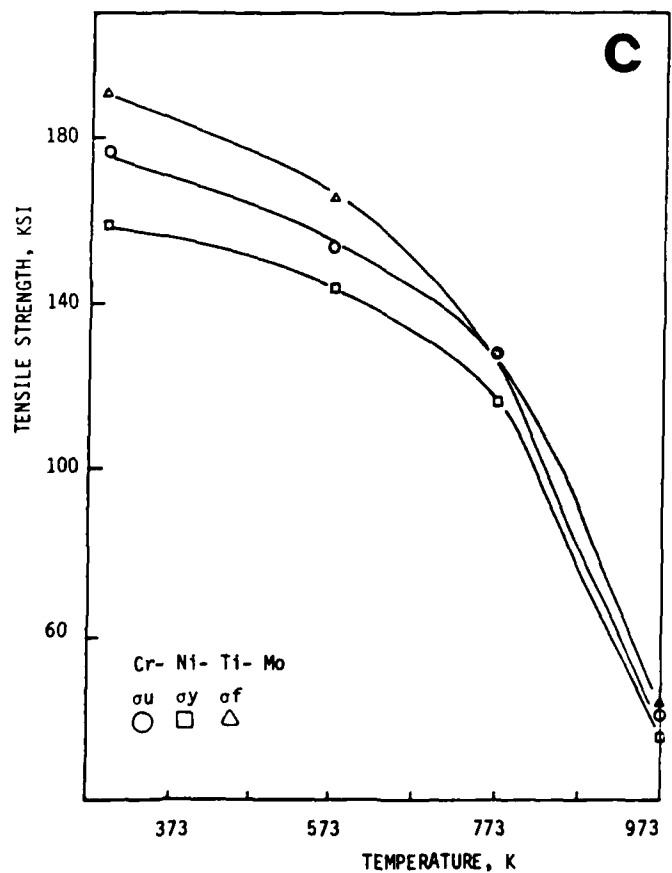
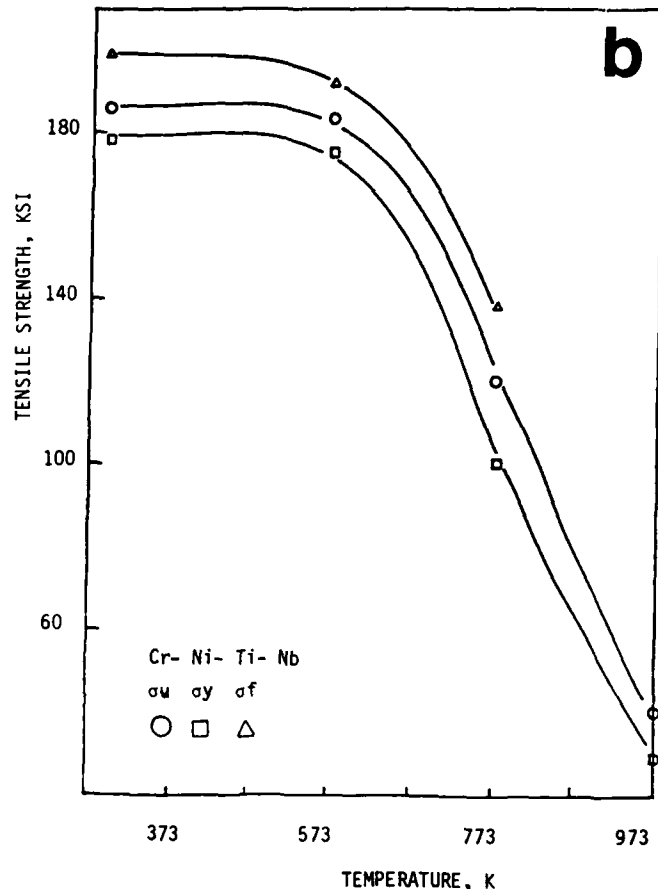
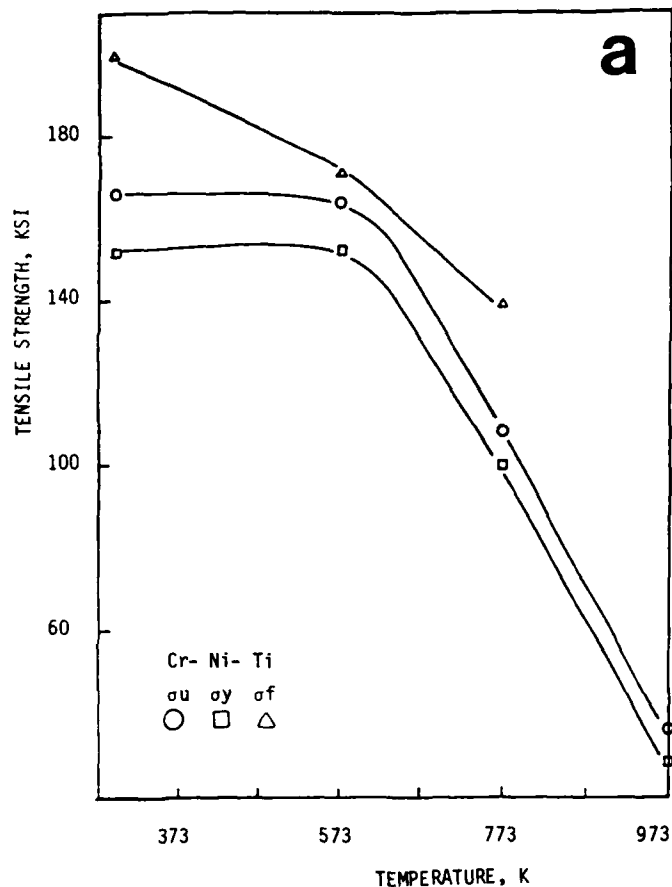


Fig.16 Elevated and high temperature mechanical behavior of MPSS showing very stable microstructures with none or very little decrease in strength up to the following temperatures: a) 573 K for Cr-Ni-Ti; b) 573 K for Cr-Ni-Ti-Nb and c) 773 K for Cr-Ni-Ti-Mo

shown in figure 16. The microstructures tested were very highly deformed (0.9 true plastic strain) and aged for one hour, which represents already overaged condition. The tensile strength at 293 K were 170 Ksi, 185 Ksi and 175 Ksi and at 773 K were 110 Ksi, 120 Ksi and 130 Ksi respectively for the Cr-Ni-Ti, Cr-Ni-Ti-Nb and Cr-Ni-Ti-Mo multiphase steels. At 773 K the elongation at fracture of all steels was approximately 10%. This shows that the Cr-Ni-Ti-Nb is a stronger multiphase steel at low temperatures, due to the very fine dispersions of NbC and martensites. The Cr-Ni-Ti-Mo multiphase steel is weaker at low temperatures, due to the very small fraction of martensites, but is most efficient in maintaining this strength at elevated temperatures, due to the fine dispersions of MoC.

#### CONCLUSIONS

Multiphase stainless steels, consisting of very fine intragranular dispersions of athermal martensite, stress assisted and strain induced martensites, TiC, NbC, MoC and Fe-Ti phosphides were designed and manufactured.

The tensile strengths of these multiphase structures were in excess of 180 Ksi at 293 K and was maintained without any significant decrease up to 573 K. The Cr-Ni-Ti-Nb multiphase stainless steel exhibited the best combination of ductility and resistance to dislocation motion in the temperature range 293 K to 773 K. In the temperature range 773 K to 973 K the best combination of these properties was exhibited by the Cr-Ni-Ti-Mo multiphase stainless steel.

The elevated temperature strength of these multiphase dispersions suggest that these steels may have a much better creep-fatigue behavior, under in situ irradiation conditions, than any commercial material currently available.

#### REFERENCES

1. Lula, R.A., "Duplex Stainless Steels", ASM (1983).
2. Spruiell, L.E., Scott, J.A., Ary, C.S. and Hardin, R.L., Met. Trans. 4 (1973) 1533.
3. Thomas, D.E., "Quality Requirements of Superduty Steels", AIME Conf. 3 (1959) 81.
4. Seeger, A., "Radiation Damage in Solids", I.A.E.A, 1 (1962) 101.
5. Cawthorne, C. and Fulton, E.J., Nature 216, 11 (1967) 575.
6. Maziasz, P.J. and Roche, T.K., J. Nucl. Mater. 103, 104 (1981) 797.
7. Russell, K.C., Acta Met. 26 (1978) 1615.
8. Kesternich, W. and Rothaut, J., J. Nucl. Mater. 103/104 (1981) 845.
9. Kesternich, W., "Electron Microscopy", 1 (1980) 188.
10. Marquis, F.D.S. and Thadhani, "Strength of Metals and Alloys", 1 (1982) 205.
11. Marquis, F.D.S., Journal de Physique C4, 12, 43 (1982) 569.
12. Marquis, F.D.S. and Fejokwu, "Deformation of Multiphase and Particle Containing Materials", Riso National Laboratory, 1 (1983) 417.
13. Marquis, F.D.S. and Fejokwu, "Strength of Metals and Alloys", Pergamon Press (1985) 2079.
14. Maziasz, P.J., "Micon 86", ASTM STP 979 (1986) 116.
15. Marquis, F.D.S., Hadji, M. and Qadri, J.H., "Deformation and Aging Behavior of Low Activation Stainless Composites", Proc. of this congress.
16. Marquis, F.D.S., Zeitschrift fur Metalkunde, 693, (1978) 157.
17. Marquis, F.D.S., unpublished work on Fe-Ni-Cr-C-X-Y Multiphase Stainless Steels.

# PRECIPITATING OF SECOND PHASE IN SOLID SOLUTIONS

Yu. I. Ustinovshikov

Physical-tech. Institute  
Izhevsk, USSR

## Abstract

The decomposition mechanism in solution is discussed. The mechanism despite the great variety of its morphological and kinetic peculiarities for different alloys is just the same.

In this paper fundamental properties of large collectivities of particles are revealed and physical generality of decomposition process is discovered. That's why division of phase transitions in solids into the first and second kinds, division of phase transitions of the first kind into those decomposing by spinodal or nucleation and growth mechanisms are to a certain degree artificial and do not find adequate experimental confirmation.

Proofs are given that solid solutions decompose by spinodal only at continuous decrease of free energy and that is why do not need fluctuational overcome of energy barrier.

The results given testify to the untenability of generally assumed 'linear' concepts of dynamics of phase segregation based on exponent increase of small fluctuations; they testify that the

incubation period before precipitation of a new phase in the solid is the process of "search" by the system of correlation distance (that is stochastic process submitting to the laws of dynamic scaling).

AT PRESENT THERE have been a great number of experimental results of studying the phenomenon of decomposition of solid solutions. A few authors, however, give a unique answer to the question of decomposition mechanism. It is conditioned by the fact that though the well-known mechanisms of decomposition in alloys-spinodal and nucleation and growth-are theoretically alternative, the morphology of the alloys supposedly decomposing by these two mechanisms actually does not differ. Even for early stages of decomposition there exist no clear distinctions in morphology. For instance, if we examine the Table it will become evident that the given "distinctions" in the morphology of alloys decomposing by spinodal or by nucleation and growth

Table - Some factors distinguishing the mechanism of nucleation and growth from the spinodal one

Nucleation and growth	The spinodal mechanism
From the moment of critical nucleus formation the composition of the second phase does not change in time.	Continuous change of the composition of both phases takes place in the time until equilibrium
From the moment of critical nucleus formation the boundary between the phases is always sharp and incoherent.	The surface between the phases is initially quite diffusional completely coherent; with time the boundary becomes gradually sharper, coherence is broken.
The tendency to random distribution of particles in the matrix takes place.	The regularity in the distribution of the second phase, characterized by modulations takes place.
The tendency to precipitation of incoherent spherical particles of the second phase takes place.	The tendency to precipitation of nonspherical coherent particles of the second phase takes place.
mechanism are most likely distinctions between the early and the later stages of decomposing, that is between the precipitation process and the process of coarsening. To define which period of decomposition is fixed-a period of nucleation or a period of coarsening - by morphological data is difficult enough.	by spinodal. Guinier considered the main difference of zones from the smallest precipitates of a new phase to be in the fact that they have the same type of the lattice as the matrix; the boundaries between the zones and the matrix are diffusional and that's why completely coherent. As completely coherent could also be the precipitates which have the lattice different from the lattice of the matrix, so both zones and precipitates can equally distort the matrix and in a number of cases lead to similar diffractive effects.
It is known that in a number of alloys before precipitation of a new phase there form GP zones. It is generally considered that existence of the zone stage, if zones are understood as described by Guinier [1], testify to decomposition of an alloy	These peculiarities can be obser-

ved in the process of aging of alloys when classical GP zones are precipitated - in Al-Cu, Al-Zn, Al-Ag, Fe-Be, etc. At present the same zones revealed at decomposition of binary Fe alloys, for example, in the systems Fe-Mo, Fe-W, Fe-Ti, Fe-Cr and others. It was shown [2-5] that before precipitation of  $\text{Fe}_2\text{Mo}$  in the structure of Fe - (3.9 + 22.0) Mo alloys Mo zones were formed. Recently a very detailed study of decomposition of the Fe-Mo alloys has been done [6,7]. Having discovered modulated structure in the Fe-20 at%Mo alloy and having found none in the Fe-13 at%Mo and Fe-15 at%Mo alloys, the authors [6,7] made the conclusion that these alloys decompose by different mechanisms - by spinodal and nucleation and growth respectively.

The assumption has been made that both spinodal and nucleation and growth mechanisms are to result in morphological differences in the structure of alloys (modulated structure and plate-shaped precipitates respectively). It has been found that the former and the latter structures of the Fe-20 at%Mo alloy coexist at 585 and 600°C and one forms at the expense of the other. Having taken these points into consideration the authors [7] concluded that the change of one mechanism by the other occurs gradually according to Binder theory [8].

**ORDERING AND SEGREGATION** - It is well-known that there are negative deviations from Raoult's law in Fe-Mo solids and consequently they must show the tendency to short-range ordering. In those cases when the composition of Fe-Mo solids is far from being stoichiometric, this tendency may

result in Mo clustering and later the  $\text{Fe}_2\text{Mo}$  phase in local volumes of alloys only. Fe-Cr alloys have positive deviations from Raoult's law and at certain temperatures of annealing segregation is observed there.

In Fe - (25-40)%Cr alloys there were found by neutron diffraction analysis spherical (radius  $\sim 20 \text{ \AA}$ ) zones, containing Cr atoms only [9]. With quantities of Cr being smaller the zones consisting of Cr atoms only were not revealed, however, it was possible to identify the Cr rich regions by Mössbauer spectroscopy (in the Fe-6 at.% Cr alloys [10]). Thus it was concluded that zones in the Fe-Cr alloys are formed by spinodal [9] mechanism

Lagneborg [11] analysed structure of decomposing Fe-30Cr. He did not discover  $\sigma$ -phase which according to the phase diagram was to appear in Fe-47Cr. His electron diffraction patterns of the structure testify that after annealing at 475° the shape of the particles is spherical and at 550° - they are disc-shaped. Using these data and having noticed that the decomposition is a much slower process at 475°C than at 550°C (it is quite natural as the temperature is lower) Lagneborg concludes that at 475° the decomposition occurs by spinodal and at 550°C by the nucleation and growth mechanisms.

However it is necessary to note that some other authors, e.g. [12] consider the spinodal to be characterized, on the contrary, by rapid kinetics. Having discovered the modulated structure after the quench it is assumed [12] that such a structure is formed by spinodal during

cooling of the alloy at the quenching time.

Considering the results [13] one can draw quite definite conclusion: independently of sign of deviation from Raoult's law decomposition process in all the solids of non-stoichiometric composition begins with clustering of atoms of the second component and occurs by uphill diffusion, that is the following ratio takes place  $\partial^2 f(c) / \partial c^2 < 0$  and  $D_{ef} < 0$ .

At the same time the theory of regular solutions leads to the conclusion that for any solutions the sign of energy of mixture always coincides with the sign  $\partial^2 f(c) / \partial c^2$  and the sign  $D_{ef}$ . As shown in [14] this inconsistency is explained by the fact, that the theory of regular solutions may be valid for the stoichiometric alloys only.

In solids of nonstoichiometric composition the process of new phase precipitation may be divided into two stages: 1) formation of clusters of solutes by uphill diffusion; 2) if during the process of annealing composition of clusters reach stoichiometric composition of new phase - formation of the lattice of such phase. When the composition of clusters does not reach the stoichiometric composition of new phase - the second stage of the phase formed process is not realised. The first stage of the process - formation of clusters of solutes-kinetically and morphologically similar to the segregation process is analogous to concentrated alloys with positive deviations from Raoult's law, however, final composition of such clusters is

different from clusters formed in alloy with positive deviations and it will be defined by tendency to the composition of the corresponding  $A_m B_n$  phase.

There may be the case when the time and temperature of tempering are not sufficient for completion of diffusion resulting in formation of  $A_m B_n$  phase in local volumes of the matrix. Then in the alloys clusters of solutes are fixed only and the latter differ insignificantly from the clusters formed as a result of segregation of alloys, having positive deviations from Raoult's law. If diffusional processes bring the system with negative deviations to the equilibrium state then the composition of clusters approaches gradually the composition of  $A_m B_n$  phase. The lattice in the clusters during the process is increasingly distorted as the result of redoubling the concentration of the solutes in clusters. Such distortions of the lattice within clusters increase gradually until their structure is described by the new lattice corresponding to the structure of  $A_m B_n$  phase.

In the case when the composition of the alloy, having negative deviations is in the one-phase region of the phase diagram one may observe the clusters in which concentration of the solute will never reach the composition of  $A_m B_n$  phase. This means that clusters in the structure of such alloys are the final product of decomposition and they differ insignificantly from the clusters formed as the result of segregation.

Thus, in non-ideal binary solids of non-stoichiometric composition

there occurs clustering during annealing regardless of the sign of their deviation from Raoult's law. Such clusters may be both the final product of decomposition (we shall call them clusters of the first kind) and intermediate product on the way towards formation of the second phase (we shall call them clusters of the second kind).

The tendency of alloys to ordering or segregation defined by the sign of deviation in the behavior of alloys from Raoult's law (plus or minus) is the chemical driving force of decomposition.

The final results to which this tendency brings depend on the chemical affinity, composition, time and temperature of aging and that is why may differ for different situations.

Uphill diffusion of solutes is known to be the mechanism resulting in segregation of the alloy into the regions enriched and depleted by solutes. Such division into enriched and depleted regions, as we have noted, occurs in the case positive deviations from Raoult's law when atoms tend to surround themselves by the similar atoms (segregation) as well as in the case of negative deviations when atoms A tend to be surrounded by atoms B (ordering). As either tendency for the alloys of nonstoichiometric composition results in formation of clusters by uphill ( $D_{ef} < 0$ ) diffusion and the sign of  $D_{ef}$  always coincides with the sign of  $\partial^2 f(c) / \partial c^2$  it may be said that such alloys decompose by spinodal only.

**PRECIPITATION MECHANISMS** - The nucleation and growth mechanism is known to be realized by fluctuation only, the process of formation of critical nuclei being possible if there is no chemical interaction between the elements, that is the latter is possible on condition that there is a tendency neither to segregation nor ordering. In fact practically all binary metallic systems are non-ideal and the signs of their deviations from Raoult's law are constantly preserved in all range of compositions. This signifies that when decomposition of such systems occurs the tendencies to either segregation or ordering are realized for any composition including those which are situated in the region, where according to the theory there must be realized the nucleation and growth mechanism.

The character of  $f(c)$  dependence determines the type of mechanism of decomposition in the concrete case. If to expand in a power free energy of the parameter of order ( $\eta = C - C_0$ ) as it has been done by Landau and Lifshitz [15] and to be limited by the fourth order term then we have the case of phase transition of the first kind [15].  $F(c)$  dependence in this case has the shape of a curve with two minimums and one maximum where in the inflection points  $\partial^2 f(c) / \partial c^2 = 0$  and there occurs the transition from one decomposition mechanism to another. When the coefficient at cubic term of expansion of free energy will identically equal zero as author [15] consider, then the phase transition of the second kind takes place. In this case  $f(c)$

dependence has only one minimum, critical phenomena are absent. If all the terms of the third or higher order in expansion of free energy are rejected as have been done by Cahn [16] and Hilliard [17],  $f(c)$  will never attain minimum at any meaning  $\eta$  that corresponds to infinite relaxation process. Thus the kind of  $f(c)$  dependence is actually defined mathematically but not physically.

SIGN OF  $F(C)$  - At present  $f(c)$  for the case of decomposition of solids is conventionally presented as a curve with two minimums and one maximum. It is considered that the spinodal mechanism takes place in the region where  $f(c)$  is convex ( $\partial^2 f(c)/\partial c^2 < 0$ ) and the mechanism of nucleation and growth works where  $f(c)$  is concave. In critical points, where  $\partial^2 f(c)/\partial c^2 = 0$ , substitute of the decomposition mechanism by another, substitute of the direction of diffusion by opposite take place.

As shown by Langer [18] in the case if  $f(c)$  described by the curve with convex and concave regions it cannot represent true free energy of the system. True free energy must be convex function of the composition only [18].

Langer's conclusions about the shape of  $f(c)$  are supported by the following consideration. It is known that in approximation of regular solids chemical potential  $\mu_1$  is bound with free energy for one part of the system,  $f(c_1)$ , by the following relation

$$\mu_1 = \left[ \partial f(c_1) / \partial c_1 \right]_{T,P} \quad (1)$$

Hence it follows that

$$\frac{\partial \mu_1}{\partial c_1} = K_B T - 2z E_{mix} C_1 (1 - C_1) \quad (2)$$

and it is possible to evaluate at what relations between thermodynamic and termic constituents the sign of the second derivative of free energy with respect to concentration will be positive and at what-negative.

Three cases are considered:

1)  $K_B T < 2z E_{mix} C_1 (1 - C_1)$ . Here correlation effects in the distribution of neighbours prevail over heat energy and, therefore, the process of a new phase formation proceeds. All the components in this relation are always positive except  $E_{mix}$ , that may accept positive (segregation) or negative (short-range ordering) signs. Let us analyse the situation at different signs of energy of mixture

a)  $E_{mix} > 0$ . In this case according to Eq. (2)

$$K_B T - 2z E_{mix} C_1 (1 - C_1)$$

will always be negative; therefore  $\partial^2 f(c_1)/\partial c_1^2 < 0$  and  $f(c)$  is convex function.

b)  $E_{mix} < 0$ . In this case  $\partial^2 f(c_1)/\partial c_1^2$  in Eq. (1) must be positive and  $f(c)$  must be concave. Thus we conclude that clustering in non-stoichiometric solids having negative deviations from Raoult's law should take place by "normal" ( $D_{ef} > 0$ ) diffusion. In fact clustering in random solid is possible by uphill diffusion only, then in this case  $\partial^2 f(c_1)/\partial c_1^2$  should be negative and therefore  $E_{mix}$  should not be negative. It is concluded that clustering in non-stoichiometric



solids does not depend on the sign of the energy of mixture, but it depends on the absolute value of the energy only. Then Eq. (2) is as follows:

$$\frac{\partial^2 f(c_1)}{\partial c_1^2} = \frac{\partial \mu_1}{\partial c_1} = K_B T - 2z |E_{\text{mix}}| c_1 (1 - c_1) \quad (3)$$

Consequently concentration dependence of non-equilibrium free energy must be convex, if clusters form in non-stoichiometric solid having negative deviations from Raoult's law. It is a most essential point in our consideration which has not been regarded properly before.

2)  $K_B T > 2z |E_{\text{mix}}| c_1 (1 - c_1)$ . In this case Brownian motion prevails over ordering processes (high temperature region) and irrespective of sign of  $E_{\text{mix}}$ ,  $\partial^2 f(c_1) / \partial c_1^2$  will always be positive, i.e.  $f(c_1)$  is a concave curve (Fig. 1, curve 1).

3)  $K_B T = 2z |E_{\text{mix}}| c_1 (1 - c_1)$ . This case refers to the state that represents the boundary between the high temperature region with random distribution of atoms and low temperature region, in which correlation effects in distribution prevail (curve 2). The temperature of the boundary equal to

$$T_0 = \frac{2z |E_{\text{mix}}| c_1 (1 - c_1)}{K_B} \quad (4)$$

coincides with  $T_K$  in the so-called critical point a on the diagram T-c.

PRECIPITATION KINETICS - Let us consider the kinetics of variation of  $f(c_1)$  for the phase diagram of AB system, having the negative energy of mixture. At temperature lowering a second phase is precipitated from the solid. The diagram T-c is shown

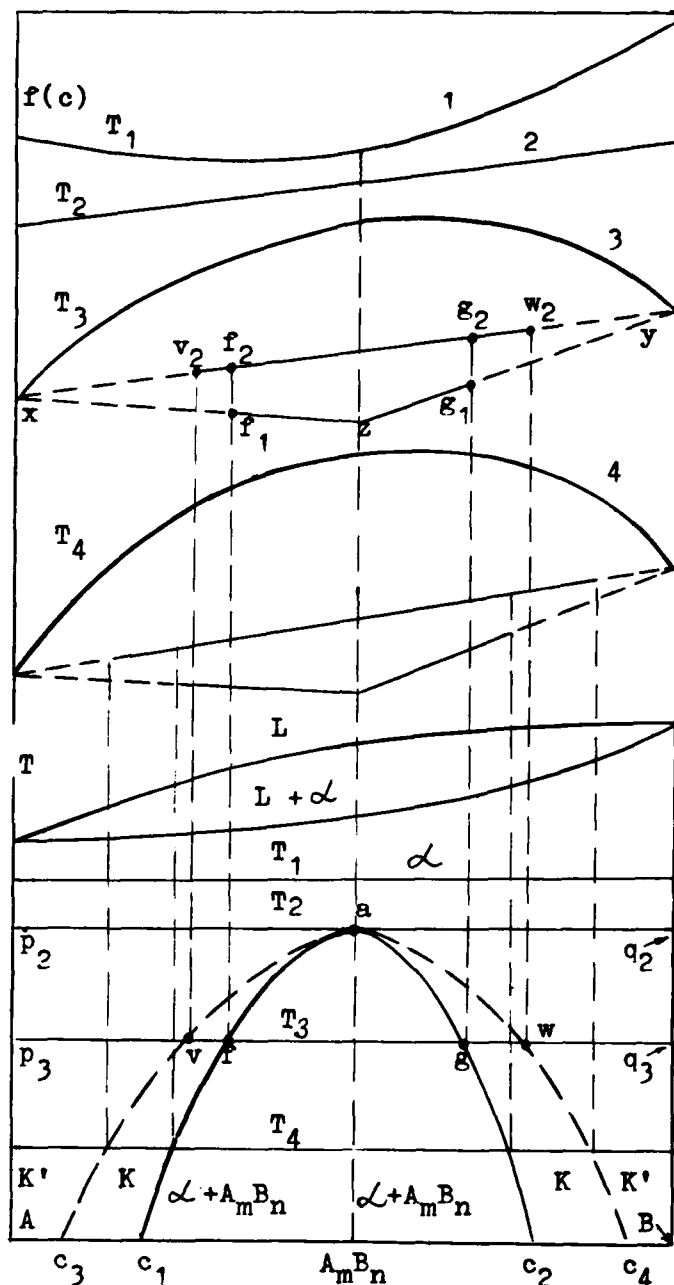


Fig. 1 - Concentration dependences of non-equilibrium and equilibrium free energy during the decomposition of the alloys of the A-B system, having negative deviations from Raoult's law. The phase diagram of the system is given in the low part of the figure. All indexation is given in the report.

in Fig. 1. Below the solidus line all the compositions in equilibrium state are  $\alpha$ -solids. At  $c_a$  and  $T < T_2$  the equilibrium state of the system represents phase  $A_m B_n$  that is formed by long-range ordering of  $\alpha$ -solid in all the volume of the alloy. In the range of the compositions limited by  $C_3 a C_1$  and  $C_2 a C_4$  curves the final state of the system which is approached at  $t \rightarrow \infty$ , represents unhomogeneous solid with clusters of solutes having the same type of the lattice as the depleted solid. Usually such a state is known as K-state. By the analogy we mark it on the diagram T-c (Fig. 1).

Final state of the alloys of A-B system in both the  $aC_3Ap_2$  and  $aC_4Bq_2$  segments of T-c diagram is a homogeneous solid in spite of  $K_B T < 2z|E_{mix}|C_1(1-C_1)$ . This situation can be understood if we consider clustering formation in solids. Let us analyse Langer's equation of structure factor. It is as follows:

$$\frac{\partial S(\vec{\beta}, t)}{\partial t} = -2M\beta^2[(f'' + \alpha^2\gamma + K\beta^2)S(\vec{\beta}, t) + \sum_{n=3}^{\infty} \frac{f^{(n)}}{(n-1)!} S_n(\vec{\beta}, t)] - 2MK_B T \beta^2 \quad (5)$$

where  $S_n(\vec{\beta}, t)$  is Fourier representation from  $G_n(\vec{r}, t) = \langle \eta^{n-1}(\vec{r}_0 + \vec{r}, t) \eta(\vec{r}_0, t) \rangle$ .

In this equation elastic stresses caused by decomposition are also taken into consideration. In Eq. (5) nucleation and growth is not described (though all constituents of free energy are considered in it) as when  $f''(C_1)$  being positive the sign of  $\partial S(\vec{\beta}, t)/\partial t$  will never be positive. Hence for the case of nucleation and growth Eq. (5) has no physical sense.

If completely random non-stoichiometric solid produced as the result of quenching at high temperatures is heated to the temperature sufficient for diffusive mobility of substituents then in it there begins the process of uphill diffusion resulting in formation of clusters.

It should be considered that the system "does not know" the size of clusters, correlation distance between them (the minimum distance between the precipitates for the given composition of the alloy and temperature of aging). The decomposition may be irreversible if this distance is reached. Such a size and a distance are to be "found" by the system.

As  $f''(c_1) < 0$ , and all the other terms in square brackets of Eq. (5) are positive it means that clustering caused by chemical potentials difference is opposed by elastic and gradient components, and Brownian motion as well.

In the initial stage of annealing in the alloy there occur directed ( $\Delta\mu_i \rightarrow 0$ ) atoms jumps which are described by transition probability for a unit of time.

$$W(C_i \rightarrow C_j) = \tau^{-1} \frac{1}{Z} e^{\Delta F / K_B T} \quad (6)$$

where

$\tau$  - characteristic time

$Z$  - statistic sum

$\Delta F$  - change of free energy at a jump.

As a result of clustering such atom distribution will be most probable and rapidly obtained when decrease of  $\Delta F$  will be minimum, i.e., roughly speaking, when two nearest-neighbor identical atoms will

form "a cluster".

Lifetime of such a "cluster" is comparable with the time of its formation, i.e. it is represented as fluctuation formed, however, not as random result of Brownian motion of B atoms but as the result of the tendency of the A-B system to decrease chemical potentials difference between its states with ordered and random distribution of atoms. At that moment there actually appear sinusoidal distribution of B atoms with wavelength  $\lambda_1 = \lambda_{min} \rightarrow 0$ . Such sinusoidal distribution of impurities cannot be homogeneous at the expense of both percolation phenomena, various bifurcations and also because of the fact that it takes place in a real alloy, but not in a structureless continuum. Formation of such fluctuations causes the growth of gradient energy in the alloy at the expense of  $\beta \rightarrow \infty$  and elastic energy at the expense of growth of  $\mathcal{E}$ .

That's why Langer's relation:

$$f''(c_1)S(\vec{\beta}, t) > (\mathcal{E}^2 Y + K \beta^2) S(\vec{\beta}, t) + K_B T \quad (7)$$

satisfaction of which is necessary for continuation of decomposition process for high values of  $\beta$  stops functioning and initially formed distribution of B atoms with  $\lambda_{min}$  will have to decompose. At such dissolving of fluctuation both the gradient and elastic components in the Eq. (7) decrease and again there appear the conditions for realization of Eq. (7). Non-uniform character of formation and as stated above dissolving of the sinusoidal distribution of atoms will lead to the situation when at the moment of

satisfiability of the Eq. (7) a new sinusoidal distribution of B atoms will never be the exact copy of the previous one, the wavelength  $\lambda_2$  will be more than  $\lambda_{min}$ , the sizes of fluctuations will be higher. Again during the formation of such a distribution gradient and elastic components will grow in Eq. (7), and once more at a certain stage realization of the eq. (7) will be impossible. Atom distribution, having formed at the moment of  $t_2$  will begin dissolving and further in its place there appears a new distribution of atoms B with another wavelength,  $\lambda_3 > \lambda_2$ , etc. Such cycling (formation - dissolving - formation of fluctuations - ...) is repeated, any new distribution being different from the previous one by the growth of the amplitudes and the wavelength of fluctuations, until at  $t_m$  the wavelength reaches  $\lambda_m$  corresponding to the so-called correlation distance. Having reached this distance the fluctuations can exist as long as possible, i.e. represent clusters which may be fixed structurally.

Structural factor  $S(\vec{\beta}, t)$  in Eq. (5) practically satisfies the relations of dynamic scaling [8]:

$$S_{T, C_B}(\vec{\beta}, t) = \mathcal{E}^{-\gamma} S[\beta \mathcal{E}^{-\gamma}, t \mathcal{E}^{\gamma Z}] \quad (8)$$

$$(C_B - C_B^{st}) \mathcal{E}^{-\beta}$$

where

$T_c$  - melting point of stoichiometric phase precipitated in solid;

$C_B^{st}$  - concentration of B in stoichiometric phase;

$Z$  - dynamic index;

$\beta, \gamma, \gamma$  - indices;

$$\mathcal{E} = (T_c - T) / T_c.$$

Dynamic scaling is explicitly revealed when non-ideal solid, random after quenching is given a chance to relax, but it is not shown the way to do it. As a result there occurs "search" of correlation distance i.e. minimum distance between the clusters of such a composition and such sizes that when this state is reached the structure factor  $S(\vec{\beta}, t)$  becomes positive and further does not change this sign, i.e. in the system stable clusters that can be observed structurally, appear.

Correlation distance and the rate of its attainment are constants for each alloy at the temperature of annealing. Increase of temperature leads to increase of correlation distance and the rate of its attainment as the result of the growth of diffusional mobility of atoms. Increase of B atoms concentration in A-B alloy decreases the correlation distance and the time required for its "search". Hence, the closer the composition of the alloy to stoichiometric and the higher temperature of annealing (a two-phase region of a diagram is meant), the shorter is the period of "search"; at certain  $T$  and at  $C_B \rightarrow C_B^{st}$  the latter may become so short that it will not be found experimentally. INCUBATION PERIOD - As is well-known, when compositions are relatively far from stoichiometric and temperatures of annealing are comparatively low, however, sufficient for diffusion mobility of atoms the so-called incubation period is observed before formation of a new phase in the alloys. The incubation period is considered to be direct proof of decomposition of such systems by

nucleation and growth mechanism, because the presence of the incubation period can't be explained by the theory of spinodal decomposition.

The curve of hardness depending on aging time is a convenient way for studying of kinetics of aging and, hence, of presence of the incubation period during precipitation. For example, hardness curves of Fe-10%Mo, Fe-15%Mo, Fe-20%Mo, quenched from 1350° into water at aging at 550°C are shown in Fig. 2.

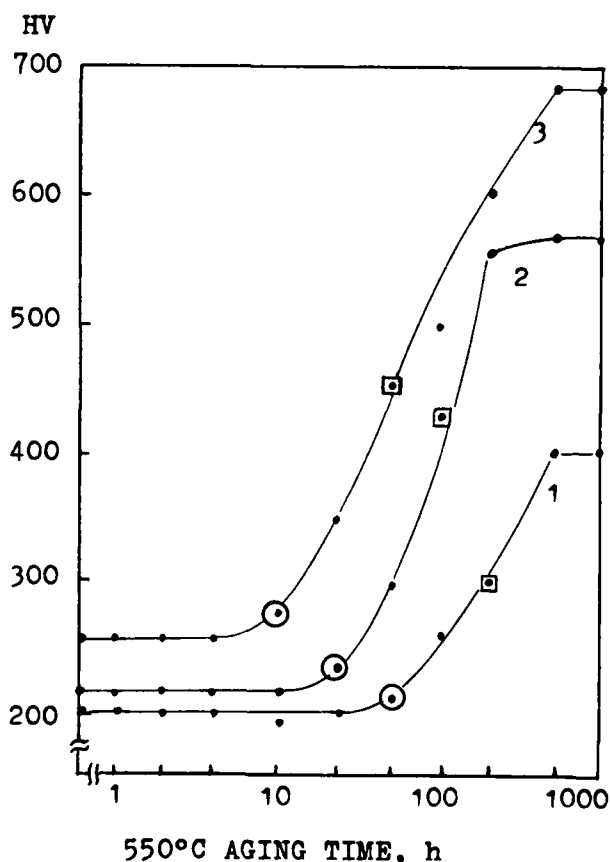


Fig. 2 - Change in hardness of Fe-10%Mo (1), Fe-15%Mo (2) and Fe-20%Mo (3) quenched from 1350°C into water, during the process of aging at 550°C. The moment of  $Fe_2Mo$  precipitation is marked by squares on hardness curves, formation of tweed structure-by circles.

Fe<sub>2</sub>Mo phase was found at the moments of aging, marked by squares on hardness curves. Tweed structure, representing modulations of a composition (but not precipitates) was observed on the electron micrographs of Fe-10%Mo, Fe-15%Mo and Fe-20%Mo alloys for 25, 50, 100 hours of aging respectively (as shown on HV curves by circles). The distance between modulations of composition measured on the electron micrographs of the Fe-15%Mo was  $\sim 5 \cdot 10^{-6}$  cm. Effective coefficient of diffusion of Mo atoms at 550°C, having the order  $D_{\text{eff}} \sim 10^{-11} \text{ cm}^2/\text{sec}$  permits to atoms of Mo to cover half the distance between neighbour modulations for about 2 sec. The delay in tweed structure formation which can be evaluated by time before circles on the hardness curves in Fig. 2, might be expected by slow growth of small clusters formed before circles and not resolved in electron microscope. However, our field-ion microscopy studies which have been carried out in the moments before formation of tweed structure show that any clusters of Mo solutes in the solid are not observed.

The latter agrees well with the assumption that the incubation period is a specific state of the alloy, far from equilibrium, in which changes accumulate gradually. Having reached certain value (correlation distance) the system is enabled to decompose. It becomes clear why at early stages of clustering we cannot find sinusoidal distribution of solutes, as has been predicted by Cahn (we do not consider the fact of formation of modulated structure to be the conse-

quence from Cahn's theory). Apparently, from the very beginning of aging sinusoidal distribution, aggravating by bifurcations, occurs with ever increasing wavelength and disappears again according to scaling laws. So it transforms to such a kind, which in no way resembles Cahn's sinewave.

From the mentioned above one can realize why in the  $\text{ac}_3\text{Ap}_2$  and  $\text{ac}_4\text{Bq}_2$  portions of T-c diagram the final state represents homogeneous solid despite the fact that in these portions of diagram

$$K_B T < 2 z \left| E_{\text{mix}} \right| C_1 (1 - C_1).$$

The system under data condition seems to be in the fluctuating regime of "search" of correlation distance, though the latter can be reached thermodynamically, practically it turns out to be unachievable. Let us mark these portion in the diagram as K'-state.

EVOLUTION OF  $F(C)$  - Consider the evolution of  $f(c_1)$  under condition at transition of the system from non-equilibrium to equilibrium state. Suppose that all the alloys of the system were heated to  $T_1$ , corresponding one-phase state  $\alpha$ -solid. In this case the concentration dependence of equilibrium free energy is represented by a concave curve 1, the temperature higher, the curvature  $f(c_1)$  becoming greater.

At lowering of the temperature in one-phase region of the diagram the concavity of the  $f(c)$  curve diminishes and at  $T_2 = T_a$   $f(c)$  dependence will represent a straight line.

Suppose that the alloys of AB system heated to  $T_1$  were sharply

quenched to  $T_3$  ( so that at the time of cooling no diffusional processes took place). In such case the concentration dependence of non-equilibrium free energy at  $t=0$  will be represented by a convex curve 3 with the relation  $\partial^2 f(c)/\partial c^2 < 0$ . After prolonged ( $t \rightarrow \infty$ ) relaxation at  $T_3$  the concentration dependence of the equilibrium free energy should represent broken line xzy with the minimum in point z, where  $A_m B_n$  is formed into the total volume of the alloy. Lines xz and zy imply the concentration dependence of free energy of the two-phase mixture -  $A_m B_n$  and the solid. As seen from the T-c diagram, however, two-phase region at  $T_3$  can exist in the range of the  $C_f - C_g$  compositions only, free energy can approximate its equilibrium values at  $T_3$  within the range of these compositions only. The  $f_1 z g_1$  part of the xzy line in  $f(c)$  diagram is shown by a solid line. The parts  $xf_1$  and  $yg_1$  will be represented by a dotted line in Fig. 1. These parts correspond to the equilibrium values of  $f(c)$  which could be reached at  $C_{p_3} + C_f$  and  $C_{g_3} + C_g$  in the two-phase region of the diagram.

Equilibrium level of free energy represented xzy at  $T_3$  can be reached through a number of intermediate states. One of such states is shown by the straight line xy, the part of which  $v_2 f_2 g_2 w_2$  characterizes the free energy of the mixture of enriched and depleted regions, clusters of the second kind being formed in the part  $C_q + C_g$ , those of the first kind being formed in the parts  $C_v + C_f$  and  $C_e + C_w$ . Portions  $C_3 a C_1$  and  $C_2 a C_4$  of phase diagram in which there form

clusters of the first kind, present regions of K-state.

$$C_{p_3} + C_v \text{ and } C_{g_1} + C_w$$

compositions of solid at  $T_3$  are in non-equilibrium state that's why in them there should be formed clusters. The fact that these clusters are not fixed structurally shows that under these conditions the system is in non-equilibrium state of "search" of correlation distance as long as possible because the B atoms concentration is low enough.

Fig. 1 also shows concentration dependences of non-equilibrium and equilibrium free energies for lower temperature  $T_4$ .

As  $f(c)$  at  $T_4$  is completely similar to that at  $T_3$  indexation in Fig. 1 was not used. It should be noted that vivid distinctions are observed when we compare  $f(c)$  at  $T_3$  and  $T_4$ : the curvature of non-equilibrium  $f(c)$  at  $T_4$  is greater; the extent of two-phase and K-state regions is longer at  $T_4$ ; the chemical potentials difference between non-equilibrium and equilibrium  $f(c)$  is greater at  $T_4$ .

Thus we may conclude that despite the great variety of morphological and kinetic peculiarities of decomposition of solids, the mechanism of the decomposition is just the same. Here fundamental properties of large collectivities of particles are revealed and physical generality of processes in different alloys is discovered.

Our ideas about the process of precipitation of new phases in metallic solids can be summarized as follows: if non-stoichiometric solid

having negative deviation from Raoult's law, is completely random after quenching the process of new phase precipitation starts with "search" of correlation distance - the minimum distance between clusters, when such clusters can exist in the system. It is noted that in the cases when under certain temperature and concentration conditions the system cannot "find" such a distance for any period of time, the solid preserves its structure (K'-state). When that distance is found two variants are possible: at low concentrations of the solutes there occurs formation of clusters of the first kind by uphill diffusion (K-state, GP zones, local short-range order, etc). The lattice of these clusters being the same as that of the matrix is distorted as the result of higher concentration of solutes in clusters (striations on electron diffraction patterns, X-ray diffraction).

At high concentrations of solutes formation of clusters of the second kind takes place (the same diffusional effects). As the concentration of solutes in clusters redoubles and tetragonal distortions of lattice in clusters grow the clusters transform into particles of a new phase (satellites on electron diffraction patterns). If a new type of the lattice, produced by tetragonal distortion of the original one, coincides with structure of equilibrium phase, this phase is stable; if there occurs no such coincidence the phase is metastable and later under appropriate conditions it rearranges into a stable one. For the stoichiometric alloys precipitation

of a new phase is the process of ordering of atoms inside the total volume of the alloy which can be correctly described by well-known theories taking into consideration concept of parameter of order. If in systems considerable part of energy of mixture compose its elastic component the defects of crystal structure i.e. dislocations and boundaries play an important role both in kinetics and thermodynamics of the process.

CONCLUSIONS - The ideas discussed may help us to avoid some discrepancy characteristic of the previous approach.

1) We may conclude that solid solutions decompose by spinodal only at continuous decrease of free energy and that is why the decomposition does not need activated nucleation, i.e. fluctuational overcome of energy barrier.

2) The mystic fog around the notion of spinodal disappears, as well as exotic ideas about spinodal decomposition. If we call the considered mechanism of decomposition by spinodal (in fact, it has many features of Cahn's spinodal) the spinodal curve in diagram T-c, as the place of points for which  $\partial^2 f(c_1) / \partial c_1^2 = 0$  in diagram f(c), will not be found because specific free energy of decomposing solid solution is described by convex curve only.

3) Thermodynamics and morphology of the notions such as clustering, formation of GP zones, short-range ordering, segregation, K-state etc. are revealed. For us all these notions mean some unity having, however, dif-

ferent historically established names.

In all the cases they are clusters of solutes in the matrix, having the same type of lattice as the matrix but different morphology and chemical composition. If clusters are formed in the alloy the composition which corresponds to one-phase region of phase diagram, then they are the final product of decomposition (clusters of the first kind). In the case when clusters are formed before precipitation of a new phase (the alloy has the composition corresponding to two-phase region) they represent one of the stages of decomposition on the way towards precipitation of a new phase (clusters of the second kind). There is not any morphological difference between the former and the latter clusters, the only difference can be in concentration of alloys. There seems to be no sufficient ground for referring such clusters to the particles of a new phase since some features of phase are not found in the clusters (at early stages there is no clear-cut demarcation between the clusters and the matrix, lattice parameter of a solid whether containing clusters or not is just the same).

The conclusions considered testify to the limitation and untenability of generally assumed 'linear' concepts of dynamics of phase segregation which are based on exponential increase of small fluctuations. The process of "search" of correlation distance which can be observed due to incubation period occurring under certain conditions, is actually the stochastic process submitting to the laws of dynamic

scaling. Such a process is characteristic only for the systems in which chemical interaction between the components takes place. This interaction occurs at any concentrations and temperatures (for instance, the tendency towards chemical interaction is usually found by defining their activity which in its turn is calculated by measuring steam pressure of the components at such compositions of solids and such temperatures when distribution of components is supposedly completely random). This tendency is realized at  $T < T_a$  only for stoichiometric alloys and at working Eq. (3) only for non-stoichiometric alloys.

#### REFERENCES

1. A.Guinier, "Unhomogeneous metal solids", Pergamon Press, New York (1957)
2. E.Hornbogen, Journ. Appl. Phys. 32, 135-139 (1961)
3. Higgins J. and P.Wilkes, Phil. Mag. 25, 599-623 (1972)
4. Marcus H.L., Fine M.E. and L.H. Schwatz, Journ. Appl. Phys. 38, 4750-4758 (1967)
5. Ericsson T. and J.R.Cohen, Acta Cryst. A27, 97-106 (1971)
6. Miyazaki T., Takagishi S., Mori H. and T.Kozakai, Acta Met. 28, 1143-1153 (1980).
7. Kozakai T. and T.Miyazaki, Trans. Jap. Inst. Metals. 24, 633-641 (1983)
8. K.Binder, "Stochastic Nonlinear Systems in Physics, Chemistry, and Biology", p. 62, Berlin, Heidelberg, New York : Springer-



Verlag (1981)

9. Vintaikin E.Z. and V.V.Colontsov,  
Fiz. Met. Metalloved. 26, 282-288  
(1968)
10. Gruzin P.L., Rodionov Y.L. and  
V.S.Mcrrthan, "Probl. Metalloved.  
and Fiz. Met.", p. 75, Metallurgia,  
Moscow (1972)
11. R.Lagneborg, Trans. ASM 60, 67-78  
(1967)
12. K.V.Chuistov, "Ageing of metal  
alloys", Naukova Dumka, Kiev  
(1985)
13. Yu.I.Ustinovshikov, Dokl. Academy  
Nauk USSR 247, 596-599 (1979)
14. Yu.I.Ustinovshikov, "Second Phase  
Precipitation in Solids", Science  
Press, Moscow (1988)
15. Landau L.D. and E.M.Lifshits,  
"Statistic Physics", part 1,  
Science Press, Moscow (1976)
16. J.W.Cahn, Acta Met. 9, 795-808  
(1961)
17. J.E.Hilliard, "Phase Transforma-  
tion", p. 497, ASM, Metals Park,  
Ohio (1970)
18. J.Langer, "Fluctuates instability  
and phase transition", p. 19,  
Pergamon Press, New York, London  
(1975)

# THERMOMECHANICAL TREATMENT OF AN Fe-Mn-Al-C SIDEBAND ALLOY

**Kwan H. Han\***

Department of Metallurgical Engineering  
and Materials Science, Carnegie-Mellon University,  
Pittsburgh, Pennsylvania 15213, USA

\*On leave of absence from  
Yeungnam University, Korea

**Tae S. Kang**

Department of Metallurgical Engineering,  
Yeungnam University, 214-1 Daedong,  
Gyongsan, Kyongbuk, Korea

**David E. Laughlin**

Department of Metallurgical Engineering  
and Materials Science, Carnegie-Mellon University,  
Pittsburgh, Pennsylvania, 15213, USA

## ABSTRACT

The influence of thermomechanical treatment on the resulting microstructure and hardening of the Fe-32Mn-8Al-0.9C-0.2Mo sideband alloy has been investigated mainly by means of optical and transmission electron microscopy and microhardness measurements. Two plastic deformation conditions, both giving rise to similar hardness levels, were employed before final aging: one consists of prior deformation only and the other is composed of preaging and warm deformation. It is observed that the prior cold deformation renders a significantly higher hardness and that it does not affect the essential mode of continuous precipitation during aging. This treatment, however, causes acceleration of the  $\alpha + \beta$ -Mn eutectoid reaction, which occurs heterogeneously. This makes the cold deformed alloys extremely brittle. In contrast, in the case of preaged and warm deformed alloys, enhanced hardening, without remarkable acceleration of the heterogeneous eutectoid reaction, is produced during final aging. The warm deformation is observed to cause disturbance in the preaged microstructure, but, apparently, it does not result in any abrupt change of the finally aged microstructure. Preliminary tensile test results indicate that the latter treatment can be effectively used for improving the mechanical properties. The results are compared with those obtained through conventional aging without prior plastic deformation.

THIS WORK has been undertaken to test the applicability of thermomechanical treatment in improving the mechanical properties of age-hardenable Fe-Mn-Al-C austenitic alloys. For this purpose we have examined two different treatments: cold deformation followed by aging and warm deformation during preaging followed by final aging. The effect of each treatment on the hardening response and microstructural change in

the Fe-32Mn-8Al-0.9C-0.2Mo alloy has been documented and compared with the conventional aging treatment (no prior plastic deformation).

The potential of age-hardenable Fe-Mn-Al-C alloys for high strength applications has been put forward by several investigators (1-3). These alloys are, however, in effect little more than derivatives of those that were developed earlier (4,5) as a low cost substitute for the traditional Fe-Cr-Ni austenitic stainless steels. The previous investigations (3,6-11) showed that the age hardening in Fe-Mn-Al-C alloys occurs in the course of continuous precipitation of the  $\kappa$  carbide phase ( $L'_{12}$  type perovskite crystal structure) from the supersaturated austenite matrix. During the initial stage of aging at about 550 °C or below, the parent matrix phase decomposes, exhibiting sidebands in diffraction patterns (6,7,9,11) along with the formation of a modulated structure (3,6-11) consisting of carbon-enriched and carbon-depleted zones alternately aligned in the  $\langle 100 \rangle$  matrix directions. It has been believed (9) that this decomposition initiates via spinodal decomposition (12). An  $L'_{12}$  ordering was also observed (3,6-10) to occur in the carbon enriched zones. A recent study (10) showed that the optimum hardening is obtained by the coarsening of this modulated structure. It was also demonstrated (10) that at least about 300 MPa increase of yield strength can be produced, while retaining the total elongation of about 40%, if aging is performed below 550 °C. Previously, an aging experiment using cold deformed alloys was performed by Krivonogov et al. (3). They did not, however, present the microstructural details of their deformed and aged alloys.

## EXPERIMENTAL PROCEDURE

The alloy (composition: Fe-31.9 wt.%Mn-8.48 wt.%Al-0.9 wt.%C-0.2 wt.%Mo) (10) was prepared by air induction melting. After homogenization and hot forging at 1200 °C, the alloy was hot rolled at 1150 °C to plates about 3 mm thick.

These plates were then cold rolled without intermediate annealing to 1 mm thick strips. The total amount of cold reduction was 67%. Using these specimens, the following heat treatments were performed:

- Treatment I - solution treatment (1027 °C, 600 sec) + 550 °C aging (conventional aging)
- Treatment II - 550 °C aging without solution treatment (aging of cold deformed specimens)
- Treatment III - solution treatment (1027 °C, 600 sec) + preaging (550 °C,  $1.44 \times 10^5$  sec) + warm deformation (15% reduction at 550 °C by rolling) + final aging at 550 °C (aging of preaged and warm deformed specimens)

The solution treatment was performed in a vertical type tube furnace under an Ar atmosphere, which was followed by quenching into water. The aging was performed in salt baths consisting of 50%NaNO<sub>2</sub>-50%KNO<sub>3</sub>.

Hardening behavior of specimens with and without prior plastic deformation during final aging was examined mainly by microhardness measurements under a load of 100 g. During the tests, care was taken to make each indentation within an austenite grain. Tensile tests were carried out using specimens with a gauge length of 16 mm and an Instron testing machine. For the tensile tests, the cross-head speed of  $3.3 \times 10^{-3}$  mm/sec (corresponding to an initial strain rate of  $2.1 \times 10^{-4}$ /sec) was used. Microstructural observations were made by optical and transmission electron microscopy (TEM). For optical metallography, specimens were etched in 5% nital solution and thin foils for TEM observations were prepared in a twin-jet electropolisher (9). TEM examination was performed utilizing a Hitachi electron microscope operating at 100 kV.

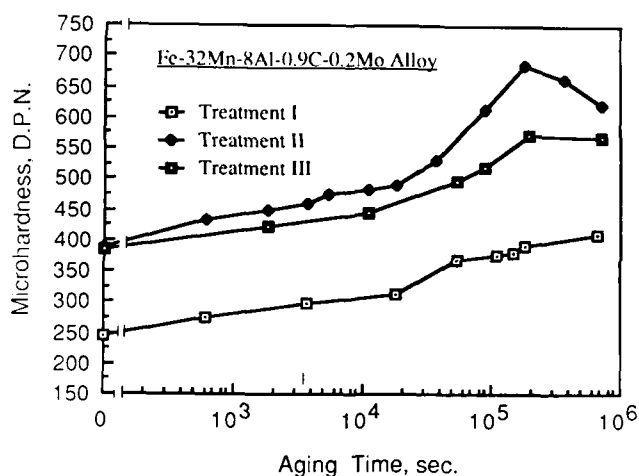


Fig. 1 - 550 °C age hardening curves of specimens with different prior treatments: Treatment I - none, Treatment II - cold deformation, and Treatment III - preaging and warm deformation at 550 °C. (For experimental details, see text.)

## RESULTS AND DISCUSSION

Fig. 1 compares the hardening response observed for specimens with and without prior plastic deformation on final aging at 550 °C. Hereafter we will present and discuss the results mainly referring to these aging data.

**CONVENTIONAL AGING (TREATMENT I) -** The results of this treatment are similar to those reported previously (10). The only difference was in the solution treating condition. In the previous work, the solution treatment was carried out at 980 °C for  $1.5 \times 10^3$  sec. This slight difference gave rise to a lower hardening in the

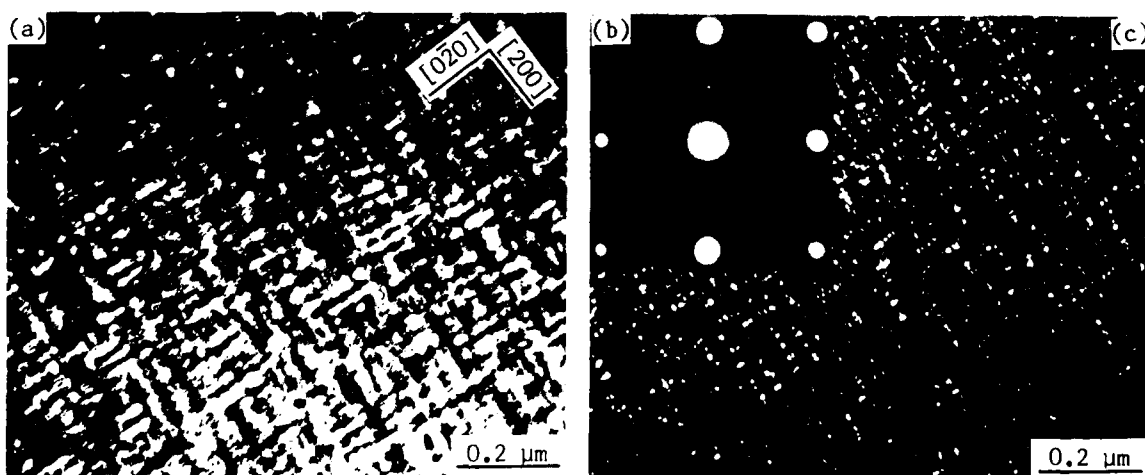


Fig. 2 - TE micrographs of non-deformed specimen after aging for  $1.44 \times 10^5$  sec at 550 °C: (a) bright field image, (b) corresponding SAD pattern and (c) dark field image taken using 100 superlattice reflection. Foil normal = [002].

present investigation, but the general hardening results were almost same as those in Ref. 10. As seen in Fig. 1, an increase in the hardening rate was observed after the initial moderate hardening. This second stage hardening occurred after aging for  $5.4 \times 10^4$  sec at 550 °C. Fig. 2 shows both bright and dark field TEM images and the corresponding selected area electron diffraction (SAD) pattern of a specimen aged for  $1.44 \times 10^5$  sec to produce nearly maximum hardening. In these micrographs, a fairly coarsened {100} two-phase modulated structure can be seen as observed previously (10).

The optical microstructure revealed an apparently austenitic structure, free from grain boundary or heterogeneous precipitation for aging times up to  $7.2 \times 10^5$  sec. Further prolonged aging, however, produced a cellular like, non-lamellar eutectoid grain boundary reaction, which resulted in the co-precipitation of the  $\beta$ -Mn phase with the ferrite ( $\alpha$ ) phase (see Fig. 3, for example). This cooperative precipitation corresponds to an  $\alpha + \beta$ -Mn eutectoid reaction, though the term " $\beta$ -Mn precipitation" frequently appears in the literature (3,6-10) to describe this grain boundary reaction. The  $\beta$ -Mn phase of this eutectoid product is extremely brittle. As a consequence, the occurrence of this eutectoid reaction causes a significant decrease in the ductility (10).



Fig. 3 - Optical micrograph revealing the non-lamellar  $\alpha + \beta$ -Mn eutectoid reaction occurred in non-deformed alloy after aging for  $4.3 \times 10^6$  sec at 550 °C.

AGING OF COLD DEFORMED SPECIMENS (TREATMENT II) - The cold deformed alloys contained severely distorted austenite grains with many wavy shear bands. TEM examination further revealed many fine bands (transition bands or subgrains (13,14)) with a slight misorientation. The band

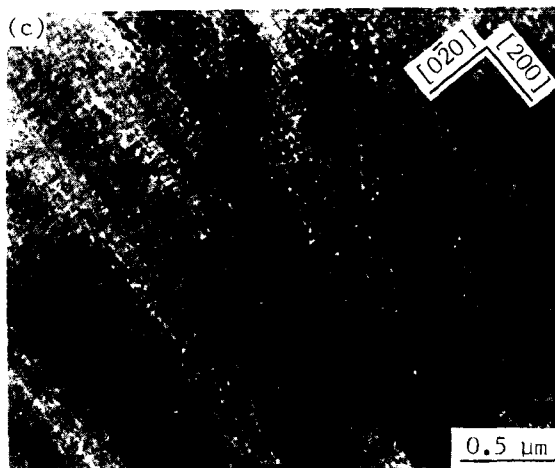
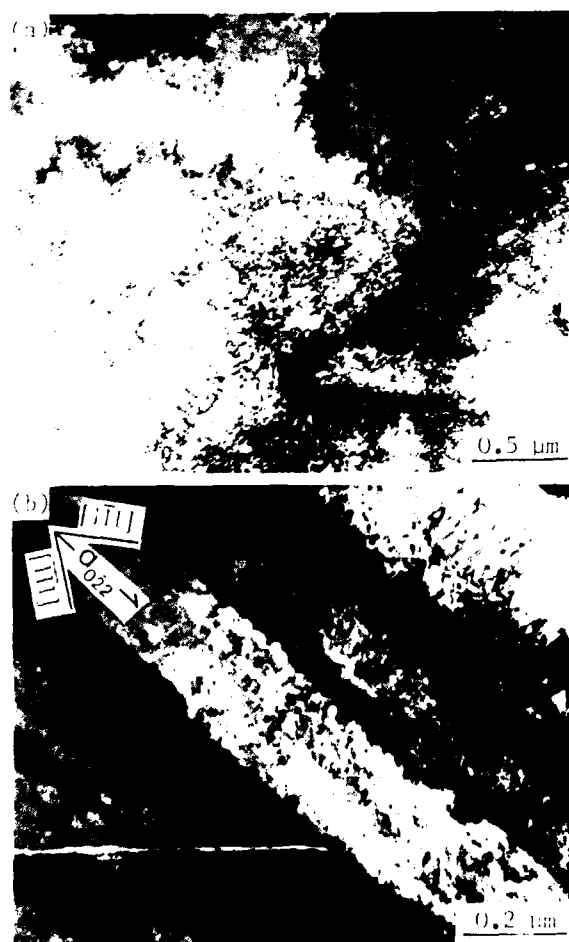


Fig. 4 - Bright field TE micrographs of cold deformed specimens: (a) as-cold deformed, and after aging at 550 °C for (b)  $9.4 \times 10^4$  sec and (c)  $3.6 \times 10^5$  sec, respectively. Foil normals; (b) [022] and (c) [002].

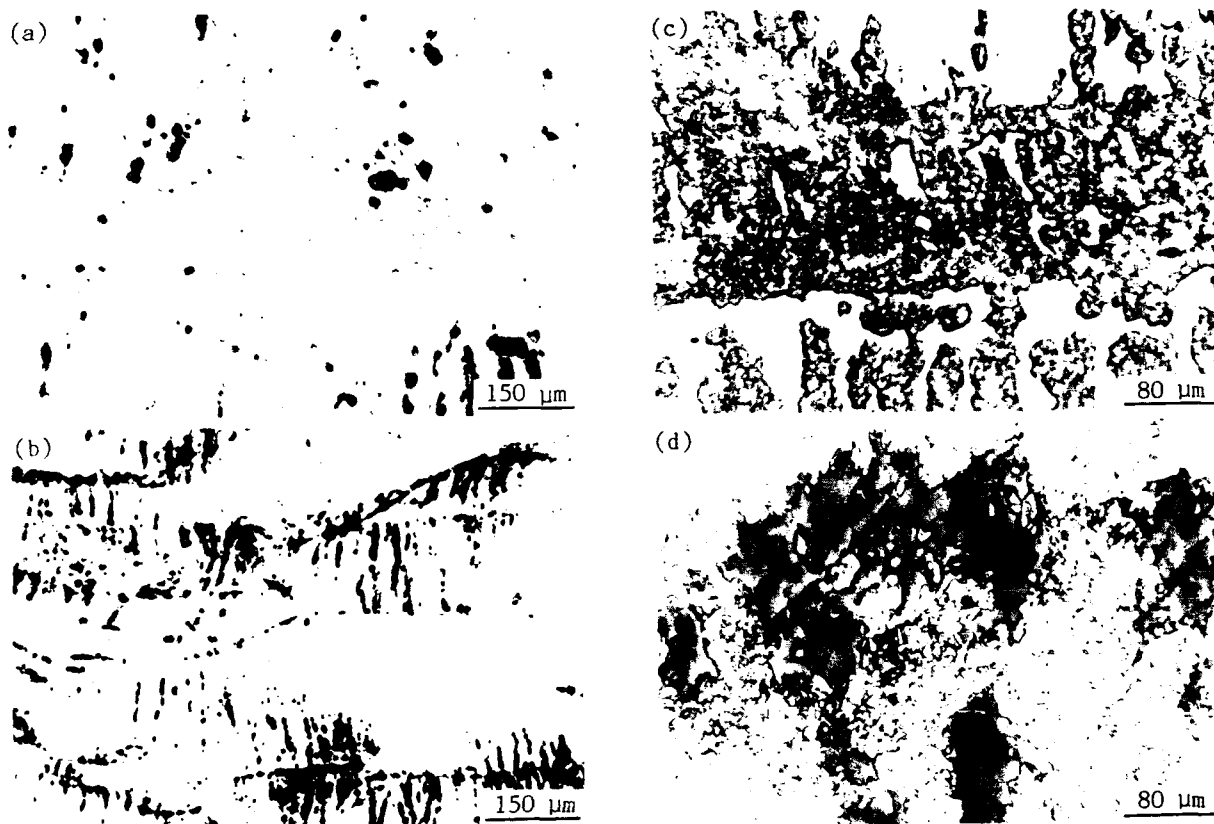


Fig. 5 - Optical micrographs of cold deformed specimens after aging at 550 °C for (a)  $5.4 \times 10^3$  sec, (b)  $1.1 \times 10^4$  sec, (c)  $3.6 \times 10^5$  sec, and (d)  $7.2 \times 10^5$  sec, respectively. Note the occurrence of the non-lamellar eutectoid reaction along the shear bands as well as at the grain boundaries.

spacing was about 0.1  $\mu\text{m}$ . Fig. 4-a, taken from an as-cold deformed specimen, shows high density of inhomogeneously distributed, tangled dislocations as well as subgrains. Aging of these cold deformed specimens produced a considerably higher hardness. However, in spite of the high density of dislocations and other defects generated during the heavy deformation, the initial rate of hardening was observed to be approximately the same at this aging temperature compared to that for the non-deformed specimens (see Fig. 1). Significantly enhanced hardening (second stage) in the cold deformed specimens occurred after aging for about  $3.6 \times 10^4$  sec.

To investigate the microstructural change responsible for this hardening TEM examination was performed. It was, however, difficult to observe the decomposed microstructure because of the high degree of deformation and the resulting large number of dislocations. Only weak superlattice reflections could be observed for aging times up to  $9.4 \times 10^4$  sec (see the corresponding microstructure in Fig. 4-b). Longer aging allowed some recovery to occur, and this enabled the observation of the underlying two-phase modulated microstructure (see Fig. 4-c). This shows that the continuous decomposition mode of spinodal decomposition in this Fe-Mn-Al-C alloy was not substantially affected by the presence

of high density of lattice defects (mainly dislocations) introduced by severe prior cold deformation. This result is also consistent with previous observations for other cold deformed spinodal alloys such as Cu-Ni-Sn (15,16), Cu-Ti (14,17), Co-Ti-X (18) and Fe-Mo based alloys (19).

The rate of increase of microhardness is seen to be approximately the same for Treatments I and II (Fig. 1). This might be interpreted to indicate that the age hardening mechanism in both is essentially the same in that the hardening occurs with the development of the modulated structure. As shown before, this decomposition process is nearly independent of the lattice defects in the initial microstructure because it occurs via the homogeneous spinodal process (9). However, after aging for about  $5 \times 10^4$  sec, the hardening in the cold deformed alloy was greater than that in conventionally aged alloy as seen in Fig. 1.

Unfortunately, however, the prior cold deformation was observed to greatly accelerate the  $\alpha + \beta\text{-Mn}$  eutectoid reaction. This can be seen in Fig. 5. It is noted in these optical micrographs that the eutectoid reaction occurred even at the shear bands, where slip localization had taken place. Hence, the fast eutectoid reaction rate as seen in Fig. 5 can be due to the

increase of favorable nucleation sites as well as enhanced diffusion owing to high density of lattice defects. Because of this fast rate of the  $\alpha + \beta$ -Mn reaction, the cold deformed alloy became extremely brittle. For this reason, it is concluded that this treatment of prior cold deformation is not desirable to obtain high strength in Fe-Mn-Al-C alloys.

**AGING OF PREAGED AND WARM DEFORMED SPECIMENS (TREATMENT III)** - This process was intended to find an alternative method to attain an improvement in hardening by effectively suppressing the acceleration of the  $\alpha + \beta$ -Mn eutectoid reaction, which occurred when we introduced plastic deformation (Treatment II). To do this we employed preaging and warm deformation treatments. The preaging condition was selected to be near the maximum hardening condition of the conventional aging (Treatment I), which produced a coarsened two-phase modulated structure as seen in Fig. 2. The warm deformation of 15% in reduction was applied to the preaged specimens, thereby making them possess nearly the same level of microhardness as that of as-cold deformed specimen of Treatment II.

In the warm deformed state, the dislocation tangles and subgrains, observed in the cold deformed alloy (Treatment II), were not observed. In addition, thin deformation twins, reported (8) in optimally aged and cold deformed (25% in reduction) Fe-Mn-Al-C alloys, were not observed either. However, the uniformity of the modulated structure of the preaged microstructure was observed to be disrupted as shown in Fig. 6-a. This disruption is obviously due to the repeated movements of dislocations during the warm deformation, which shear the modulated structure. Nevertheless, the modulation wavelength was apparently unchanged (about 27 nm). It is likely, however, that some change in the amplitude of the fluctuations have occurred during deformation as observed in fatigued Cu-Ni-Sn spinodal alloys (20).

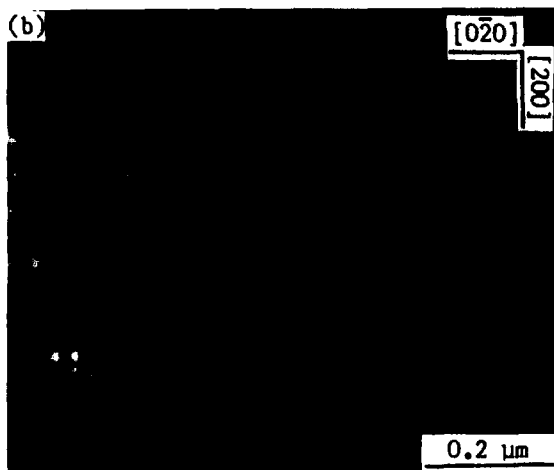
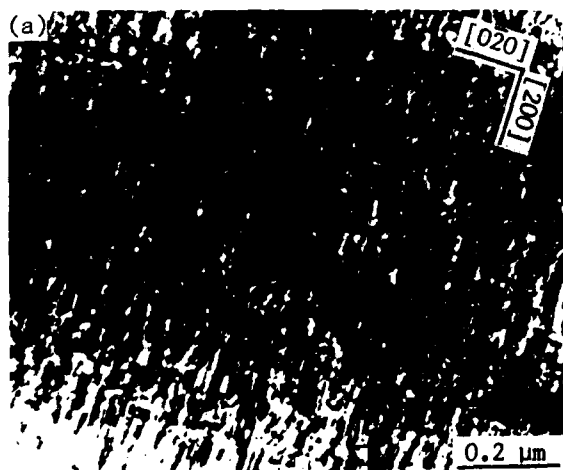


Fig. 6 - Bright field TE micrographs of preaged and warm deformed specimens: (a) as-warm deformed and (b) after aging for  $9.4 \times 10^4$  sec. Foil normals = [002].

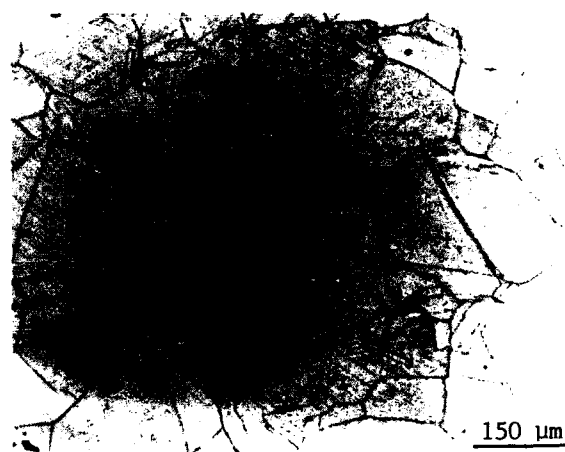


Fig. 7 - Optical micrograph of preaged and warm deformed alloy after final aging for  $1.94 \times 10^5$  sec at 550 °C.

As seen in Fig. 1, a considerable hardening was further attained by the final aging treatment of the warm deformed alloys. In particular, it is interesting to note that, although the warm deformed alloys have experienced the pre-aging to produce near maximum hardening in the non-deformed state, further age hardening occurred with a rate almost the same as that of non-deformed alloys. In Fig. 6-b, the TEM microstructure of the warm deformed specimen after aging for  $9.4 \times 10^4$  sec is shown. It is seen that this aged microstructure looks more like that of non-deformed alloy (Fig. 2) than that of the as-warm deformed alloy (Fig. 6-a). That is, the modulations are more uniform; in effect the microstructure has recovered without remarkable coarsening.

Of importance in this thermomechanical treatment is that the improvement of hardening could be obtained successfully without inducing accel-

Table 1 Comparison of room temperature tensile properties of non-deformed (Treatment I) and preaged and warm deformed (Treatment III) specimens after aging at 550 °C

Heat treating condition	0.2% yield stress (MPa)	Ultimate tensile stress (MPa)	Elongation (%)
As-solution treated*	373	801	52
Non-deformed after aging for $1.44 \times 10^5$ sec	666	1035	38
Preaged and warm deformed after aging for $1.94 \times 10^4$ sec	898	1135	30

\* Tensile data of these specimens are somewhat different from those of previous work (10). This may be due to difference in the solution treating condition and tensile test condition.

eration of the  $\alpha + \beta$ -Mn eutectoid reaction. Fig. 7 shows the optical microstructure of the warm deformed specimen after aging for  $1.94 \times 10^5$  sec, which produced the maximum hardness. The absence of the grain boundary (eutectoid) reaction can be noted in this micrograph.

The above results obtained through introducing the preaging and warm deformation before final aging implies that this kind of thermomechanical treatment can be effectively used for improving the mechanical properties of Fe-Mn-Al-C sideband alloys. To evaluate this implication we performed preliminary tensile tests. The test results are given in Table 1. It is noted that, as expected from the microhardness and optical metallography results, a considerable increase of yield strength was achieved without significant sacrifice in elongation: the 0.2% yield stress increment was as high as about 260 MPa, compared to that of non-deformed specimen, and this yield stress was about 2.4 times higher than that of as-solution treated specimen.

To optimize the process parameters in the development of mechanical properties and to obtain a better understanding of structure/property relationships of the preaged and warm deformed alloys further work will be undertaken.

#### SUMMARY

Two thermomechanical treatments were examined to test their applicability in improving the mechanical properties of Fe-Mn-Al-C sideband alloys. For this purpose, the influence of these treatments on the microhardness and the resulting microstructure was investigated using the Fe-32Mn-8Al-0.9C-0.2Mo alloy. It was observed that prior cold deformation produces a significantly higher hardness during the subsequent aging and that it does not alter the essential mode of continuous precipitation. This treatment, however, did induce the acceleration of the undesirable  $\alpha + \beta$ -Mn eutectoid reaction, thereby making the cold deformed alloys extremely brittle after aging. On the other hand, by utilizing preaging and warm deformation before final aging, enhanced hardening could successfully be attained by suppressing the accelera-

tion of the eutectoid reaction. Preliminary tensile tests showed that, by employing preaging and warm deformation, a high yield strength increase could be attained without significant sacrifice in elongation. The present results suggested that the thermomechanical treatment composed of preaging, warm deformation and final aging can be effectively used for improving the mechanical properties of the Fe-Mn-Al-C sideband alloys.

#### ACKNOWLEDGMENT

The financial support of the Korea Science and Engineering Foundation (KHH) and the National Science Foundation, DMR-84-13115 at Carnegie-Mellon University (DEL) is gratefully acknowledged.

#### REFERENCES

1. R.E. Cairns and J.L. Ham, U.S. Patent no. 3,111,405
2. G.L. Kayak, Met. Sci. Heat Treat., (2), 95-97 (1969)
3. G.S. Krivonogov, M.F. Alekseyenko and G.G. Solov'yeva, Phys. Met. Metall., 39, 86-92 (1975)
4. J.L. Ham and R.E. Cairns, Product Eng., 29, 50-52 (1958)
5. D.J. Schmatz, Trans. ASM, 52, 898-913 (1960)
6. N.J. Storchak and A.G. Drachinskaya, Phys. Met. Metall., 44, 123-130 (1977)
7. K.H. Han and W.K. Choo, Metall. Trans. A, 14A, 973-975 (1983)
8. I.S. Kalashnikov, V.S. Litvinov, M.S. Khadyev and L.D. Chumakova, Phys. Met. Metall., 57, 160-164 (1984)
9. K.H. Han, J.C. Yoon and W.K. Choo, Scripta Metall., 20 (1986)
10. K.H. Han, W.K. Choo, D.Y. Choi and S.P. Hong, Proceedings of Alternate Alloying for Environmental Resistance, G.R. Smolik and S.K. Banerji Eds., 91-106 (1987)
11. K.H. Han and W.K. Choo, unpublished research
12. J.W. Cahn, Trans. AIME, 242, 166-180 (1968)
13. R.D. Doherty, Metal Sci., 8, 132-142 (1974)

14. J. Dutkiewicz, Metall. Trans. A, 8A, 751-761 (1977)
15. J.T. Plews, Metall. Trans. A, 6A, 537-544 (1975)
16. S. Spooner and B.G. Lefevre, Metall. Trans. A, 11A, 1085-1093 (1980)
17. J. Dutkiewicz, Met. Technol., 5, 333-340 (1978)
18. J. Singh, J. Mater. Sci., 21, 1134-1138 (1986)
19. M. Doi, H. Tanabe and T. Miyazaki, J. Mater. Sci., 22, 1328-1334 (1987)
20. M.P. Quin and L.H. Schwartz, Mater. Sci. Eng., 46 (1980)



# THE EFFECT OF WARM ROLLING AND INTERCRITICAL ANNEALING ON THE MICROSTRUCTURE OF A HSLA STEEL

Ronaldo Barbosa, Dagoberto B. Santos

Dept. of Metallurgical Engineering,  
Universidade Federal de Minas Gerais  
Rua Espírito Santo 35, s.206- Centro  
30160- Belo Horizonte- M.G.- Brazil

## ABSTRACT

The effect of warm rolling on the microstructure and hardness of a Nb-microalloyed steel has been examined. It has been observed that ferrite recrystallizes simultaneously with carbide spheroidization. Subcritical annealing produces rapid spheroidization of carbides. Austenitization at 800 °C after warm rolling refines the original austenite grain size from 338 to 8  $\mu\text{m}$ . Ferrite recrystallization is slower in Nb-steels than in C-Mn ones. This has been attributed to the retarding effect of Nb in solid solution and as precipitates.

**HOT ROLLING OF LOW CARBON** or microalloyed steels is carried out in the austenite and in the dual phase regions (1,2). In the latter, the aim is to obtain a fine ferrite grain size with a work hardened substructure. However, the presence of a recovery substructure increases the transition temperature (3) which is not desirable for HSLA steels. On the other hand, fine ferrite grains can be generated by recrystallization without any detrimental effects on ductility.

During intercritical annealing, two main phenomena will happen: formation of austenite and recrystallization of ferrite. The former has been extensively studied (4-7). Austenitization at 740 °C has been reported to follow essentially the same trend for plain C and Nb-steels (8). Recrystallization of ferrite has been investigated in cold rolled C-Mn steel (9). However, little work has been carried out for Nb microalloyed steels.

The present study was performed to examine austenite formation and ferrite recrystallization in a warm rolled Nb-steel.

## EXPERIMENTAL TECHNIQUE

The chemical composition of the material is, in wt%, 0.17C, 1.45Mn, 0.018S, 0.025P, 0.39Si, 0.04Nb and 0.004N. The as-received microstructure is shown in Figure 1. A specimen measuring 150x100x25 mm<sup>3</sup> was heated at 1200 °C for 1 hour and then air cooled.

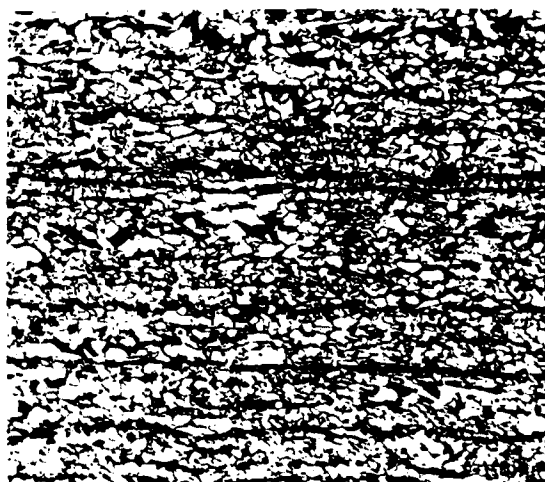


Figure 1. Microstructure of the as-received material. Pearlite and ferrite. Note presence of MnS inclusions. Nital 2%. 100X.



Figure 2. Soaked at 1200 °C during 1 hour and air cooled. Pro-eutectoid ferrite and bainite. Nital 2%. 100X.

The starting microstructure was formed of ferrite and bainite. The microstructure obtained is shown in Figure 2. The starting austenite grain size obtained was 338  $\mu\text{m}$ . Smaller samples (70 x 40 x 9 mm<sup>3</sup>) were machined from the heat treated material and warm rolled. Care was taken to eliminate the decarburized layers acquired during normalizing. A thermocouple was inserted into the rear part of a specimen which was used for calibration. The sample was then heated at 700 °C for 12 minutes and warm rolled immediately. A nominal reduction of 20% was given in the first pass. The specimen was then returned to the furnace and its temperature was homogenized at 700 °C. Warm rolling and soaking operations took 7 minutes. Samples without an embedded thermocouple could be manipulated more rapidly. After homogenization, a second pass of 20% was applied. The specimen was then returned to the furnace for a period of 6 minutes and subjected to a third pass of 20%. The final reductions attained were 24, 43 and 58%. Specimens were then annealed at 750 and 800 °C for 1 hour. Samples with reductions of 24 and 58% were also annealed at 700 °C for 60 to 15,000s.

Grain size measurements were carried out using the mean linear intercept method. The statistical errors were kept to within 10%. Point counting was employed to assess ferrite recrystallized fraction. A number of counts was performed to ensure an error less than 10%. In both cases, the evaluations were made for a 95% level of confidence. Vickers hardness (15 kg) measurements were performed in a Heckert durometer. Samples for quantitative assessments were polished in the standard way. Etching was carried out with nital to reveal ferrite. Prior austenite grains were etched using a saturated solution of picric acid and teepol.

## RESULTS AND DISCUSSION

**Qualitative Observations** - The predominant processes observed were recrystallization of ferrite, and spheroidization and coarsening of carbides. Figure 3 shows the microstructure of the material as-warm rolled at 700 °C. It is essentially composed of heavily deformed ferrite and involves a coarse acicular structure. Both structures are aligned with the rolling direction. The evolution of the microstructure during subcritical annealing is shown in Figure 4. It can be seen that pro-eutectoid ferrite recrystallizes in samples deformed 24 and 58%. Ferrite recrystallizes first in layers around bainite. Recrystallization can even occur during short annealing periods (~60 s). However, the directionality caused by warm rolling still persists even after long annealing treatments. Carbides are found regularly distributed in the samples. The fragmentation of carbides is more accentuated as the pre-deformation increases.

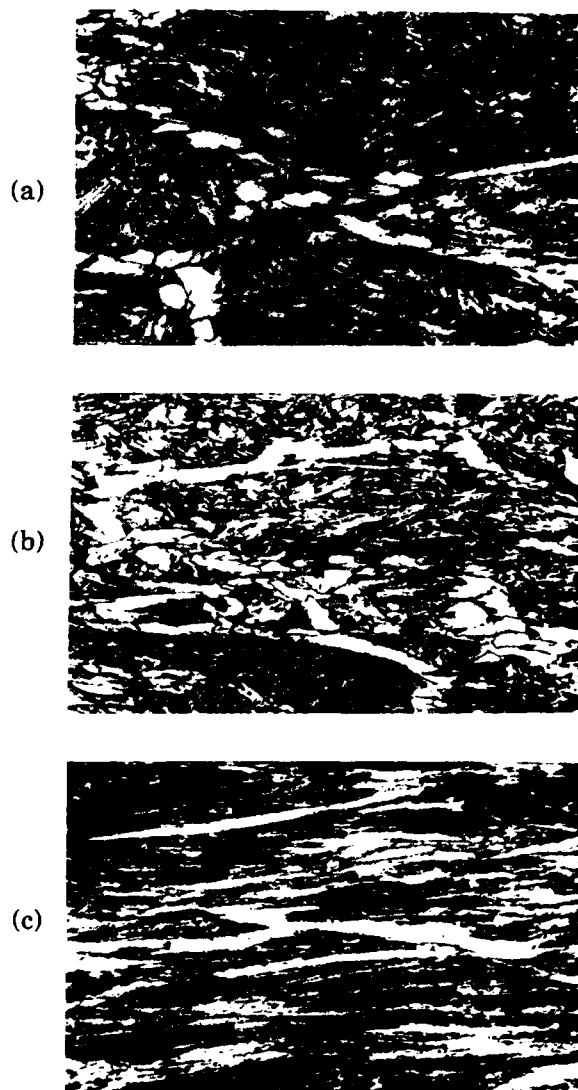
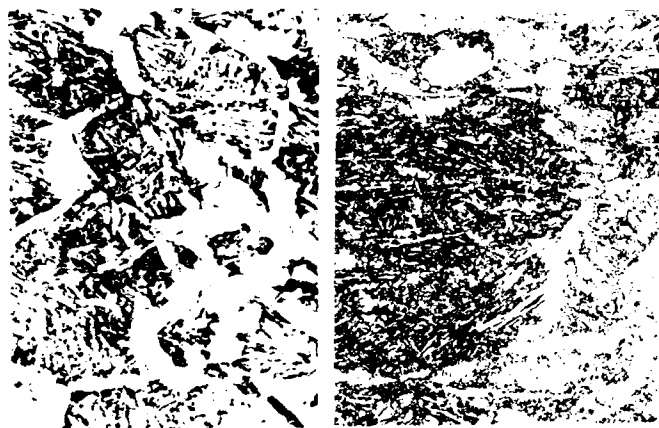


Figure 3. Microstructure after warm rolling in passes of : a- 24%, b- 43% and c- 58%. Nital 2%, 100X.

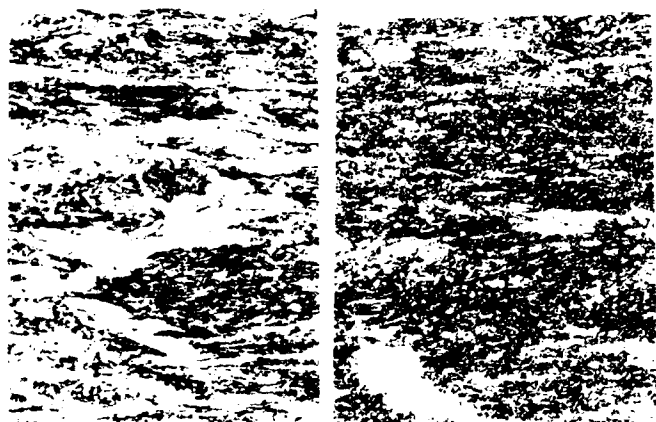
This, in turn, causes them to be more susceptible to spheroidization. Figure 5a shows clearly that spheroidization even occurs for short annealing (60 s). Rapid spheroidization during sub-critical annealing has also been reported elsewhere (9). Figure 5a also shows that the ferrite substructure is not fully recovered. By contrast, carbides are coarsened after long periods of annealing (7260 s) (Figure 5b). Here, there is no visible evidence of ferrite substructure. Therefore, spheroidization occurs long before full recrystallization of the ferrite, as indicated in Figure 4. This is in agreement with previous observations reported in the literature (9).

The structure after annealing at 750 °C for 1 hour is comprised of recrystallized ferrite, bainite



(a)

(b)



(c)

(d)

Figure 4- Microstructure of specimens warm rolled and annealed at 700 °C under the following conditions:

	Reduction, %	Annealing time, s
a	24	60
b	24	10860
c	58	120
d	58	15420

and martensite (Figure 6a). An equilibrium fraction of 45% of austenite is attained after heat treatment. This is in agreement with values reported for microalloyed steels (8). However, smaller fractions have been reported for C-Mn steels (9). Annealing at 800 °C produces 67% volume fraction of formed austenite (Figure 6b). This is much larger than the 40% reported for C-Mn steels (8). Newly formed austenite grains are considerably finer (7.5  $\mu\text{m}$ ) than the original ones (335  $\mu\text{m}$ ), as seen in Figure 7. Increasing the deformation at 700 °C decreases the austenite grain size at 800 °C slightly from 8 to 7  $\mu\text{m}$ . The formation of austenite in undeformed ferrite-pearlite steels has been divided into three



(a)



(b)

Figure 5- Samples annealed at 700 °C with pre-deformation of 58% (a) and 24% (b). The annealing times were 60s (a) and 7260s (b). SEM, nital 2% 100X.

different stages (4): (i) rapid growth of austenite into pearlite until it is completely dissolved, (ii) slow growth of the austenite into ferrite and finally, (iii) equilibrium between ferrite and austenite. In a ferrite-bainite microstructure, the formation of austenite on reheating will begin by dissolving bainite. This is equivalent to stage (i) above. Then, growth of austenite into ferrite and carbides is expected. It has been reported (9) that austenite forms firstly from deformed ferrite. After ferrite has recrystallized however, austenite is formed from spheroidized carbides. Figure 8 illustrates the formation of austenite from the dissolution of carbides. For deformed microstructures, however, it is noticeable that



(a)



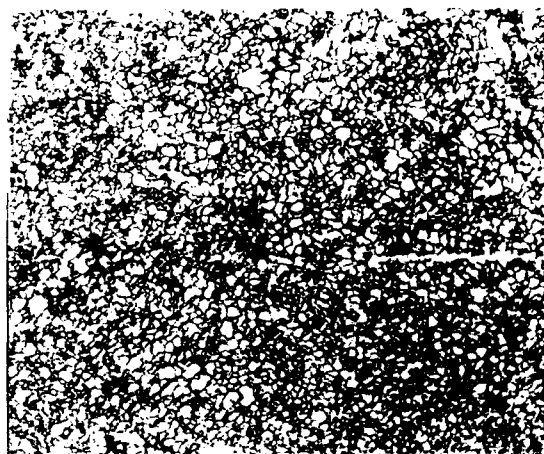
(b)

Figure 6- Specimens deformed at 700 °C and annealed for 1 hour. Martensite and ferrite. Nital 2%. 100X. Deformation and annealing conditions are as follows:

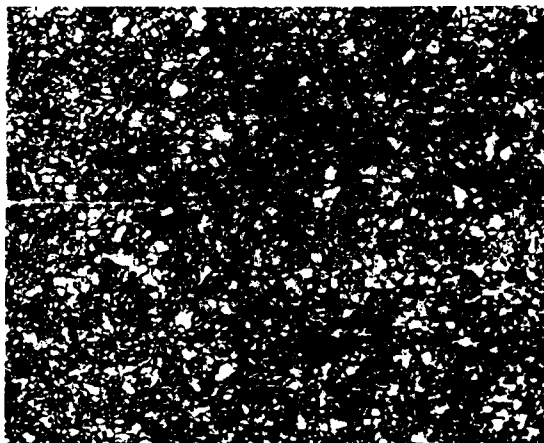
	Reduction, %	Temperature, °C
a	24	750
b	58	800

there is a simultaneous consumption of recrystallized ferrite grains.

**Quantitative Observations** - Figure 9 shows the dependence of the recrystallized fraction of ferrite on the annealing time. The behaviour of a C-Mn steel (9) is also presented for comparison purposes. The rate of ferrite recrystallization is slower in the Nb than in the C-Mn steels. The rolling deformation applied in both cases was similar but rolling in the C-Mn steel was performed at room temperature. However, such differences in pre-deformation conditions will not be responsible for an increase of 2 orders of magnitude in the rate of recrystallization. In fact, the time for 30% of recrystallization increases from 40 s in the cold pre-deformed material to



(a)



(b)

Figure 7- Refining austenite grain size. Samples were deformed at 700 °C and annealed at 800 °C. Deformations applied were 24% (a) and 58% (b). Grain sizes are 7.9 μm (a) and 6.9 μm (b). Picric acid 100X.

1200 s in the present work. Furthermore, in the Nb steel, the recrystallization of ferrite is not completed. The maximum volume fraction attained is 36%. After this plateau is reached, there is no visible microstructural change for times as long as 12,000 s. Therefore, two main events are taking place: (i) an overall delay of the kinetics and (ii) an interruption of the recrystallization process. At this point, it is thought that Nb either in solution or as a precipitate plays an important part in the delay and suppression of recrystallization.

Figure 10 shows the dependence of hardness on annealing time. The hardness decreases slightly during the first 1000 s of annealing. This softening is associated with recrystallization.

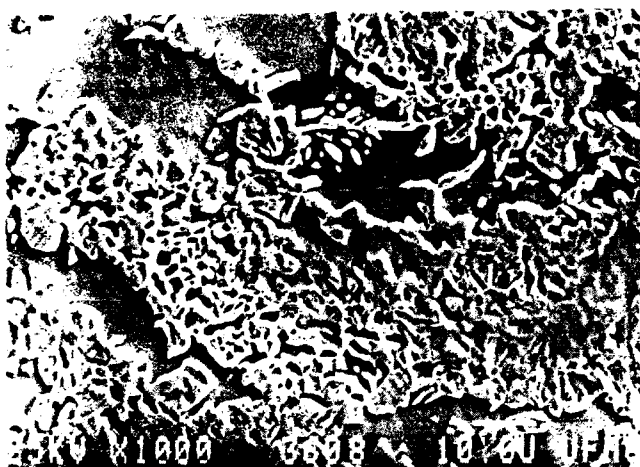


Figure 8- Formation of austenite from the dissolution of carbides. Ferrite in the background and martensite in the foreground. Specimen pre-deformed 24% at 700°C and annealed at 750 °C for 1 hour. SEM, Nital 2%.

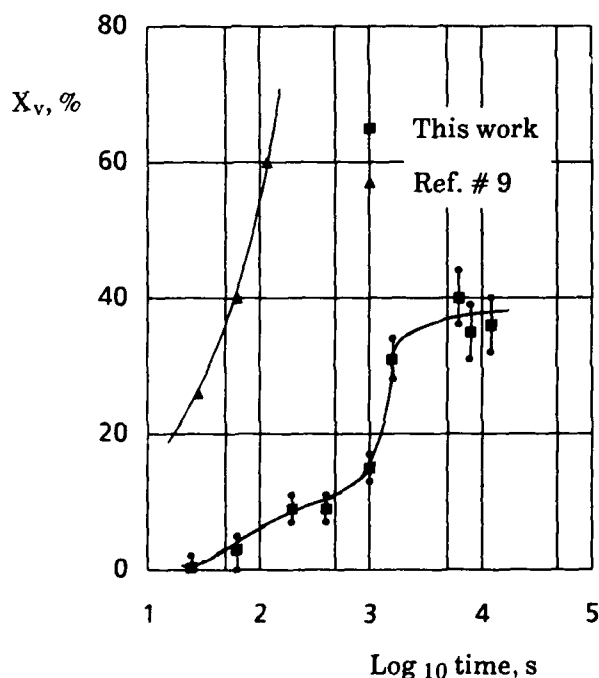


Figure 9. Dependence of the volume fraction of recrystallized ferrite,  $X_v$ , on the annealing time.

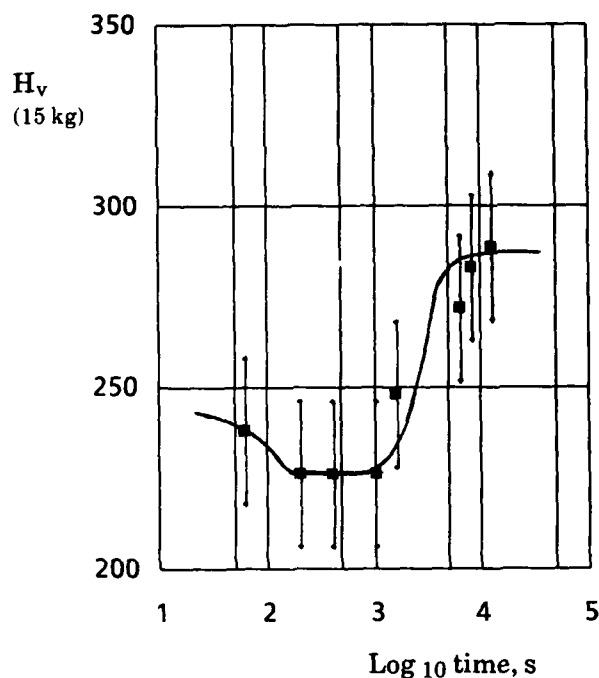


Figure 10. Dependence of the hardness of the material on the annealing time.

After this period, it increases and reaches a plateau at 6300 s. Here, it appears that the increase in hardness is associated with Nb carbonitride precipitation in the deformed ferrite. A similar arrest of recrystallization has been associated with the onset of Nb(CN) precipitation in austenite (10). Such precipitation begins in Nb steels at  $\sim 10$  s at  $\sim 900$  °C (11). This is valid for strain induced precipitation. Longer times for the initiation of precipitation in austenite are expected if no deformation is applied to the material. For example, the nose of the PTT curve for a Nb steel can be displaced from  $\sim 10$  to  $\sim 100$  s in the absence of strain induced precipitation (12). The start of precipitation at 900 °C has been reported to be of the order of 1000 to 2000 s in unstrained austenite (13, 14). Therefore, it is possible that for the present material, not all the Nb(CN) is precipitated during normalizing prior to warm rolling. In this way, some Nb is likely to have remained in solid solution and become available for precipitation in the ferrite.

The increase in hardness occurs for annealing times between 1000 and 1580 s. Recrystallization stops occurring between 1550 and 2500 s (Figure 9). Thus, there is a slight delay between the precipitation start and recrystallization stop times. This is, a certain volume fraction of ferrite is required to stop recrystallization.

## CONCLUSIONS

- 1- Ferrite recrystallizes during subcritical annealing of a Nb-steel. Recrystallization takes place concurrently with carbide spheroidization.
- 2- Warm rolling and subsequent subcritical annealing cause rapid spheroidization of the carbides.
- 3- Intercritical annealing after warm rolling produces considerable refinement of the austenite grain size.
- 4- Formation of austenite occurs by the dissolution of carbides after ferrite recrystallization. Ferrite grains are simultaneously consumed by the austenitization reaction.
- 5- The recrystallization of ferrite in Nb-steels is slower than in C-Mn ones. This is attributed to the retarding effect of Nb in solid solution.
- 6- The recrystallization of ferrite in Nb-steels is suppressed when Nb(CN) precipitation in ferrite is initiated.

## ACKNOWLEDGEMENTS

The authors are indebted to Usinas Siderúrgicas de Minas Gerais, USIMINAS for supplying the steel. Thanks are also due to Professor J.J.Jonas and Dr. S.Yue of McGill University for their many helpful comments and continuing encouragement. RB expresses his thanks to the World University Service of Canada for the award of a travelling fellowship and to the UFMG for granting a period of sabbatical leave during which this work was carried out. DBS acknowledges with gratitude the financial support received from FINEP and CNPq during this investigation.

## REFERENCES

- 1- Shams, N., J. Met. 12, 21-4 (1985)
- 2- Gohda, S., K. Watanabe and Y. Hashimoto, Trans. Iron Steel Inst. Jpn. 21, 6-15 (1981)
- 3- Hawkins, D.N. and A.A. Shuttleworth, J. of Mech. Working Tech. 2, 333-45 (1979)
- 4- Speich, G.R., V.A. Demarest and R.L. Miller, Metall. Trans. A 12A, 1419-28 (1981)
- 5- Lawson, R.D., D.K. Matlock and G. Krauss: in Fundamentals of Dual-Phase Steels, R.A. Kot and B.L. Bramfitt, eds., TMS-AIME, Warrendale, PA, 1981, pp. 347-81
- 6- Garcia, C.A. and A.J. DeArdo, Metall. Trans.A 12A, 521-30 (1981)
- 7- Xue-Ling Cai, A.J. Garratt-Reed and W.S. Owen, Metall. Trans.A 16A, 543-57 (1985)
- 8- Souza, M.M., J.R.C. Guimaraes and K.K. Chawla, Metall. Trans.A 13A, 575-9 (1982)
- 9- Yang, D.Z., E.L. Brown, D.K. Matlock and G. Krauss, Metall. Trans.A 16A, 1385-91 (1985)
- 10- Andrade, H.L., M.G. Akben, and J.J.Jonas, Metall. Trans.A 14A, 1967- (1983)

- 11- Sellars, C.M.: in HSLA Steels Metallurgy and Applications, J.M.Gray, T.Ko, Zhang Shouhua, Wu Baorong and Xie Xisham, eds., ASM International, Metals Park, OH, 1986, pp. 73-81
- 12- Weiss, I. and J.J. Jonas, Met.Trans.A 10A, 831-40 (1980)
- 13- Le Bon, A., J. Rofes-Vernis and C. Rossard, Met. Sci. 9, 36-40 (1975)
- 14- Simoneau, R., G. Bégin and A.H. Marquis, Met. Sci. 12, 381-386 (1978)

# STRAIN-AGING OF LOW-CARBON MARTENSITE

Yang-Jun Li, Guang Yu, Hui-Jiu Zhou

Research Institute for Mechanical Behavior  
of Metals, Xian Jiaotong University,  
Xian, The People's Republic of China

## Abstract

The effect of strain-aging on mechanical behavior and structure changes of low-carbon martensites has been investigated by using 3 low-carbon, low-alloy steels treated to fully lath martensitic structure. Stress-strain curves in tension and S-N curves in fatigue were determined before and after strain-aging for different amounts of prestrain and different aging temperatures and times.

The results have shown that optimum strain aging effect can be obtained with significant increase in the yield strength, and especially that of proportional limit of the material without apparent impairing its ductility. Fatigue strength is also noticeably increased correspondingly. Among the above strain-aging parameters the amount of prestrain plays a major role. When the prestrain exceeds a certain amount potential weakening effect becomes evident which shows a sudden drop on the s-e curve immediately after yielding and local necking begins promptly. The presence of micro-voids and micro-cracks due to over-straining may be responsible for the weakening effect.

ONE OF THE SHORTCOMINGS OF LOW-CARBON MARTENSITE is its comparatively low proportional limit in the as quenched or low-temperature tempered state [1] [2], which limits its use where strict elastic properties are desired. Strain-aging is generally considered as one of effective means for overcoming this weak point. On the other hand the pinning of dislocations during the precipitation of interstitial solute elements (C,N) as a result of strain-aging generally raises the strength while lowers the ductility of the material [3]-[9], and may make the yield/ultimate strength ratio approach unity [6],[7]. This again throws a shadow to the practical value of strain-aging.

In this paper we have made investigations on the effect of strain-aging parameters: amount of prestrain, temperature and time of aging on the static strength, ductility and fatigue properties of low-carbon martensite obtained from

Table I Chemical Composition Of Steels Tested (wt%)

steel	C	Si	Mn	P	S	V	Ti	B	N
15MnB	0.18	0.20	1.31	0.016	0.017	/	0.048	0.0013	0.004-0.006
20MnB	0.22	0.24	1.35	0.012	0.020	/	/	0.0037	0.004-0.006
15MnVB	0.17	0.10	1.49	0.022	0.032	0.1	0.013	0.0023	0.004-0.006

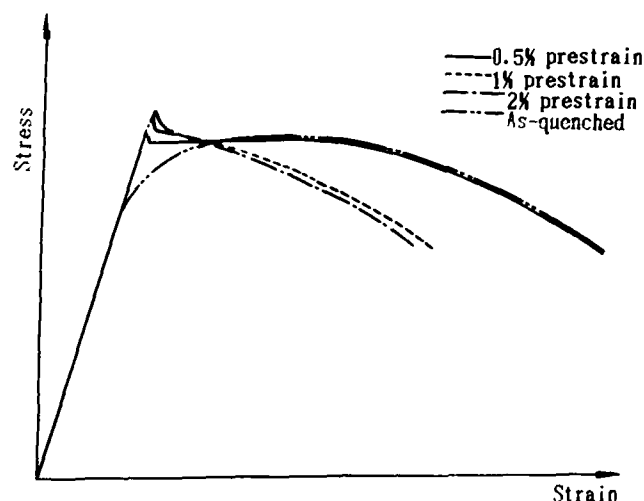


Fig.1 Stress-strain curves showing the effect of strain-aging on tension behavior of 20MnB steel

three low-carbon Mn-B series steels. Changes in properties are correlated to changes in structure.

Chemical composition of materials used are given in Table I. All specimens are heat treated to guarantee through hardening to fully low-carbon martensitic structure, pre-

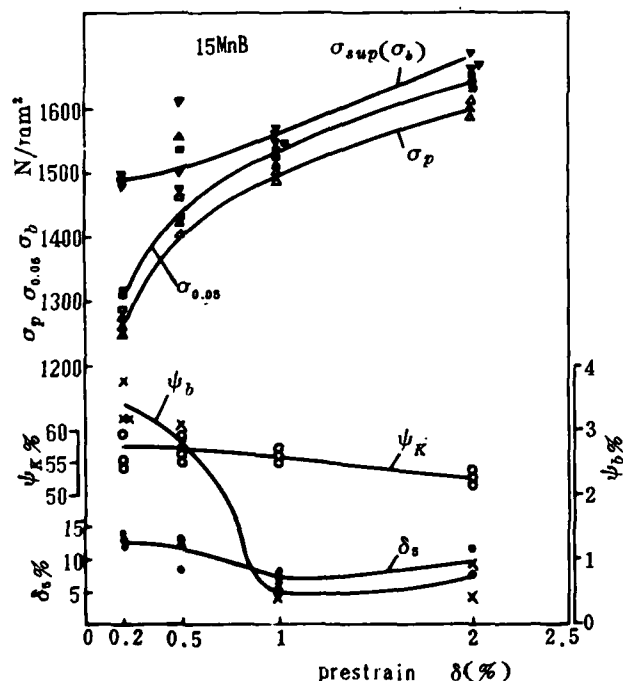
strained to a prescribed value and aged at 100 °C, 120 °C, 150 °C or 180 °C for a duration of 1, 2, 3 hours respectively.

### Tensile Properties

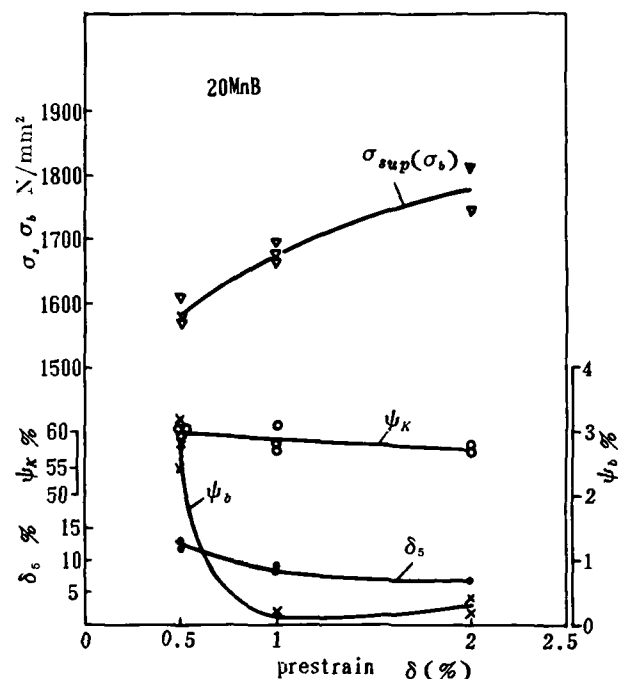
Fig.1 shows typical stress-strain curves of 20MnB steel for 0.5-2% prestrain, aged at 150 °C for one hour, tested in tension at a strain rate of 0.006mm/sec. It can be seen that for all specimens prestrained 0.5% and over there appears an upper yield point. For the 0.5% prestrained specimen prolonged yielding occurs immediately after the yield point drop which extends up to about 2%. Lüders bands appear clearly on the specimen surface at this stage of yielding (Fig.2). For 1% and up prestrained specimens necking occurs immediately after the yield drop, showing negligible uniform elongation which signifies that UTS is nearly equal to Y.S and yield ratio approaches unity. 0.2% prestrained specimen after aging shows no upper yield point and its s-e curve



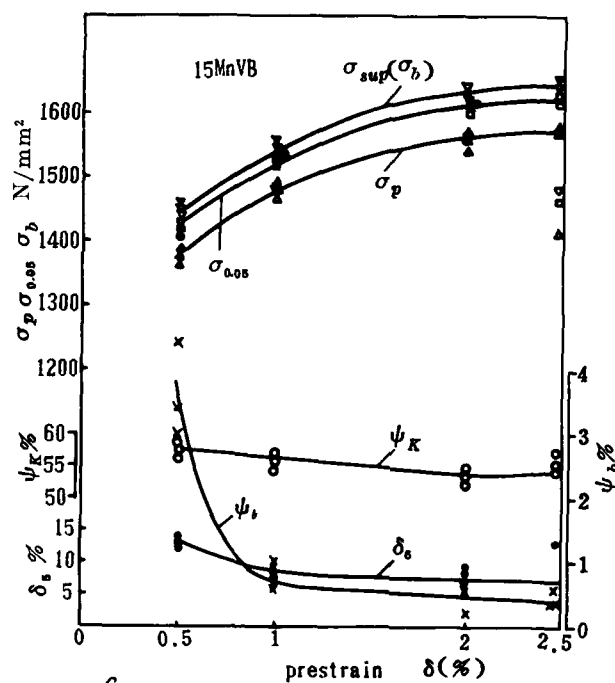
Fig.2 Lüders bands on the specimen surface of 20MnB steel, quenched, 0.5% prestrained, aged for 1 h at 150 °C, tested at a strain rate of 0.006 mm/sec.



A



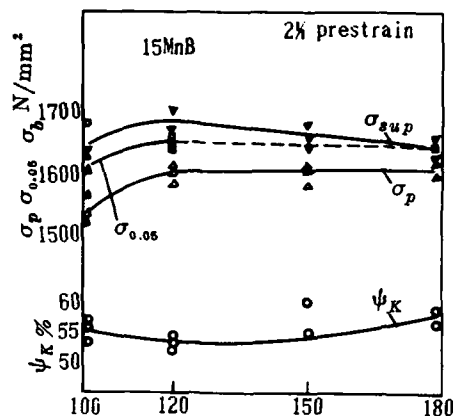
B



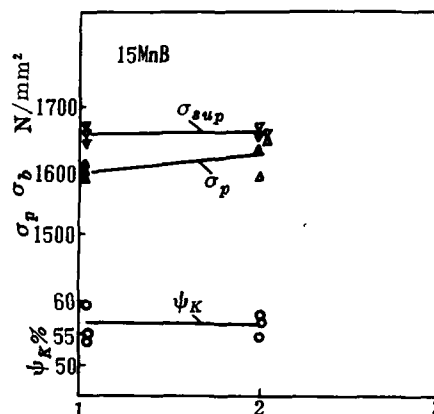
C

Fig.3 The effect of prestrain on the tensile properties  
A. 15MnB steel, aged for 1 h at 120 °C  
B. 20MnB steel, aged for 1 h at 150 °C  
C. 15MnVB steel, aged for 1 h at 120 °C

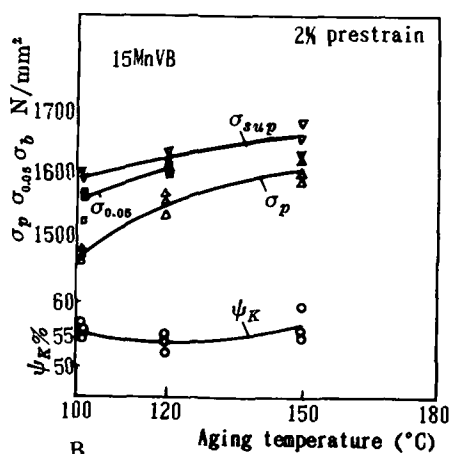




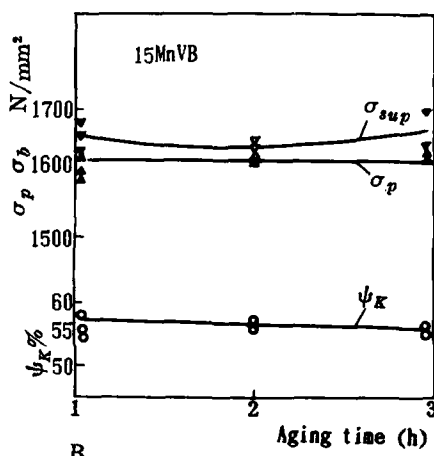
A



A



B



B

Fig. 4 The effect of aging temperature for 1 h after 2% prestrain on the tensile properties

Fig. 5 The effect of aging time at 150 °C after 2% prestrain on the tensile properties

(not show in Fig. 1) approaches that as quenched without strain aging, except its Y.S and proportional limit are higher.

Keeping aging temperature and time constant, the variations of tensile properties with amount of prestrain are shown in Fig. 3. It is evident that the most significant raise with increase of prestrain is in the proportional limit ( $\sigma_p$ ), 0.05% proof stress ( $\sigma_{0.05}$ ), and upper yield stress ( $\sigma_{sup}$ ), while the uniform reduction of area  $\psi_u$  drops sharply from 0.2% to 1% prestrain. Elongation ( $\delta_5$ ) and reduction of area at fracture ( $\psi_K$ ) drop, both gradually.

Fig. 4 shows the variation of tensile properties with aging temperature for specimens of two steels prestrained 2% and aged for one hour. It can be seen that for both steels,  $\sigma_p$ ,  $\sigma_{sup}$  and  $\sigma_{0.05}$  all have the same trend of increase from aging temperature 100 °C to 120 °C (for 15MnVB, up to 150 °C) and further increase in aging temperature results in no more benefit.

Fig. 5 shows the effect of aging time, keeping prestrain at 2% and aging temperature at 150 °C. There seems to be an

apparent difference between the two steels tested. This might be attributable to presence of V in steel 15MnVB which robs the carbon atoms from the solid solution and form stable vanadium carbides.

Table 2 is a collection of data for 3 steels to compare comprehensive mechanical properties in as-quenched, 200 °C tempered and some typical strain-aged conditions. It is apparent that those subjected to 0.2-2.0% strain and subsequent aging have had noticeable raise in proportional limit and yield strength over as-quenched or 200 °C tempered states. Uniform contraction  $\psi_u$  and elongation  $\delta_5$  also show some noticeable change, especially  $\psi_u$  approaches zero when pre-strain is larger than 1%, while the maximum lowering of  $\delta_5$  amounts to 27.2%. The change of contraction at fracture is negligible.

It is worthy to notice that when the pre-strain is equal or smaller than 0.5%, after aging the loss of ductility is very slight but the gain in proportional limit and yield strength is appreciable. This is very significant

Table 2 Tensile Properties of Steels Tested in Various Condition

steel	heat treatment	$\sigma_p$	$\sigma_f^{(1)}$	$\sigma_{0.2}^{(2)}$ or $\sigma_{sup}$	$\sigma_b$	$\delta_5$	$\psi_b$	$\psi_k$	comparision of aged state with as-quenched state				comparision of aged state with 200°C tempered state			
		N/mm <sup>2</sup>				%		%	$\Delta\sigma_s/\sigma_{0.2}^A$	$\Delta\sigma_p/\sigma_p^A$	$\Delta\sigma_b/\sigma_b^A$	$\Delta\delta_5/\delta_5^A$	$\Delta\sigma_s/\sigma_{0.2}^T$	$\Delta\sigma_p/\sigma_p^T$	$\Delta\sigma_b/\sigma_b^T$	$\Delta\delta_5/\delta_5^T$
									%	%	%	%	%	%	%	%
15MnB	as-quenched	605		1098	1439		3.9	58								
	q + 200°C temp.	948		1216	1409	14.1	4.2	62.6								
	0.2% prestrain 1 h, 120°C	1261	1098	1330	1488	13.5	3.4	56.4	21.2	108.4	3.4		9.4	33	5.6	2.8
	0.5% prestrain 1 h, 120°C	1462	1274	1530	1530	11.2	2.9	57.2	39.3	141.7	6.3		25.8	54.2	8.6	17.0
	2% prestrain 1 h, 120°C	1600	1450	1673	1673	9.6	0.4	52.8	52.4	164.5	16.3		37.6	68.8	18.7	17.7
	2% prestrain 1 h, 150°C	1598	1450	1656	1656		0.7	56.5	50.8	164.1	15.1		36.2	68.2	17.5	
20MnB	0.5% prestrain 1 h, 150°C	1587	1350	1587	1587	12.8	2.8	59.8	33.8	136.9	0	9.5				
	2% prestrain 1 h, 150°C	1780	1530	1780	1780	8.7	0.3	59.2	50.1	165.7	12.1	27.2				
	as-quenched	670		1186	1588	14.7	4.1	59.8								
15MnVB	as-quenched	598		1049												
	q + 200°C temp.	923		1183	1377	11.8	4.4	58.8								
	0.5% prestrain 1 h, 120°C	1380	1242	1447	1447	13.5	3.6	57.4	37.9	130.8			22.3	49.5	5	
	2% prestrain 1 h, 120°C	1557	1412	1629	1629	8.4	0.27	53.8	55.3	160.4			37.7	68.7	18.3	11.9
	2% prestrain 1 h, 150°C	1611	1412	1658	1658	8.8		56.3	58.1	169.4			40.2	74.5	20.4	8.5

(1) This is flow stress of as-quenched state at given prestrain

(2) Upper yield stress is adopted when the amount of prestrain is equal to or over 0.5%

(3)  $\Delta\delta_5 = \delta_5^A - \delta_{pre} - \delta_5^A$  ( $\delta_5^A$  -- as-quenching,  $\delta_{pre}$  -- prestraining,  $\delta_5^A$  -- strain-aging),or  $\Delta\delta_5 = \delta_5^T - \delta_{pre} - \delta_5^A$  ( $\delta_5^T$  -- 200°C tempering)

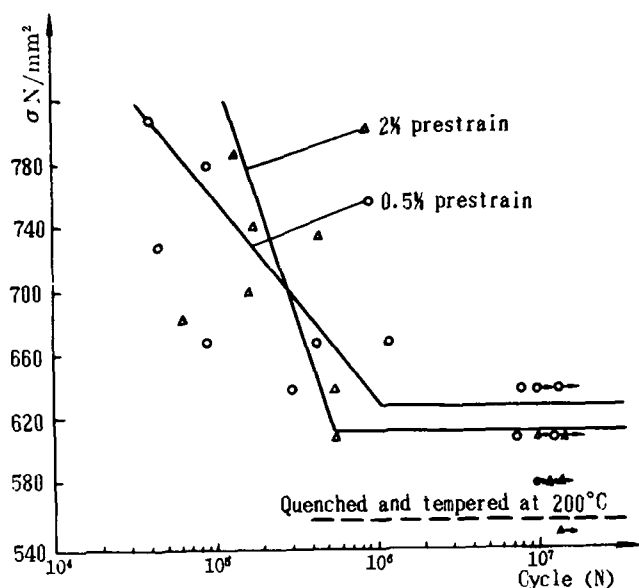


Fig.6 Fatigue curves of 15MnVB steel strain-aged at 150°C for 1 h



Fig.7 Micro-cracks in specimens of 20MnB steel after 0.5% prestrain 1000X

characteristic in engineering.

#### FATIGUE STRENGTH

Rotative bending fatigue tests were carried out on steel 15MnVB with 0.5%, 2% strain-aging and 200°C tempering. Their fatigue limit  $\sigma_{-1}$  are 631 N/mm<sup>2</sup>, 615 N/mm<sup>2</sup> and 558.6 N/mm<sup>2</sup> respectively (Fig.6). Thus strain-aging can enhance not only the static strength but also the fatigue strength of low-carbon martensite. In view of the fact the higher strain-aging may induce structural injury, 0.5% strain-aging has higher fatigue strength is reasonable.

#### CHANGES IN MICRO-STRUCTURE DUE TO STRAIN AGING

Optical microscopic examination has proven that all three steels are hardened through and their microstructures are typical of low-carbon lath martensite. Therefore all the

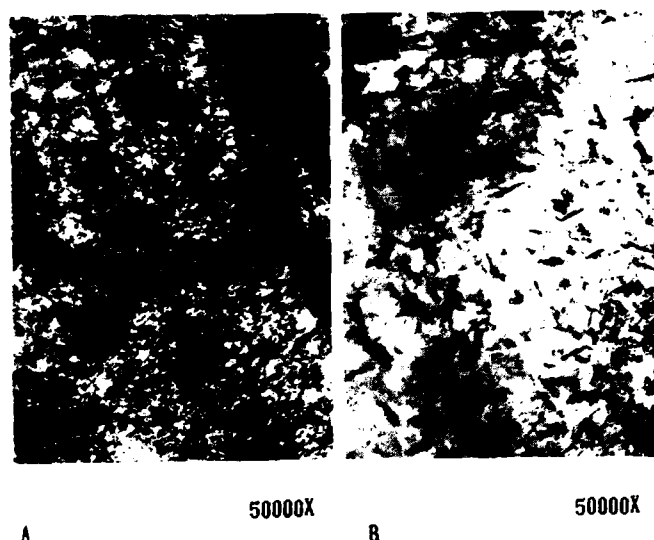


Fig.8 Transmission electron micrographs of as-quenched 20MnB steel  
A. Dislocations and granular carbides  
B. Rod-shaped carbides

above mentioned mechanical properties are typical of full low-carbon martensitic structure.

Microscopic examination of longitudinal section of the central portion of specimens after tensile test has revealed that micro-voids and micro-cracks are found in all 0.5%-2.5% prestrained and aged specimens. (see Fig.7). They are generally perpendicular to or in 45° angle with the axial direction. Their amount as well as dimensions increase with increase of the amount of pre-strain. They are apparently resulted from the process of pre-straining, for no such

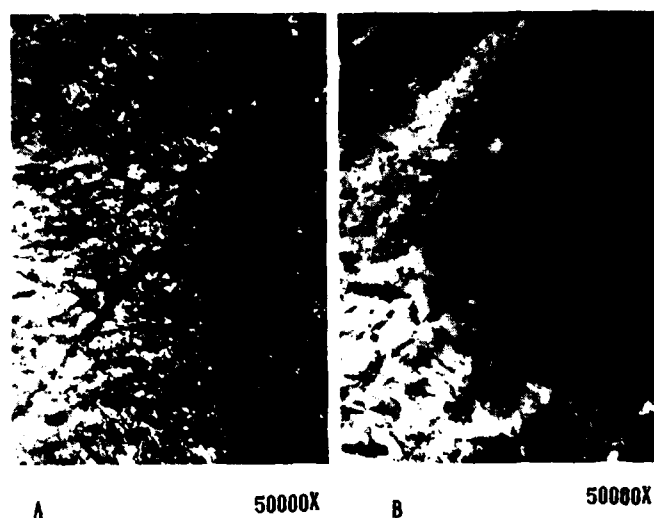
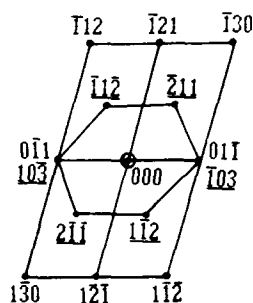
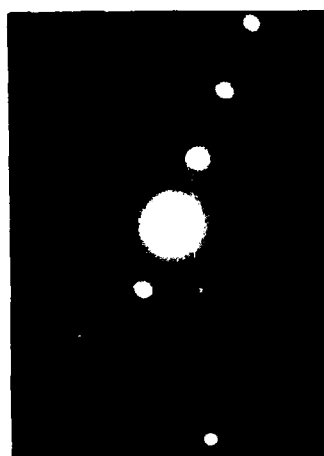
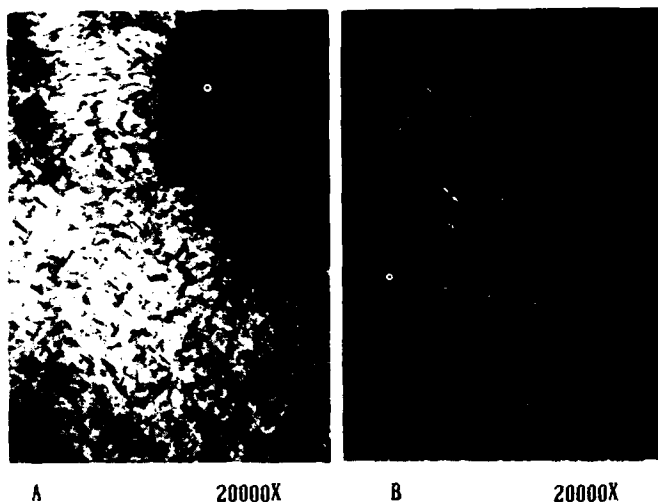


Fig.9 Transmission electron micrographs of 20MnB steel 2% prestrained, aged for 1 h at 150°C  
A. Dislocations and granular carbides  
B. Rod-shaped carbides



D  $M: [311]hkl$   $Fe_3C: [351]hkl$

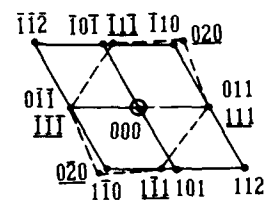
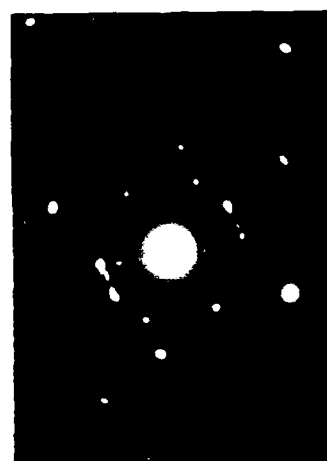
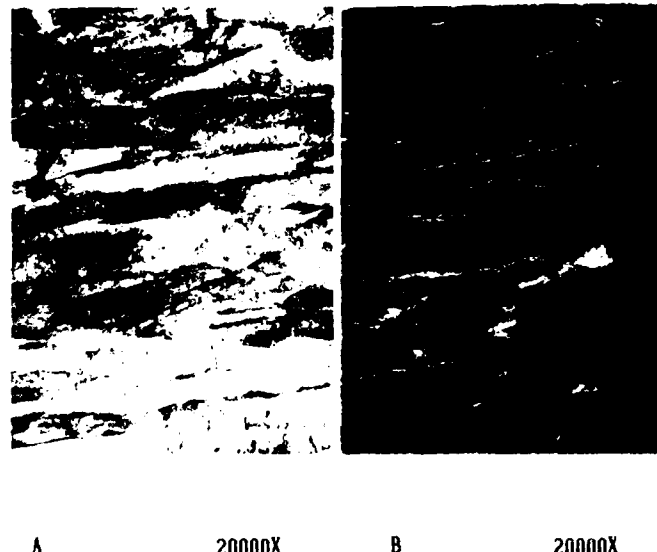
Fig.10 Carbides in 20MnB steel after 0.5% prestraining and aging at 150°C for 1 h.  
A. Bright field. B. Dark field  
C. Diffraction pattern  
D. Analysis of diffraction pattern

micro-voids or micro-cracks were found in non-pre-strained specimens.

TEM observation of thin foils made out of strain-aged specimens of 20MnB and 15MnVB steel has shown that the dislocation density in the laths increases appreciably as compared with the as-quenched specimens, as shown in Fig.8 A and Fig.9 A. This increase in dislocation density is enhanced by increasing pre-strain.

The amount of carbides seems to be also increase after strain-aging, especially dispersed granular carbides precipitated along dislocations, while the dimensions of rod-shaped carbides grow, at least this is true for those aged at 120°C and higher. (see Fig 8B, 9B). Indexing of diffraction pattern has proven that carbides are still  $Fe_3C$  (see Fig.10).

Inter-lath residual austenite films can be universally



D  $M: hkl$   $(011)_A // (111)_A$   
 $A: hkl$   $(111)_A // (101)_A$   
 $(211)_A // (121)_A$

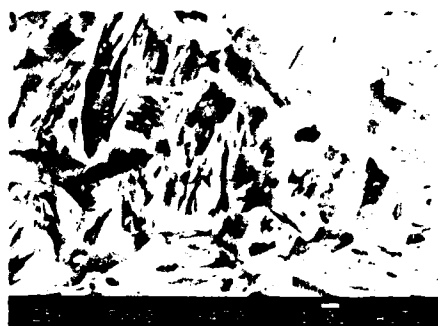
Fig.11 Retained austenite in 15MnVB steel after 2.5% prestraining and aging at 120°C for 1 h.  
A. Bright field. B. Dark field  
C. Diffraction pattern  
D. Analysis of diffraction pattern

observed in all 0.5-2.5% strain-aged specimens (see Fig.11). It is generally considered that the mechanical stability of retained austenite in lath martensite is rather low [10, 11]. But in our experiments, retained austenite can be found without exception even for 2.5% pre-strained specimens.

SEM observations of longitudinal cut strain-aged 20MnB specimens have revealed similar features as optical microscopy. Micro-voids and micro-crack are observed such as

Table 3 The Proportional Distribution of Fracture Area Under Tension for 20MnB Steel (%)

Heat treatment	stable propagation zone	rapid propagation zone	shear-lip zone
as-quenched	37	39.6	23.3
0.5% strain-aged	25	39	36
1% strain-aged	26	44	30
2% strain-aged	26	53	17



A

B

Fig.13 Fracture morphology near the crack origin zone of rotative bending fatigue specimen made of 15MnVB steel

A. Quenched and tempered at 200°C

B. 2% prestrained and aged for 1 h at 150°C

shown in Fig.12. For specimen with 0.5% pre-strain microvoids predominate. With increase in degree of prestrain

micro-cracks increase and grow in length. The longest micro-cracks observed may reach 7μm. Most micro-cracks are located at lath boundaries, they are also found at boundaries of lath packets, original austenitic grains or inclusion interfaces. Besides some micro-cracks pass across lath packets.

Both as-quenched and strain aged 20MnB tensile specimens show cup and cone type of fracture. Cracks initiate at center and mode of fracture for all 4 states are similar, i.e. dimple structure. The difference lies in the proportional distribution of fracture areas. (see Table 3).

Observations of fatigue fractures have revealed that all fatigue cracks are initiated on the surface and striations and secondary cracks are found in crack propagation areas. No secondary cracks are found in the origin zone of as-quenched state specimens. For the 0.5% strain-aged specimens shallow secondary cracks appear when the crack has propagated from the origin to about 20μm, while for the 2% strain-aged ones deep secondary cracks closely join up with the origin (fig.13). This is probably closely connected with the damage caused by pre-straining.

Table 4 The Increment of Flow Stress Induced by Strain-aging

steel	heat treatment	$\sigma_f^{(2)}$ N/mm <sup>2</sup>	$\sigma_{sup}^{(3)}$ N/mm <sup>2</sup>	$\Delta y (\sigma_{sup} - \sigma_f)$ N/mm <sup>2</sup>	$\Delta y / \sigma_f$ %
15MnB	0.2% prestrain, 1 h 120°C	1098	1261 <sup>(1)</sup>	163	14.8
	0.5% prestrain, 1 h 120°C	1274	1530	256	20.1
	2% prestrain, 1 h 120°C	1450	1673	223	15.4
	2% prestrain, 1 h 150°C	1450	1656	206	14.2
20MnB	0.5% prestrain, 1 h 150°C	1350	1587	237	17.6
	2% prestrain, 1 h 150°C	1530	1780	250	16.3
	0.5% prestrain, 1 h 120°C	1240	1447	205	16.5
15MnVB	2% prestrain, 1 h 120°C	1412	1629	217	15.4
	2% prestrain, 1 h 150°C	1412	1658	246	17.4

(1) This value is the proportional limit since there is no upper yield point on 0.2% strain-aging specimen

(2)  $\sigma_f$  --flow stress of as-quenched state at given prestrain

(3)  $\sigma_{sup}$  --upper yield stress of aging state

## DISCUSSIONS

From the data given in Tab.4, it can be seen that the increment of flow stress induced by strain-aging amounts to from 14% to 20%. Such large increment can hardly be attributed to Snoek rearrangement. Micro-structure analysis further shows no coherent  $\epsilon$ -carbide present in strain-aged specimens. Therefore the increment in flow stress can only be attributed to the Cottrell atmosphere of C and N atoms. The appearance of yield plateau and Lüders bands is also an evidence of the action of Cottrell atmosphere.

For pre-strain equal to or larger than 1%, yield extension is absent after aging and local necking initiates immediately after yielding drop. This is mainly caused by the presence of micro-cracks as a result of pre-straining. High stress nearly equal UTS of as-quenched condition promotes the propagation of these cracks which in turn results in the weakening effect overcoming that of strengthening effect in the course of deformation and necking begins. This explains the phenomenon that there is nearly no stage of uniform deformation and the low value of  $\psi_b$  and  $\delta_s$  in the tensile test.

## CONCLUSION

- 1) Strain-aging of low-carbon martensites brings about significant raise in their proportional limit and yield strength as well as fatigue strength, lowering in uniform deformation criterion  $\psi_b$  and  $\delta_s$ , no noticeable change in reduction of area at fracture. For pre-strain around 0.5% after aging there appears upper yield point and yield extension, to-gather with Lüders bands after the yield drop.
- 2) The large increment in strength parameters is mainly attributable to the formation of Cottrell atmosphere during aging which pins the dislocations. Pre-strains can produce potential weakening effect in the form of micro-voids and micro-cracks which gives rise to early local necking after the yield drop and negligible uniform deformation, for prestrain equal or over 1%.
- 3) All strain-aging parameters: amount of pre-strain, temperature and time of aging have effect on the results of strain-aging. Within the scope of our experiments it has been noted that the effect of amount of pre-strain is the strongest while that of aging time is less noticeable.

## REFERENCES

- [1] Zhou Huijiu, Wang Xiaotian, Huang Mingzhi and Lou Qifu, Scientific Journal of Higher Educational Institution, Mechanical Engineering Issue (in Chinese), 2, 109(1964)
- [2] Zhou Huijiu, Li Yongjun and Qi Jingyuan, "Heat Treatment Shanghai '83", P5.111-5.119, Bell. T. The Metals Society, London (1984)
- [3] Baird, J.D, "The Inhomogeneity of Plastic Deformation", P.191, ASM, Metals Park, Ohio (1973).
- [4] Owen, W.S and M.J.Roberts, "Dislocation Dynamics", P.357, Rosenfield, A.R, G.T.Hahn, A.L.Bement and R.I.Jaffee, McGraw-Hill Book Company, New York (1968)
- [5] Chakravartty, J.K, S.L.Wadekar, T.K.Sinha and M.K.Asundi, Journal of Nuclear Materials, 119, 51-58 (1983)
- [6] Busby, C.C, M.F.Hawkes and H.W.Paxton, Trans. ASM, 47, 135-156(1955)
- [7] Stephenson, E.T and M.Cohen, Trans. ASM, 54, 72-83(1961)
- [8] Rashid, M.S, Met. Trans., 6A, 1265-1268(1975)
- [9] Rashid, M.S, Met. Trans., 7A, 497-503(1976)
- [10] Low, N.C, P.R.Howell and D.V.Edmonds, Metal Science, 13, 507-515(1979)
- [11] Ritchie, R.O and R.M.Horn, Met. Trans., 9A, 331-341(1978)

# DEFORMATION AND AGING BEHAVIORS OF LOW ACTIVATION STAINLESS STEEL COMPOSITES

F. D. S. Marquis, M. Hadji, N. AroonKiatkong, R. Bhatnagar

South Dakota School of Mines and Technology  
Department of Metallurgical Engineering  
Rapid City, South Dakota 57701, USA

## ABSTRACT

The microstructural changes which occur during deformation and aging of low activation stainless composites have been studied. Four types of composites with two metal matrices were designed and manufactured: Fe-Mn-Al-C, Fe-Mn-Al-C-Ti, Fe-Mn-Al-C-V and Fe-Mn-Al-C-Ti-V. This paper reports the results obtained mainly on the Fe-Mn-Al-C-V composite, also called LASC3. Deformation and aging processing were developed to produce either a good combination of tensile strength and ductility ( $\sigma_u=115$  ksi,  $E1=50\%$ ) or a high strength with a ductile type of fracture ( $\sigma_u=190$  ksi,  $E1=12\%$ ) after aging up to 500 hours at 593 K. Aging at 893 K led to a significant decrease in strength and ductility due to the formation of the brittle  $\beta_{Mn}$  phase. However aging at 1073 K showed considerable increase in strength and ductility ( $\sigma_u=125$  ksi,  $E1=31\%$ ). The Fe-Mn-Al-C-V composite exhibited superplasticity at 1073 K typically  $E1=180\%$  with a strain rate of  $2 \times 10^{-4}$  sec $^{-1}$ . The highest elongation was observed when the precipitation of very fine grains of ferrite within the laminated austenite matrix was achieved.

THE OBJECTIVES OF THIS WORK are to design, manufacture and evaluate double metal matrices composites with an optimized combination of the following properties: low activation, high resistance to void swelling helium and hydrogen embrittlement, high resistance to dislocation motion, high formability and fracture toughness and high oxidation and corrosion resistance. Special design criteria, which are reported under results, were used in order to optimize each of these properties. The approach was to design a wide range of (1) matrices, (2) reinforcing phases and (3) matrix/reinforcing phases interfaces, by controlled phase transformations. This allowed a methodic investigation of the effect of the nature of

(1), (2) and (3) on the properties described above.

## RADIATION DAMAGE

The response of materials subjected to bombardment by fast neutrons falls within one or two of the following primary types of response: displacements and transmutations. In the first, atoms are displaced from their lattice sites, with the creation of lattice vacancies, lattice interstitials, and pairs of lattice defects. In the second, helium and hydrogen gas is produced in the material by  $(n, \alpha)$  and  $(n, p)$  transmutations. The primary responses cause changes in the physical and mechanical properties of materials which are designated as secondary responses. The first type of primary responses causes swelling, change in resistance and change in conductivity. The second type produces induced radioactivity and composition changes. As a consequence either of the first

Table 1- Structural Materials Response to Fast Neutron Bombardment

<u>Primary Response</u>	<u>Secondary Response</u>
Displacements	Void swelling Change in resistance Change in conductivity  Dimensional changes and instabilities Changes in yield strength Loss of ductility and He/H <sub>2</sub> embrittlement Changes in creep rate Losses in fracture toughness
Transmutations	Reduced radioactivity Changes in composition

and/or the second type of primary response the following secondary responses have also been observed: dimensional instabilities and changes, change in yield strength, loss of ductility and embrittlement, change in the creep rate and losses in fracture toughness. This is presented in Table 1.

Two of the secondary responses have become technologically very critical: void swelling and loss in fracture toughness. Thus it is very important to understand and control the mechanisms by which they develop. In the first one, the interstitials are highly mobile and insoluble in the lattices so that they tend to form loops, leaving an excess of vacancies in the lattice. These vacancies precipitate into three dimensional voids if the temperature is sufficiently high and if there are nucleation sites. These microstructural changes have no macroscopic effects until after a certain dpa threshold level has been reached, after which the material begins to swell. In the second, the hardening of the lattice of the matrix occurs within the grains due to the displacements. This causes deformation to occur along grain boundaries under stress. In these circumstances the collection of helium and/or hydrogen at the grain boundaries aggravates the problem by preventing grain boundary sliding, which would otherwise relieve the stresses. This mechanism produces the nucleation of microcracks which after a threshold value lead to instable fracture.

#### EXPERIMENTAL PROCEDURE

The compositions of the low activation stainless composites in this investigation are presented in Table 2. Figure 1 shows a flow diagram of the sequences of deformation and aging processing carried out in order to achieve the required microstructural design. Table 3 defines the precise nature of each process of deformation and aging. In the interpretation of this table and of the nomenclature presented in this paper, the following code must be used:

C designates a composite microstructure  
LASC = Low activation stainless composite  
ST = Solution treatment  
WQ = Water quenching  
R = Recrystallization  
CW = Cold work  
H = Hours  
M = Minutes  
A = Aging (t=variable up to 1000 hours, T=constant)  
B = Aging or Annealing (t, T=constants)

The first digit equal to 0 means a solution treatment, equal to 1 means that cold work is applied after solution treatment before aging, equal to 2 means that sequential aging is applied after solution treatment before cold working.

The second digit means: 0, no treatment

Table 2 - Compositions of Low Activation Stainless Composites

Composite-> Composition		LASC1 Mn-Al-C	LASC2 Mn-Al-C -Ti	LASC3 Mn-Al-C -V	LASC4 Mn-Al-C -Ti-V
Type1	Mn	27.80	27.14	28.76	28.60
	Al	6.71	6.74	6.60	6.49
	Si	1.30	1.31	1.24	1.25
Type2	Cr	4.74	4.73	4.68	4.58
	Ni	1.30	1.27	1.25	1.28
Type3	Ti	0.04	1.82	0.006	1.75
	V	---	---	0.54	0.57
	Mo	0.089	0.089	0.10	0.10
Type4	C	0.38	0.35	0.37	0.35
	N	0.01	0.01	0.01	0.01
	P	0.019	0.020	0.027	0.024
	B	0.06	0.07	0.06	0.06
Type5	S	0.01	0.01	0.09	0.09
	O	0.001	0.003	0.01	0.01

or terminal aging after solution treatment; 1, first cycle of deformation with 65% cold work; 2, recrystallization after cold work; 3, second cycle of deformation with 55% of cold work.

The third digit designates an investigation of an age hardening behavior with the following meaning: 0, no aging; 1, t=variable T=593 K; 2, t=variable T=693 K; 3, t=variable T=743 K; 4, t=variable T=893 K; 5, t=variable T=993 K; 6, t=variable T=1023 K; 7, t=variable T=1073 K; 8, t=100 hours T=743 K and 9, t=100 hours T=1173 K.

The microstructures were characterized by optical microscopy, scanning electron microscopy (SEM), conventional transmission electron microscopy (CTEM), and scanning transmission analytical electron microscopy (STAEM), (24). X-ray diffractometry, selected area diffraction (SAD), microdiffraction (MD), and magnetic measurements were used to identify, characterize, and measure the amounts of the phases formed during each process of deformation and aging. Precipitate extraction methods were applied on grip portions of the tensile specimens which were immersed in a 10% solution of bromide in methanol, initially for 24 hours. The residues were then collected and prepared for X-ray diffraction analysis. Mechanical properties were measured using a Vickers diamond pyramid hardness tester, a Knoop microhardness indenter, and an MTS mechanical testing machine. The yield strength  $\sigma_y$ , tensile strength  $\sigma_u$  and elongation at fracture, % El, were measured in the temperature range, 293 K to 1073 K, and in the strain rate range,  $10^{-5}$  to  $10^{-3}$  sec $^{-1}$ .

#### RESULTS AND DISCUSSION

Both theoretical and experimental results,



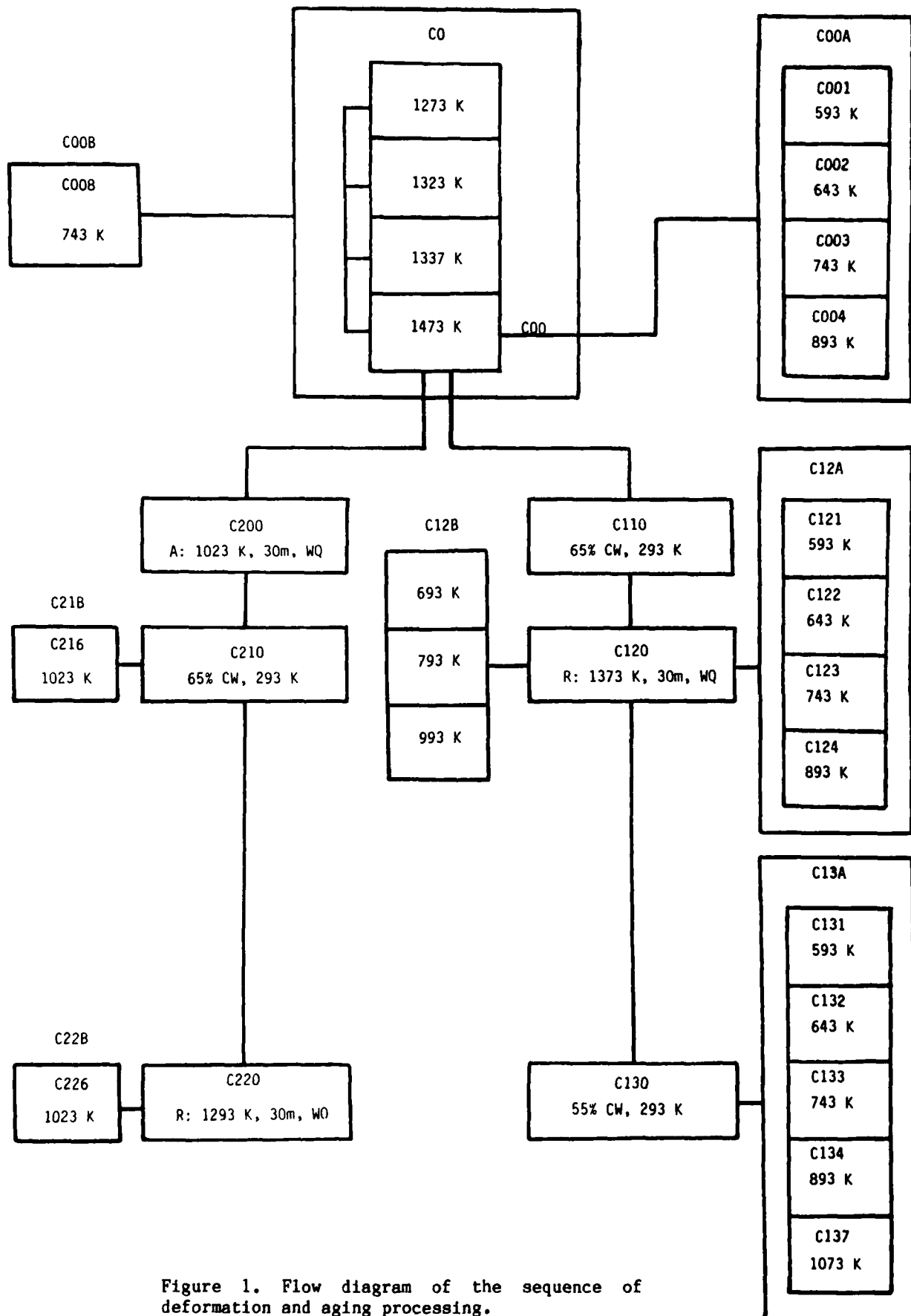


Figure 1. Flow diagram of the sequence of deformation and aging processing.

Table 3 - Deformation and Aging Processing

Proc. No.	Nature of Process
CO	ST: 1423 K or 1373 K or 1323 K or 1273 K, 30M, WQ.
COO	ST: 1423 K, 30M, WQ.
COOA	Aging hardening of COO, t=variable, T= constant.
COOB	Aging of COO, t, T=constants.
C110	65% CW at 392K of COO.
C120	Recrystallization of C110: 1173 K, 30 M WQ.
C12A	Age hardening of C120.
C130	55% CW OF C12.
C13A	Aging hardening of C130.
C200	Sequential aging of COO.
C210	65% CW at 293 K of C210.
C21B	Annealing for superplasticity of C210
C220	Recrystallization of C210: 1293 K, 30M, WQ.
C22B	Annealing for superplasticity of C220

which are part of those obtained in this research program are presented and discussed below:

#### DESIGN OF STAINLESS COMPOSITES

The methods used for the production of composite materials may be grouped in two main categories: The first category includes those methods in which two basic operations are involved: the fabrication of the strengthening phase (fibers or laminae) and the subsequent insertion into a single matrix. The second category includes those methods in which the strengthening phase is produced directly in the matrix in a single operation or in a sequence of operations. Each of these categories has its advantages and disadvantages.

The first category offers very good control of the nature of the matrix, the nature of the strengthening phase and of the volume fraction of each phase. However, the control of the nature of the matrix/strengthening phases interfaces and the nature of the interface phases that may be produced during manufacturing of the composite, is difficult. As a consequence, problems such as poor formability and poor fracture toughness are inherited.

The second category offers very good control of the nature of the matrix/strengthening phase interfaces (which in many cases can be developed as coherent or semicoherent), and of the nature of the interface phases. However, it has serious limitations on: the range of matrices and strengthening phases that can be designed and manufactured and on the range of their volume fractions.

The work reported here addresses the design, manufacture and testing of composites with two

metal matrices starting from duplex, austenite-ferrite microstructures, with an exceptional strong bonding between the two phases. This allows the two matrices to be plastically deformed up to very high levels of plastic strain by rolling, extrusion and wire drawing, at room and elevated temperatures without debonding or failure of the interfaces. This new manufacturing technology has the highest potential for the development of fibrous and laminate double metal matrices composites with very good strength, formability, and fracture toughness. The microstructural design started with materials which were casted and processed to control volume fractions of two matrices: austenite and ferrite with very strong and ductile interfaces. The morphology of the composite was designed through the control of the initial volume fractions of the two matrices, the nature of the deformation process (rolling and wire drawing), its temperature, the amounts of strains involved in each cycle and intermediate thermomechanical treatments. Two morphologies were designed: fibrous and laminated. The strength, formability and fracture toughness of these composites were controlled mainly by: athermal, deformation-induced and isothermal transformations designed within each of the two original matrices; the nature of the interfaces; and the nature of the interface phases.

#### DESIGN FOR LOW ACTIVATION AND VOID SWELLING RESISTANCE

It appears to be possible to simplify the storage of radioactive reactor components by developing materials, with reduced levels of long living transmutations, in which the induced radioactivity decays in a reasonable time to such a level that the waste no longer requires maintenance. The most serious safety and environmental concerns for fusion reactors involve induced-radioactivity in the first-wall and in the blanket structure. Different elements exhibit different nuclear behavior when bombarded by neutrons, resulting in a variety of activation products, activation levels, and decay times. Obviously these factors depend on the neutron flux and spectrum, and on the exposure time. However, one can conclude that the selection of materials can produce significant differences in the activation levels and decay times after exposure. This work used the guidelines for the classification and disposal of low level nuclear wastes that have been established by the U.S. Nuclear Regulatory Commission (2). On the basis of these guidelines, initial concentration limits were calculated for various common alloying elements.

Previous work (3) showed that concentrations of Ni, Mo and N must be severely restricted in steels considered for nuclear applications. Based on these considerations, nuclear resistance input was obtained to the present

chemical design. Initial concentration limits were calculated for various common alloying elements, ten years after the shutdown of a reactor, for the three waste classes for first-wall and blanket structures, given 9MW/year/m<sup>2</sup> exposure (4).

The limiting values were those for a given element when no other restricted element was present in the alloy. The "sum of fractions" rule applied if other restricted elements were present. In this case the concentrations of each restricted element were divided by its allowable concentration and the fractions thus obtained for all restricted elements were added. The sum of these fractions was less than unity.

Thus in the chemical design of these composites, four major considerations were taken into account: (1) partial substitution of Cr by Al and Si, and Ni by Mn (2) elevated temperature strength and microstructural stabilization (3) prevention of void swelling helium and hydrogen embrittlement and (4) low activation.

The substitution of Cr by Al and Si, in stainless steels has been the subject of various investigations (5 to 11). These results indicate that the oxidation and corrosion resistance would be comparable to conventional grades of stainless steels: 304, 316 and PCA. However, virtually no data is available concerning their elevated temperature deformation and aging behaviors. Thus, in order to obtain the formation of a passive oxide film and insure an effective corrosion resistance, the Al, Si and Cr contents were kept at 6.7, 1.3 and 4.7 wt% respectively. The analysis of the work reported in (12) shows that Mn has a much lower activation than Ni and Mo. This makes it a much better candidate as an austenite stabilizer in the design of low activation stainless composites. However, recent studies have shown that in Mn-Cr austenitic steels, the void formation responsible for swelling tended to be suppressed in steels with a small amount of Ni (13). Thus, the Mn content was adjusted in order that  $M_s$  is below room temperature and  $M_f$  is above 77 K, and kept at 28 wt%. In order to simultaneously decrease the amount of void swelling, but insure a low level of radioactivity, the Ni content was kept at 1.3 wt%.

In order to increase the elevated temperature strength and thermally stabilize the austenite, small additions of Mo and N were kept around 0.1 and 0.01 wt% respectively. In order to increase the creep strength and the strength of the boundaries, 60 ppm of boron were added (14).

Two strong carbide formers, Ti and V, were added in order to produce very fine dispersions of intragranular MC carbides which were designed as: elevated and high temperature strengtheners and as traps for He and H bubbles, thus preventing them to cluster at grain boundaries. For the same second purpose, P was introduced at a level of 0.02 wt% in order to produce a very

fine dispersion of phosphides. One of the major ideas in this design concept is the creation of multiple stable interfaces, which are expected to act as sink for vacancies, thus reducing the void formation, and consequently reduce the void swelling.



Figure 2. Typical LASC3 microstructure showing the austenite and ferrite matrices in the solution treated condition.

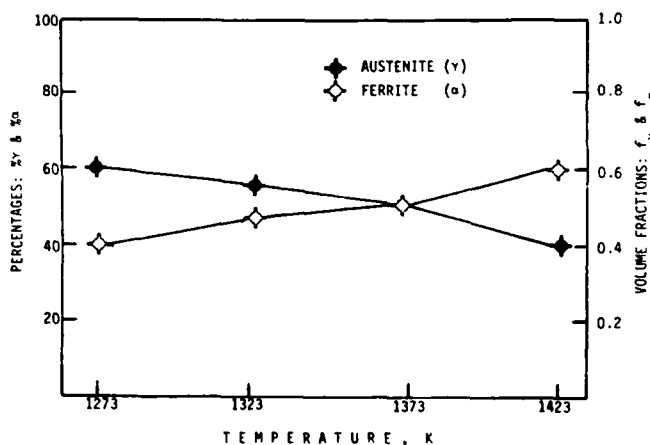


Figure 3. Effect of solution treatment temperature on the volume fraction of each matrix.

#### DESIGN FOR HELIUM EMBRITTLEMENT RESISTANCE

Recently, significant studies have been carried out in order to minimize He and H<sub>2</sub> embrittlement in stainless steels of the type 304, 316 and PCA (4, 14 to 19). Preliminary results show that this problem may be avoided on low activation stainless composites by the creation of multiphase-interfaces and very fine dispersions of stable intra-granular MC carbides and phosphides (14, 19, 20, 24). It appears that these very fine dispersions do act as traps for He and H<sub>2</sub> bubbles and permit them to cluster at grain boundaries. Although the dispersion/matrix interface appears to play a significant part, virtually no information is available on

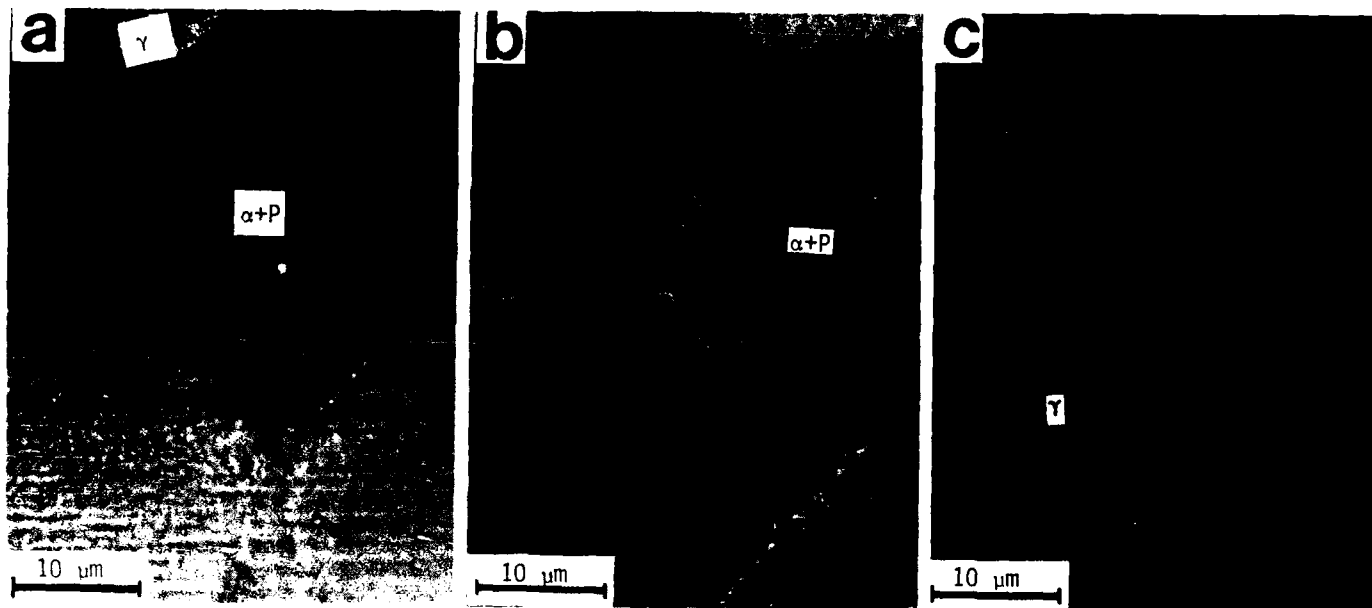


Figure 4. Effect of prior aging temperature on the COOB microstructures: a) 1323 K; b) 1373 K; c) 1423 K.

the mechanisms by which this trapping may occur.

#### OPTIMIZATION OF SOLUTION TREATMENTS

Figure 2 is a typical microstructure of the Mn-Al-C-V composite (LASC3) after casting and thermomechanical processing, solution treated at 1423 K for 30 minutes and water quenching, i.e. COO. It shows a microstructure consisting of two metallic matrices: the austenite,  $\gamma$  (dark areas) and the ferrite,  $\alpha$  (light areas). In the design of these composites microstructures consisting of two metallic matrices, three sets of manufacturing variables become very important: the volume fraction of each matrix:  $f_\gamma$  and  $f_\alpha$ , the solute concentration of each matrix  $C_\gamma$  and  $C_\alpha$  and the grain size of each matrix  $d_\gamma$  and  $d_\alpha$ .

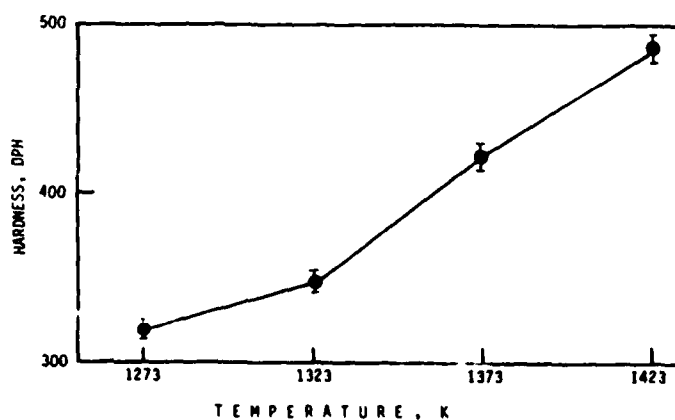


Figure 5. Effect of solution treatment temperature on the hardness of CO microstructures aged at  $T=743$  K and  $t=100$  hours.

These three sets of manufacturing variables are controlled by the solution treatment, i.e. the temperature, the time and the quenching rate. During further microstructural development they are controlled by the deformation, aging, transformation (athermal and deformation induced) and recrystallization processing. Figure 3 shows the effect of the solution treatment temperature (STT), for a constant solution treatment time (STt) of 30 minutes, on the volume fraction of each matrix. Thus we can adjust the volume fraction of ferrite from just below 0.4 to just above 0.6 by varying STT between 1273 K and 1423 K. As previously

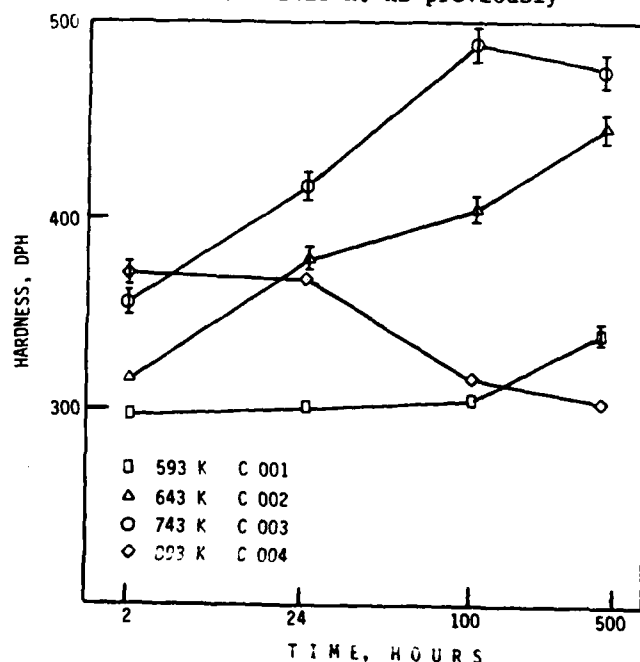


Figure 6. Age hardening behavior of COO matrices.

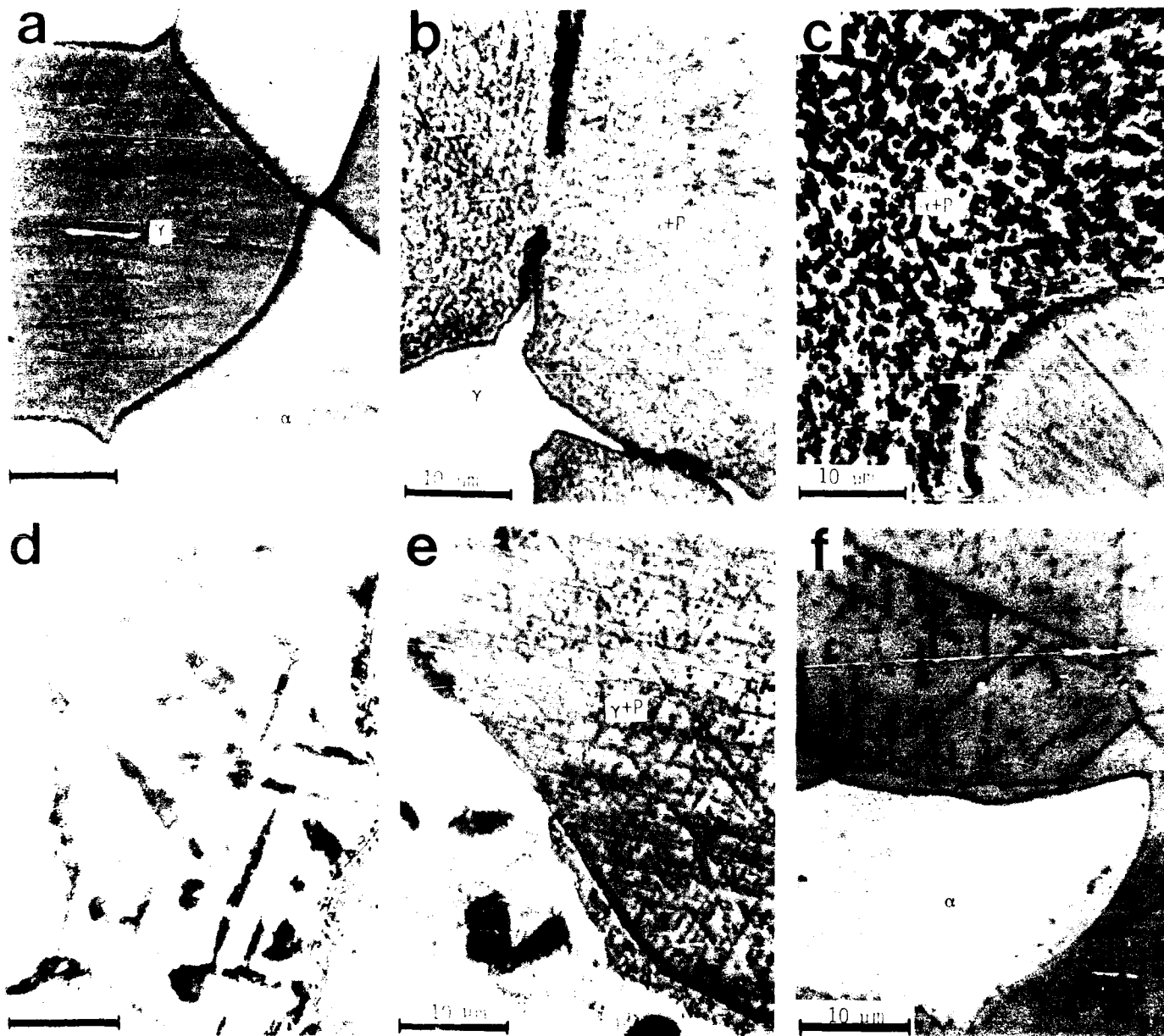


Figure 7. Effect of prior aging temperature ( $t=100$  hours) on the microstructural developments of C00A composites: a) 593 K; b) 693 K; c) 793 K; d) 893 K; e) 993 K; f) 1173 K.

reported the solubility of each of the solute elements in these composites, both in  $\alpha$  and in  $\gamma$  increases very significantly with STT. A preliminary investigation of the aging response of this composite, consisting of two matrices, was carried out by aging the solution treated microstructures (box 20 in figure 1) at 743 K for 100 hours. The resultant microstructures (STTB) are shown in figure 4 and the age hardening behavior is shown in figure 5. A considerable increase in hardness ( $\sim 200$  DPH) is obtained on the aged microstructure when STT is increased from 1273 K to 1423 K. This is explained mainly by the dispersions of fine precipitates occurring in ferrite (figure 4a and

4b), which is possible due to the original high temperature, higher solubility, in the ferrite matrix. It is important to notice that these microstructures are thermally quite stable. The microstructure shown in figure 4c shows that low energy interfaces are beginning to predominate at 1423 K, instead of curved high energy interfaces shown at 1323 K. Thus the C00 solution treatment was selected to carry out future composite microstructural development.

#### AGING BEHAVIOR OF MATRICES

The degree of supersaturation developed in the ferrite matrix by water quenching from 1423 K

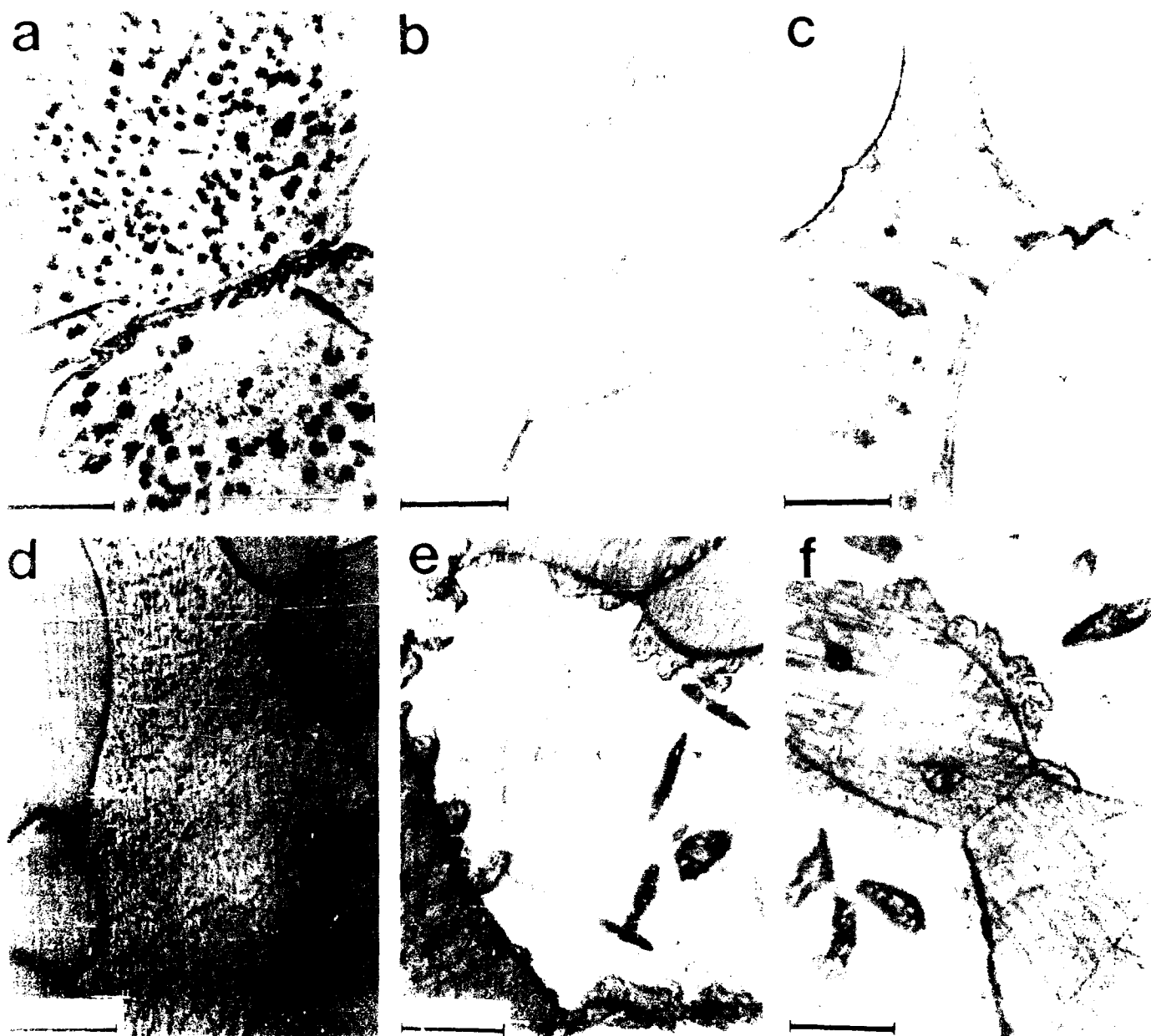


FIGURE 1. Ultrastructural development of the developing eye of the larva of the parasitic wasp, *Microgaster* sp. (Hymenoptera: Braconidae). (a) 1st stage, (b) 2nd stage, (c) 3rd stage, (d) 4th stage, (e) 5th stage, (f) 6th stage.

the developing eye of the larva of the parasitic wasp, *Microgaster* sp. (Hymenoptera: Braconidae). The eye is composed of several layers of cells, including the cornea, the crystalline cone, the photoreceptor layer, and the pigment layer. The photoreceptor layer is the most prominent feature of the eye, and it is composed of several layers of cells, including the outer segment, the inner segment, and the cell body. The outer segment is the part of the photoreceptor that is exposed to the light, and it is composed of several layers of cells, including the outer segment, the inner segment, and the cell body.

The inner segment is the part of the photoreceptor that is located between the outer segment and the cell body. It is composed of several layers of cells, including the inner segment, the cell body, and the pigment layer. The cell body is the part of the photoreceptor that is located between the inner segment and the pigment layer. It is composed of several layers of cells, including the cell body, the pigment layer, and the pigment layer. The pigment layer is the part of the photoreceptor that is located between the cell body and the pigment layer. It is composed of several layers of cells, including the pigment layer, the pigment layer, and the pigment layer. The pigment layer is the part of the photoreceptor that is located between the cell body and the pigment layer. It is composed of several layers of cells, including the pigment layer, the pigment layer, and the pigment layer.

consequent precipitation hardening effect. The maximum precipitation hardening effect was observed at 743 K for an aging time of 100 hours. This is explained by the intertwining of various dispersions of fine precipitates. The metallographic data presented in figures 6 and 7 and X-ray diffraction analysis data of overaged conditions is consistent with the existence of the dispersions of the following carbides VC,  $Mn_5C_4$ ,  $Fe_{0.2}Mn_{5.4}C_2$  and  $(FeMn)_3AlC$ . Aging between 893 K and 993 K leads to early overaging which is explained by the heterogeneous precipitation of the  $\beta_{Mn}$  phase. The sequence of phase transformations which occur during aging at 893 K is presented in figures 8a (1 hour), 8b (2 hours), 8c (6 hours) and 7d (100 hours) which show: 8a, well developed precipitates within the ferrite and the beginning of  $\beta_{Mn}$  precipitation at the  $\alpha/\alpha$  interfaces; 8b, well developed  $\beta_{Mn}$  precipitates at the  $\alpha/\alpha$  interfaces; 8c, formation of  $\beta_{Mn}$  at the  $\gamma/\alpha$  interface, side; 7d, intertwining of various dispersions of precipitates in ferrite and grain boundaries.

The sequence of phase transformation which occurs during aging at 993 K is presented in figures 8d (10 minutes), 8e (2 hours), 8f (5 hours) and 7e (100 hours), which show: 8d, fine precipitation of VC within the ferrite; 8e, coarsening of the precipitates within the ferrite and formation of  $\beta_{Mn}$  phase at the  $\gamma/\alpha$  interfaces; 8f, precipitation of fine fibrous Mn carbides within the austenite; 7e, beginning of precipitation of Mn carbides (light areas) within the ferrite and full development of the fibrous strengthening phase of the austenite. In the temperature range 1023 K to 1173 K the  $(FeMn)_3AlC$  carbide precipitation mainly at the interfaces, as shown in figure 8f. In this temperature range no  $\beta_{Mn}$  phase was observed to occur.

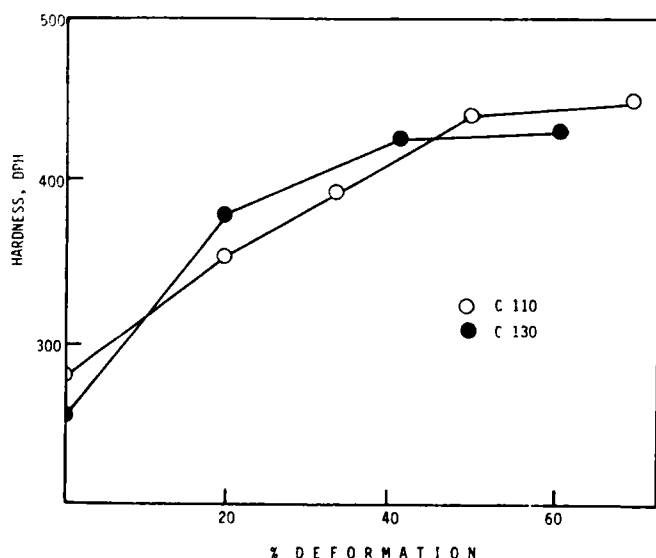


Figure 9. Strain hardening behavior during the production of laminate composites.

## PRODUCTION OF LAMINATED COMPOSITES

Figure 9 shows the strain hardening behavior during the production of laminate composites in the first cycle of deformation (C110 microstructures) and in the second cycle of deformation (C130 microstructures). Typical laminate microstructures developed during the first cycle are presented in figure 10a. Figure 14 a and b present typical laminate microstructures developed during the second cycle. It was observed that at this deformation temperature the austenite deformed by the formation of deformation twins either before and or after recrystallization. This was possible for following reasons: first Mn lowered considerably the stacking fault energy of the composite (11), second the calculated  $M_d$  temperature was below room temperature.

## AGE HARDENING OF RECRYSTALLIZED LAMINATES

As shown in figure 1 the recrystallization of the C110 microstructures (figure 10a) produced the C120 microstructures (figure 10b). The aging of C120 microstructures produced the C12A microstructures shown in figure 10: (c), (d), (e) and (f) developed during 100 hours of aging at 593 K, 643 K, 743 K and 893 K respectively. The details presented in figure 10 are: a) the laminated matrices  $\gamma$  and  $\alpha$  are strengthened by transformation and deformation hardening respectively; b) recrystallization of each matrix; c) no significant precipitation strengthening in  $\alpha$  or in  $\gamma$  matrices; d) initial stages of very fine precipitation in the matrix with the formation of PFZ in the  $\alpha$  adjacent to the  $\alpha/\gamma$  interfaces; e) development of uniformly distributed precipitates in  $\alpha$  only; f) beginning of the precipitation of  $\beta_{Mn}$  in the  $\gamma/\alpha$  interface. Specimens aged at 743 K develops

Table 4 - Room Temperature Mechanical Behavior of LASC3 (ksi,  $n = 2 \times 10^{-3} \text{ sec}^{-1}$ ).

MICRO	MECH. PROP.	AGING TIME, HOURS			
		2	24	100	500
C 122 T=643 K	$\sigma_u$	107	---	100	---
	$\sigma_y$	75	---	81	---
	% El	42	---	14	---
C 132 T=643 K	$\sigma_u$	190	186	200	---
	$\sigma_y$	170	171	188	---
	% El	18	10	7	---
C 123 T=743 K	$\sigma_u$	112	---	96	90
	$\sigma_y$	80	---	82	84
	% El	31	---	8	7
C 133 T=743 K	$\sigma_u$	192	---	155	145
	$\sigma_y$	175	---	131	134
	% El	12	---	9	5

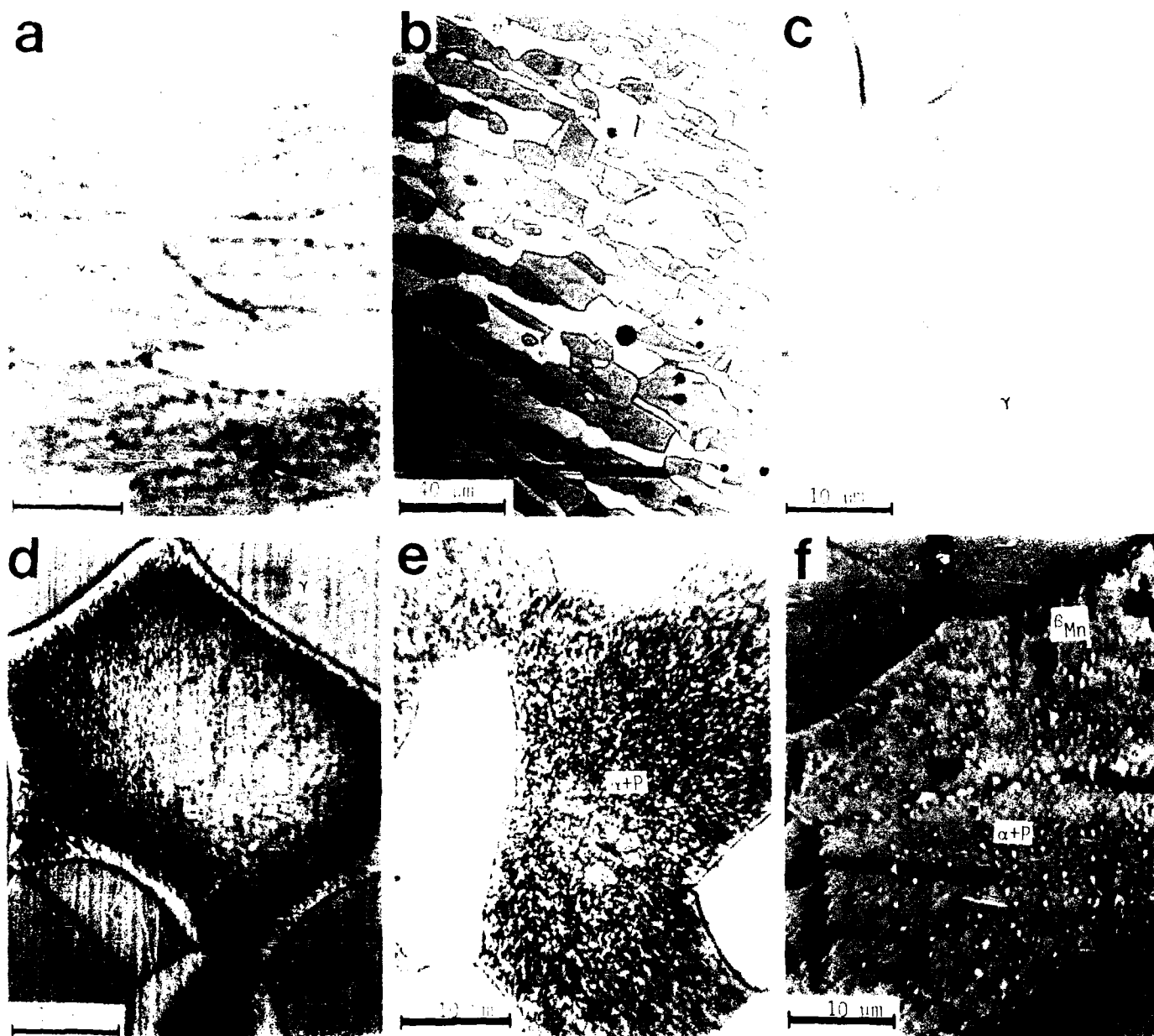


Figure 10. Age hardening of recrystallized laminates: a) C110 laminate; b) C120 recrystallized laminate aged for 100 hours at: c) 593 K; d) 643 K; e) 743 K and f) 893 K.

precipitate free zone (PFZ), where the precipitation of the  $\beta$  phase appears to be associated with the formation of the PFZ shown in figure 10d.

The age hardening behavior of C120 microstructure is presented in figures 11 and 12. Figure 11 shows the effect of the aging temperature on the hardness for a constant aging time of 100 hours. Figures 12 and 13 show the effect of aging temperature and aging time on the strength of the laminates.

As temperature of combination of strength and ductility was achieved after aging up to 500 hours at 743 K as shown in figure 13. However, no significant decrease in strength was observed after aging up to 500 hours at 893 K. This small

decrease in strength and ductility appears to be associated with the formation of the  $\beta$  phase.

#### AGE HARDENING OF DOUBLE LAMINATES

The age hardening response of C130 laminates is shown in figures 9, 12, 13 and 15. Typical C13A microstructures are presented in figure 14, showing: a) C130 microstructure showing strengthening of the  $\alpha$  and  $\beta$  matrices by transformation and deformation hardening; b) C131 beginning of heterogeneous precipitation; c) C132 very fine precipitation in ferrite with formation of precipitate free zones (PFZ); d)



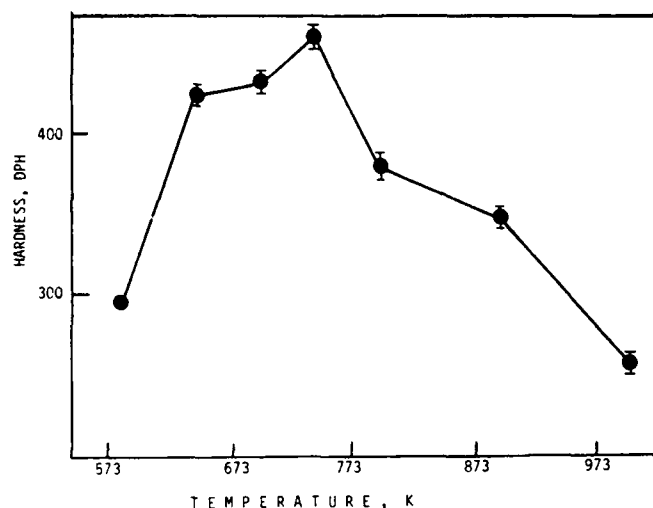


Figure 11. Effect of aging temperature on the hardening behavior of C120 composites,  $t=100$  hours.

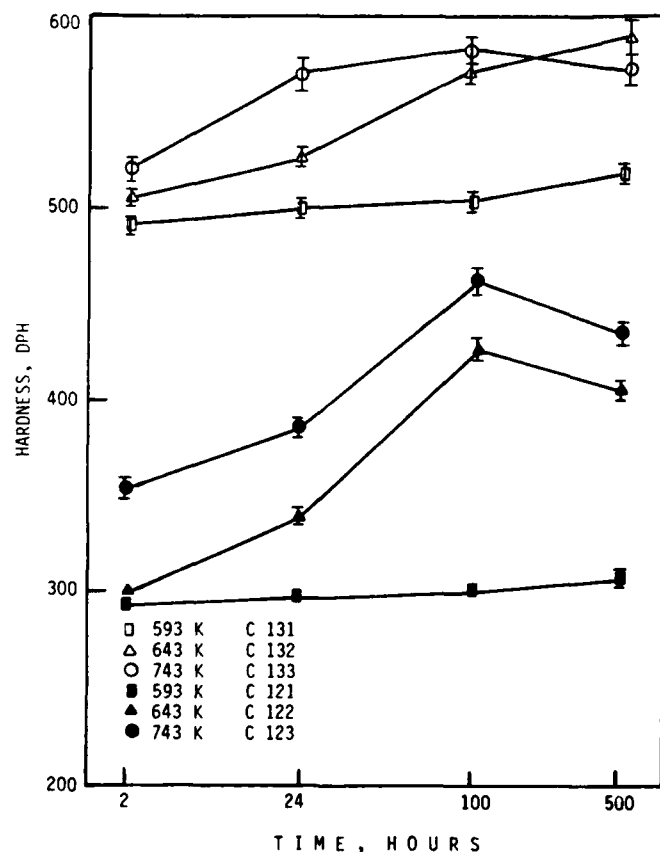


Figure 12. Effect of prior aging time and temperature on the hardening behavior of C121 and C131 laminate composites.

C133 significant homogeneous and heterogeneous precipitation in the deformation twins within the austenite matrix and in slip bands in within the ferrite matrix; e) coarsening of precipitates in ferrite and at grain boundaries; f) precipitation of secondary equiaxed ferrite within the austenite.

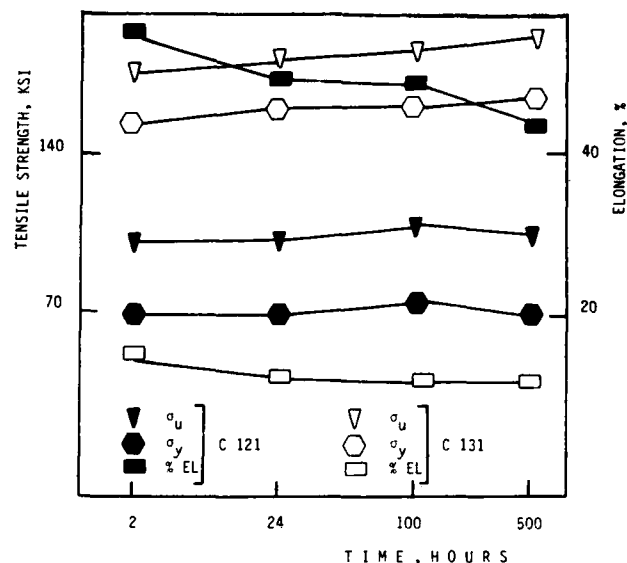


Figure 13. Effect of prior aging time and temperature on the mechanical properties of C121 and C131 laminate composites.

As shown aging at 593 K produced very high strength and good ductility. Typical microstructures are shown in figures 14b and 18b. Aging at 643 K leads to precipitation within the ferrite matrix: VC, AlCr and FeMn<sub>4</sub>. At 743 K the precipitation starts taking place in the austenite matrix and at 893 K coarsening is observed, and  $\beta_{Mn}$  nucleates at interfaces. The sharp decrease in strength and ductility observed at 893 K (figure 15) is attributed to the formation of the  $\beta_{Mn}$  phase.

No  $\beta_{Mn}$  or sigma phases were observed on aging at 1073 K or above up to 100 hours. This is explained by the higher solubility of Mn in the austenite matrix at elevated and high temperatures. An extraordinary increase simultaneously in ductility and strength was observed above 893 K. At 1073 K typical values obtained were  $\sigma_u=125$  ksi,  $EL=31\%$ , for aging

Table 5 - Room Temperature Mechanical Behavior of LASC3 (ksi,  $\dot{\epsilon} = 2 \times 10^{-3} \text{ sec}^{-1}$ )

MICRO	MECH. PROP.	AGING TEMP., T=1023 K	
		AGING TIME, HOURS	
		24	100
C 215	$\sigma_u$	103	99
	$\sigma_y$	70	68
	% EL	38	36
C 225	$\sigma_u$	101	100
	$\sigma_y$	67	65
	% EL	40	37

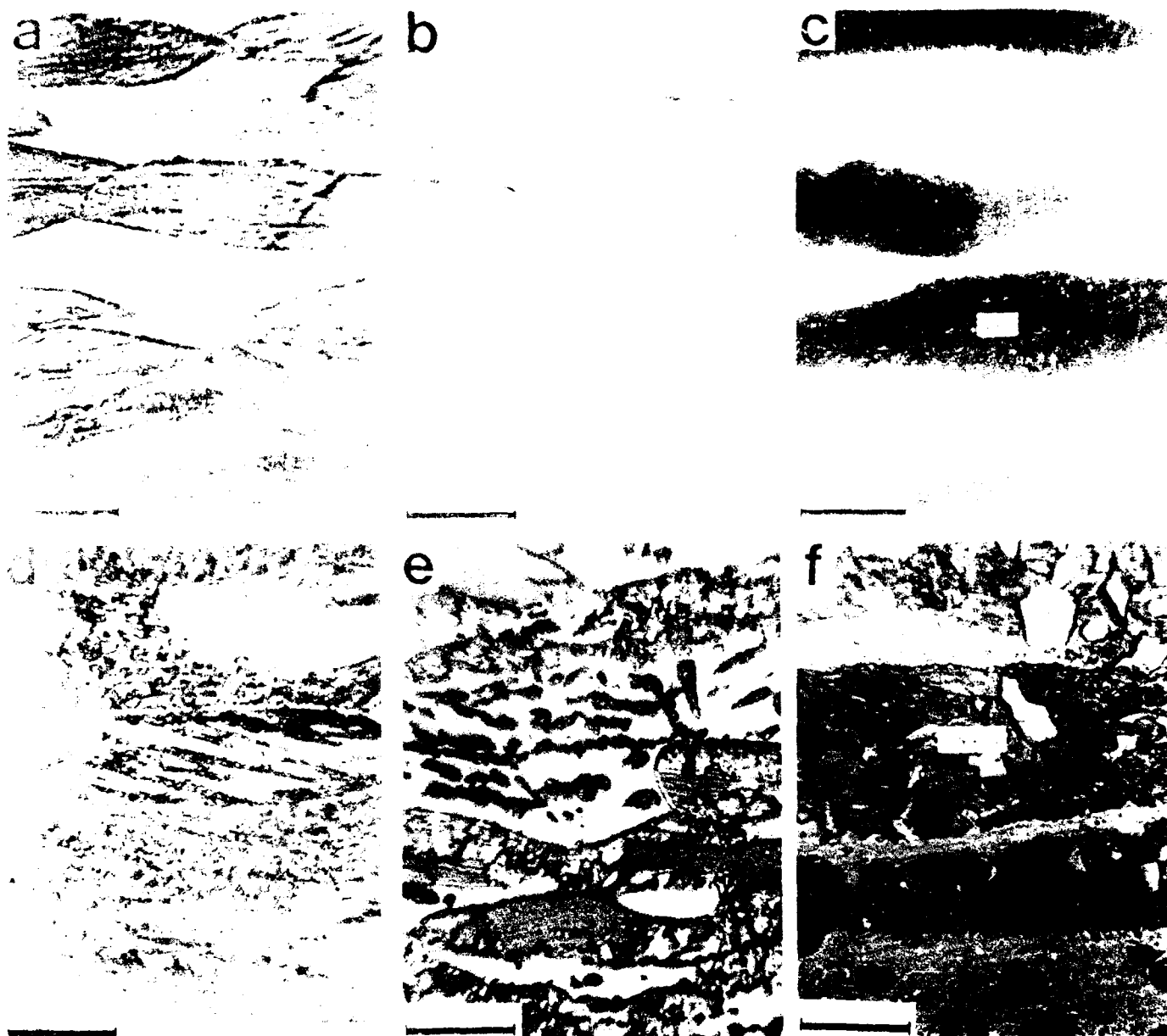


Fig. 1. Photomicrographs of the sandstone showing the microstructure of well-sorted laminated sandstone. (a) and (b) show primary bedding structures. (c) shows a secondary structure with a small white box. (d) and (e) show more complex bedding with some dark, possibly cemented, areas. (f) shows a highly deformed area with a small white box.

The sandstone is a well-sorted, medium-grained, quartzitic sandstone. The grains are generally rounded to subangular, and the matrix is composed of fine-grained sand and silt. The sandstone is laminated, with the primary bedding planes generally parallel to the horizontal. The sandstone is well-sorted, with the grains generally rounded to subangular, and the matrix is composed of fine-grained sand and silt.

The sandstone is a well-sorted, medium-grained, quartzitic sandstone. The grains are generally rounded to subangular, and the matrix is composed of fine-grained sand and silt. The sandstone is laminated, with the primary bedding planes generally parallel to the horizontal. The sandstone is well-sorted, with the grains generally rounded to subangular, and the matrix is composed of fine-grained sand and silt.

The sandstone is a well-sorted, medium-grained, quartzitic sandstone. The grains are generally rounded to subangular, and the matrix is composed of fine-grained sand and silt. The sandstone is laminated, with the primary bedding planes generally parallel to the horizontal. The sandstone is well-sorted, with the grains generally rounded to subangular, and the matrix is composed of fine-grained sand and silt.

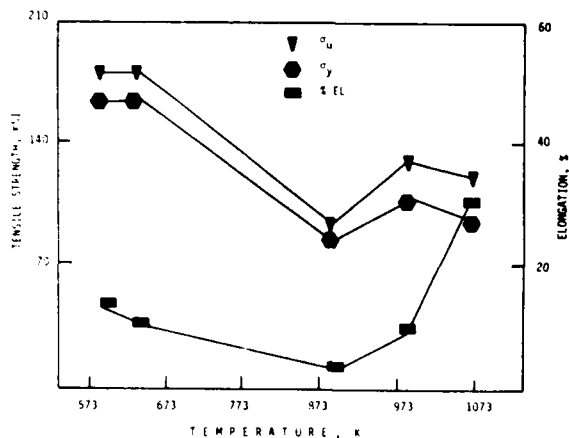


Figure 15. Effect of prior aging temperature ( $t=24$  H) on the room temperature mechanical properties of C13A composites.

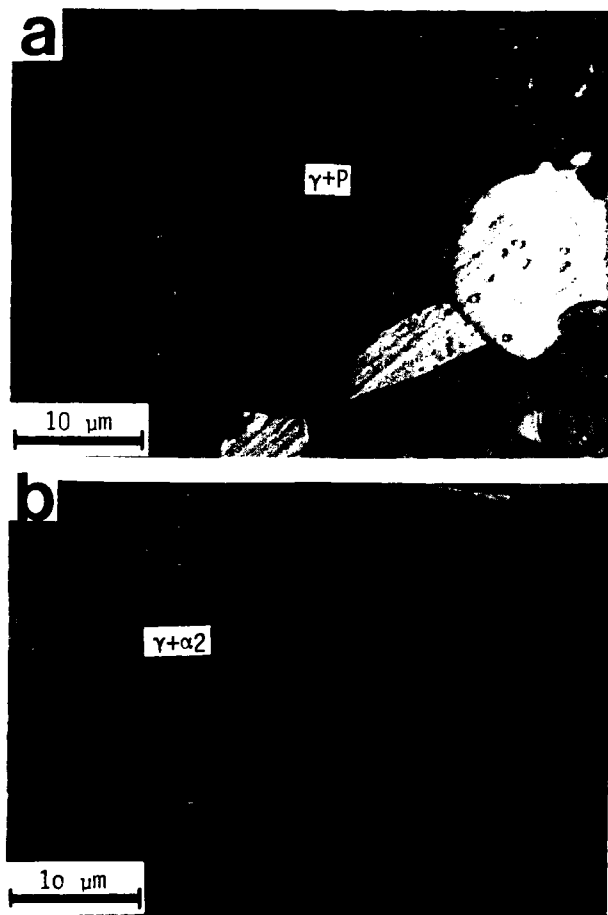


Figure 16. Thermal stability of C22B and C21B composites aged at 1023 K for 100 hours.

hours. The mechanical behaviour is shown in figure 17 and table 5.

#### COMPOSITE MORPHOLOGIES

Figure 16a and 16b compare the C226 and C216 morphologies developed during the lamination of aged matrices. They show the development of

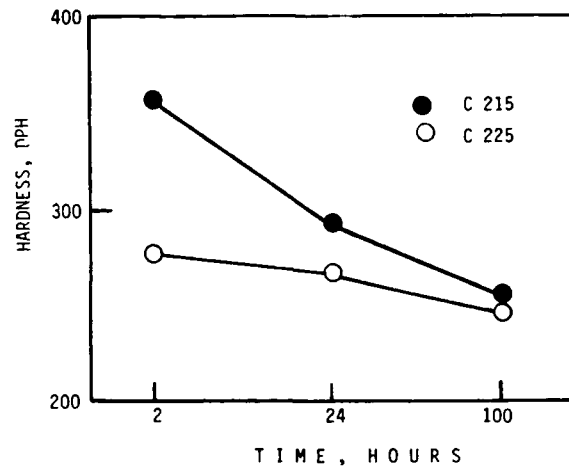


Figure 17. Effect of prior annealing time on the high temperature annealing behavior of C215 and C225 composites.

superplasticity in C216 due to the production of secondary ferrite in laminated austenite. Figure 18 compares the morphologies developed by single and double lamination of solution treated and single lamination of aged matrices. It shows: a) C121 aging of partial spheroidized laminated matrices; b) C131 aging of double laminated matrices; c) tri-dimensional representation of b); d) C216 precipitation strengthening of ferrite and austenite matrices during annealing for superplasticity for 30 minutes at 1023 K.

#### ELEVATED AND HIGH TEMPERATURE MECHANICAL BEHAVIOR

In addition to 293 K two other temperatures were selected for tensile testing. The first 593 K was above 0.3 of the melting point ( $T_m$ ) and was selected for the elevated temperature behaviour. The second 1073 K, was just above 0.6  $T_m$ , was selected for the high temperature behaviour. Figure 15 and Table 6 show that LASC3: C121, C131, C215 and C225 exhibited very good microstructural stability with no brittle phases precipitating during aging up to 500 hours.

C22B and C21B microstructures were tested at 1073 K with a strain rate of  $2 \times 10^{-4} \text{ sec}^{-1}$ . The C21B exhibited an elongation of 180 %. This is explained by the formation of very fine grains of ferrite inside the austenite as shown in figure 16b, which was not present in the C22B microstructure. C121 and C131 specimens were also tested at 593 K with a strain rate of  $2 \times 10^{-3} \text{ sec}^{-1}$ . Both specimens did show a decrease of strength when tested at 593 K. However the drop in strength from 293 K to 593 K, was very small, 25 ksi max, both C121 and for C131. Table 6 presents results of tensile properties tested at 593 K and 1073 K.

These results represent a considerable improvement on the best duplex alloys which exhibit superplasticity under certain microstructural and deformation conditions: ultra fine grained stable duplex equiaxed

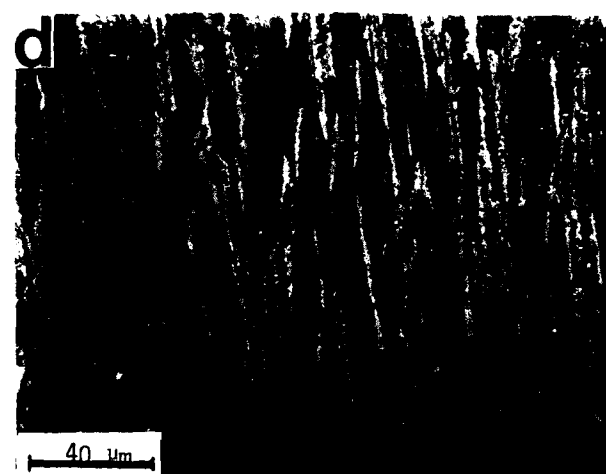
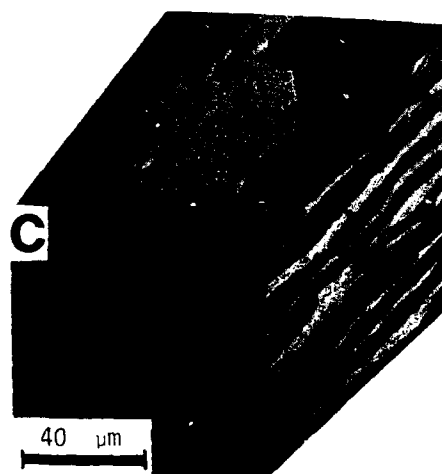
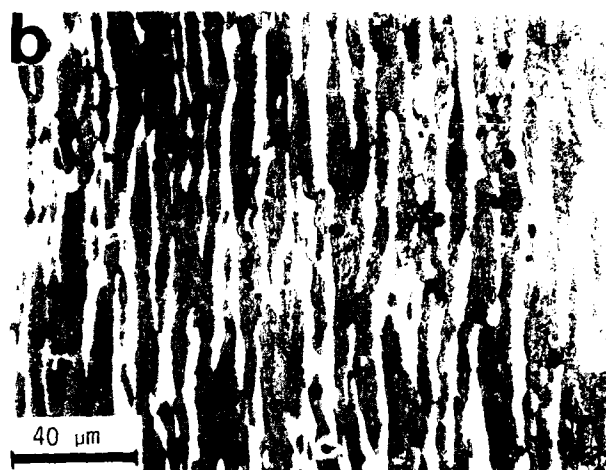
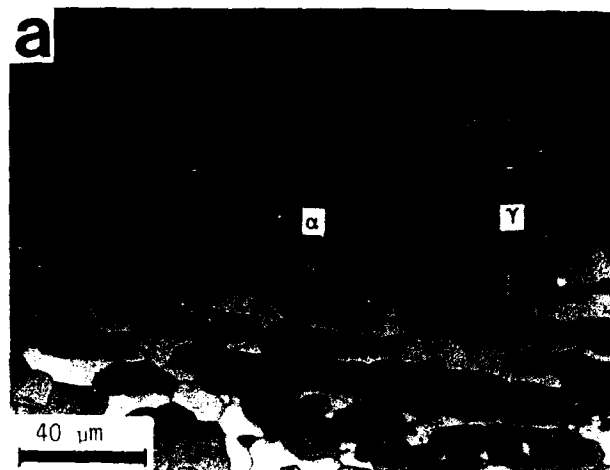


Figure 18. Matrices and strengthening phases morphologies in a) C121, b) C131 aged for 24 hours; c) Tridimensional representation of C131 and d) C215 composites aged for 30 minutes.

structures, deformed at about  $0.5 T_m$  and a lower strain rate (21). Their best results obtained on a duplex stainless steel showed an elongation of 95.7 % at 1098 k with a strain rate of  $2.8 \times 10^{-4} \text{ sec}^{-1}$  (21).

Table 6- Elevated and High Temperature Mechanical Behavior of LASC3 (Aged:  $T=1023 \text{ K}$ ,  $t=24 \text{ H}$ ,  $\dot{\epsilon} = 2 \times 10^{-4} \text{ sec}^{-1}$ ).

MICRO	PROPERTY	$\sigma_u$	$\sigma_y$	%E1
		ksi	ksi	%
593 K	C121	89	48	50
	C131	164	130	15
1073 K	C215	8	---	180
	C225	15	---	61

## SUMMARY AND CONCLUSIONS

The microstructural development during deformation and aging, mechanical and thermal behavior of low activation stainless composites have been studied. Four different sequences of microstructural development were designed: C12A, C13A, C21B and C22B with following characteristics:

C12A: good combination of strength and ductility at 593 K (better than duplex stainless steels).

C13A: Ductile fracture with very high strength at 593 K. Decrease of strength and ductility due to formation of  $\beta_{Mn}$  phase. Large increase in strength and ductility above 993 K due to the formation of the secondary ferrite within the austenite and the absence of any brittle phases.

C21B: Very good combination of strength and ductility after annealing at 1023 K, due to absence of any brittle phases and to a high thermal stability, and to the precipitation of

secondary ferrite in the austenite.

C22B: Similar behavior to C21B at room temperature and after annealing at 1023 K. Fine, fibrous precipitation of Mn carbides in the austenite.

The tensile properties of the C121 and C131 at 593 K are almost the same as at room temperature, this means high thermal stability at 593 K. Thus LASC3 has the potential to be used safely at 593 K. However further work is needed to evaluate its performance under irradiation conditions.

A high degree of superplasticity can be achieved in these composites with two laminated matrices: ferrite and austenite and the development of secondary equiaxed ferrite within the austenite matrix.

#### REFERENCES

1. Kesternich, W., Meertens, D., Acta Met. 34, 6 (1986) 1071.
2. Nuclear Regulatory Commission, 10 CFR Part 61, Federal Registry 47, 248 (1982) 57446.
3. Klueh, R.L. and Bloom, E.E., in "Optimizing Materials for Nuclear Applications", Ed. by Garner, F.A., Gelles, D.S. and Witten, F.W., Publ. TMS, AIME (1973) 73.
4. Bosquez, A.G. and Kesternich, W., Scripta Met. 19 (1985) 57.
5. Banerji, S.K., Metal Progress (1978) 59.
6. Charles, J., Berghezan, A., Lutts, A. and Dancoisne, P.L., Metal Progress (1981) 71.
7. Floreau, S., Met. Trans. 13A (1982) 2003.
8. Muca, B., These de Docteur-Ingenier, Universite P. et M. Curie (1983).
9. Dunning, T.S., Glen, M.L. and Leavenworth, H.W., Metal Progress (1984) 19.
10. Benz, J.C. and Leavenworth, H.W., J. Metals. (1985) 36.
11. Kim, Y.G., Park, Y.S. and Han, J.K., Met. Trans. 16A (1985) 1689.
12. Conn, R.W., Bloom, E.E., Davis, J.W., Gold, R.E., Little, R., Schultz, K.R., Smith, D.L., Wiffen, F.W., Fusion, 5 (1984) 291.
13. Takahashi, H., Takeyama, T., Tanikawa, K., Mivra, R., J. Nucl. Mater. 133/4 (1985) 566.
14. Kesternich, W., and Rothaut, T., J. Nucl. Mater. 103/4 (1981) 845.
15. Thiele, B.A., Diehl, H., Nuclear Technology 66 (1984) 597.
16. Watanabe, K.T., Kondo, T., Nuclear Technology 66 (1984) 630.
17. Yamamoto, N., Shiraishi, H., Kamitsubo, H., Kohno, I. and Shikata, T., J. Nucl. Mater. 133/4 (1985) 493.
18. Davis, J.W., Fusion Technology 8 (1985) 1931.
19. Marquis, F.D.S., unpublished work on Fe-Ni-Cr-C-X-Y Multiphase Stainless Steels.
20. Maziasz, P.J., "Micon 86", ASTM STP 979 (1986) 116.
21. Afonja, A.A., in "Duplex Stainless Steels" Ed. Lula, R.A., ASM (1983) 143.
22. Solomon, H.D. and Devine, T.M. in "Duplex Stainless Steels" Ed Lula R.A., ASM (1983) 693.
23. Klueh, R.L. and Tanaka, M.P., J. Metals 16 (1985).
24. Marquis, F.D.S., unpublished work on Fe-Mn-Al-C-X-Y Low Activation Composites.

# INFLUENCE OF DYNAMIC STRAIN AGING ON THE WORK HARDENING OF A Fe-Mn-Al STEEL IN THE TEMPERATURE RANGE 20 TO 700°C

Cristina Godoy, Berenice Gonzalez, Paulo Roberto Cetlin,  
Evando Mirra de Paula e Silva

Dept. of Met. Engr., Fed. Univers. at  
Minas Gerais, Belo Horizonte, Brazil

## ABSTRACT

The effects of dynamic strain aging on the strain hardening behaviour of an austenitic Fe-Mn-Al-Si alloy containing 0,13%C were investigated by means of tensile tests performed in the temperature range 20 to 700°C at a strain rate of  $6,0 \times 10^{-4} \text{ s}^{-1}$ . The work hardening coefficient was determined from "log  $\sigma$  versus log  $\epsilon$ " plots and two stages of deformation were observed at lower temperatures. Curves of the work hardening coefficient as a function of temperature showed two peaks at 300 and 550°C, corresponding to the two stages of deformation. Analysis of the difference in the intensity of these two peaks suggests that it is due to different mechanisms of aging operating in the different temperatures.

DYNAMIC STRAIN AGING (DSA) in austenitic alloys is being studied at length<sup>(1,2)</sup>; many aspects of the phenomenon remain to be clarified. The mechanisms involved in DSA, in this case, are the interaction of dislocations with vacancy/interstitials associations, or of dislocations with substitutionals. The need of consideration of the association of point defects is a consequence of the values of the dislocation/interstitial interaction energy for these alloys, which is lower than for FCC systems.

The study of the evolution of the work hardening exponent and of work hardening rate with testing temperature when considered in its different regions, confirm the proposed mechanisms for DSA in FCC systems. This is shown in the present paper for an austenitic Fe-Mn-Al-Si alloy with 0,13%C.

## EXPERIMENTAL PROCEDURES

A 2,5kg ingot was produced in an induction furnace with the following average composition: 0,13%C; 1,1%Si; 6,7%Al; 37,3%Mn, balance Fe. The ingot was forged at 900-1100°C down to square section bars 10 x 10mm. After the last forging step, the bars were held at 1100°C for 15 minutes and water quenched. The bars were then cold rolled down to a 2mm thickness, and the material was annealed for 1 hour at 900°C. Flat tensile specimens were then machined with a 27,7mm gage length and 1,08mm thickness. Tensile testing was performed in a INSTRON model T10, under an Argon atmosphere; crosshead speed was 0,1cm/min, leading to a strain rate  $\dot{\epsilon} = 6,0 \times 10^{-4} \text{ sec}^{-1}$ . The temperature range was 20-700°C. Tensile specimens grip ends were cut for metallographic and X-Rays analysis.

## EXPERIMENTAL RESULTS

The microstructure of the alloy consisted of only one phase, the austenite, with ASTM grain size 5. X-Rays analysis confirmed the presence of this phase, which had a 3,667Å lattice parameter. Serrated yielding was observed in the stress-strain curves in the temperature interval 200°C-550°C. Figure 1 shows yield and tensile strength as a function of temperature.

The work hardening coefficient  $n$  and the coefficient  $K$  from Hollomon's equation  $\sigma = K\epsilon^n$  was evaluated through a computer program, to which 40 to 60 true stress-true strain data points were fed. These pairs were taken before the onset of necking. Curves of log  $\sigma$  x log  $\epsilon$  (fig.2) show that one actually has two linear ranges, whose size is temperature dependent. As temperature rises, the slopes of the two straight

lines get closer, till only one slope is observed. The slope of the higher strain line was always higher than that of the lower strain range. Figure 3 shows the evolution of  $n$  with temperature for both ranges. Figure 4 shows the change in true stress at different strain levels with temperature. In order to analyse the work hardening behavior in both ranges, the parameter  $d\sigma/d\epsilon = K n \epsilon^{n-1}$  was calculated for  $\epsilon = 5\%$  and for  $\epsilon = 12\%$ , using the values of  $n$  and  $K$  from the computer program, which are listed in Table 1. The change of  $d\sigma/d\epsilon$  with temperature is shown in fig.5.

#### DISCUSSION

Curves in fig.1 show an anomalous behaviour, which were identified in a previous paper(1) as due to dynamic strain aging. The  $300^\circ\text{C}$  peak was interpreted as resulting of a reordering of vacancy/carbon atoms pairs in the dislocation stress fields, following a Snoek-Schoek mechanism. It has been suggested that the  $550^\circ\text{C}$  peak is caused by the interaction of dislocations with substitutionals, involving long range diffusion and following Cottrell's model. In the present case, the substitutional would be the Aluminum.

The curves in fig.4 also showed peaks at the above mentioned temperatures, as observed for FCC systems by other authors(4). The work hardening curves in fig.5 also show peaks around  $300^\circ\text{C}$  and  $500-600^\circ\text{C}$ , instead of showing a smooth decrease in  $n$ , which is typical of materials where DSA is not observed.

For the 5% curve (Fig.5), the  $300^\circ\text{C}$  peak associated with a Snoek-Schoek mechanism is not very strong probably due to the weak pinning typical of this interaction. The strong peak at  $600^\circ\text{C}$  would be due to formation of Aluminum atmospheres around the dislocations, leading to a strong Cottrell pinning.

The  $300^\circ\text{C}$  peak in the 12% curve (Fig.5) is weaker than for the 5% curve. At 12% strain both vacancy concentration and dislocation density are higher than for 5%, and it is possible that the number of pairs undergoing reorientation is lower for 12% strain. The second peak in the 12% curve (Fig.5) is at a temperature lower than in the 5% curve. This is probably due to a higher diffusion of Aluminum caused by the higher vacancy concentration. There is probably an interaction between the two peaks in the 12% curve, making difficult a comparison of the second peak for 5% and 12% strain.

#### CONCLUSIONS

1. The curves for the change with temperature of the flow stress at different strain levels, showed peaks around  $300^\circ\text{C}$

and  $550^\circ\text{C}$ , due to dynamic strain aging.  
 2.  $\log \sigma \times \log \epsilon$  curves have shown two stages, leading to two values of the work hardening exponent  $n$ , which were smaller for the first stage.  
 3. Curves of  $d\sigma/d\epsilon$  versus temperature have shown peaks whose amplitude depends on temperature and strain level (1st or 2nd stage). Higher peaks were observed around  $600^\circ\text{C}$ , and these were considered as coming from Aluminum atmospheres formed in the dislocations stress fields. The peaks at  $300^\circ\text{C}$  are small, and this was attributed to the mechanism of reorientation of pairs vacancy/carbon atoms, in the stress fields of dislocations. The  $300^\circ\text{C}$  peak at higher strain is even smaller, probably due to a smaller ratio dislocation density/number of vacancies.

#### REFERENCES

1. Hannula, S.P.; Korhonen, M.A. and Li, C.Y.; Met. Trans. A, 17A, 1757-67 (1986).
2. Cribb, E.R. and Reed-Hill, R.E.; Met. Trans. A, 8A, 71-76 (1983).
3. Godoy, C. and Paula e Silva, E.M.; Anais do XXXVIII Congresso Anual da ABM, 2, 187-97 (1983).
4. Jenking, C.F. and Smith, G.V.; Transaction of the Metallurgical Society of AIME, 245, 2149, 56 (1969).
5. Reed-Hill, R.E.; Reviews on the Deformation Behavior of Materials 2, 217-42 (1977).

Table 1 - Values of n, k and correction coefficient (s) at different temperatures

TEMPERATURE	Stage I			Stage II		
	n	K(MN/m <sup>2</sup> )	s	n	K/MN/m <sup>2</sup>	s
20°C	0,24	83	0,988	0,48	145	0,999
200°C	0,37	77	0,996	0,63	139	0,999
300°C	0,38	77	0,999	0,63	135	0,999
400°C	0,32	64	0,998	0,59	122	0,998
500°C	0,29	58	0,989	0,56	117	0,999
550°C	0,34	61	0,989	0,52	95	0,999
600°C	0,36	63	0,999	0,49	86	0,997
650°C	0,32	51	0,999	0,42	68	0,996
700°C	0,38	53	0,999	0,30	44	0,980



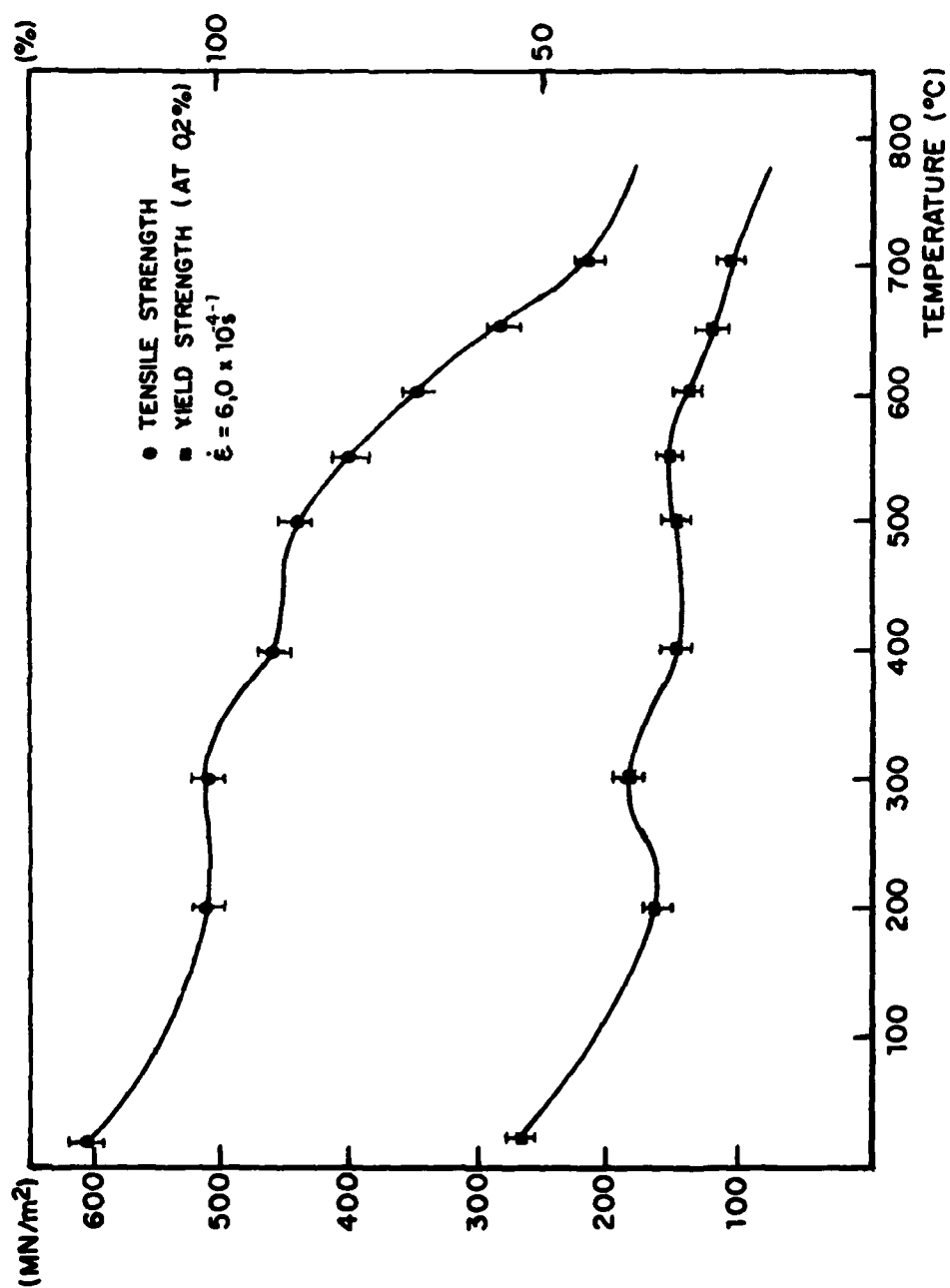


Figure 1 - Change in yield and tensile strength with temperature.

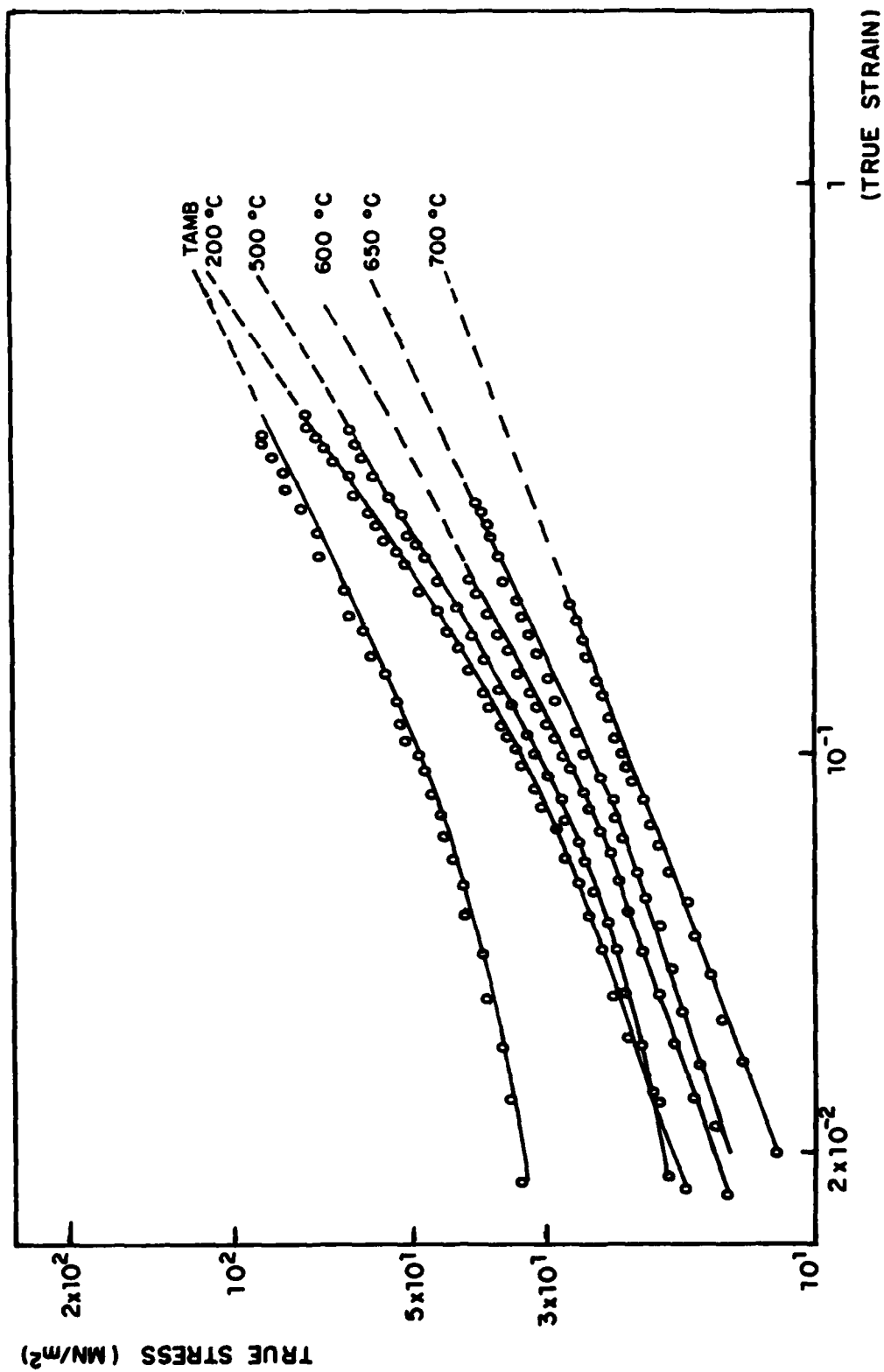


Figure 2 - True stress-true strain curves in log-log scale, at several temperatures.

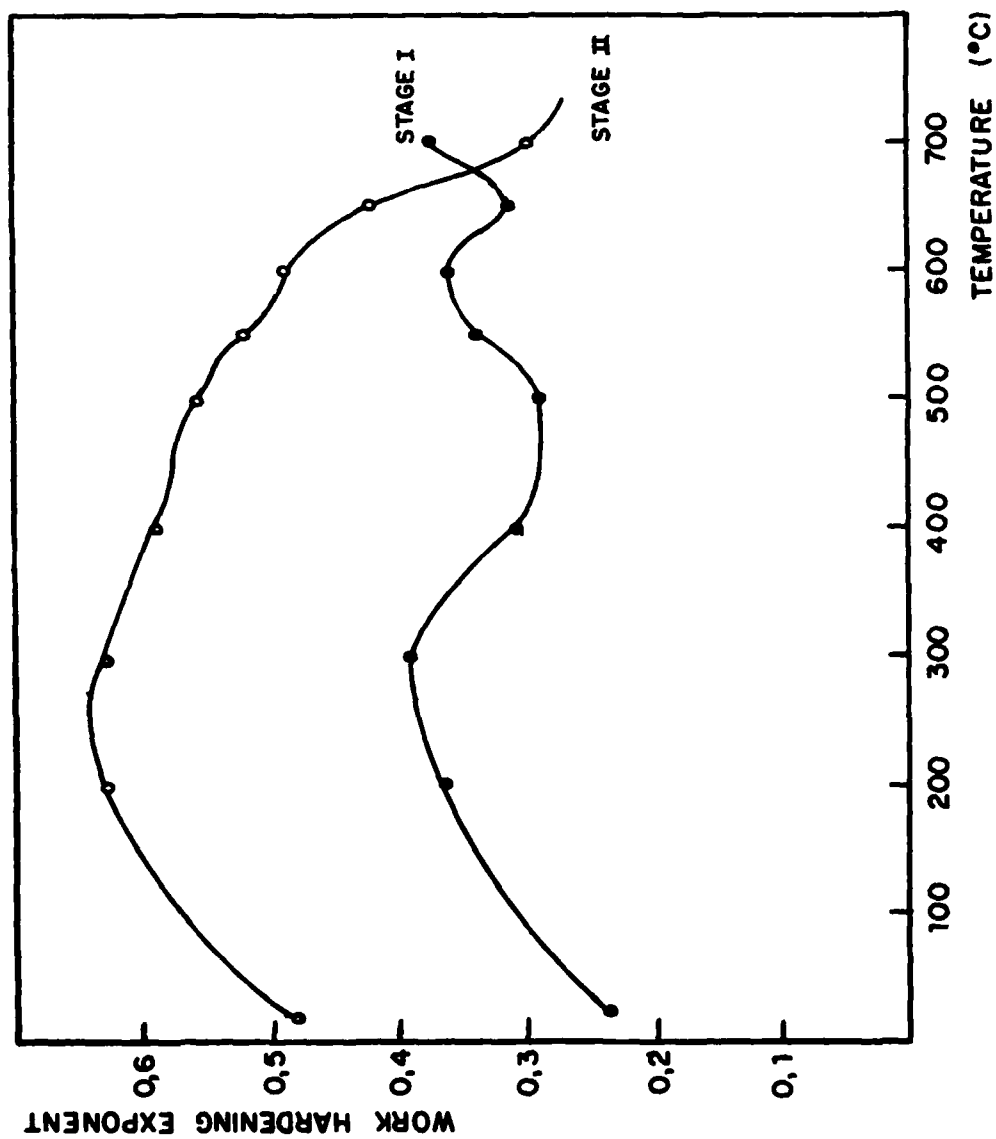


Figure 3 - Evolution of the Work Hardening Coefficient with Temperature for Stage I ( $\epsilon=5\%$ ) and Stage II ( $\epsilon=12\%$ )

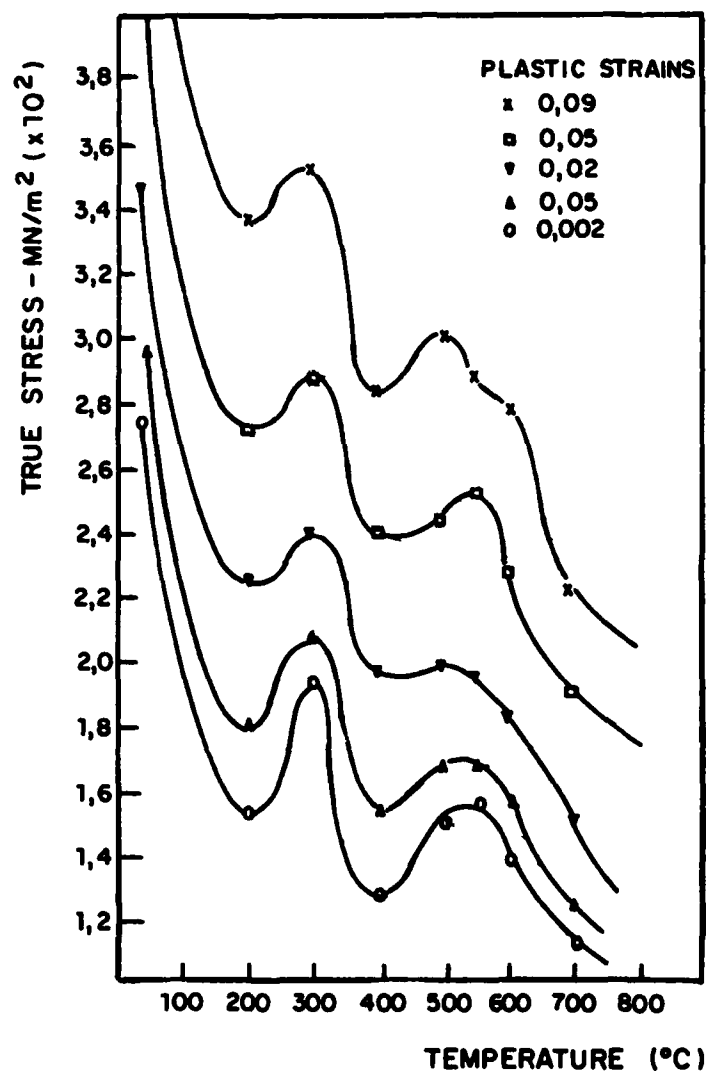


Figure 4 - Evolution of true stress at different strains with temperature.  $\dot{\epsilon} = 6,0 \times 10^{-4} \text{ s}^{-1}$

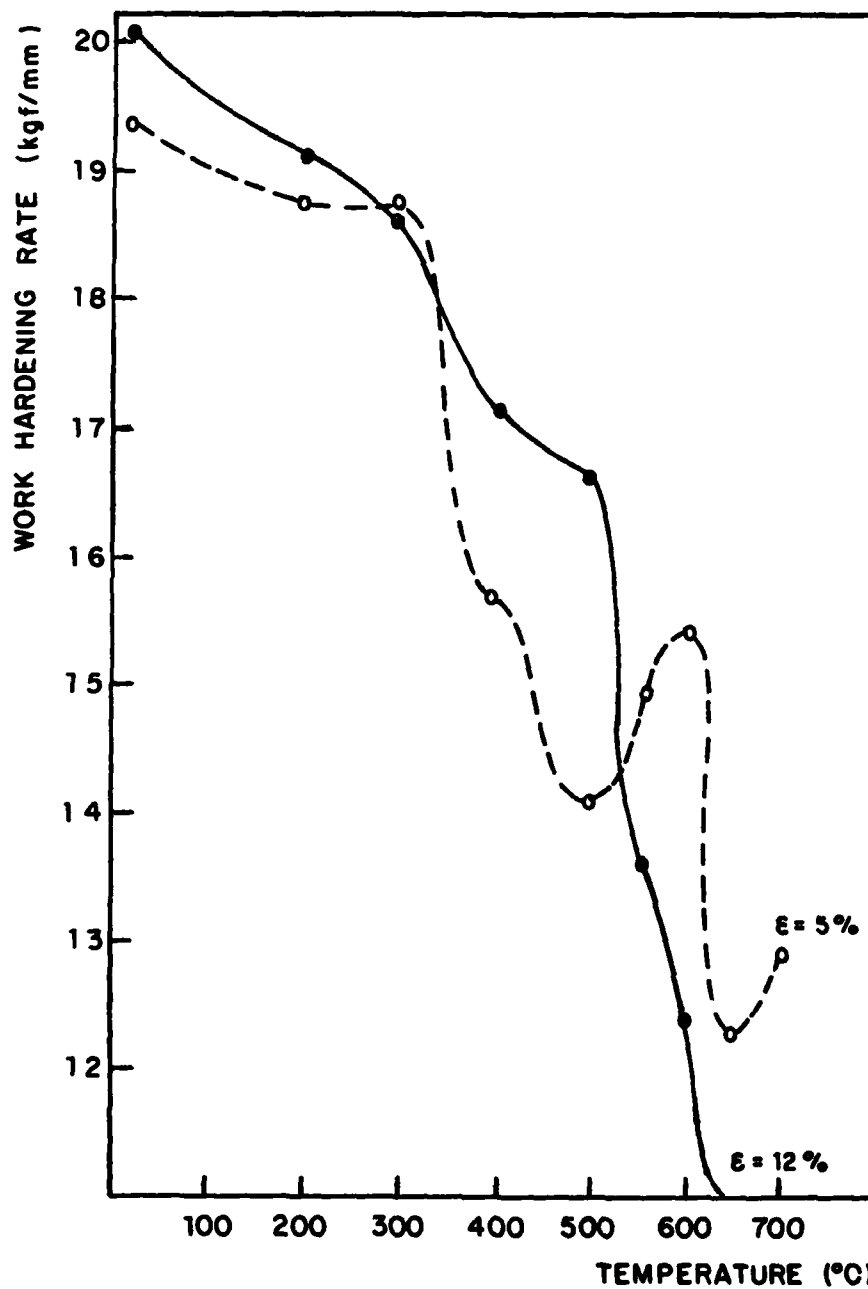


Figure 5 - Evolution of Work Hardening Rate ( $d\sigma/d\epsilon$ ) with temperature for Stage I ( $\epsilon=5\%$ ) and Stage II ( $\epsilon=12\%$ )